FABRICATION AND CHEMICAL MODIFICATIONS OF PHOTONIC CRYSTALS PRODUCED BY MULTIPHOTON LITHOGRAPHY

A Dissertation
Presented to
The Academic Faculty

by

Vincent Wingsang Chen

In Partial Fulfillment
of the Requirements for the Degree
Doctorate of Philosophy in the
School of Chemistry and Biochemistry

Georgia Institute of Technology
December 2011

FABRICATION AND CHEMICAL MODIFICATIONS OF PHOTONIC CRYSTALS PRODUCED BY MULTIPHOTON LITHOGRAPHY

Approved by:

Dr. Joseph W. Perry, Advisor
School of Chemistry and Biochemistry
Georgia Institute of Technology

Dr. Mohan Srinivasarao
School of Materials Science and Engineering
Georgia Institute of Technology

Dr. Jean-Luc Brédas
School of Chemistry and Biochemistry
Georgia Institute of Technology

Dr. Rick Trebino
School of Physcis
Georgia Institute of Technology

Dr. Andrew Lyon
School of Chemistry and Biochemistry
Georgia Institute of Technology

Date Approved: November 8, 2011

To my parents, Sarah and Alex.

ACKNOWLEDGEMENTS

I would like to thank my advisor, Dr. Joseph Perry, for his guidance and confidence in me. He has always been extremely understanding, patient and supportive throughout my career. He showed me the excitement in working diligently to perform experiments and obtain results even late into the night. This motivation stuck with me though many late nights gathering last minute results for program review deadlines and conferences throughout the years. Without his hard work and dedication to obtain a seemingly unlimited supply of funding, I would have been stuck performing experiments with an antiquated fabrication system that required manual input to perform each mundane step instead of the state of the art system that we have built together that can generate arrays of samples at the push of a button.

I would also like to thank Dr Joel Hales for his help and friendship. He is the senior figure who I wished was with the group when I first joined. His knowledge in photophysics, optics and electronics, along with his ability to explain concepts in ways I can understand, was instrumental to my development. He is always available to provide answers my many questions and valuable advices when Joe was otherwise occupied.

This work could not have been accomplished without the help and support from our group members and collaborators. I would especially like to thank Nathan Jarnagin for numerous SEM sessions during nights and weekends, Dr Yadong Zhang for the help with photoresist formulations and the metallization project, Dr Yunnan Fang for the help in the materials aspects of the titania and diatom projects, and Kelly Perry for showing

me the ropes of LabView that has enabled me to write the automation software to control the fabrication system used for this work.

Finally, I would like to thank my family for their continuing support. Without my wife Sarah's support throughout the years, and especially the times I had to work away from home these past few months, I would not have been able to complete this degree. And our baby son Alex, born shortly after my six months review, has been cooperative throughout these crucial last months, although at times he is more difficult to understand than unexpected experimental results.

TABLE OF CONTENTS

LIST OF TABLES

Page

LIST OF FIGURES

SUMMARY

This thesis is concerned with the fabrication methodology of polymeric photonic crystals operating in the visible to near infrared regions and the correlation between the chemical deposition morphologies and the resultant photonic stopband enhancements of photonic crystals.

Multiphoton lithography (MPL) is a powerful approach to the fabrication of polymeric 3D micro- and nano-structures with a typical minimum feature size ~ 200 nm. The completely free-form 3D fabrication capability of MPL is very well suited to the formation of tailored photonic crystals (PCs), including structures containing well defined defects. Such structures are of considerable current interest as micro-optical devices for their filtering, stop-band, dispersion, resonator, or waveguiding properties. More specifically, the stop-band characteristics of polymer PCs can be finely controlled via nanoscale changes in rod spacings and the chemical functionalities at the polymer surface can be readily utilized to impart new optical properties.

Nanoscale features as small as 65 ± 5 nm have been formed reproducibly by using 520 nm femtosecond pulsed excitation of a 4,4'-bis(di-*n*-butylamino)biphenyl chromophore to initiate crosslinking in a triacrylate blend. Dosimetry studies of the photoinduced polymerization were performed on chromophores with sizable two-photon absorption cross-sections at 520 and 730 nm. These studies show that sub-diffraction limited line widths are obtained in both cases with the lines written at 520 nm being smaller. Three-dimensional multiphoton lithography at 520 nm has been used to fabricate polymeric woodpile photonic crystal structures that show stop bands in the visible to near-infrared spectral region.

85 ± 4 nm features were formed using swollen gel photoresist by 730 nm excitation MPL. An index matching oil was used to induce chemical swelling of gel resists prior to MPL fabrication. When swollen matrices were subjected to multiphoton excitation, a similar excitation volume is achieved as in normal unswollen resins. However, upon deswelling of the photoresist following development a substantial reduction in feature size was obtained. PCs with high structural fidelity across 100 μm × 100 μm × 32 layers exhibited strong reflectivity (>60% compared to a gold mirror) in the near infrared region. The positions of the stop-bands were tuned by varying the swelling time, the exposure power (which modifies the feature sizes), and the layer spacing between rods.

Silver coatings have been applied to PCs with a range of coverage densities and thicknesses using electroless deposition. Sparse coatings resulted in enhanced reflectivity for the stop band located at ~5 μm, suggesting improved interface reflectivity inside the photonic crystal due to the Ag coating. Thick coatings resulted in plasmonic bandgap behavior with broadband reflectivity enhancement and PC lattice related bandedge at 1.75 μm. Conformal titania coatings were grown onto the PCs via a surface sol-gel method. Uniform and smooth titania coatings were achieved, resulting in systematically red-shifted stopbands from their initial positions with increasing thicknesses, corresponding to the increased effective refractive index of the PC. High quality titania shell structures with modest stopbands were obtained after polymer removal.

Gold replica structures were obtained by electroless deposition on the silica cell walls of naturally occurring diatoms and the subsequent silica removal. The micron-scaled periodic hole lattice originated from the diatom resulted in surface plasmon interferences when excited by infrared frequencies. The hole patterns were characterized and compared with hexagonal hole arrays fabricated by focused ion beam etching of similarly gold plated substrate. Modeling of the hole arrays concluded that while diatom

replicas lack long-ranged periodicity, the local hole to hole spacings were sufficient to generate enhanced transmission of 13% at 4.2 μm.

The work presented herein is a step towards the development of PCs with new optical and chemical functionalities. The ability to rapidly prototype polymeric PCs of various lattice parameters using MPL combined with facile coating chemistries to create structures with the desired optical properties offers a powerful means to produce tailored high performance photonic crystal devices.

CHAPTER 1

INTRODUCTION

1.1 Introduction to Photonic Crystals

Photonic crystals (PC) are an interesting class of optical material where the periodic modulation of the refractive index forbids the propagation of photons with specific frequencies through these structures, analogous to the electronic band gap in semiconductor crystals [1-3]. These photonic bandgaps can be engineered to the desired operational frequencies by manipulation of the PC's lattice periodicity and refractive index [4-6]. While PCs with large dielectric contrast can act as perfect reflectors or filters [5], much of the research interest had involved the incorporation of line defects to control the direction of light propagation and spot defects to form microcavites for lasing applications [7]. The development of these various functionalities should enable the creation of photonic circuits that can carry out signal processing on a photonic chip [8], much like the integrated circuits for electronics.

Whereas photonic bandgaps inhibit light propagation in all directions, PCs that exhibit directional stopbands can be achieved in a much wider range of materials and designs due to the reduced restrictions in the refractive index contrast. These photonic stopbands can be utilized in a broad range of applications, for example: 1) superprism effects where the dispersion of the angle of refraction can be used to spatially separate wavelengths for signal processing [9, 10], 2) sensing applications where attachment of analytes alter the local refractive index resulting in a shift of the band position, 3) superpositioning of stopband spectra to modify the intensity distribution of an emission spectrum [11], reduction of lasing thresholds [12], and fluorescence enhancement through the elimination of forward optical loss [13].

1.2 Challenges in the Fabrication of Photonic Crystals

Numerous techniques have been employed to fabricate PCs with a wide range of lattices and various materials compositions, ranging from semiconductor-based structures [5], to self-assembly of microspheres [14, 15], as well as through holographic lithography [16, 17]. While each technique has its merits, lengthy fabrication times coupled with limited structural variability hinders their application versatility. In contrast, multiphoton lithography (MPL) is a versatile fabrication method because of the ability to rapidly generate PCs of different symmetries, periodicities and defects through a free-form lithography process that can be defined through a simple CAD file defining the desired structural parameters [18]. The fabrication process can be relatively straightforward as the photoinduced crosslinking of the 3D patterned volume can be developed in a single solvent wash step [19]. Furthermore, wide-ranging photosensitive materials, including acrylates, epoxys, organic-inorganic hybrids, as well as sol-gels, can be patterned by MPL to obtain the desired mechanical, chemical and optical properties [20-24].

Two critical features in the MPL fabrication of PCs are spatial resolution and material dielectric contrast: the spatial resolution of the crosslinked volume controls the spectral position of the photonic stopbands while the dielectric contrast affects the intensity of the stopbands. The operational frequency of the PC scales can also be controlled through manipulation of its lattice constants. A typical MPL systems utilizes an excitation wavelength of ~800 nm from a mode-locked Ti:sapphire laser to produce volume elements with minimum dimensions of ~200 nm in the lateral direction and ~500 nm in the axial direction [25-27]. Therefore, these sizes dictate the minimum achievable layer spacing of fabricated PCs and, as a result, the range of photonic stopbands is limited on the short wavelength side to the near-infrared spectral region (~1 to 1.3 μm) [4, 26]. While there have been several reports on resolution improvements in feature sizes by reducing the crosslinking density in the exposed volume [20, 28-30], most of these

methods rely on mechanical support designs that cannot be translated to formation of three-dimensional PCs. Post fabrication modification of PCs has been presented as an alternative route for resolution improvement, however these routes typically result in either anisotropic feature reduction, as in plasma etching [31] or thermal liberation of organic species [24], or structural deformation as found during a sol-gel condensation approach [21].

The intensity of the photonic stopbands is dependent on the refractive index contrast imparted to the PC; typical polymerizable materials possess moderate refractive indices (1.5 to 1.6) which result in reduced PC intensities thereby limiting potential applications [4, 25, 26, 32]. Chemical modification to the polymeric PCs and/or deposition of metals or semiconductors onto the structures provides a way to manipulate the dielectric contrast to enhance stopband performance and thereby broaden the range of applications [33-38]. Additionally, through the metallization approach, once the thickness of the metal becomes greater than the skin depth, the coated polymeric PCs behave like metallic structures [35, 36], which show promise as filters for thermal and terahertz applications [39].

In addition to the aforementioned synthetic PCs, there are PCs that also exist naturally including opals [14] as well as a wide range of biologically produced photonic structures [40-42]. The intricate ordering found in beetle scales [43, 44], butterfly wings [45], peacock feathers [46], and diatoms [47] not only exhibit interesting optical properties [48-50], but are also ideal templates for investigating surface modifications and their resulting optical changes [51]. These benefits are due to their microporous morphology that is reminiscent of the MPL fabricated PCs as well as the scalable syntheses afforded by these naturally occurring objects.

1.3 Objectives of Dissertation Work

MPL has been demonstrated to be a powerful technique for the fabrication of a wide range of microstructures. The versatility of this method has been employed in the production of PCs with a broad range of lattice parameters typically resulting in photonic stopbands in the infrared wavelength region. Researchers have begun to address the materials limitations imposed by the photopolymerizable resin systems through chemical modifications. Most of these efforts thus far, however, have been driven by proof-of-concept type demonstrations. For instance, very few reports have investigated the coating morphologies of the microporous PCs and their effect on the resultant optical characteristics. Furthermore, many reports on improved resolution of MPL generated features demonstrate the feasibility of achieving finer feature sizes without considering the practicality of these approaches for building free standing 3D structures.

The objectives of this dissertation work were two-fold. The first objective was to develop methods to improve the resolution of MPL for the fabrication of PCs with expanded stopband tunability towards the visible portion of the electromagnetic spectrum. The key questions addressed were:

1. Does the wavelength dependence of the diffraction-limited focal volume translate to improved MPL fabrication resolution at shorter excitation wavelengths?
2. Will the reduction of crosslinkable groups within the excitation focal volume lead to a systematically-controllable method for feature size reduction and will this method give rise to isotropic resolution improvement compared to other published approaches?

Two independent routes were utilized for the fabrication of PCs with sub-100 nm resolution. Spatial resolution is directly proportional to the size of the focal volume, which itself scales with excitation wavelength; thus reducing the excitation wavelength

should result in improved resolution. Chapter 4 describes how short wavelength excitation (520 nm) using a biphenyl-based two-photon initiator produced feature sizes down to 65 nm with PCs possessing visible stopbands. While this approach is feasible even with commonly used Ti:Sapphire lasers, excitation power constraints coupled with the lack of efficient two-photon initiators in this spectral region may hinder its practicality. Consequently, an alternative method was adopted where the fabrication medium was modified while the traditional instrumentation and fabrication process was preserved. Chapter 5 reports on the use of chemically-induced mechanical swelling of photoresists to reduce the fraction of crosslinkable groups available in the excitation volume which gave rise to feature sizes down to 85 nm after development. Stopbands with peak reflectivities of over 60% were achieved with central wavelengths continuously tunable between 1 and 2 μm.

The second objective was to impart novel functionalities to the polymeric PCs through surface modification and subsequent deposition of metal and metal oxide. The questions to be address were:

1. Are the coating morphologies and optical characteristics found for flat surfaces the same as for the surfaces of the PCs?
2. Can a uniform coating of metal or metal oxide be applied conformally onto microporous PCs with stopbands in the telecommunications spectral region? Can this conformal coating be effectively delivered to the interior of PC?
3. What is the relationship between coating morphology and the resultant optical properties? Can the morphology be tailored for specific applications?

In order to generate the number of PC structures necessary to test and optimize the wet chemical processing conditions, a high speed instrumentation system was designed and algorithms were developed to enable the rapid fabrication of PCs. This automated system, described in Chapter 3, utilizes fabrication speeds of 10 mm/s (compared to typical speeds of ~100 μm/s) which permitted investigation of various

lattice parameters necessary for achieving desired photonic stopband positions. Furthermore, owing to structural distortions that subsequent solution processing can induce, modification of the PC lattice parameters was also necessary to achieve the optimal combination of mechanical stability and stopband intensity. Once the proper lattice parameters were obtained, arrays of PCs were fabricated to facilitate characterization and optimization of processing conditions as well as for reproducibility.

To increase the reflectivity and to tune the positions of the initial polymeric PC stopbands, silver and titania were chemically deposited onto the PCs. Chemical modification of the non-crosslinked acrylates on the polymer surfaces with amines provided the ability to preferentially deposit materials onto the PCs only. Chapter 6 reports on the formation of silver coated PCs via electroless deposition. Different coating morphologies resulted in different optical properties: enhanced stopband reflectivities were observed in sparsely coated PCs whereas broadband reflectivity enhancement was observed, along with the presence of plasmonic band edges, when the coating was thick and continuous. Tuning the effective refractive index of the polymer PCs by titania deposition is described in Chapter 7. The coatings resulted in a thickness-dependent red-shifting of the stopband positions. Following optimization of the ratio of polymer to titania material thickness, titania shell structures were able to be produced after high temperature sintering with only minor cracking.

Diatoms are naturally occurring algae which possess periodic arrangements of holes in the nanometer to micrometer scale, resulting in two-dimensional PC slabs that provide good templates for surface modification. Consequently, the metallization of diatoms with gold coatings was pursued and is described in Chapter 8 along with their resulting extraordinary optical transmission properties. Effectively, the periodicity in the diatom hole arrangement led to interference of surface plasmons for incident excitation wavelengths resulting in enhanced transmission of selected wavelengths. Analyses

aimed at understanding these surface plasmon-mediated transmission changes are also presented in Chapter 8.

While most two-photon initiators used for MPL in the literature have been mainly attributed to initiation following intersystem crossing from the lowest excited singlet state to the triplet state [52], the multiphoton initiator used in this dissertation work, *E*,*E*-1,4-*bis*[4-(di-*n*-butylamino)styryl]-2,5-dimethoxybenzene (DABSB), and other two-photon absorbing chromophores with the same structural motifs have been found to efficiently initiate radical crosslinking via electron transfer [25]. The unique characteristics of DABSB are its high fluorescence quantum yield [53] which is suggestive of a low triplet yield, its cubic irradiance dependence on the fabrication of features via MPL [54], and its inability to efficiently induce polymerization under UV illumination which could be indicative of initiation from an upper level excited state. Femtosecond transient absorption experiments (detailed in the Appendix) were performed on solutions of DABSB with and without additives in attempt to elucidate the initiation mechanism. While many interesting phenomena were observed, the population of photogenerated cations proved to be too small to provide any definitive support for a particular mechanism using this technique.

A summary of the findings and the conclusions drawn from these investigations are reported in Chapter 9. Ongoing investigations and potential future extensions of this work are included in the discussion.

REFERENCES

1. S. John, "Strong localization of photons in certain disordered dielectric superlattices," Physical Review Letters **58**, 2486 (1987).

2. E. Yablonovitch, "Inhibited Spontaneous Emission in Solid-State Physics and Electronics," Physical Review Letters **58**, 2059 (1987).

3. J. Joannopoulos, S. Johnson, J. Winn, and R. Meade, *Photonic Crystals: Molding the Flow of Light (Second Edition)* (Princeton University Press, 2008).

4. M. Straub, and M. Gu, "Near-infrared photonic crystals with higher-order bandgaps generated by two-photon photopolymerization," Opt. Lett. **27**, 1824-1826 (2002).

5. S. Y. Lin, J. G. Fleming, D. L. Hetherington, B. K. Smith, R. Biswas, K. M. Ho, M. M. Sigalas, W. Zubrzycki, S. R. Kurtz, and J. Bur, "A three-dimensional photonic crystal operating at infrared wavelengths," Nature **394**, 251-253 (1998).

6. D. F. Sievenpiper, M. E. Sickmiller, and E. Yablonovitch, "3D Wire Mesh Photonic Crystals," Physical Review Letters **76**, 2480 (1996).

7. A. Tandaechanurat, S. Ishida, D. Guimard, M. Nomura, S. Iwamoto, and Y. Arakawa, "Lasing oscillation in a three-dimensional photonic crystal nanocavity with a complete bandgap," Nat Photon **5**, 91-94 (2011).

8. Y. A. Vlasov, M. O'Boyle, H. F. Hamann, and S. J. McNab, "Active control of slow light on a chip with photonic crystal waveguides," Nature **438**, 65-69 (2005).

9. J. Serbin, and M. Gu, "Experimental Evidence for Superprism Effects in Three-Dimensional Polymer Photonic Crystals," Advanced Materials **18**, 221-224 (2006).

10. J. Serbin, and M. Gu, "Superprism phenomena in waveguide-coupled woodpile structures fabricated by two-photon polymerization," Opt. Express **14**, 3563-3568 (2006).

11. M. Barth, A. Gruber, and F. Cichos, "Spectral and angular redistribution of photoluminescence near a photonic stop band," Physical Review B **72**, 085129 (2005).

12. V. I. Kopp, B. Fan, H. K. M. Vithana, and A. Z. Genack, "Low-threshold lasing at the edge of a photonic stop band in cholesteric liquid crystals," Opt. Lett. **23**, 1707-1709 (1998).

13. Y.-Q. Zhang, J.-X. Wang, Z.-Y. Ji, W.-P. Hu, L. Jiang, Y.-L. Song, and D.-B. Zhu, "Solid-state fluorescence enhancement of organic dyes by photonic crystals," Journal of Materials Chemistry **17**, 90-94 (2007).

14. F. Marlow, Muldarisnur, P. Sharifi, R. Brinkmann, and C. Mendive, "Opals: Status and Prospects," Angewandte Chemie International Edition **48**, 6212-6233 (2009).

15. D. J. Norris, E. G. Arlinghaus, L. Meng, R. Heiny, and L. E. Scriven, "Opaline Photonic Crystals: How Does Self-Assembly Work?," Advanced Materials **16**, 1393-1399 (2004).

16. M. Campbell, D. N. Sharp, M. T. Harrison, R. G. Denning, and A. J. Turberfield, "Fabrication of photonic crystals for the visible spectrum by holographic lithography," Nature **404**, 53-56 (2000).

17. S. Jeon, J.-U. Park, R. Cirelli, S. Yang, C. E. Heitzman, P. V. Braun, P. J. A. Kenis, and J. A. Rogers, "Fabricating complex three-dimensional nanostructures with high-resolution conformable phase masks," Proceedings of the National Academy of Sciences of the United States of America **101**, 12428-12433 (2004).

18. V. Mizeikis, K. K. Seet, S. Juodkazis, and H. Misawa, "Three-dimensional woodpile photonic crystal templates forthe infrared spectral range," Opt. Lett. **29**, 2061-2063 (2004).

19. B. H. Cumpston, S. P. Ananthavel, S. Barlow, D. L. Dyer, J. E. Ehrlich, L. L. Erskine, A. A. Heikal, S. M. Kuebler, I. Y. S. Lee, D. McCord-Maughon, J. Qin, H. Rockel, M. Rumi, X.-L. Wu, S. R. Marder, and J. W. Perry, "Two-photon polymerization initiators for three-dimensional optical data storage and microfabrication," Nature **398**, 51-54 (1999).

20. J. Saulius, and et al., "Two-photon lithography of nanorods in SU-8 photoresist," Nanotechnology **16**, 846 (2005).

21. A. Ovsianikov, X. Shizhou, M. Farsari, M. Vamvakaki, C. Fotakis, and B. N. Chichkov, "Shrinkage of microstructures produced by two-photon polymerization of Zr-based hybrid photosensitive materials," Opt. Express **17**, 2143-2148 (2009).

22. I. Sakellari, A. Gaidukeviciute, A. Giakoumaki, D. Gray, C. Fotakis, M. Farsari, M. Vamvakaki, C. Reinhardt, A. Ovsianikov, and B. Chichkov, "Two-photon polymerization of titanium-containing sol–gel composites for three-dimensional structure fabrication," Applied Physics A: Materials Science & Processing **100**, 359-364 (2010).

23. S. Passinger, M. S. M. Saifullah, C. Reinhardt, K. R. V. Subramanian, B. N. Chichkov, and M. E. Welland, "Direct 3D Patterning of TiO2 Using Femtosecond Laser Pulses," Advanced Materials **19**, 1218-1221 (2007).

24. J. Li, B. Jia, and M. Gu, "Engineering stop gaps of inorganic-organic polymeric 3D woodpile photonic crystals with post-thermal treatment," Opt. Express **16**, 20073-20080 (2008).

25. S. M. Kuebler, M. Rumi, T. Watanabe, K. Braun, B. H. Cumpston, A. A. Heikal, L. L. Erskine, S. Thayumanavan, and J. W. Perry, "Optimizing Two-Photon Initiators and Exposure Conditions for Three-Dimensional Lithographic Microfabrication," Journal of Photopolym. Sci. Technol **14**, 657-668 (2001).

26. M. Deubel, G. von Freymann, M. Wegener, S. Pereira, K. Busch, and C. M. Soukoulis, "Direct laser writing of three-dimensional photonic-crystal templates for telecommunications," Nat Mater **3**, 444-447 (2004).

27. S. Kawata, H.-B. Sun, T. Tanaka, and K. Takada, "Finer features for functional microdevices," Nature **412**, 697-698 (2001).

28. K. Takada, H.-B. Sun, and S. Kawata, "Improved spatial resolution and surface roughness in photopolymerization-based laser nanowriting," Applied Physics Letters **86**, 071122 (2005).

29. J.-F. Xing, X.-Z. Dong, W.-Q. Chen, X.-M. Duan, N. Takeyasu, T. Tanaka, and S. Kawata, "Improving spatial resolution of two-photon microfabrication by using photoinitiator with high initiating efficiency," Applied Physics Letters **90**, 131106 (2007).

30. L. Yan, and et al., "Nonuniform shrinkage and stretching of polymerized nanostructures fabricated by two-photon photopolymerization," Nanotechnology **19**, 055303 (2008).

31. G. von Freymann, T. Y. M. Chan, S. John, V. Kitaev, G. A. Ozin, M. Deubel, and M. Wegener, "Sub-nanometer precision modification of the optical properties of three-dimensional polymer-based photonic crystals," Photonics and Nanostructures - Fundamentals and Applications **2**, 191-198 (2004).

32. S. Maruo, O. Nakamura, and S. Kawata, "Three-dimensional microfabrication with two-photon-absorbed photopolymerization," Opt. Lett. **22**, 132-134 (1997).

33. D. Buso, E. Nicoletti, J. Li, and M. Gu, "Engineering the refractive index of three-dimensional photonic crystals through multilayer deposition of CdS films," Opt. Express **18**, 1033-1040 (2010).

34. J. Li, M. D. M. Hossain, B. Jia, D. Buso, and M. Gu, "Three-dimensional hybrid photonic crystals merged with localized plasmon resonances," Opt. Express **18**, 4491-4498 (2010).

35. V. Mizeikis, S. Juodkazis, R. Tarozaite, J. Juodkazyte, K. Juodkazis, and H. Misawa, "Fabrication and properties of metalo-dielectric photonic crystal structures for infrared spectral region," Opt. Express **15**, 8454-8464 (2007).

36. A. Tal, Y.-S. Chen, H. E. Williams, R. C. Rumpf, and S. M. Kuebler, "Fabrication and characterization of three-dimensional copper metallodielectric photonic crystals," Opt. Express **15**, 18283-18293 (2007).

37. J. Li, B. Jia, G. Zhou, and M. Gu, "Fabrication of three-dimensional woodpile photonic crystals in a PbSe quantum dot composite material," Opt. Express **14**, 10740-10745 (2006).

38. Z.-Z. Gu, S. Kubo, W. Qian, Y. Einaga, D. A. Tryk, A. Fujishima, and O. Sato, "Varying the Optical Stop Band of a Three-Dimensional Photonic Crystal by Refractive Index Control," Langmuir **17**, 6751-6753 (2001).

39. T. Drysdale, "Transmittance of a tunable filter at terahertz frequencies," Appl. Phys. Lett. **85**, 5173 (2004).

40. P. Vukusic, and J. R. Sambles, "Photonic structures in biology," Nature **424**, 852-855 (2003).

41. V. Welch, and J. P. Vigneron, "Beyond butterflies—the diversity of biological photonic crystals," Optical and Quantum Electronics **39**, 295-303 (2007).

42. M. Srinivasarao, "Nano-Optics in the Biological World: Beetles, Butterflies, Birds, and Moths," Chemical Reviews **99**, 1935-1962 (1999).

43. J. W. Galusha, L. R. Richey, M. R. Jorgensen, J. S. Gardner, and M. H. Bartl, "Study of natural photonic crystals in beetle scales and their conversion into inorganic structures via a sol-gel bio-templating route," Journal of Materials Chemistry **20**, 1277-1284 (2010).

44. A. R. Parker, V. L. Welch, D. Driver, and N. Martini, "Structural colour: Opal analogue discovered in a weevil," Nature **426**, 786-787 (2003).

45. K. Michielsen, and D. G. Stavenga, "Gyroid cuticular structures in butterfly wing scales: biological photonic crystals," Journal of The Royal Society Interface **5**, 85-94 (2008).

46. J. Zi, X. Yu, Y. Li, X. Hu, C. Xu, X. Wang, X. Liu, and R. Fu, "Coloration strategies in peacock feathers," Proceedings of the National Academy of Sciences **100**, 12576-12578 (2003).

47. T. Fuhrmann, S. Landwehr, M. El Rharbi-Kucki, and M. Sumper, "Diatoms as living photonic crystals," Applied Physics B: Lasers and Optics **78**, 257-260 (2004).

48. J. Noyes, M. Sumper, and P. Vukusic, "Light manipulation in a marine diatom," Journal of Materials Research **23**, 3229-3235 (2008).

49. L. De Stefano, I. Rea, I. Rendina, M. De Stefano, and L. Moretti, "Lensless light focusing with the centric marinediatom Coscinodiscus walesii," Opt. Express **15**, 18082-18088 (2007).

50. E. De Tommasi, I. Rea, V. Mocella, L. Moretti, M. De Stefano, I. Rendina, and L. De Stefano, "Multi-wavelength study of lighttransmitted through a single marinecentric diatom," Opt. Express **18**, 12203-12212 (2010).

51. M. R. Weatherspoon, Y. Cai, M. Crne, M. Srinivasarao, and K. H. Sandhage, "3D Rutile Titania-Based Structures with Morpho Butterfly Wing Scale Morphologies," Angewandte Chemie International Edition **47**, 7921-7923 (2008).

52. L. H. Nguyen, M. Straub, and M. Gu, "Acrylate-Based Photopolymer for Two-Photon Microfabrication and Photonic Applications," Advanced Functional Materials **15**, 209-216 (2005).

53. M. Rumi, J. E. Ehrlich, A. A. Heikal, J. W. Perry, S. Barlow, Z. Hu, D. McCord-Maughon, T. C. Parker, H. Röckel, S. Thayumanavan, S. R. Marder, D. Beljonne, and J.-L. Brédas, "Structure−Property Relationships for Two-Photon Absorbing Chromophores: Bis-Donor Diphenylpolyene and Bis(styryl)benzene Derivatives," Journal of the American Chemical Society **122**, 9500-9510 (2000).

54. W. Haske, V. W. Chen, J. M. Hales, W. Dong, S. Barlow, S. R. Marder, and J. W. Perry, "65 nm feature sizes using visible wavelength 3-D multiphoton lithography," Opt. Express **15**, 3426-3436 (2007).

CHAPTER 2

BACKGROUND

2.1 Photonic Crystals

2.1.1 Review of Photonic Crystals

Photonic crystals (PCs) are a class of optical materials that provides a means to manipulate the propagation of light [1-3]. A periodic modulation to the refractive index in the PC creates constructive and destructive interferences along the path which light travels through. This interference is wavelength dependent and is based on the change in refractive index and the lattice constants. At a fixed refractive index modulation, the length scale of the lattice constant dictates which wavelengths are reflected while others are transmitted. This unique characteristic of PCs is analogous to the electronic bandgap observed in semiconductor crystals, and in analogy to electrical circuits, have led to significant interests in developing photonic circuits to manipulate light [4, 5].

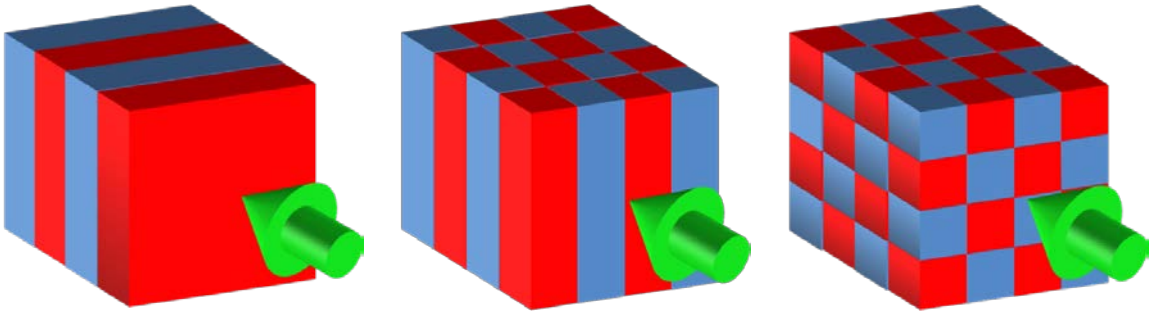

(a) (b) (c)

Figure 2.1. Schematic of 1D (a), 2D (b), 3D (c) PC with red and blue volumes representing different refractive indices and green arrow representing light propagation.

The simplest form of PCs is a multilayered film, where layers of alternating refractive indices are stacked together, forming a one-dimensional PC (1DPC, Figure2.1(a)). This type of PC was investigated as early as 1887 by Lord Rayleigh [6]. These multilayer stacks are typically fabricated by vapor deposition or adhesion of alternating materials. The wavelengths on the order of the periodicity creates coherent scattering, giving rise to photonic bandgaps, where no propagation is allowed. The choice of materials and layer thicknesses can be engineered to form one-dimensional stopbands, where specific wavelengths are reflected, for example ultra-high reflectivity Ti:sapphire laser mirrors, hot and cold mirrors, or dielectric beamsplitters.

For wavelengths inside photonic bandgap:

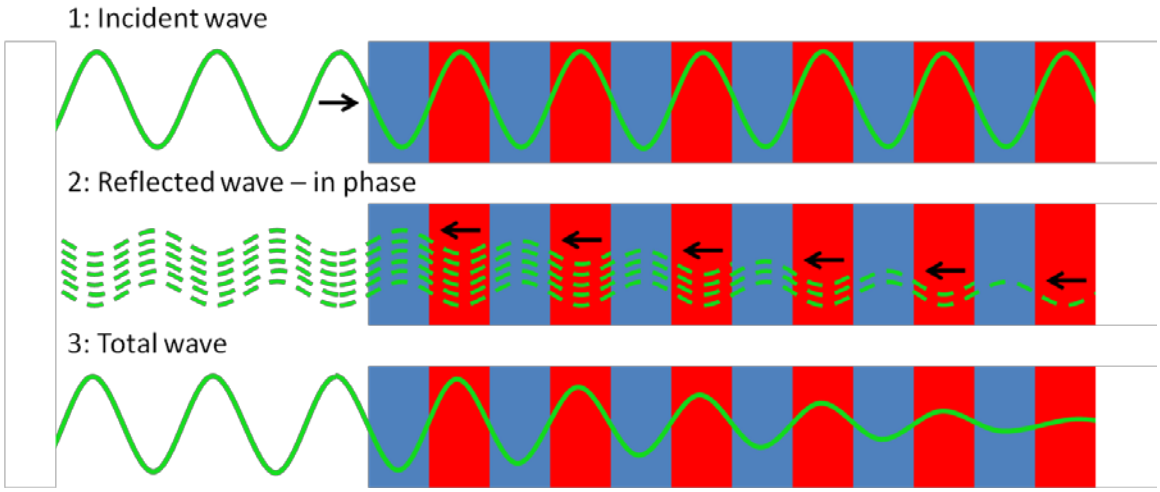

For wavelengths outside photonic bandgap:

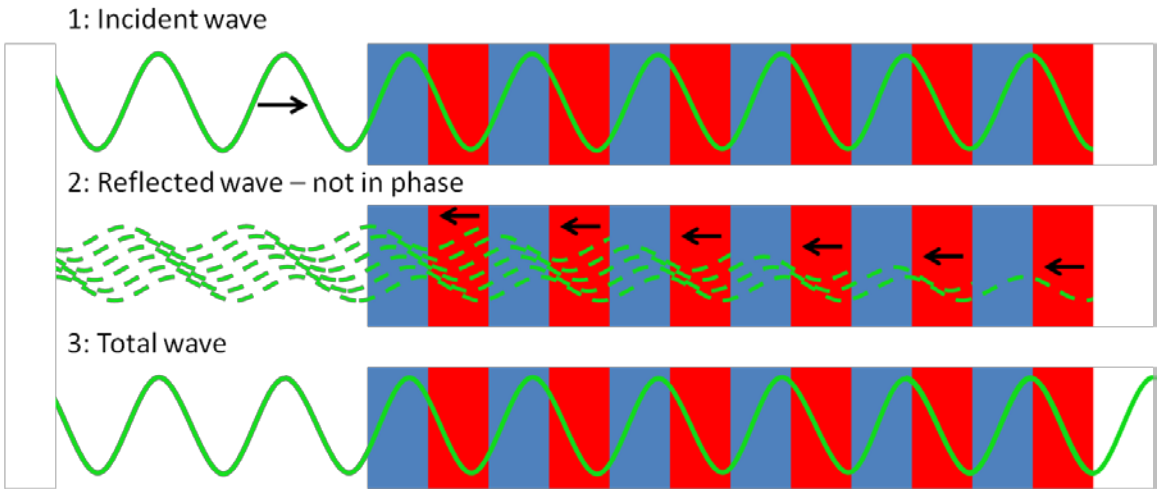

Figure 2.2. Bragg reflection picture of interaction between incident light and a 1DPC where wavelengths within the photonic stopband are reflected while others can be transmitted [7].

Figure 2.2 demonstrates the propagation of light in a 1DPC. For wavelengths within the photonic bandgap, the back reflection from the index boundaries are in phase, preventing the forward propagation of light. Reflections of wavelengths outside the photonic bandgap are not in phase and cancels out one another, thus the transmission of incident wavelength is maximal. Expansion of the dimensionality to 2DPC and 3DPC provides control of the light propagation in 2 and 3 dimensions, respectively.

Two-dimensional PC (2DPC) possesses refractive index change in two directions along the light propagating direction which provides an additional control to the flow of light. (Figure 2.1(b)) A widely investigated class of 2DPCs is silicon PC slabs where air holes, typically hexagonal or square lattices, are etched in a thin silicon slab to form a photonic chip. Whereas a perfectly arranged 2D hole array behaves like a mirror and reflects light of certain wavelengths in-plane of the slab, out-of-plane loss is controlled by total internal reflection. Introduction of line or spot defects within a perfect crystal

provides a way to manipulate the propagation direction of incident light in the form of waveguides [8] or laser cavities [5, 9]. More advanced designs with the modification of hole sizes [10] and arrangements have led to the development of various signal processing devices, such Mach-Zehnder interferometers and wavelength selective transmission filters [11, 12]. Another type of 2DPCs is PC fibers [13], where light is trapped within the fiber based on the photonic bandgap surrounding the core of the fiber as supposed to total internal reflection found in conventional step index fibers. This modified design significantly broadens the range of materials available and improved performance due to the higher effective refractive index contrast between the core and cladding [14].

Increasing the refractive index periodicity in another dimension, to form three dimensional PC (3DPC), affords the control of light in all three dimensions. (Figure 2.1(c)) With this additional control, more complex designs can be accomplished, for example a 3D laser cavity can eliminate the out-of-plane losses and improve lasing performance [15], and the superprism effect where the wavelength dependent angle of refraction can be engineered to spatially separate different wavelengths into different channels [16]. The first 3DPC with complete photonic bandgap, where propagation of light is inhibited in all directions, was created by Yablonovitch *et al.* by drilling a triangular array of cylindrical holes into a dielectric slab [17], operated in the microwave range.

Particle self assembly is another method utilized to form a 3D lattice of cubic close packed microspheres, termed opals, by slow solvent evaporation [18]. Inverse opals are formed by subsequent infiltration of high index material and the removal of the original template [19]. Layer-by-layer technique, where repeated cycles of 2D patterning, etching, deposition and polishing, has been used to form silicon [20] and tungsten woodpile PCs [21]. The woodpile design was first introduced by Ho *et al.* in

1994 [22] as a modified diamond lattice that can be readily produced by this layer-by-layer method while retaining the possibility for complete photonic bandgap as the simulation shows in Figure 2.3(a).

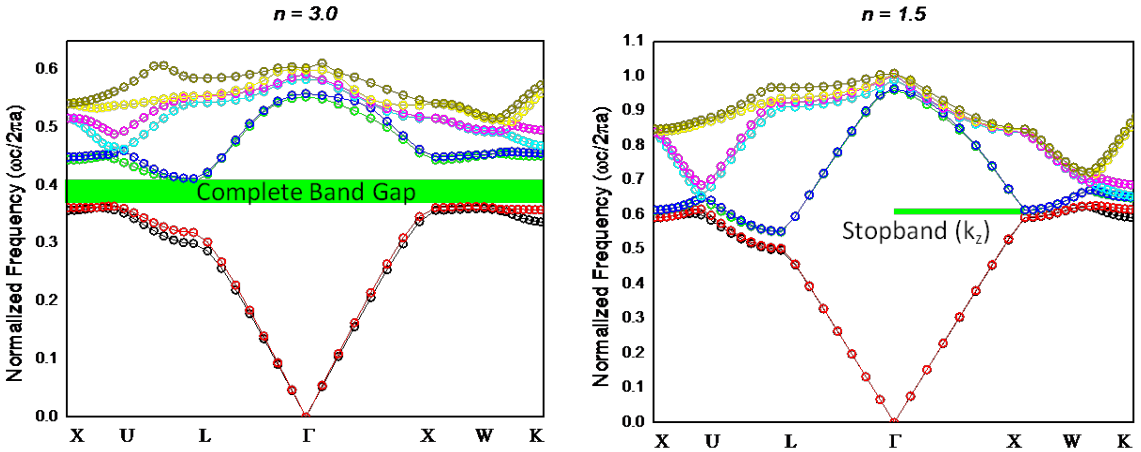

Figure 2.3. Computed band diagram showing the frequencies of allowed propagation as a function of angles in reciprocal space of a woodpile PC lattice. Both plots simulated the same physical design with the difference in refractive index, at n = 3.0 a complete bandgap is observed (a), whereas n = 1.5 only a stopband along Γ-X direction (along the woodpile stacking direction) is present (b). (RSoft, BandSOLVE)

Whereas photonic bandgaps inhibit light propagation in all directions, PCs that exhibit directional stopbands (Figure 2.3(b)) can be achieved in a much wider range of materials and designs due to the reduced restrictions in the refractive index contrast. These photonic stopbands can be utilized in a broad range of applications, for example: 1) superprism effects where the dispersion of the angle of refraction can be used to spatially separate wavelengths for signal processing [23, 24], 2) sensing applications where attachment of analytes alter the local refractive index resulting in a shift of the band position, 3) superpositioning of stopband spectra to modify the intensity distribution

of an emission spectrum [25], reduction of lasing thresholds [26], and fluorescence enhancement through the elimination of forward optical loss [27].

While several synthetic PCs have been discussed, there are numerous examples of PCs that occur naturally. The variety of intricate designs not only offer low cost PC templates for materials engineering but also provide inspiration for synthetic PCs. PCs found in nature include opals [18] and a wide range of biologically produced photonic structures [28-30], ranging from beetle scales [31, 32], butterfly wings [33], to peacock feathers [34]. More recently, there has been much interest in diatoms, a type of single-celled algae encapsulated in silica cell walls, due to the presence of periodic arrangements of nano- to micro-scaled pores. A diverse range of shapes, sizes and surface morphologies can be found in different species, specifically centric diatoms contain 2D nanopore arrangements [35] similar to 2DPCs that exhibit wavelength selective transmission [36] and laser focusing [37, 38].

2.1.2 Photonic Crystal Fabrication Techniques

A wide range of fabrication techniques have been developed to achieve PCs in the infrared and visible wavelengths. This section is focused on the fabrication technique employed in the fabrication of 3DPCs.

The layer-by-layer lithography technique was adopted from the 2D patterning methods used in semiconductor fabrications. To form 3D structures, each layer is produced by photopatterning, wet or dry etching, vapor deposition of the desired material, followed by chemical mechanical polishing, a new resist layer is then deposited on top for the second layer pattern. The registration of this subsequent layer to the underlying one is crucial in forming a uniform PC. This process is repeated for each additional layer. This technique was used by Lin *et al.* to form a five-layered silicon

woodpile PC with an inplane line spacings of 5 μm and a corresponding stopband at 12 μm was observed [20]. This technique is complex, labor intensive, time-consuming and expensive to perform, limiting the ability to rapidly investigate different designs and incorporation of defects.

Self assembly of spherical particles is an inexpensive means to create large area 3DPCs. Opals films are typically fabricated by slow evaporation of the solvent in a micro-nanosphere suspension onto a vertically submerged substrate [39]. This slow drying allows for formation of nearly perfect closely packed lattice. The microspheres used in the formation of opals are typically polystyrene [40] or silica [41]. The refractive contrasts between those materials and air (0.59 and 0.45 respectively) are insufficient to form complete bandgaps. Infiltration with silicon by low-pressure chemical vapor deposition generated complete bandgap at 1.3 μm [42]. While this technique allows for large area coverage, the self assembly method often results in dislocations, grain boundaries and missing spheres. The incorporation of defects using this technique is also difficult, severely limiting their application.

Holographic photolithography is a facile method to generate 3DPCs in a single step exposure. A 3D holographic interference pattern is created either by multiple interfering laser beams overlapped in the sample from different angles [43] or by the use of a phase-mask with one beam [44]. By superimposing the holographic pattern with a photoresist and controlling the exposure dose, the intensity pattern can be recorded into a 3D volumetric after solvent development. While the exposure procedure for a periodic array is simple using this method, alteration to the lattice parameter requires additional calculation and optimization to the setup configuration. Moreover, this technique is not amendable to generate arbitrary features like waveguides or defects, necessitating a second fabrication process with an alternative technique like two- or multi-photon lithography (MPL). While the principle of this combination technique has been

demonstrated, proper alignment of MPL fabricated defects to the lattice direction of the interference lithographically generated PC still proofs to be challenging [45-47].

Two- or multi-photon lithography is based on the principle of two-photon absorption (TPA), which was theoretically predicted by Göppert-Mayer in 1931 [48]. However due to the high photon intensities required, it was not experimentally demonstrated until after the advent of lasers [49]. For two-photon absorption to occur, two photons must be absorbed simultaneously to promote the molecule from the ground to excited state. Due to this nonlinear relation between laser intensity and probability of the absorption, photoexcitation can be confined in the focal volume of a focused laser beam. This 3D confinement was first utilized for fluorescence microscopy by Denk *et al.* in 1990, where two photon excitation was used to achieve z-sectioning through a 3D sample [50]. This process has also been applied to induce photochemistry in photoresists, for example radical initiation [51] and acid generation [52]. The unique ability to generate arbitrary 3D patterns has led to much interest in MPL fabrication of 3DPCs. In the next section, the principle of MPL including the fundamental of two photon absorption, the 3D confinement and the resolution of MPL, as well as the two-photon initiated polymerization will be introduced.

2.2 Multiphoton Lithography

MPL is typically performed using crosslinkable monomers in a liquid cell or a solid photoresist containing a two-photon absorbing photoinitiator. The excitation laser is focused tightly into the photoresist by a microscope objective. The photocrosslinking reaction is initiated by the laser within the focal volume which renders the exposed volume insoluble during solvent development. Typical photoinitiators have been

borrowed from the well established UV lithography, although several initiators with higher two-photon absorption cross sections have recently been developed to improve initiation efficiencies [51, 53-56]. The two-photon photoinitiator used in this work, *E*,*E*-1,4-*bis*[4-(di-*n*-butylamino)styryl]-2,5-dimethoxybenzene (DABSB), has been demonstrated to be an efficient radical initiator with high two-photon absorption cross section at 730 nm [53], a more detailed description is provided in the following chapter.

2.2.1. Multiphoton Absorption

Multiphoton absorption is a nonlinear process involving the absorption of two or more photons simultaneously to excite the molecule from the ground to an excited state, whereas linear or one-photon excitation is accomplished by the absorption of one photon.

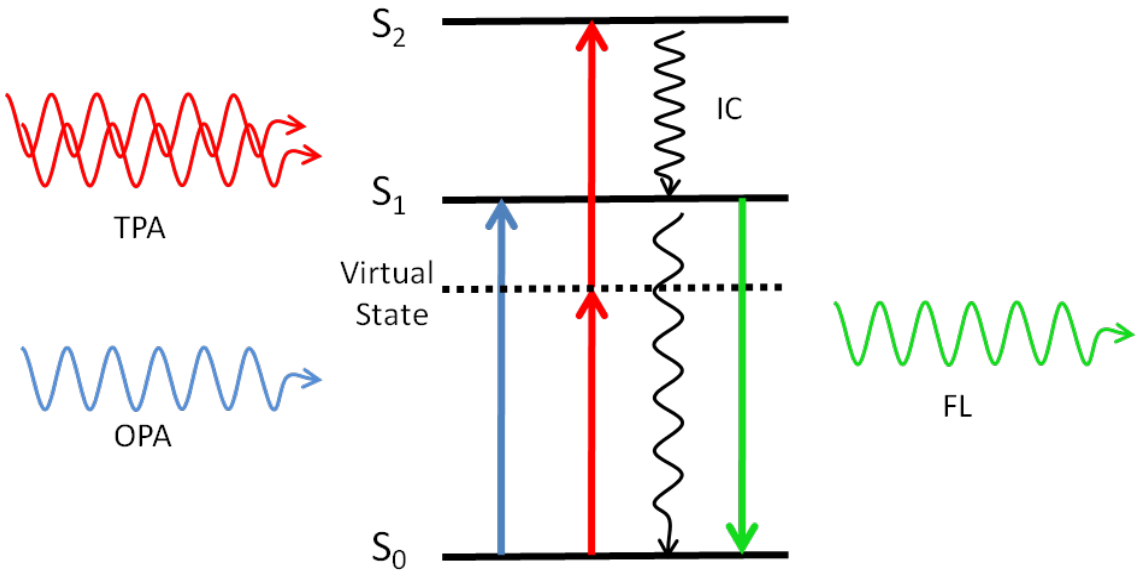

Figure 2.4. Energy diagram of one- and two-photon absorption process.

For centrosymmetric molecules like DABSB, the two-photon transition will only occur between states with same parity, like g→g and u→u. As illustrated in Figure 2.4, the two-photon transition between S_0 and S_2 is allowed while the transition between S_0

and S_1 is only one-photon allowed. The process of TPA can be visualized as one photon is excited to a virtual state (the dot line in Figure 2.4) followed by the absorption of another photon within the very short lifetime of the virtual state (within several femtoseconds). Each of the two photons does not possess enough energy to excite the molecule individually. After excitation, the molecule relaxes quickly from the S_2 state to the lowest excited S_1 state by internal conversion followed by fluorescence emission or by nonradiative decay. In addition, energy or electron transfer to another molecule can also occur.

The TPA response depends on the size of TPA cross section (δ) of a material and the excitation intensity (I). The rate of excitation is

$$\frac{dN_{S2}}{dt} = \frac{1}{2}\delta N_{S0} I^2$$

where N is the population density of S_0 and S_2 state. The units of δ are $m^4 \cdot s \cdot photon^{-1}$. As shown in the equation above, the unique quadratic or higher-order intensity dependence of two- or multi-photon excitation provides for confined excitation along the axial direction under focusing conditions. The photograph of fluorescence generated via two- (TPA) and one-photon (OPA) excitation in a cuvette and the drawing in Figure 2.5 demonstrates such confinement. Under one-photon conditions (for example in the UV), the probability of exciting a molecule is the same throughout the laser's path. However, under multi-photon conditions (for example using the IR photons), since each photon possesses less energy, the probability for excitation outside the focus is negligible and the transition only occurs at the focus where the irradiance is the highest. This confinement effect is resultant from the nonlinear relationship between the laser intensity and the rate of excitation shown above. As the light intensity decreases proportionally with the

squared beam radius away from the focal plane ($I \propto z^{-2}$), the combination results in a forth power reduction of excitation rate as a function of distance from the focal plane.

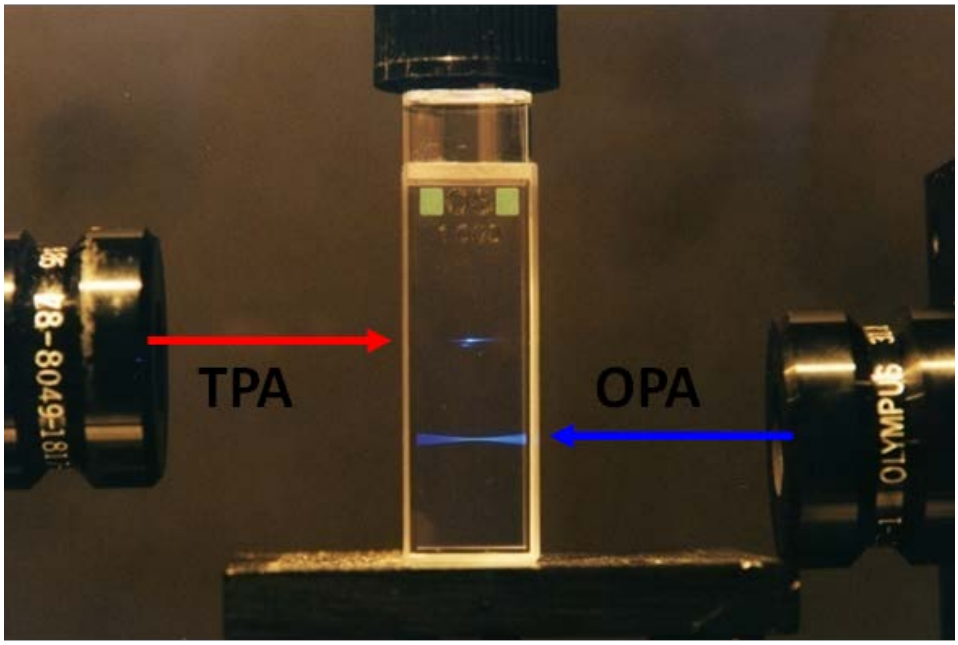

Figure 2.5. Photograph of fluorescence generated by two- and one- photon excitation, demonstrating the difference between the excitation probabilities. (Image courtesy of Dr Wim Wenseleers.)

Two physical effects resulting from the localized excitation favors the use of multiphoton for 3D fabrication. One is the improved penetration into the sample, where one-photon absorption in the out-of-focus region would decrease the number of photons reaching the focal plane, the other is the ability to confine excitation within a focal volume. These properties lead to the ability to form any arbitrary 3D microstructures with multiphoton excitation whereas one photon process is generally limited to 2D patterning.

2.2.2 Resolution of Multiphoton Excitation

The 3D confined excitation volume significanly limits the resolution of MPL. For multiphoton microscopy and microfabrication, the excitation laser is typically focused by a microscope objective to achieve the a small focus spot. When a laser beam with a flat top profile is brought into a focus, the intensity profile at the focus is the fourier transform of the beam intensity distribution, and is described by the point spread function. The plot profile is called an airy pattern and is plotted in Figure 2.6.

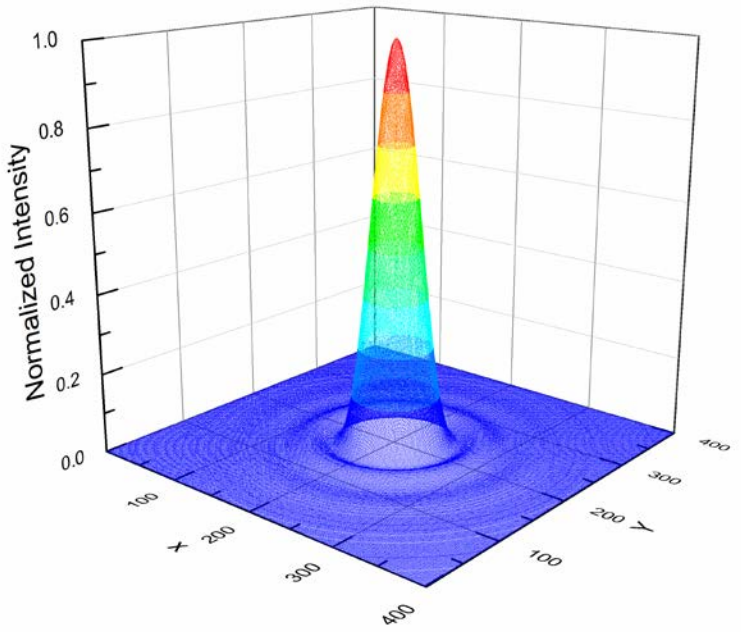

Figure 2.6. Intensity profile plot at the focus of a flat-top laser beam.

The lateral intensity distribution in the focal (xy) plane is defined by:

$$I(u=0,v) \propto \left(\frac{2J_1(v)}{v}\right)^2, v = r\frac{2\pi}{\lambda}NA$$

where $J_1(v)$ is the Bessel function of the first kind and r is the radius from the central axis, λ is the wavelength, and NA is the numerical aperture of the focusing objective. The axial intensity distribution along the propagation direction is defined by:

$$I(u, v = 0) \propto \left(\frac{sin(u/4)}{u/4}\right)^2, u = z\frac{2\pi}{\lambda}\frac{NA^2}{n}.$$

The linear intensity distribution along with its squared and cubed profiles are plotted below in Figure 2.7 to demonstrate the improved resolution due to the multiphoton intensity dependence for two (TPA) and three (3PA) photon absorptions respectively.

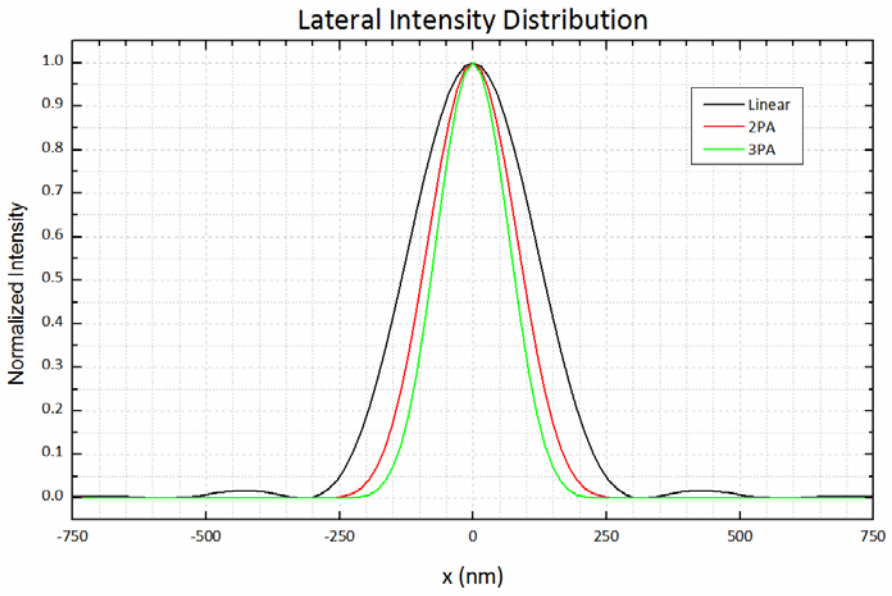

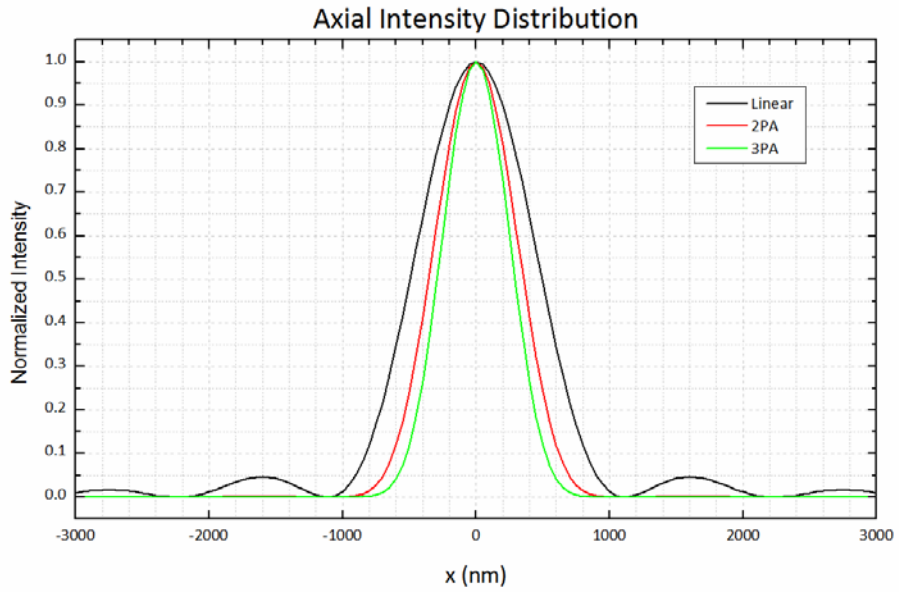

Figure 2.7. Intensity profiles for one-, two- and three-photon excitation in the lateral (top) and axial (bottom) directions.

The respective resolutions under two photon excitation conditions in HW1/*e* are [57]:

$$w_{xy} = \begin{cases} \dfrac{0.320\lambda}{\sqrt{2}NA}, & NA \leq 0.7 \\ \dfrac{0.325\lambda}{\sqrt{2}NA^{0.91}}, & NA > 0.7 \end{cases} \qquad w_z = \frac{0.532\lambda}{\sqrt{2}}\left[\frac{1}{n - \sqrt{n^2 - NA^2}}\right]$$

The lateral (xy) and axial (z) resolutions computed using typical experimental parameters, NA = 1.40, λ = 730 nm and *n* = 1.5 are 123.5 and 285.6 nm, respectively, giving rise to an excitation volume of 1:2.3 aspect ratio.

2.2.3 Multiphoton Initiated Polymerization

The radical polymerization used in this work is based on the crosslinking of acrylate monomers. A schematic of the chemical reaction process initiated by two-photon absorption is shown in Figure 2.8. The initiation step involved two-photon excitation of the initiator (**I**), followed by the generation of free radicals (**R·**) and reaction with monomers (**M**). The polymerization propagates as additional monomer subunits are attached to the chained radicals, and the process is terminated when radicals react with each other or with an inhibitor.

Initiation	$\mathbf{I + 2\ h\nu \rightarrow 2\ R\cdot}$	**I** : Initiator
	$\mathbf{R\cdot + M \rightarrow R - M\cdot}$	**R·** : Radical
Propagation	$\mathbf{R - M_n\cdot + M \rightarrow R - M_{n+1}\cdot}$	**M** : Monomer
Termination	$\mathbf{2\ R\cdot - M_n \rightarrow R - M_{2n} - R}$	

Figure 2.8. Photochemical reaction for two-photon radical polymerization [58].

The ability to generate individual features stems from the solubility contrast between the highly crosslinked exposed volumes with high molecular weight and the unexposed monomers during solvent development. When laser excitation is focused into a photosensitive resin, the excitation volume described in the previous section is translated into a voxel, volume pixel, by photo-crosslinking. A voxel is the basic building block for any 3D micofabricated structures. The voxel has an ellipsoidal shape as the excitation profile is longer along the axial than the radial direction. The size of the voxel is controlled by the dose, a combination of exposure power and dwell time.

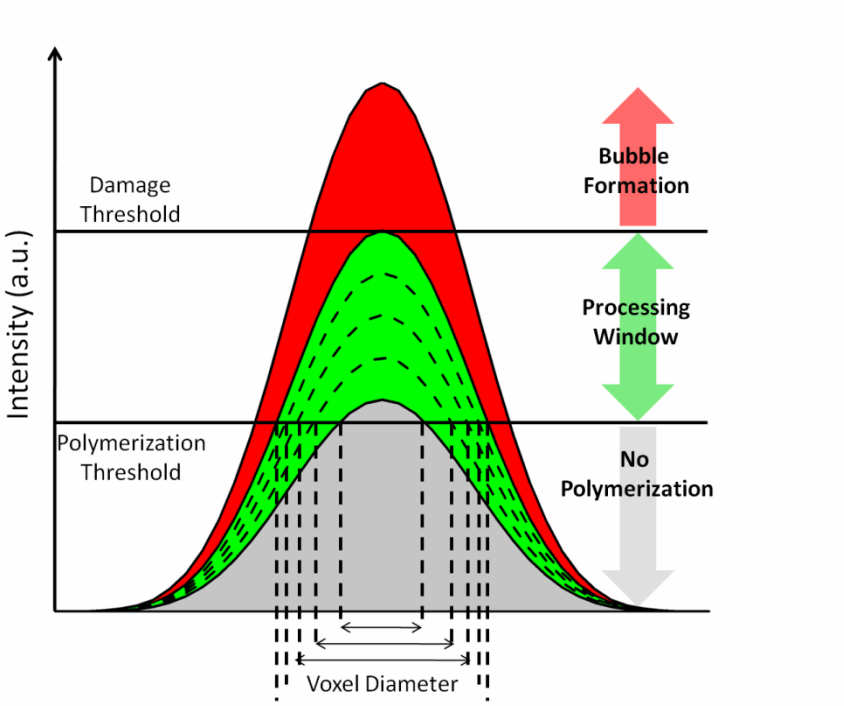

Figure 2.9. Cross sections of the intensity profiles at the focal point and their relation to the polymerized voxel lateral resolution [59].

The minimum voxel size is determined by the polymerization threshold, as depicted in Figure 2.9. Sufficient power must be delivered to the focal volume in order to crosslink a sufficient number of monomers together to render the feature insoluble during the development process. Above this crosslinking threshold, voxels of varying sizes could be formed, where the intensity profile above threshold defines the voxel size, until the damage threshold is reached. At the damage threshold, thermal effects significantly increase the rate of polymerization, causing bubbles to form in the resin and features unusable. Aspect ratio of voxels generated in by MPL are typically larger than the calculated value in the previous section due to radical diffusion [60] and possible self-focusing effect caused by the change in refractive index upon polymerization [61].

This photoinitiation process has received significant interest in 3D photolithography where the spatially localized reaction is used to for structures with nano- to micro- scaled features. 3D exposure patterns in a photoresist can be achieved either by a scanning laser beam or by translation of the sample with respect to a fixed focal position. Due to the high intensities needed for two-photon absorption to occur, femtosecond pulsed lasers are typically employed where the combination of high peak powers and high repetition rate are favorable for efficient photoinitiation. Early microstructures demonstrated by Cumpston et al. in 1999 included PCs, tapered waveguides and cantilevers [51]. Kawata et al. further demonstrate the flexibility of this technique with complex microbull statues [62]. The resolutions achievable and the flexibility in the exposure designs make this the ideal tool for PC fabrication.

2.3 History and Recent Progress on MPL Fabrication of Photonic Crystals

One of the earliest demonstration of MPL fabricated 3DPCs with optical characterization was by Sun et al. [63], line widths of 600 nm were generated in an acrylate resin and a photonic stopband of intensity of ~25% was observed at 3.9 μm. 50% stopbands were observed by Straub et al. at 2.0 and 2.2 μm from 200 nm line widths [64]. Deubel et al. used SU-8, a multifunctional epoxy monomer, to fabricate 180 nm feature sizes and forming PCs that exhibit 72% stopbands between 1.3 and 1.7 μm [65]. 300 nm line widths were obtained by Wu et al. in SR348, a widely available difunctional acrylate resin, resulted in a baseline-corrected (for scattering loss) 39% stopband at 2.1 μm [66].

Although it MPL fabricated PCs typically do not possess complete photonic bandgaps, their stopbands can be utilized in a broad range of applications, for example 1) superprism effects where the wavelength dependent property of the angle of refraction can be used to spatially separate wavelengths for signal processing [23, 24], 2) sensing

applications where attachment of analytes alter the local refractive index resulting in a shift of the band position, 3) superpositioning of emission and stopband spectra to modify of the intensity distribution of emission spectrum [25], reduce lasing threshold [26], and fluorescence enhancement by eliminating forward optical loss [27].

Several challenges remain in the widespread use of MPL in the fabrication of PCs, namely the resolution of the fabricated features and the refractive index of the resultant structures.

2.3.1 Resolution of MPL Fabricated Features

While PCs with photonic stopbands in the infrared region have been widely studied, as discussed in the previous section, diffraction limits the fundamental excitation volume and the produced voxel. Typical voxels have an aspect ratio ranging from width to height of ~ 1:2.5-4.5 due to the focusing geometry. This limitation hinders the layer spacings achievable in the fabrication of PCs and the operating range of stopbands has generally been limited to the infrared. In order to push the photonic stopbands into visible wavelengths, several methods from engineering of the materials to instrumentation have been employed.

Typical MPL instrumentation utilize laser excitation in the range of 700-800 nm and the finest line features between 180 [65] and 200 nm [53] for free-standing PCs had been reported. Several methods had been proposed to generate finer features using specialized support-structure designs such as post-exposure bake induced acid diffusion inside nanoscale channels [67], the use of additional radical quenchers to fabricate features directly on the substrate [68], or stretching of polymerized rods spanning shrinking supports [69]. These attempts have achieved finer resolution down to 30 nm but cannot be used for building free-form structures.

Post fabrication processings was another route utilized to obtain reduced feature sizes. Plasma etching of PCs [70] resulted in reduced line widths at the top layers of the structures, however the process did not effectively remove polymer at the interior of the structures, leading to inhomogeneous feature sizes from the top down. Condensation removal of alkoxy groups in PCs fabricated from a sol-gel matrix during baking resulted in a 35% reduction of line widths to 160 nm [71]. However this process creates significant structural shrinkage (18%) and the design for relieving this stress, offsetting the structures from the substrate by posts, resulted in warping and displacement from designated locations.

Recent developments in MPL had been inspired by stimulated-emission-depletion microscopy pioneered by Hell, theoretically in 1994 [72] and experimentally in 1999 [73]. The improvement in resolution is achieved by spatially overlapping a secondary deactivation laser beam to depopulate part of the multiphoton excited focal volume [74]. This process has recently (2011) been demonstrated to produce feature sizes down to ~130 nm laterally and ~180 nm axially in PCs and stopbands throughout the visible range was achieved [75]. This process however is limited to initiators with an excited state that could efficiently undergo stimulated emission as supposed to other absorption processes. Furthermore, the complex instrumental configuration limits the applicability of this technique.

2.3.2 Functionalization of Polymeric PCs

The intensity of the photonic stopbands is dependent on the refractive index contrast experienced in the PC, typical polymerizable material possess moderate refractive indices (1.5 to 1.6) which results in limited applications [53, 58, 64, 65]. Chemical modification and deposition of metals or semiconductors onto the polymeric

PCs provides a way to manipulate the dielectric contrast to enhance stopband performances and broaden the range of applications [76-81].

Metallic photonic crystals (MPCs) have been of much interest in their electromagnetic and high temperature properties for applications including enhanced metal absorption [82] and thermal emission suppression [83]. Several groups have investigated wet chemical approaches and polymer chemistries to impart selectivity. Farrer et al has demonstrated selective gold and copper coatings on various microstructures (chains and coils) based on the preferential reaction with acrylates over methacrylates [84]. Formanek et al has demonstrated deposition of silver on microstructures containing styrenes [85]. Kuebler et al has demonstrated silver plating via amine modification of the polymer surface to achieve silver mirrors [86] and PCs [87]. MPCs and the resultant modification to the optical characteristics were explored in copper [79] and nickel [78] from SU-8 polymer templates, where plasmonic bandedges were observed at ~ 3.5 μm accompanied by broadband infrared reflectance enhancements at wavelengths above this bandedge.

Another major focus of the research of MPL fabricated PCs is to achieve a complete photonic bandgap, calculations revealed a refractive index of ~ 2.5-2.7 is necessary for complete bandgap with woodpile type PCs [88, 89]. However, a majority of the published works have been based on acrylates or epoxys as the starting materials give the relatively low refractive index (~ 1.5 – 1.6), preventing the observation of complete bandgaps. One approach that have been widely explored in the fabrication of inverse opal PCs was infiltration of the low index templates with high index metal oxides or semiconductors, for example titania (TiO_2, n = 2.2-2.7) by atomic layer deposition (ALD) [90], selenium (n = 2.5) by melt processing at 275ºC [91], cadmium selenide (n = 2.5) by electroplating [92], amorphous silicon (n = 3.5) by chemical vapor deposition (CVD) [42]. Most of these processes require high temperature processing conditions that

are not compatible with the thermal stability of polymers and none are selective to the structure only. A few of these techniques have been adopted for polymer PCs fabricated, such as backfilling with liquid-phase titania [93], and surfacing coating with gas-phase titania ALD [94] or silicon CVD on silica inverted PC [95] techniques. Although these processes were able to generate higher index structures, the alteration to the structure design, non selective blanket coverage, the complex and extensive processing hinders their applicability. Buso et al. [76] have recently demonstrated structure selective, high index cadmium sulfide coating (n = 2.3) on low index PCs. Although the refractive index and the quality of the coating was insufficient to produce a complete bandgap, a 17% enhancement of the original stopband intensity was observed, accompanied by red-shifted stopband positions.

REFERENCES

1. J. Joannopoulos, S. Johnson, J. Winn, and R. Meade, *Photonic Crystals: Molding the Flow of Light (Second Edition)* (Princeton University Press, 2008).

2. E. Yablonovitch, "Inhibited Spontaneous Emission in Solid-State Physics and Electronics," Physical Review Letters **58**, 2059 (1987).

3. S. John, "Strong localization of photons in certain disordered dielectric superlattices," Physical Review Letters **58**, 2486 (1987).

4. J. D. Joannopoulos, P. R. Villeneuve, and S. Fan, "Photonic crystals: putting a new twist on light," Nature **386**, 143-149 (1997).

5. K. J. Vahala, "Optical microcavities," Nature **424**, 839-846 (2003).

6. J. W. Strutt, "On the maintenance of vibrations by forces of double frequency, and on the propagation of waves through a medium endowed with a periodic structure," Philosophical Magazine **24**, 145-159 (1887).

7. E. Yablonovitch, "Photonic crystals: Semiconductors of light," in *Scientific American*(2001).

8. S.-Y. Lin, E. Chow, V. Hietala, P. R. Villeneuve, and J. D. Joannopoulos, "Experimental Demonstration of Guiding and Bending of Electromagnetic Waves in a Photonic Crystal," Science **282**, 274-276 (1998).

9. Y. Akahane, T. Asano, B.-S. Song, and S. Noda, "High-Q photonic nanocavity in a two-dimensional photonic crystal," Nature **425**, 944-947 (2003).

10. S. G. Johnson, P. R. Villeneuve, S. Fan, and J. D. Joannopoulos, "Linear waveguides in photonic-crystal slabs," Physical Review B **62**, 8212 (2000).

11. Y. A. Vlasov, M. O'Boyle, H. F. Hamann, and S. J. McNab, "Active control of slow light on a chip with photonic crystal waveguides," Nature **438**, 65-69 (2005).

12. M. Notomi, A. Shinya, S. Mitsugi, E. Kuramochi, and H. Ryu, "Waveguides, resonators and their coupled elements in photonic crystal slabs," Opt. Express **12**, 1551-1561 (2004).

13. R. F. Cregan, B. J. Mangan, J. C. Knight, T. A. Birks, P. S. J. Russell, P. J. Roberts, and D. C. Allan, "Single-Mode Photonic Band Gap Guidance of Light in Air," Science **285**, 1537-1539 (1999).

14. P. Russell, "Photonic Crystal Fibers," Science **299**, 358-362 (2003).

15. S. Ogawa, M. Imada, S. Yoshimoto, M. Okano, and S. Noda, "Control of Light Emission by 3D Photonic Crystals," Science **305**, 227-229 (2004).

16. H. Kosaka, "Photonic crystals for micro lightwave circuits using wavelength-dependent angular beam steering," Appl. Phys. Lett. **74**, 1370 (1999).

17. E. Yablonovitch, T. J. Gmitter, and K. M. Leung, "Photonic band structure: The face-centered-cubic case employing nonspherical atoms," Physical Review Letters **67**, 2295 (1991).

18. F. Marlow, Muldarisnur, P. Sharifi, R. Brinkmann, and C. Mendive, "Opals: Status and Prospects," Angewandte Chemie International Edition **48**, 6212-6233 (2009).

19. A. Blanco, E. Chomski, S. Grabtchak, M. Ibisate, S. John, S. W. Leonard, C. Lopez, F. Meseguer, H. Miguez, J. P. Mondia, G. A. Ozin, O. Toader, and H. M. van Driel, "Large-scale synthesis of a silicon photonic crystal with a complete three-dimensional bandgap near 1.5 micrometres," Nature **405**, 437-440 (2000).

20. S. Y. Lin, J. G. Fleming, D. L. Hetherington, B. K. Smith, R. Biswas, K. M. Ho, M. M. Sigalas, W. Zubrzycki, S. R. Kurtz, and J. Bur, "A three-dimensional photonic crystal operating at infrared wavelengths," Nature **394**, 251-253 (1998).

21. J. G. Fleming, S. Y. Lin, I. El-Kady, R. Biswas, and K. M. Ho, "All-metallic three-dimensional photonic crystals with a large infrared bandgap," Nature **417**, 52-55 (2002).

22. K. M. Ho, C. T. Chan, C. M. Soukoulis, R. Biswas, and M. Sigalas, "Photonic band gaps in three dimensions: New layer-by-layer periodic structures," Solid State Communications **89**, 413-416 (1994).

23. J. Serbin, and M. Gu, "Experimental Evidence for Superprism Effects in Three-Dimensional Polymer Photonic Crystals," Advanced Materials **18**, 221-224 (2006).

24. J. Serbin, and M. Gu, "Superprism phenomena in waveguide-coupled woodpile structures fabricated by two-photon polymerization," Opt. Express **14**, 3563-3568 (2006).

25. M. Barth, A. Gruber, and F. Cichos, "Spectral and angular redistribution of photoluminescence near a photonic stop band," Physical Review B **72**, 085129 (2005).

26. V. I. Kopp, B. Fan, H. K. M. Vithana, and A. Z. Genack, "Low-threshold lasing at the edge of a photonic stop band in cholesteric liquid crystals," Opt. Lett. **23**, 1707-1709 (1998).

27. Y.-Q. Zhang, J.-X. Wang, Z.-Y. Ji, W.-P. Hu, L. Jiang, Y.-L. Song, and D.-B. Zhu, "Solid-state fluorescence enhancement of organic dyes by photonic crystals," Journal of Materials Chemistry **17**, 90-94 (2007).

28. P. Vukusic, and J. R. Sambles, "Photonic structures in biology," Nature **424**, 852-855 (2003).

29. V. Welch, and J. P. Vigneron, "Beyond butterflies—the diversity of biological photonic crystals," Optical and Quantum Electronics **39**, 295-303 (2007).

30. M. Srinivasarao, "Nano-Optics in the Biological World: Beetles, Butterflies, Birds, and Moths," Chemical Reviews **99**, 1935-1962 (1999).

31. J. W. Galusha, L. R. Richey, M. R. Jorgensen, J. S. Gardner, and M. H. Bartl, "Study of natural photonic crystals in beetle scales and their conversion into inorganic structures via a sol-gel bio-templating route," Journal of Materials Chemistry **20**, 1277-1284 (2010).

32. A. R. Parker, V. L. Welch, D. Driver, and N. Martini, "Structural colour: Opal analogue discovered in a weevil," Nature **426**, 786-787 (2003).

33. K. Michielsen, and D. G. Stavenga, "Gyroid cuticular structures in butterfly wing scales: biological photonic crystals," Journal of The Royal Society Interface **5**, 85-94 (2008).

34. J. Zi, X. Yu, Y. Li, X. Hu, C. Xu, X. Wang, X. Liu, and R. Fu, "Coloration strategies in peacock feathers," Proceedings of the National Academy of Sciences **100**, 12576-12578 (2003).

35. T. Fuhrmann, S. Landwehr, M. El Rharbi-Kucki, and M. Sumper, "Diatoms as living photonic crystals," Applied Physics B: Lasers and Optics **78**, 257-260 (2004).

36. J. Noyes, M. Sumper, and P. Vukusic, "Light manipulation in a marine diatom," Journal of Materials Research **23**, 3229-3235 (2008).

37. L. De Stefano, I. Rea, I. Rendina, M. De Stefano, and L. Moretti, "Lensless light focusing with the centric marinediatom Coscinodiscus walesii," Opt. Express **15**, 18082-18088 (2007).

38. E. De Tommasi, I. Rea, V. Mocella, L. Moretti, M. De Stefano, I. Rendina, and L. De Stefano, "Multi-wavelength study of lighttransmitted through a single marinecentric diatom," Opt. Express **18**, 12203-12212 (2010).

39. D. J. Norris, E. G. Arlinghaus, L. Meng, R. Heiny, and L. E. Scriven, "Opaline Photonic Crystals: How Does Self-Assembly Work?," Advanced Materials **16**, 1393-1399 (2004).

40. İ. İ. Tarhan, and G. H. Watson, "Photonic Band Structure of fcc Colloidal Crystals," Physical Review Letters **76**, 315 (1996).

41. P. Jiang, J. F. Bertone, K. S. Hwang, and V. L. Colvin, "Single-Crystal Colloidal Multilayers of Controlled Thickness," Chemistry of Materials **11**, 2132-2140 (1999).

42. Y. A. Vlasov, X.-Z. Bo, J. C. Sturm, and D. J. Norris, "On-chip natural assembly of silicon photonic bandgap crystals," Nature **414**, 289-293 (2001).

43. M. Campbell, D. N. Sharp, M. T. Harrison, R. G. Denning, and A. J. Turberfield, "Fabrication of photonic crystals for the visible spectrum by holographic lithography," Nature **404**, 53-56 (2000).

44. S. Jeon, J.-U. Park, R. Cirelli, S. Yang, C. E. Heitzman, P. V. Braun, P. J. A. Kenis, and J. A. Rogers, "Fabricating complex three-dimensional nanostructures with high-resolution conformable phase masks," Proceedings of the National Academy of Sciences of the United States of America **101**, 12428-12433 (2004).

45. V. Ramanan, "Three dimensional silicon-air photonic crystals with controlled defects using interference lithography," Appl. Phys. Lett. **92**, 173304 (2008).

46. K. Ohlinger, "Photonic crystals with defect structures fabricated through a combination of holographic lithography and two-photon lithography," J. Appl. Phys. **108**, 073113 (2010).

47. P. V. Braun, S. A. Rinne, and F. García-Santamaría, "Introducing Defects in 3D Photonic Crystals: State of the Art," Advanced Materials **18**, 2665-2678 (2006).

48. M. Göppert-Mayer, "Über Elementarakte mit zwei Quantensprüngen," Annalen der Physik **401**, 273-294 (1931).

49. W. Kaiser, and C. G. B. Garrett, "Two-Photon Excitation in CaF_{2}: Eu^{2+}," Physical Review Letters **7**, 229 (1961).

50. W. Denk, J. Strickler, and W. Webb, "Two-photon laser scanning fluorescence microscopy," Science **248**, 73-76 (1990).

51. B. H. Cumpston, S. P. Ananthavel, S. Barlow, D. L. Dyer, J. E. Ehrlich, L. L. Erskine, A. A. Heikal, S. M. Kuebler, I. Y. S. Lee, D. McCord-Maughon, J. Qin, H. Rockel, M. Rumi, X.-L. Wu, S. R. Marder, and J. W. Perry, "Two-photon polymerization initiators for three-dimensional optical data storage and microfabrication," Nature **398**, 51-54 (1999).

52. W. Zhou, S. M. Kuebler, K. L. Braun, T. Yu, J. K. Cammack, C. K. Ober, J. W. Perry, and S. R. Marder, "An Efficient Two-Photon-Generated Photoacid Applied to Positive-Tone 3D Microfabrication," Science **296**, 1106-1109 (2002).

53. S. M. Kuebler, M. Rumi, T. Watanabe, K. Braun, B. H. Cumpston, A. A. Heikal, L. L. Erskine, S. Thayumanavan, and J. W. Perry, "Optimizing Two-Photon

Initiators and Exposure Conditions for Three-Dimensional Lithographic Microfabrication," Journal of Photopolym. Sci. Technol **14**, 657-668 (2001).

54. G. Lemercier, J.-C. Mulatier, C. Martineau, R. Anémian, C. Andraud, I. Wang, O. Stéphan, N. Amari, and P. Baldeck, "Two-photon absorption: from optical power limiting to 3D microfabrication," Comptes Rendus Chimie **8**, 1308-1316 (2005).

55. J.-F. Xing, W.-Q. Chen, X.-Z. Dong, T. Tanaka, X.-Y. Fang, X.-M. Duan, and S. Kawata, "Synthesis, optical and initiating properties of new two-photon polymerization initiators: 2,7-Bis(styryl)anthraquinone derivatives," Journal of Photochemistry and Photobiology A: Chemistry **189**, 398-404 (2007).

56. J.-F. Xing, X.-Z. Dong, W.-Q. Chen, X.-M. Duan, N. Takeyasu, T. Tanaka, and S. Kawata, "Improving spatial resolution of two-photon microfabrication by using photoinitiator with high initiating efficiency," Applied Physics Letters **90**, 131106 (2007).

57. W. R. Zipfel, R. M. Williams, and W. W. Webb, "Nonlinear magic: multiphoton microscopy in the biosciences," Nat Biotech **21**, 1369-1377 (2003).

58. S. Maruo, O. Nakamura, and S. Kawata, "Three-dimensional microfabrication with two-photon-absorbed photopolymerization," Opt. Lett. **22**, 132-134 (1997).

59. A. Ovsianikov, and B. N. Chichkov, "Two-Photon Polymerization – High Resolution 3D Laser Technology and Its Applications in Nanoelectronics and Photonics," A. Korkin, and F. Rosei, eds. (Springer New York, 2008), pp. 427-446.

60. H. Sun, "Scaling laws of voxels in two-photon photopolymerization nanofabrication," Appl. Phys. Lett. **83**, 1104 (2003).

61. A. S. Kewitsch, and A. Yariv, "Self-focusing and self-trapping of optical beams upon photopolymerization," Opt. Lett. **21**, 24-26 (1996).

62. S. Kawata, H.-B. Sun, T. Tanaka, and K. Takada, "Finer features for functional microdevices," Nature **412**, 697-698 (2001).

63. H.-B. Sun, S. Matsuo, and H. Misawa, "Three-dimensional photonic crystal structures achieved with two-photon-absorption photopolymerization of resin," Applied Physics Letters **74**, 786-788 (1999).

64. M. Straub, and M. Gu, "Near-infrared photonic crystals with higher-order bandgaps generated by two-photon photopolymerization," Opt. Lett. **27**, 1824-1826 (2002).

65. M. Deubel, G. von Freymann, M. Wegener, S. Pereira, K. Busch, and C. M. Soukoulis, "Direct laser writing of three-dimensional photonic-crystal templates for telecommunications," Nat Mater **3**, 444-447 (2004).

66. S. Wu, M. Straub, and M. Gu, "Single-monomer acrylate-based resin for three-dimensional photonic crystal fabrication," Polymer **46**, 10246-10255 (2005).

67. J. Saulius, and et al., "Two-photon lithography of nanorods in SU-8 photoresist," Nanotechnology **16**, 846 (2005).

68. K. Takada, H.-B. Sun, and S. Kawata, "Improved spatial resolution and surface roughness in photopolymerization-based laser nanowriting," Applied Physics Letters **86**, 071122 (2005).

69. L. Yan, and et al., "Nonuniform shrinkage and stretching of polymerized nanostructures fabricated by two-photon photopolymerization," Nanotechnology **19**, 055303 (2008).

70. G. von Freymann, T. Y. M. Chan, S. John, V. Kitaev, G. A. Ozin, M. Deubel, and M. Wegener, "Sub-nanometer precision modification of the optical properties of three-dimensional polymer-based photonic crystals," Photonics and Nanostructures - Fundamentals and Applications **2**, 191-198 (2004).

71. A. Ovsianikov, X. Shizhou, M. Farsari, M. Vamvakaki, C. Fotakis, and B. N. Chichkov, "Shrinkage of microstructures produced by two-photon polymerization of Zr-based hybrid photosensitive materials," Opt. Express **17**, 2143-2148 (2009).

72. S. W. Hell, and J. Wichmann, "Breaking the diffraction resolution limit by stimulated emission: stimulated-emission-depletion fluorescence microscopy," Opt. Lett. **19**, 780-782 (1994).

73. T. A. Klar, and S. W. Hell, "Subdiffraction resolution in far-field fluorescence microscopy," Opt. Lett. **24**, 954-956 (1999).

74. L. Li, R. R. Gattass, E. Gershgoren, H. Hwang, and J. T. Fourkas, "Achieving λ/20 Resolution by One-Color Initiation and Deactivation of Polymerization," Science **324**, 910-913 (2009).

75. J. Fischer, and M. Wegener, "Three-dimensional direct laser writing inspired by stimulated-emission-depletion microscopy [Invited]," Opt. Mater. Express **1**, 614-624 (2011).

76. D. Buso, E. Nicoletti, J. Li, and M. Gu, "Engineering the refractive index of three-dimensional photonic crystals through multilayer deposition of CdS films," Opt. Express **18**, 1033-1040 (2010).

77. J. Li, M. D. M. Hossain, B. Jia, D. Buso, and M. Gu, "Three-dimensional hybrid photonic crystals merged with localized plasmon resonances," Opt. Express **18**, 4491-4498 (2010).

78. V. Mizeikis, S. Juodkazis, R. Tarozaite, J. Juodkazyte, K. Juodkazis, and H. Misawa, "Fabrication and properties of metalo-dielectric photonic crystal structures for infrared spectral region," Opt. Express **15**, 8454-8464 (2007).

79. A. Tal, Y.-S. Chen, H. E. Williams, R. C. Rumpf, and S. M. Kuebler, "Fabrication and characterization of three-dimensional copper metallodielectric photonic crystals," Opt. Express **15**, 18283-18293 (2007).

80. J. Li, B. Jia, G. Zhou, and M. Gu, "Fabrication of three-dimensional woodpile photonic crystals in a PbSe quantum dot composite material," Opt. Express **14**, 10740-10745 (2006).

81. Z.-Z. Gu, S. Kubo, W. Qian, Y. Einaga, D. A. Tryk, A. Fujishima, and O. Sato, "Varying the Optical Stop Band of a Three-Dimensional Photonic Crystal by Refractive Index Control," Langmuir **17**, 6751-6753 (2001).

82. S. Y. Lin, J. G. Fleming, Z. Y. Li, I. El-Kady, R. Biswas, and K. M. Ho, "Origin of absorption enhancement in a tungsten, three-dimensional photonic crystal," J. Opt. Soc. Am. B **20**, 1538-1541 (2003).

83. S.-Y. Lin, J. G. Fleming, E. Chow, J. Bur, K. K. Choi, and A. Goldberg, "Enhancement and suppression of thermal emission by a three-dimensional photonic crystal," Physical Review B **62**, R2243 (2000).

84. R. A. Farrer, C. N. LaFratta, L. Li, J. Praino, M. J. Naughton, B. E. A. Saleh, M. C. Teich, and J. T. Fourkas, "Selective Functionalization of 3-D Polymer Microstructures," Journal of the American Chemical Society **128**, 1796-1797 (2006).

85. F. Formanek, N. Takeyasu, T. Tanaka, K. Chiyoda, A. Ishikawa, and S. Kawata, "Three-dimensional fabrication of metallic nanostructures over large areas by two-photon polymerization," Opt. Express **14**, 800-809 (2006).

86. Y. S. Chen, A. Tal, D. B. Torrance, and S. M. Kuebler, "Fabrication and Characterization of Three-Dimensional Silver-Coated Polymeric Microstructures," Advanced Functional Materials **16**, 1739-1744 (2006).

87. Y.-S. Chen, A. Tal, and S. M. Kuebler, "Route to Three-Dimensional Metallized Microstructures Using Cross-Linkable Epoxide SU-8," Chemistry of Materials **19**, 3858-3860 (2007).

88. J. Serbin, A. Ovsianikov, and B. Chichkov, "Fabrication of woodpile structures by two-photon polymerization and investigation of their optical properties," Opt. Express **12**, 5221-5228 (2004).

89. S. Wong, M. Deubel, F. Pérez-Willard, S. John, G. A. Ozin, M. Wegener, and G. von Freymann, "Direct Laser Writing of Three- Dimensional Photonic Crystals

with a Complete Photonic Bandgap in Chalcogenide Glasses," Advanced Materials **18**, 265-269 (2006).

90. J. E. G. J. Wijnhoven, L. Bechger, and W. L. Vos, "Fabrication and Characterization of Large Macroporous Photonic Crystals in Titania," Chemistry of Materials **13**, 4486-4499 (2001).

91. P. V. Braun, R. W. Zehner, C. A. White, M. K. Weldon, C. Kloc, S. S. Patel, and P. Wiltzius, "Epitaxial Growth of High Dielectric Contrast Three-Dimensional Photonic Crystals," Advanced Materials **13**, 721-724 (2001).

92. P. V. Braun, and P. Wiltzius, "Electrochemical Fabrication of 3D Microperiodic Porous Materials," Advanced Materials **13**, 482-485 (2001).

93. K. Awazu, X. Wang, M. Fujimaki, T. Kuriyama, A. Sai, Y. Ohki, and H. Imai, "Fabrication of two- and three-dimensional photonic crystals of titania with submicrometer resolution by deep x-ray lithography," Journal of Vacuum Science & Technology B **23**, 934-939 (2005).

94. J. S. King, E. Graugnard, O. M. Roche, D. N. Sharp, J. Scrimgeour, R. G. Denning, A. J. Turberfield, and C. J. Summers, "Infiltration and Inversion of Holographically Defined Polymer Photonic Crystal Templates by Atomic Layer Deposition," Advanced Materials **18**, 1561-1565 (2006).

95. N. Tétreault, G. von Freymann, M. Deubel, M. Hermatschweiler, F. Pérez-Willard, S. John, M. Wegener, and G. A. Ozin, "New Route to Three-Dimensional Photonic Bandgap Materials: Silicon Double Inversion of Polymer Templates," Advanced Materials **18**, 457-460 (2006).

CHAPTER 3

MATERIALS AND METHODS

3.1 Experimental Setup

3.1.1 Optics and Mechanics

Multiphoton excitation source used for the majority of the work in this dissertation was a femtosecond Ti:Sapphire laser (80 MHz 15 W Millennia-pumped Tsunami, Spectra Physics) operating at 730 nm (~ 5-10 nm spectral width/FWHM, 100-120 fs pulse width). The exposure power was varied using a waveplate-polarizer pair, where the half-waveplate was mounted in a computer-controlled rotation stage (PR50-PP, Newport Corporation) and the transmitted power was measured by a power meter (Display 1835-C, Head, Newport Corporation). High speed modulation of the laser was accomplished with an electro-optic modulator (Power Supply 275, Modulator 350-160, ConOptics) with 10 MHz bandwidth and an extinction ratio of ~ 450:1, connected to the controlling computer with an arbitrary waveform generator card (PCIe-6120, National Instruments). The laser beam was expanded 20x (52-71-20X-730, Special Optics) to ensure uniform intensity distribution (< 10% variation) across the back aperture of the microscope objective (60x Oil-immersion, NA = 1.4, Nikon) which focused the excitation laser beam into the sample. The sample was mounted on a computer-controlled high speed three-axis translation stage, the X and Y stages (XM2000-160, Newport Corporation) with speeds up to 30 cm/s and 5 mm/s for the Z stage (VP-5Z, Newport Corporation). The optical layout is shown in Figure 3.1.

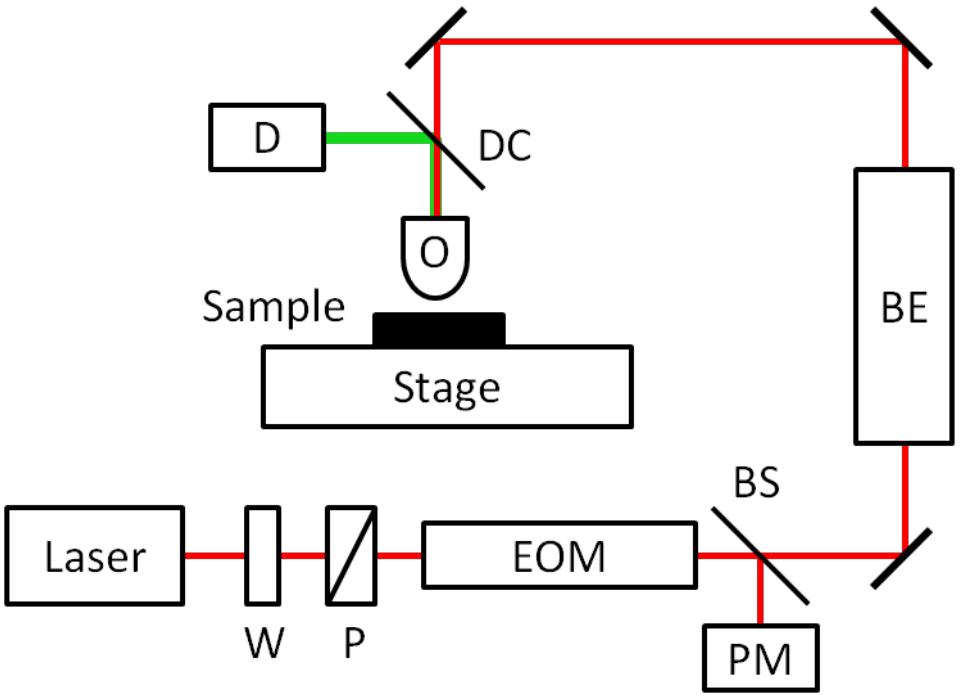

BE: Beam Expander
BS: Beam Sampler
D: Detector
DC: Dichroic Mirror
EOM: Electro-Optic Modulator
O: Objective
P: Polarizer
PM: Power Meter
W: Waveplate

Figure 3.1. Optical layout for MPL.

Two-photon excited fluorescence generated from the sample was collected and collimated using the same microscope objective. Fluorescence signal was separated from the excitation beam using a dichoric mirror with band edge at 710 nm (91-96% transmission from 720 to 1100 nm and < 4% between 400 and 680 nm (710dcxr, Chroma Technology Corporation), the residual excitation wavelengths, scattering and ambient room light were blocked using a short-pass filter (550 nm, Thorlabs) prior to a fiber coupled photo-receiver (FemtoWatt, New Focus) with a gain of 10^{11} V/W. Voltage readout was collected via a data acquisition card (6025E, National Instruments) to the controlling computer.

All communications to and from the various instruments were managed via the instrument computer using a homebuilt LabView program (Version 8.2, National Instruments).

3.1.2 Sample Translation

Each stage motion consists of an acceleration ramp-up, a constant velocity period and a deceleration ramp-down. Early work in our group and other reports in the literature utilize slow movements, typically between 50 and 300 micron/s for stepper motors and piezoelectric translators, where the ramp distances between zero and constant speed are negligible. The motivation behind building this fabrication system was to increase the efficiencies in fabrication time and patterned area to promote the study of chemical modification of the fabricated structures. Higher stage movement speeds translate to longer ramp distances before the constant speed is reached. To ensure even dosage across the entire fabricated structure, ramp distances for a range of speeds were experimentally determined by monitoring the stage's position at fixed time intervals along each stage movement:

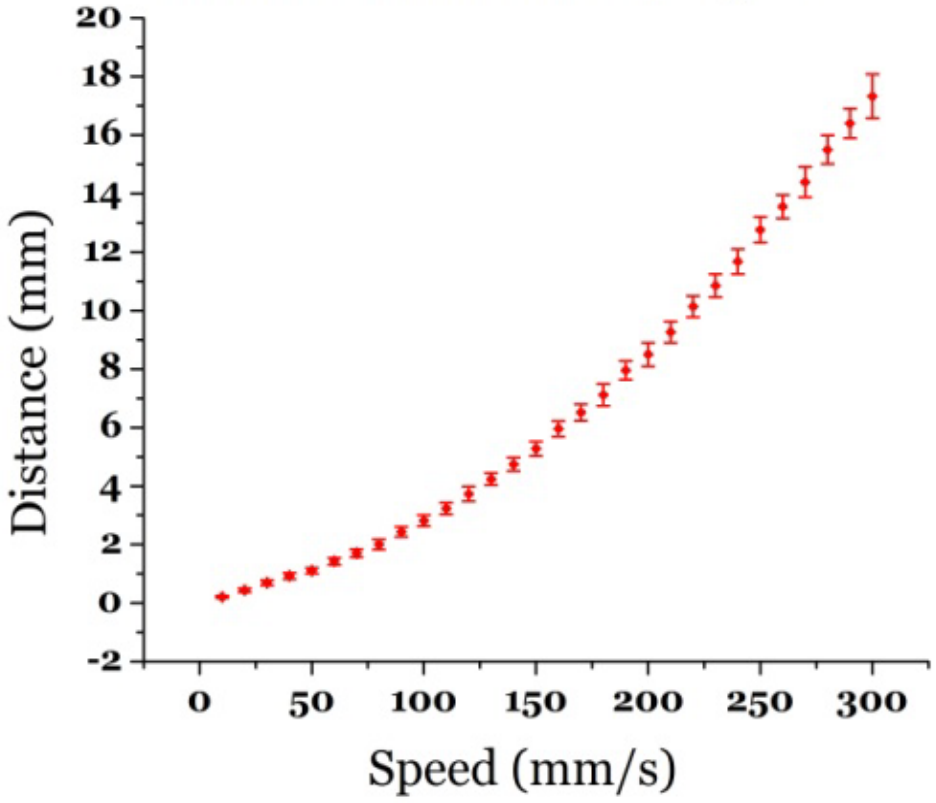

Figure 3.2. Ramp distance as a function of stage speed.

The typical velocity used in the work presented in this thesis is 10 mm/s; the ramp distance for this speed had been experimentally determined to be ~ 1.2 mm. The compensation of this ramp distance had been built into the software by pre-compensating the starting point, a fix distance opposite to the direction of movement and extending the ending point to the same distance. A triggering function of the stage controller was used to generate a TTL pulse at the starting and ending position of the desired segment to communicate with an external shutter or modulator.

3.1.3 Excitation Modulation

The modulation of the laser excitation was achieved using an electro-optic modulator. Timing of the switching between the on/off states was synchronized to the TTL trigger pulse from the stage controller. When a start pulse was received by the

arbitrary waveform generator (AWG), a step waveform loaded in the onboard memory was sent from the AWG to the amplifier, which in turn applied the voltage necessary to rotate the laser polarization through KD*P crystal to match the exiting polarizer. The opposite waveform was used to reject the laser beam when the stop pulse was received. The stage movement profile, the associated triggering signals and laser modulation are shown in the Figure 3.3.

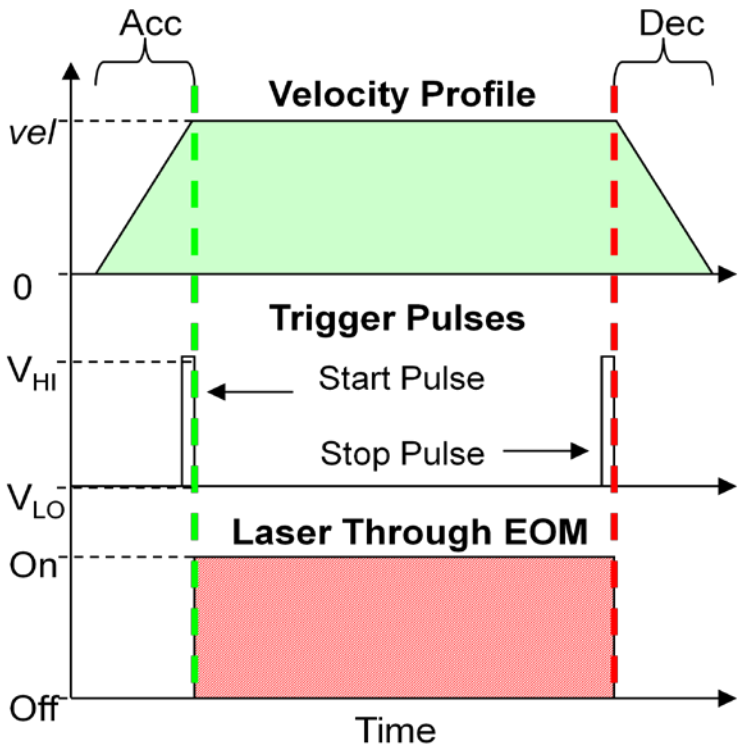

Figure 3.3. Schematic of exposure pattern in relation to stage movement.

Since dosage is a function of exposure time, which is inversely related to the speed, failure to deflect the laser during the ramping sequences would result in over exposure or optical damage of the sample. An extended version of this modulation was applied for creating segments in multiple structures in an array. Introducing multiple on/off segments in a single stage movement reduces the number of ramping sequences,

which in turn improves the fabrication time per structure dramatically. Details of this method are described in the next section.

Further optimization of the fabrication time can be accomplished through calibration of the temporal profile of the ramping sequences and creating a complex waveform and alter the transmitted power to achieve constant dosage throughout the entire stage motion. The system can also be adapted for complex arbitrary structures by converting the exposure pattern into a series of waveforms that modulates the excitation laser as the stage raster in the xy plane.

3.1.4 Power Adjustment

A combination of waveplate-polarizer was used to control the amount of laser light transmitted to the sample. The birefringence of the half-waveplate induces change in the polarization, and the exiting polarization is controlled by rotating the fast axis of the waveplate with respect to the fixed laser polarization. The overlap between the rotated polarization and the stationary polarizer on the exit side of the waveplate determines the transmitted power. A beam splitter was used to pick off ~2% of the laser beam to monitor the power. A schematic of this arrangement is shown in Figure 3.4.

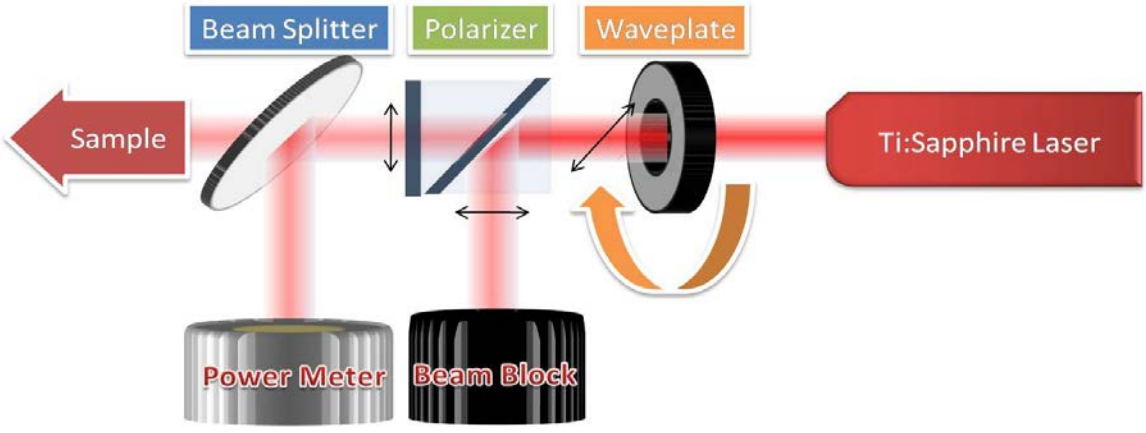

Figure 3.4. Schematic of the set-up used for laser power tuning .

The waveplate was mounted on a computer-controlled rotation stage and the transmission was recorded as a function of degree of rotation (Figure 3.5). This look-up table was then used by the software to perform on-the-fly power tuning during the experiment.

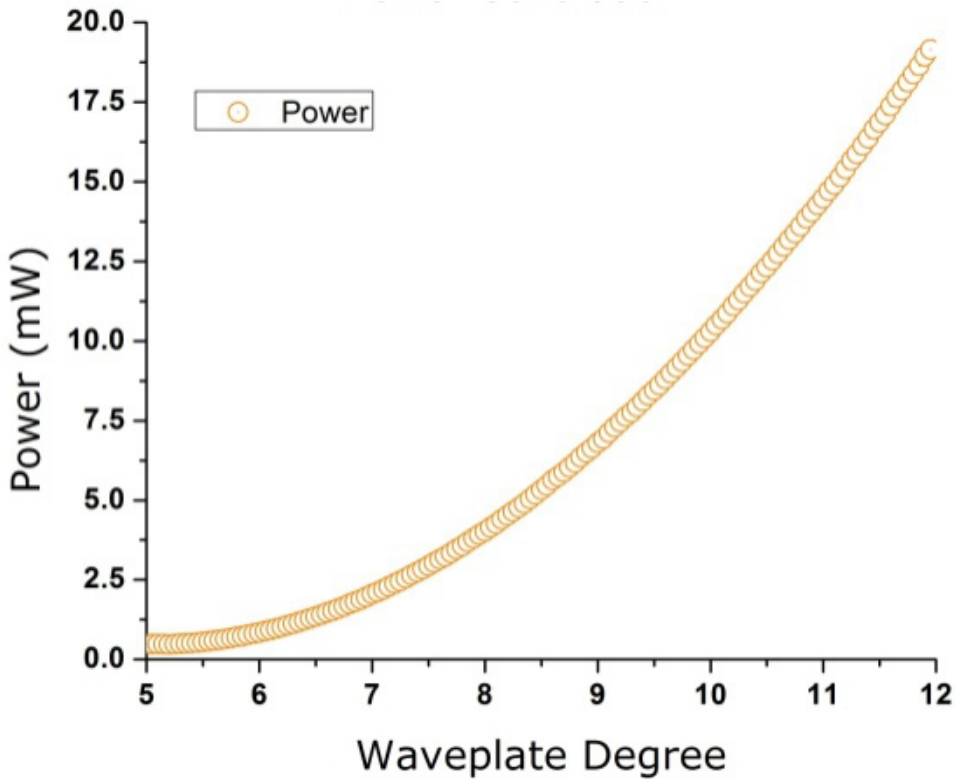

Figure 3.5. Calibration curve of transmitted power as a function of waveplate rotation.

Changes in the environment cause the laser output power to drift over time; this would lead to an undesired change in dosage for extended experiments. A power search sequence was utilized to overcome this problem. A starting rotation degree was first calculated from the look-up table, followed by measurement of powers at fixed offsets at greater and smaller angles, the next center angle used was calculated from the two points. The magnitude of the angular offset was sequentially reduced until the power was within

a set tolerance of 0.5-1.0%. A representation of the tuning sequence is shown in Figure 3.6 below.

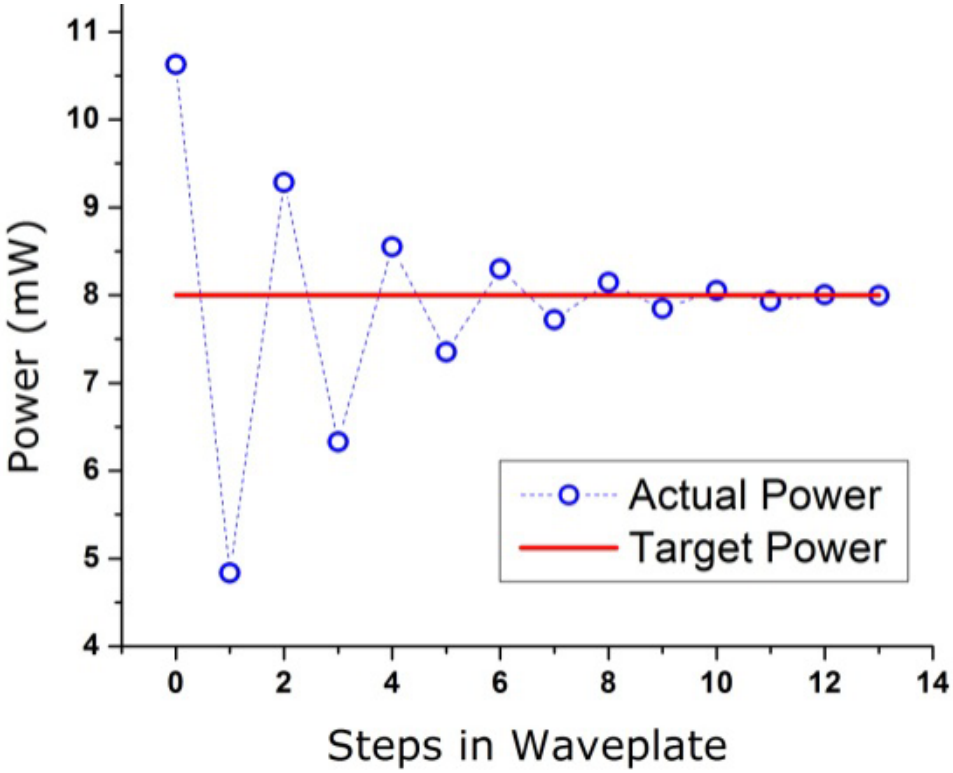

Figure 3.6. Example of a power tuning sequence used to compensate for the drift in laser output power.

Usage of this algorithm allowed for continuous fabrication for up to 48 hours without any user intervention.

3.1.5 Interface Determination

The range of conditions used in multiphoton initialized crosslinking typically affords voxel elements with a height of 500 to 1000 nm. It is critical to determine the location of the interface between the substrate and the sample accurately to ensure proper anchoring of any structures onto the substrate. Fluorescence of the two-photon

photoinitiator was used as a gauge of the location of the focal plane with respect to the stage position along the z-axis. Fluorescence z-scans were performed using excitation below the crosslinking threshold (~0.5 mW) to avoid unwanted polymerization. The sample was moved along the z direction while the laser focus was fixed as depicted in Figure 3.7.

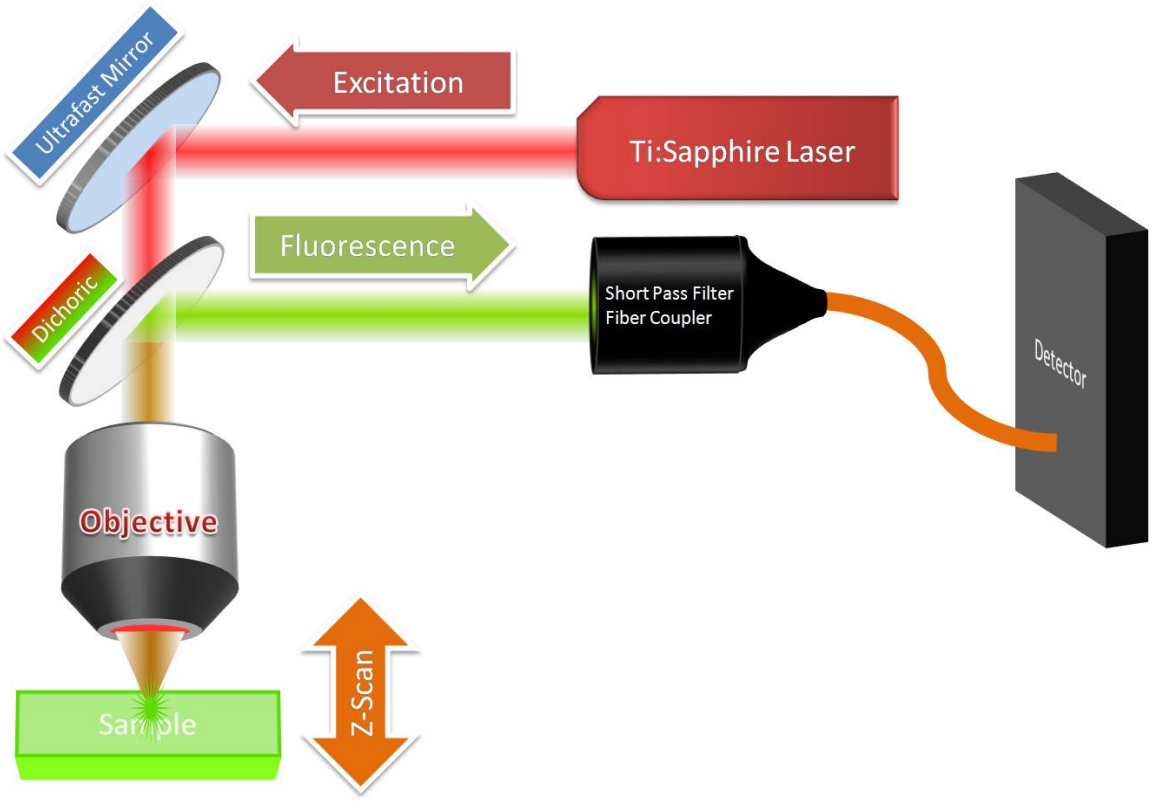

Figure 3.7. Optical layout for fluorescence detection.

The fluorescence signal recorded by the photoreceiver was plotted as a function of z-positions. The resultant intensity profile was then used to locate the interfacial point. When the focus was located within the substrate, no fluorescence signal was detected. A sharp increase in the detector voltage was observed as the focus began to overlap with the initiator-doped resin. The detected voltage remained high while the focus was within the resin and began to drop as it migrates into the immersion oil. A typical fluorescence

profile in Figure 3.8 represents a liquid sample cell, where the resin is sandwiched between a microscope slide (z > 1.990 mm) and a cover-slip (z < 1.915 mm).

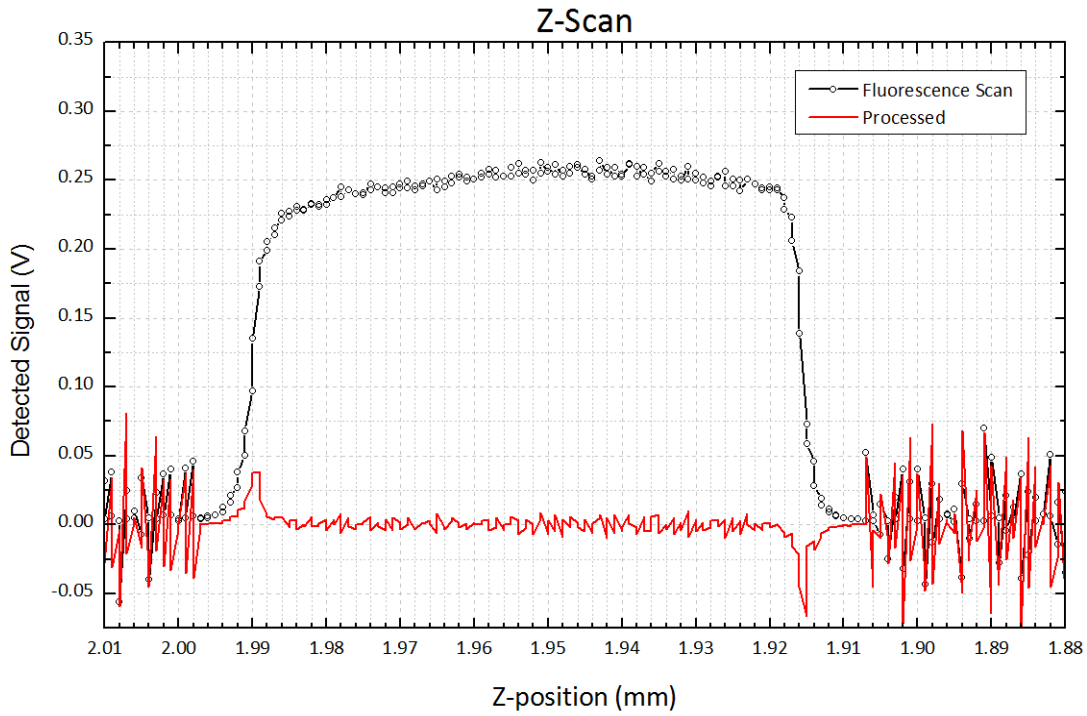

Figure 3.8. Fluorescence profile and its derivative obtained by scanning through a photoresist coated on a glass substrate.

Derivatives of the fluorescence profiles were taken to better illustrate the mid-point between the focus located entirely within the substrate versus the resin. The peak in the processed signal (z = 1.990 mm) was used to define the substrate-sample interface. Fluorescence z-scans were performed at each fabrication location to correct for tilting of the substrate over large areas (typically ~1 μm in z per 1 mm in xy).

3.2 Experimental Procedure

Laser system and all equipments were turned on and allowed to warm up and stabilize for one hour prior to experiment. Laser emission was optimized to maximum power output at the desired wavelength of 730 nm and the bandwidth adjusted to 5.5 nm at FWHM. Stability under these conditions was monitored for 30 minutes and re-optimization was performed again if the output fluctuation was greater than 1%. Adjustments to routing mirrors through the preset apertures ensured proper alignment of the laser beam to the sample. A gold mirror was mounted onto the stage and the back reflection of the laser beam was used to align the beam normal to the stage surface.

After the sample was mounted onto the translation stage, immersion oil was applied to the sample and brought into contact with the microscope objective. Coarse positioning of the focus was achieved by visually monitoring the fluorescence intensity, through a short pass 550 nm filter, and translation of the objective into the resin.

From this point forward, all controls were performed on the computer by the LabView software code. A power calibration scan was first performed to establish the waveplate position and the associated transmitted power. The desired fabrication location was entered into the software and fluorescence z-scans were performed at each of these coordinates using exposure powers of 0.5 mW. Interface information was then loaded into the built-in structure generators which served as origins for each fabricated structures.

To perform the work presented in this thesis, a photonic crystal structure generator was used. The program processes lattice parameters, size and location of the photonic crystals and generates a set of ascii commands related to triggering and coordinates information. These sets of commands were then sent to the stage controller leading to the fabrication of the described photonic crystals. Experimental conditions

related to the lattice parameters, exposure powers and stabilities were logged into text files upon completion.

3.3 MPL System Performance Characteristics

One main focus of this thesis is to develop, characterize and analyze various chemical methods of surface modification to engineer the PC stopband position and refractive index. A broad range of processing conditions has to be examined, necessitating a large number of samples for comparisons. Our group's previous work and others in the literature utilize speeds in the range of 100 μm/s, which translates to approximately 15 minutes for the fabrication of a typical PC. This limitation severely hinders the fabrication efficiencies and to improve the fabrication efficiency, the high speed capability of our MPL system was employed.

3.3.1 Large-area High-speed Fabrication

Initial fabrication of large area PCs at high speeds were attempted prior to the construction of a mechanically stable laser delivery gantry system, therefore the results were less than ideal. However, the initial attempts provided valuable insights into the mechanical issues that have since been addressed. A stage speed of 40 mm/s was used to fabricate the 1×1 cm^2 PCs with 5 μm line spacing and 4 μm layer spacing in Figure 3.9.

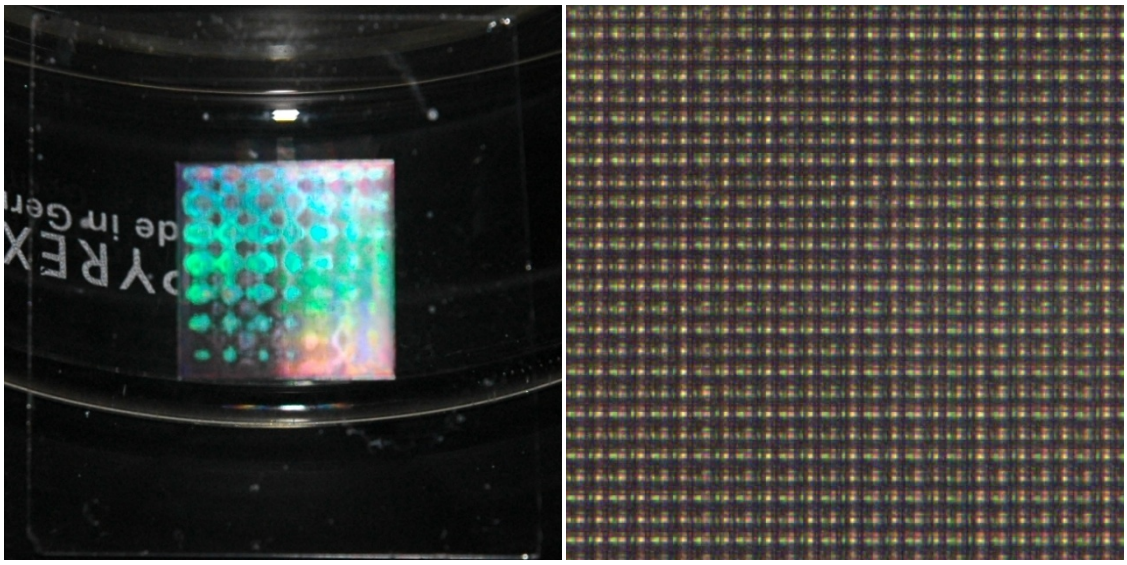

Figure 3.9. Photograph of the 1 × 1 cm^2 PC (left) and under the microscope with a 40× objective.

The modulation observed was due to uncontrolled collapse of different areas of the structure and possibly vibration-isolation issues with the fabrication setup. Another feature found was the reflection and opacity seems to be at an angle, creating what seems to be a gradient from the -x, -y (upper right) corner to the +x, +y (lower left) corner. This is most likely due to a tilting of the sample over these long distances (typical 1 μm/mm). Other than these artifacts, microscope transmission images (Figure 3.9) indicated a periodic structure was obtained.

Our second attempt utilized 200 mm/s translation speeds to fabricate 2.5 × 2.5 mm^2 × 30 layered PC with 5 micron line spacing and 3 micron layer spacing in under two hours. SEM images of this large area structure are shown in Figure 3.10.

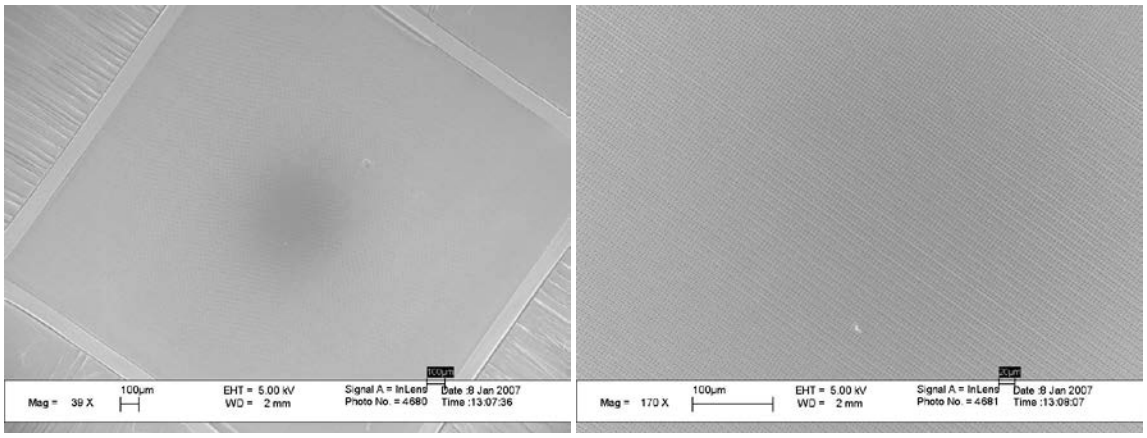

Figure 3.10. SEM images of a 2 mm x 2 mm photonic crystal structure fabricated with a scan speed of 20 cm/s. Left: overview of structure; right: close up view.

A support frame was fabricated to provide structural support, however the shrinkage induced stress have led to the delamination of the structure at the edges, as observed in the upper portion of Figure 3.10. The central portion of the PC did show reasonable quality, however the lack of structural support resulted in distortion of the periodicity during development, preventing the observation of a stopband.

To assess the fabrication efficiency at high speeds, the time spent during the extended acceleration and deceleration distances has to be accounted for. The velocity profiles of the stage were recorded for a range of translation speeds as a function of travel distance. The efficiency was characterized by the duration at which the stage travels at the defined velocity divided by the time for the total travel. The results are reported in percentages in Figure 3.11.

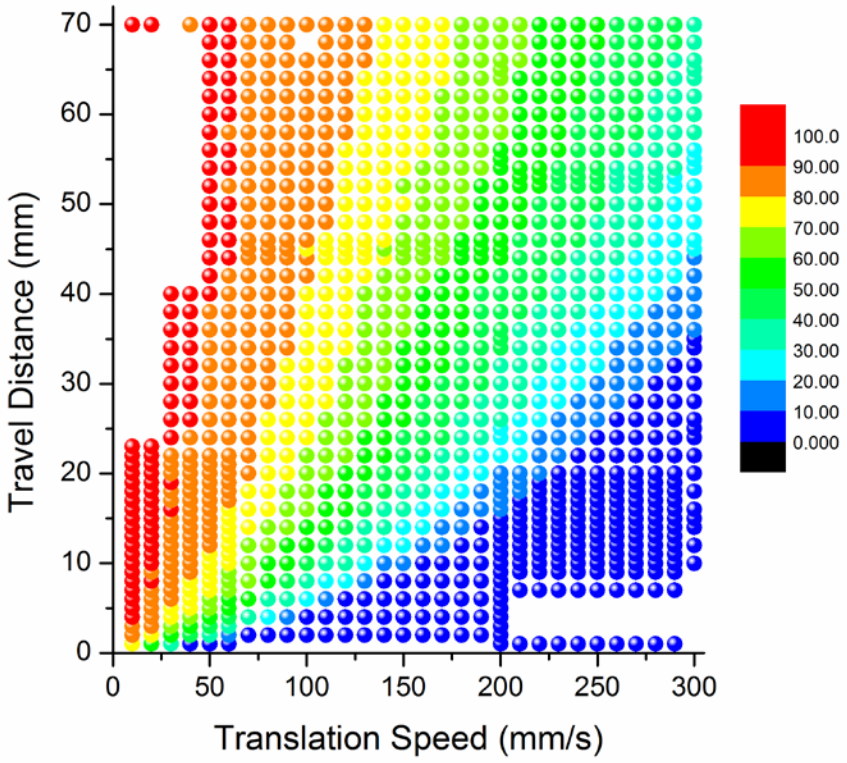

Figure 3.11. Fabrication efficiency reported as the time at set velocity divided by the total travel time in percentage.

Typical PCs used for the optimization of stopband reflectivity are of 100 to 200 µm in edge length. For these short travel distances, fabrication speeds higher than 10 mm/s are inefficient due to the small portion of the actual fabrication time compared to the total travel time.

3.3.2 Array Fabrication

To take advantage of the high speed fabrication and the area achievable with this system, an alternative method was developed to circumvent the stress related distortion. The laser excitation was modulated during a long distance travel to fabricate multiple line

segments for an array of PCs. The schematic of the excitation modulation in relation to the stage travel is shown in Figure 3.12.

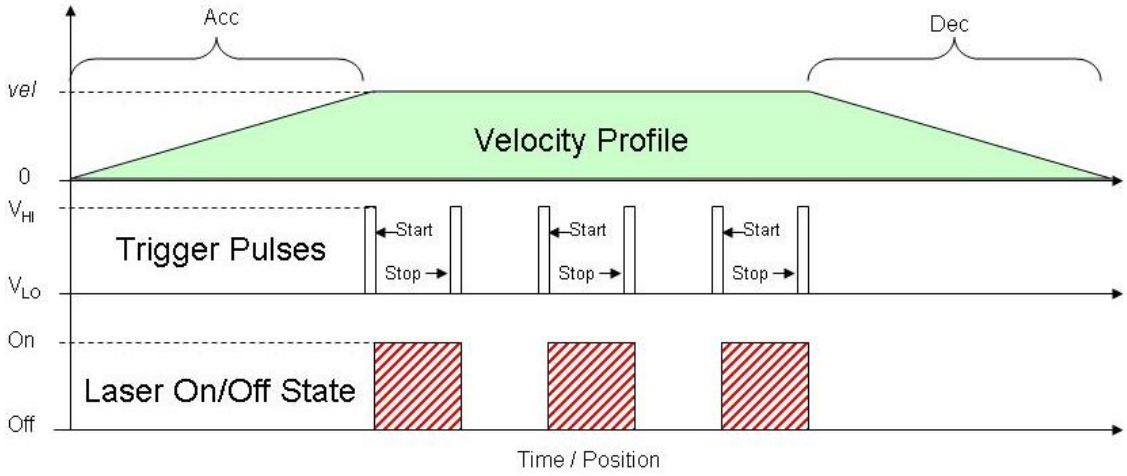

Figure 3.12. A new scheme developed illustrating the fabrication of three segments in a single translation of the stage.

This modified method was used to fabricate 16 PCs in a 4 × 4 array with each stage translation creating line segments in 4 PCs. Lattice parameters used to demonstrate this method were 4 microns line spacing and 1.5 micron layer spacing, 100 × 100 micron^2 × 16 layers at 10 mm/s. Fabrication of this 4 × 4 array (16 structures total) was completed in 6.5 minutes while fabrication of each structure separately required 16 minutes. This 2.5× improvement of fabrication speed is expected to increase at higher speeds due to the longer acceleration times. Example of infrared reflection spectra of PCs fabricated using this array method is shown in Figure 3.13 to demonstrate the reproducibility.

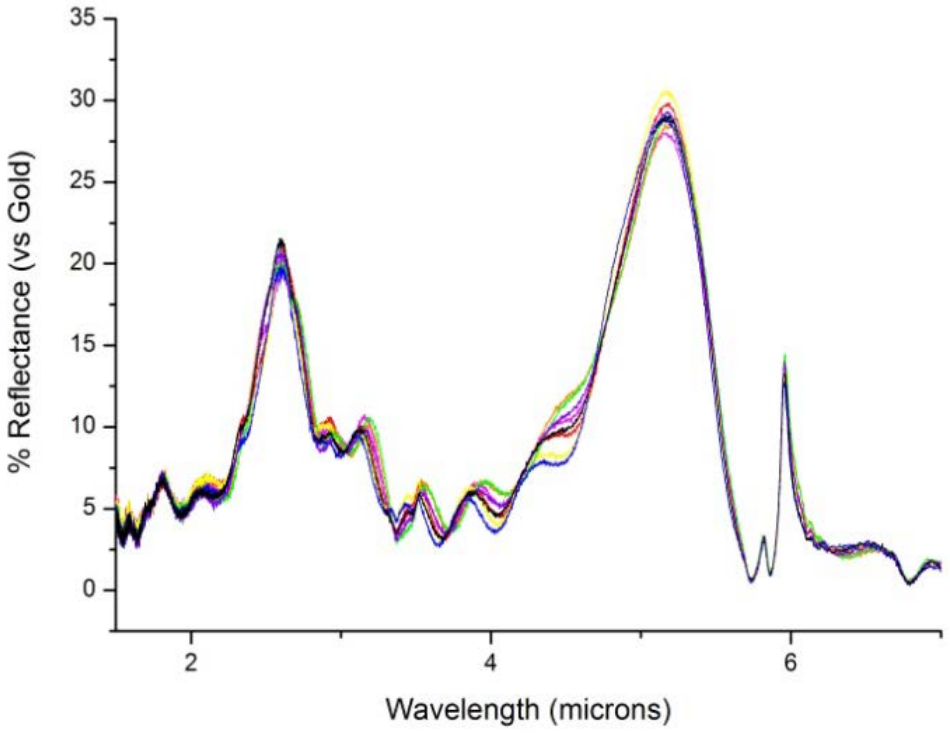

Figure 3.13. Infrared reflection spectra of PCs generated using the array method.

3.4 Material Systems

3.4.1 Multiphoton Initiator

The photoinitiator used in this study was *E*,*E*-1,4-*bis*[4-(di-*n*-butylamino)styryl]-2,5-dimethoxybenzene (DABSB), the chemical structure and its linear, two-photon absorption and fluorescence spectra are shown in Figure 3.14. This molecule has been demonstrated to be an extremely effective two-photon absorbing radical photoinitiator [1, 2] with a maximum two-photon absorption cross-section of 900 GM at 730 nm [3].

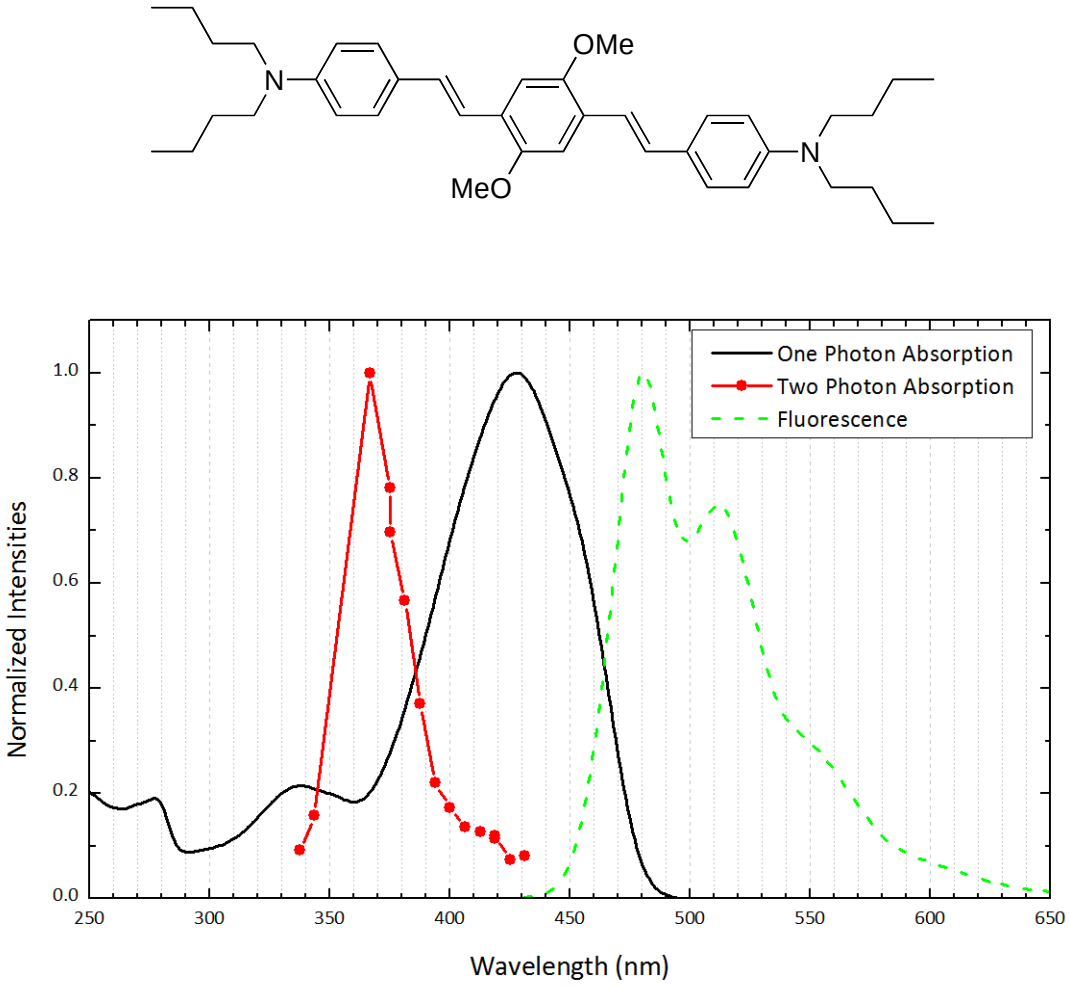

Figure 3.14. Molecular structure of the two-photon photoinitiator DABSB (top). Linear absorption spectrum in dioxane, two-photon absorption [3] and fluorescence spectra in toluene (bottom).

3.4.2 Resin Systems

Photosensitive resin systems used in this work is based on radical polymerization of multifunctional acrylate monomers. A previously developed resist formulation is used [2], where a binder polymer was incorporated into mixtures of triacrylate monomers to form gel-like semi-solid photoresists. A liquid version of the same formulation with the

absence of the binder has also been adopted for reduced shrinkage and rapid solvent development.

The two-photon photoinitiator DABSB was doped into the resin systems at 0.1 weight % to induce crosslinking reaction upon laser exposure. Mixture of multifunctional acrylate monomers were used to formulate a liquid resin at room temperature. One component of the multifunctional acrylate was an alkoxylated trifunctional acrylate ester (SR9008), a proprietary product from Sartomer that promotes adhesion to glass surfaces, and the other was tris(2-hydroxyethyl)isocyanurate triacrylate (SR368, Figure 3.15), a triazin compound for strength at 50:50% by weight.

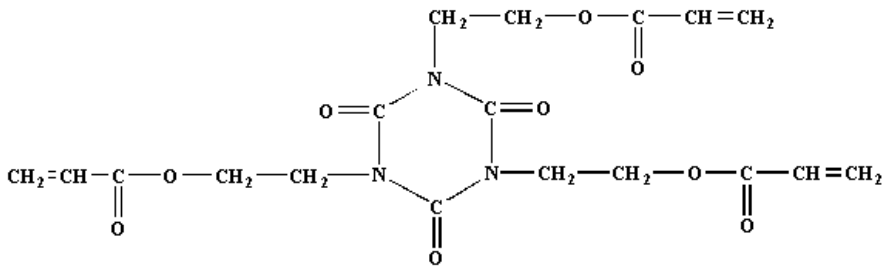

Figure 3.15. Molecular structure of triacrylate monomer SR368.

0.1 weight % of 4-methoxyphenol (Aldrich, 99%), a widely used inhibitor, was added to the above mentioned resin system to prevent thermal crosslinking as the blend phase-separates over several days of storage and reheating of the resin is required for further use. The liquid resin was sandwiched between an adhesion promoter coated microscope slide substrate and a No. 0 cover slip (Electron Microscopy Sciences, Gold Seal), spaced by Teflon spacers (Aldrich) between 25 and 100 microns in thickness, to form a cell for MPL fabrication. The adhesion promoter coated slides were prepared by treatment of acetone cleaned glass microscope slides with 10 vol% 3-(trimethoxysilyl)propyl methacrylate (Aldrich, 98%) in ethanol (Aldrich, 200 proof, anhydrous, 99.5%) and baked on a hot plate at 130°C for three cycles. The methacrylate

silane was chosen over the acrylate version to distinguish the surface functional groups of the crosslinked polymer from the substrate to achieve selectivity in subsequent chemical modifications.

The same liquid mixture was formed into a gel-like semi-solid photoresist by the addition of poly(styrene-*co*-acrylonitrile) (PSAN, Polyscience, Inc., 75:25 styrene:acrylonitrile). The monomer mixture was dissolved in dioxane along with PSAN to form a final mixture of 35% SR9008, 35% SR368 and 30% PSAN. The photoresists films were formed by blade casting the viscous dioxane solution to adhesion promoted glass substrates. Thicknesses of the resulting photoresists were controlled by the resin concentration and the blade thickness. A 1:1 volume ratio of casting solvent to solids was blade cast at twice the thickness to form photoresist of the desired thickness after 12 hours of slow solvent evaporation and 5 hours of vacuum drying.

3.4.3 Sample Development after MPL

At the end of the experiment, the photoresists or liquid cells were developed in 4-methyl-2-pentanone (MIBK, Aldrich, 99%) to remove unexposed material while crosslinked structures remained insoluble. Development was carried out in slide staining jars (60 mL MIBK) with stirring for 10 minutes in the case of the liquid cells and 15-30 minutes for thicker photoresists. The sample was exchanged into a new bath every 5 minutes to reduce the concentration of unreacted material in the developer to eliminate residues on the substrate. Finally, the sample was placed in a bath of hexane (for 2 minutes) to remove trapped MIBK in microporous domains of the structures and promote fast drying under a gentle stream of nitrogen.

3.5 Sample Characterization

3.5.1 Dosage Characterization

Dosing experiments were performed to establish the relationship between the exposure conditions and the sizes of the fabricated elements. Two structural designs were used to perform this task. The simpler design was to fabricate cords that span across macro structures, the schematic and an example of the fabricated structure is shown in Figure 3.16.

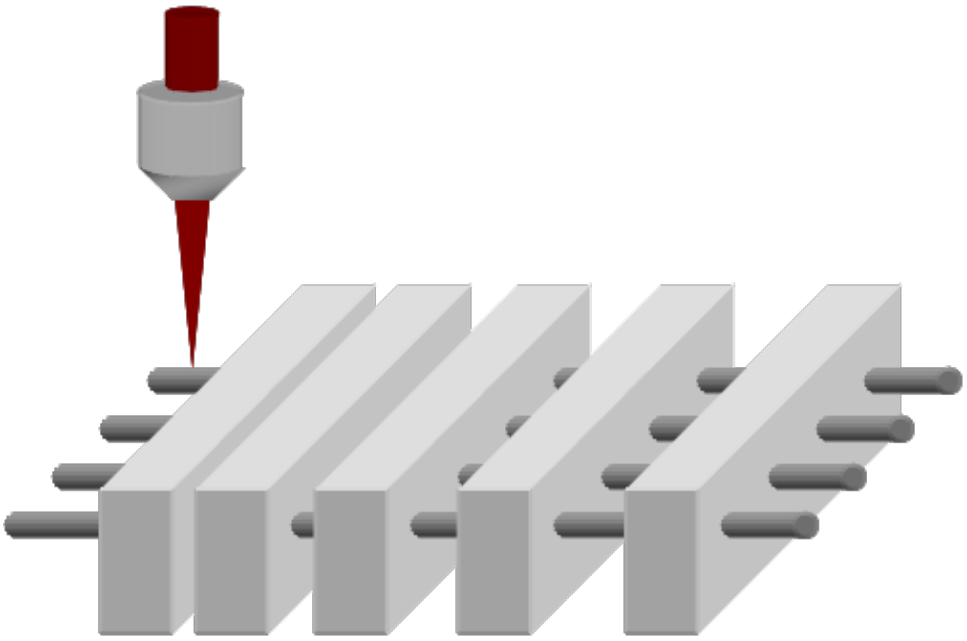

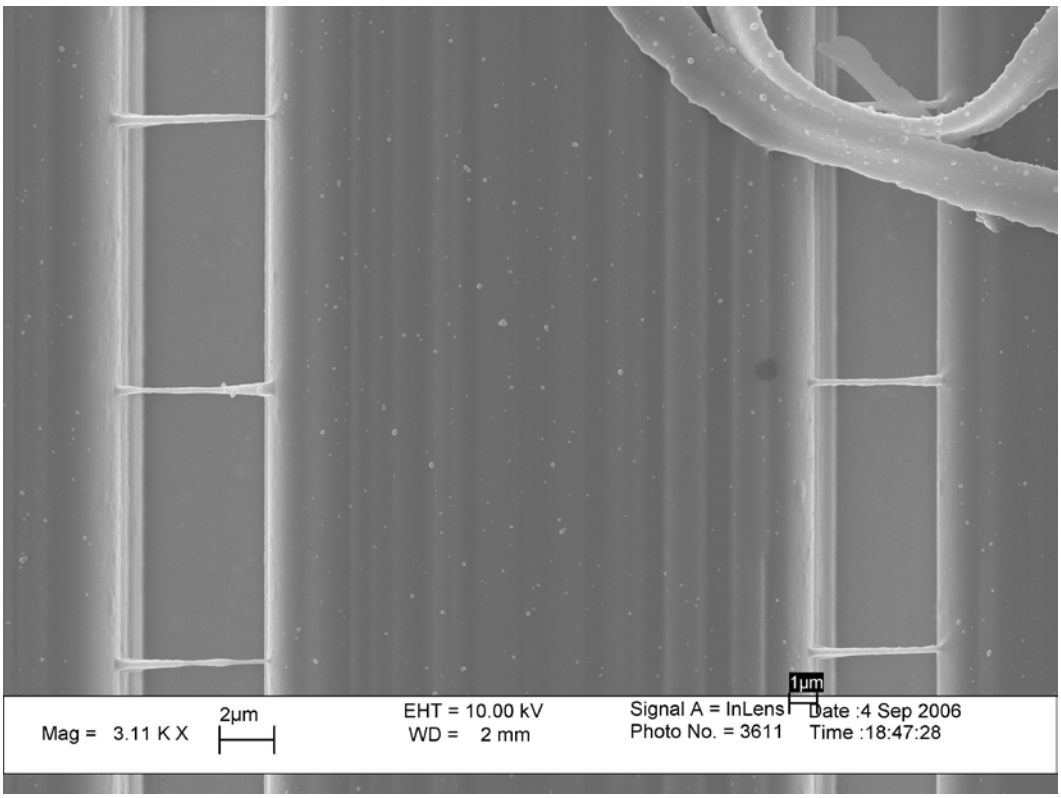

Figure 3.16. Structural design and SEM image of test structures used for line width characterization.

In this design, rectangular blocks of macrostructures were fabricated at high dose first, with widths and heights of 20 µm, these blocks were then spaced apart to form channels where the cords will span. The variation of the channel widths provides additional information on the mechanical strength for the given exposure parameters. This design allows for rapid testing of a wide range of exposure conditions once the support structures were fabricated. One drawback of this design, however, is that it does not take into account the effect of shrinkage. As the exposure condition approaches the crosslinking threshold, the combination of elasticity of the cords and mechanical strength of the supporting blocks causes the cords to stretch in the free-spanning gap. This effect masks the physical ability to use these features as building blocks for free-standing structures.

PCs are better suited to assess the exposure conditions for building free-standing structures. The macroporous, low fill-fraction nature of this type of structure not only reveals the post-shrinkage cord dimensions but also their mechanical strength towards supporting additional mass. Using fixed PC lattice parameters and fixed stage speed, the exposure power was varied and the resultant structures were imaged under SEM. An example demonstrating the relationship between exposure power and cord widths is plotted in Figure 3.17.

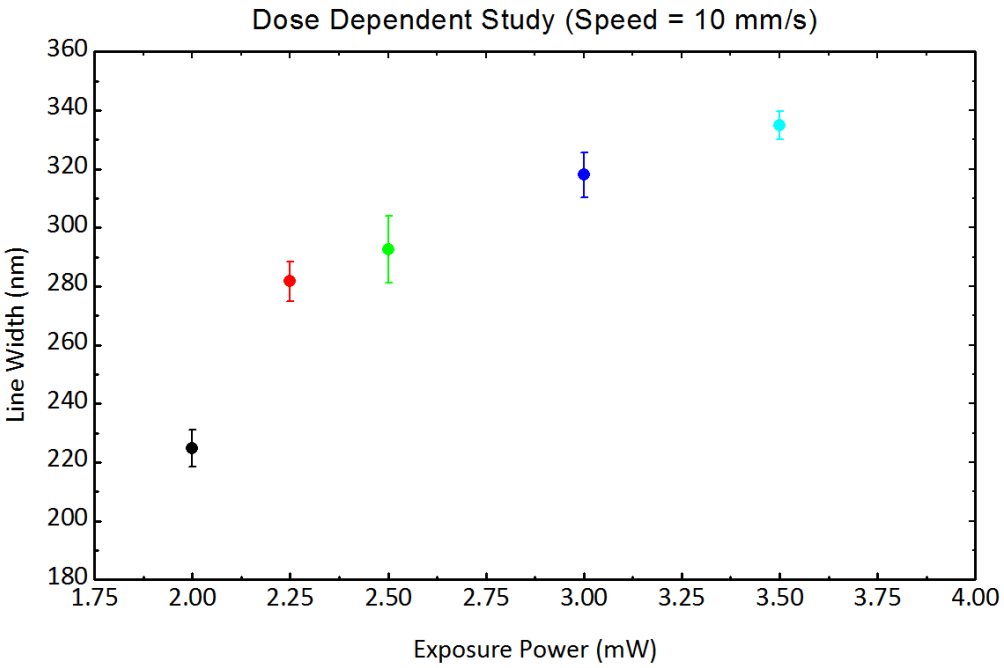

Figure 3.17. Dose dependent study of line widths achieved under varying excitation powers.

The data above shows a non-linear relationship between the exposure power and cord widths as a result of the combined effect of the multiphoton absorption process and the threshold requirements for the polymerization process [4]. The highest resolution features obtained using these conditions was 223 ± 7 nm, which is in good agreement with other reports in the literature [5, 6].

Another advantage of the PC test platform is the relationship between the structural quality and the axial resolution, or the height, of the cords. The axial confinement of multiphoton excitation is also a function of dose, rough estimates of this height can be obtained by varying the layer to layer spacing in the PC lattice at fixed exposure powers. If the cord height was smaller than the layer to layer spacing, the cords would be washed away, and if the overlapping volumes between adjacent layers were not sufficient, the structure would collapse. Both of these scenarios can be immediately observed under an optical microscope and the parameters can be adjusted accordingly.

3.5.2 Fourier-transform Infrared Microscopic Characterization of PCs

Photonic stopbands generated by the PCs are related to the specific lattice parameters and feature sizes. The spatial arrangement of the rods causes light within a narrow range of frequencies to reflect or refract stronger than the rest of the spectrum, resulting in unique reflection and transmission bands, commonly called a stopband, observable by spectroscopy. The resolution afforded by fabrication using near-IR excitation dictated stopbands to exist in the near to mid infrared region. A FTIR microscope was used to characterize these microstructures.

PCs fabricated were typically between 100 × 100 to 200 × 200 micron^2. The small size of these structures necessitated analysis under a microscope with apertures to ensure information acquired only pertains to the region of interest. The FTIR spectrometer-microscope setup provided the capability to divert the infrared irradiation from the typical macro sample chamber into a microscope equipped with mirror optics to focus and collect infrared spectra from micro-scaled samples. The schematic of the reflection and transmission measurement geometries are shown in Figure 3.18.

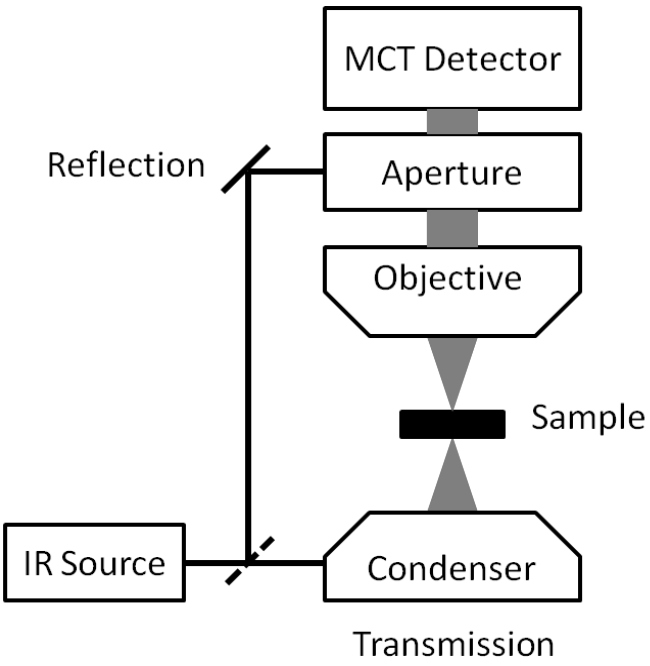

Figure 3.18. Schematic of infrared measurements in transmission and reflection modes.

15× Schwarzschild objectives were used in both reflection and transmission mode to focus and collect infrared light from the sample. The double curved mirror design of these objectives creates a conical focusing geometry with an inner and outer angle of 14º (NA=0.24) and 30º (NA=0.5) respectively. A ray diagram of this optic is shown in Figure 3.19.

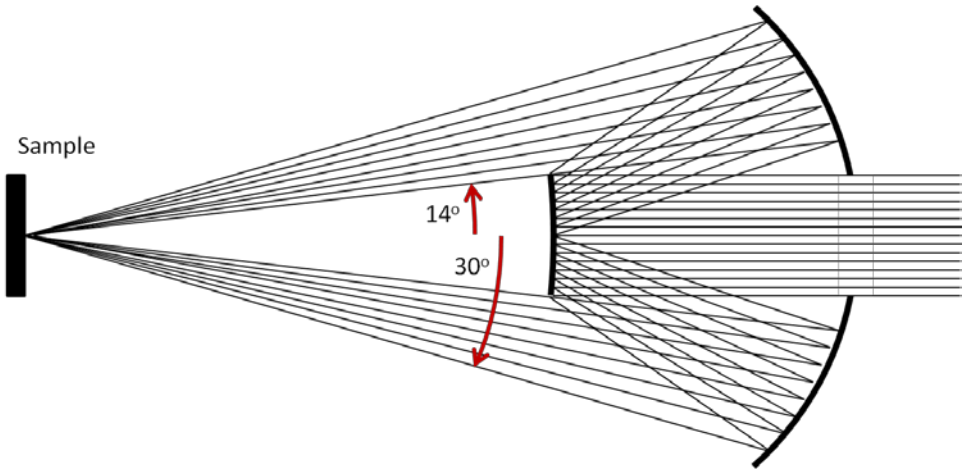

Figure 3.19. Ray diagram of Schwarzschild objective used for FTIR measurements.

The sample was brought to focus by translation of the sample stage and observation through the microscope binoculars. In the reflection mode, since the focusing and collection were performed by the same objective, no additional alignment was necessary, however in the case of transmission, the condenser was adjusted for maximum detector signal intensity. The apertures were then reduced to 80% of the structure's edge lengths and remained fixed once the background spectrum was acquired. In reflection mode, a gold mirror was used as the reference, while the sample substrate was used for transmission reference. Two sets of sources and optics span the spectral range between 1 and 14.5 microns, a tungsten lamp with quartz beam splitter for the near-IR range (1 – 3.5 μm) and a high temperature ceramic emitter with KBr beam splitter for the mid-IR range (1.6 – 14.5 μm). A liquid nitrogen cooled mercury cadmium telluride detector was used to collect the spectra. Averages of 16 scans were used for the collection of spectra. Examples of PC stopband spectra collected are shown in Figure 3.20.

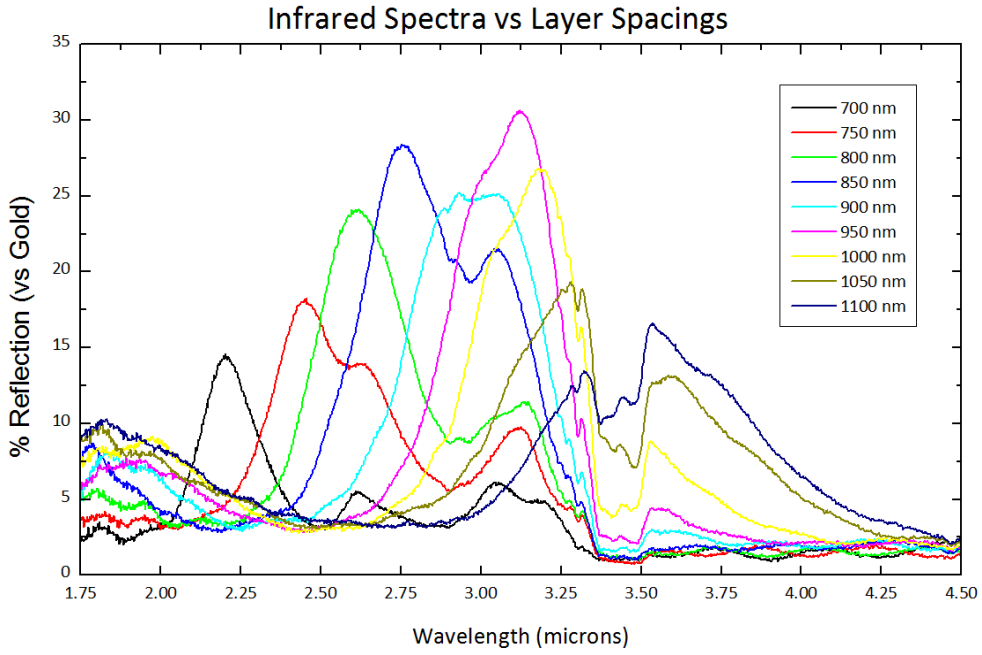

Figure 3.20. Infrared reflection spectra collected from PCs.

REFERENCES

1. S. M. Kuebler, B. H. Cumpston, S. Ananthavel, S. Barlow, J. E. Ehrlich, L. L. Erskine, A. A. Heikal, D. McCord-Maughon, J. Qin, H. Roeckel, M. C. Rumi, S. R. Marder, and J. W. Perry, "Three-dimensional microfabrication using two-photon-activated chemistry," in *Proc. SPIE 3937*(SPIE, 2000), pp. 97-105.

2. B. H. Cumpston, S. P. Ananthavel, S. Barlow, D. L. Dyer, J. E. Ehrlich, L. L. Erskine, A. A. Heikal, S. M. Kuebler, I. Y. S. Lee, D. McCord-Maughon, J. Qin, H. Rockel, M. Rumi, X.-L. Wu, S. R. Marder, and J. W. Perry, "Two-photon polymerization initiators for three-dimensional optical data storage and microfabrication," Nature **398**, 51-54 (1999).

3. M. Rumi, J. E. Ehrlich, A. A. Heikal, J. W. Perry, S. Barlow, Z. Hu, D. McCord-Maughon, T. C. Parker, H. Röckel, S. Thayumanavan, S. R. Marder, D. Beljonne, and J.-L. Brédas, "Structure−Property Relationships for Two-Photon Absorbing Chromophores: Bis-Donor Diphenylpolyene and Bis(styryl)benzene Derivatives," Journal of the American Chemical Society **122**, 9500-9510 (2000).

4. S. M. Kuebler, M. Rumi, T. Watanabe, K. Braun, B. H. Cumpston, A. A. Heikal, L. L. Erskine, S. Thayumanavan, and J. W. Perry, "Optimizing Two-Photon Initiators and Exposure Conditions for Three-Dimensional Lithographic Microfabrication," Journal of Photopolym. Sci. Technol **14**, 657-668 (2001).

5. S. Kawata, H.-B. Sun, T. Tanaka, and K. Takada, "Finer features for functional microdevices," Nature **412**, 697-698 (2001).

6. M. Deubel, G. von Freymann, M. Wegener, S. Pereira, K. Busch, and C. M. Soukoulis, "Direct laser writing of three-dimensional photonic-crystal templates for telecommunications," Nat Mater **3**, 444-447 (2004).

CHAPTER 4

65 NM FEATURE SIZES USING VISIBLE WAVELENGTH 3-D MULTIPHOTON LITHOGRAPHY

Wojciech Haske[†], Vincent W. Chen[†], Joel M. Hales, Wenting Dong, Stephen Barlow, Seth R. Marder, Joseph W. Perry*

[†]*These authors contributed equally to this work*

School of Chemistry and Biochemistry and Center for Organic Photonics and Electronics, Georgia Institute of Technology, Atlanta, GA 30332-0400

Copy of manuscript published in Optics Express

ABSTRACT

Nanoscale features as small as 65 ± 5 nm have been formed reproducibly by using 520 nm femtosecond pulsed excitation of a 4,4'-bis(di-*n*-butylamino)biphenyl chromophore to initiate crosslinking in a triacrylate blend. Dosimetry studies of the photoinduced polymerization were performed on chromophores with sizable two-photon absorption cross-sections at 520 and 730 nm. These studies show that sub-diffraction limited line widths are obtained in both cases with the lines written at 520 nm being smaller. Three-dimensional multiphoton lithography at 520 nm has been used to fabricate polymeric woodpile photonic crystal structures that show stop bands in the near-infrared spectral region.

PERSPECTIVE

Since the 2007 publication of the manuscript that comprises the following chapter, there have been several reports of resolution improvement using a spatially deactivating photochemical or photophysical process. Andrew et al. have reported the fabrication of 36 nm features by using two different wavelengths of light to spatially control photoactivation and deactivation of an organic photochromic layer to create a switchable mask [1]. This process utilizes a high intensity deactivating optical beam to create an opaque grating pattern with intensity-dependent transparent slit widths for photoexcitation; however this switching is inherently limited to 2D patterning and nanometer sample thicknesses due to the evanescent nature of the transmitted intensity. Another approach used by Scott et al. was independent photoactivation of initiators and inhibitors [2]. Inhibitors were activated using a doughnut shaped focal volume to produce mono-functional molecules which terminated the propagation of polymerization. This photoinhibition process, however, is non-reversible, thereby precluding the possibility of forming continuous features once the inhibiting species have been formed.

The Stimulated-Emission-Depletion (STED) approach pioneered by Hell for microscopy, predicted theoretically in 1994 [3] and demonstrated experimentally in 1999 [4], has been adopted by Li et al. to control the excited state population of the photoinitiator [5]. The improvement in resolution is achieved by spatially overlapping a secondary deactivation laser beam to depopulate a portion of the multiphoton excited focal volume, preventing the initiation of polymerization. This process has recently been demonstrated to produce feature sizes in PCs down to ~130 nm in the lateral dimension and ~180 nm in the axial dimension which allowed for production of stopbands in the visible spectral range [6]. However, this process is limited to initiators with excited states that can efficiently undergo stimulated emission as supposed to other absorption processes, for example excited state absorption or triplet state absorption. Furthermore,

the complex instrumental configuration which includes custom phase masks to create the modified point spread function as well as a secondary deactivation laser, limits the applicability of this technique.

This following chapter describes improved resolution using a simple, single beam excitation geometry found in typical MPL experimental setups. The resolution improvement results from efficient radical generation using a two-photon absorbing initiator excited with short wavelength excitation (520 nm). Additionally, the chemistry within the photoresist remains the same as for typical excitation conditions, where the volume surrounding the exposed region remains unaffected and uniform features can be generated in a continuous manner to form 3D structures. While the STED based approach affords improved axial resolution, the improvement in the lateral direction remains 2× larger than the 65 nm achieved from this short wavelength excitation approach.

REFERENCES

1. T. L. Andrew, H.-Y. Tsai, and R. Menon, "Confining Light to Deep Subwavelength Dimensions to Enable Optical Nanopatterning," Science **324**, 917-921 (2009).

2. T. F. Scott, B. A. Kowalski, A. C. Sullivan, C. N. Bowman, and R. R. McLeod, "Two-Color Single-Photon Photoinitiation and Photoinhibition for Subdiffraction Photolithography," Science **324**, 913-917 (2009).

3. S. W. Hell, and J. Wichmann, "Breaking the diffraction resolution limit by stimulated emission: stimulated-emission-depletion fluorescence microscopy," Opt. Lett. **19**, 780-782 (1994).

4. T. A. Klar, and S. W. Hell, "Subdiffraction resolution in far-field fluorescence microscopy," Opt. Lett. **24**, 954-956 (1999).

5. L. Li, R. R. Gattass, E. Gershgoren, H. Hwang, and J. T. Fourkas, "Achieving λ/20 Resolution by One-Color Initiation and Deactivation of Polymerization," Science **324**, 910-913 (2009).

6. J. Fischer, and M. Wegener, "Three-dimensional direct laser writing inspired by stimulated-emission-depletion microscopy [Invited]," Opt. Mater. Express **1**, 614-624 (2011).

4.1 Introduction

Laser-excited two-photon or multiphoton photochemistry allows for the patterning of materials with true three-dimensional (3D) spatial resolution and provides a method for the direct laser writing of arbitrary three-dimensional structures. 3D multiphoton lithography (MPL) has matured significantly as a 3D fabrication technology since its inception. Significant progress has been made in the development of photoactive materials systems for MPL, including negative [1] and positive [2] tone polymer systems, inorganic-organic hybrid materials [3], and metal nanocomposites [4], which provide means for 3D fabrication in a variety of material types. The development of chromophores with large two-photon absorption (2PA) cross-sections [5] and sizable quantum yields for generation of reactive species has resulted in efficient materials, which can be patterned with low-power femtosecond lasers [6]. 3D microstructures and devices fabricated using MPL include photonic crystals [7], mechanical structures with moveable [8] or interlocking parts [6], microchannel and microfluidic devices [2], and biocompatible templates [9].

There is considerable interest in the potential for the fabrication of 3D structures with nanoscale resolution using MPL. It has been shown that feature widths below the diffraction limit of one-photon processes can be obtained with MPL. Kuebler *et al.* [6] have reported on the fabrication of woodpile structures with line widths of 200 nm using 730 nm laser excitation [6]. Features with 120 nm [10] and later 100 nm resolution obtained through introduction of radical quenchers [11] have been reported by Kawata *et al.* and narrower features have been obtained through the use of controlled post-fabrication shrinkage [12]. Misawa *et al.* [13] have reported very narrow widths, which have been attributed to exposure based “baking” of features; however, the reproducibility of these features was limited. Although sub-diffraction-limited transverse feature sizes can be obtained, it is clear that the attainable resolution is controlled by the width of the

nonlinear dose function at or above the dose threshold of the material and that this width is fundamentally related to the wavelength of the excitation radiation. While there are a few reports of MPL using visible excitation [14], [15], the initiating systems used were typically un-optimized and the feature sizes produced were not exceedingly small (> 200 nm). Accordingly, we have investigated the resolution of MPL in a radical-initiated, crosslinkable acrylate resin system using a "donor-π-donor" chromophore designed for effective excitation at a shorter wavelength than has been typically utilized, and for good solubility in the resin.

In this paper, we report on the reliable fabrication of nanoscale polymeric features with a width as small as 65 nm using 520 nm femtosecond pulse excitation. We present studies of the scan speed and power dependence of the feature widths for 520 and 730 nm excitation to determine the dose dependence of the widths, which provide insight into the order of the excitation process. We also demonstrate the fabrication of woodpile-type face-centered tetragonal photonic crystal (PC) structures with 65 nm line widths and lateral periodicity of 500 nm. These photonic bandgap (PBG) structures were found to have fundamental stop bands in the 700 – 1000 nm spectral region.

4.2 Experiment

4.2.1 Materials

The photosensitive resin used for the MPL consisted of a 50:50 wt% blend of triacrylate monomers (Sartomer SR9008 and SR368, used as received) along with 0.1 wt% photoinitiator consisting of either 4,4'-bis(di-*n*-butylamino)biphenyl (DABP) or *E*,*E*-1,4-bis[4-(di-*n*-butylamino)styryl]-2,5-dimethoxybenzene (DABSB). The chemical structures of the photoinitiators are shown in Figure 4.1. DABSB has been shown to be an extremely effective two-photon absorbing radical photoinitiator [1] that exhibits a maximum 2PA cross-section at 730 nm of 900 GM (1 GM = 1×10^{-50} cm^4 sec $photon^{-1}$)

[5]. DABP is a "donor-π-donor" chromophore with shorter conjugation length than DABSB that has been shown to possess a peak 2PA cross-section (~200 GM) at an excitation wavelength of 520 nm [16]. It should be noted that for resin systems that excluded both of these photoinitiators, no photoinduced polymerization was observed.

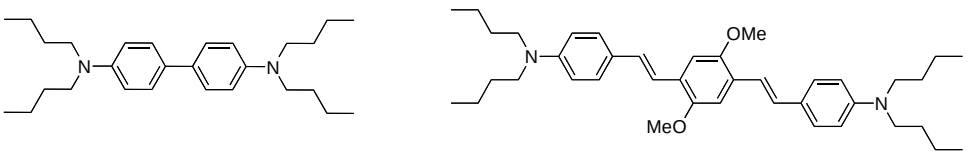

Figure 4.1. Molecular structures of photoinitiators used in this work, DABP (left) and DABSB (right).

The liquid resin was contained in a sample cell consisting of a microscope slide and a coverslip substrate separated by a 100 μm thick Teflon ring spacer. The coverslip was treated with an adhesion promoter (3-(trimethoxysilyl)propyl methacrylate). Following exposure, the sample was rinsed twice in methanol for a total of 15 minutes to remove the unexposed resin. The refractive indices of the resin system were determined using an Abbe refractometer (Milton Roy) at wavelengths close to those used for excitation.

4.2.2 Dose-Dependent Photoinduced Polymerization Studies

Two different laser systems were used during the course of this work. The first system consisted of a tunable optical parametric amplifier (OPA-800CF, Spectra-Physics) pumped via a Ti:Sapphire regenerative amplifier (Spitfire, Spectra-Physics) providing ~100 fs pulses at a repetition rate of 1 kHz and tunable from 460 nm to 2100 nm. This system was employed for feature writing in the dose-dependent studies as well as for fabrication of the PCs and spectral characterization of the finished PBG structures. The second system was a Ti:Sapphire oscillator (Tsunami, Spectra-Physics) operating at 730

nm and a repetition rate of 82 MHz with 80 fs pulses. This system was used for the fabrication of support structures (see below) in the dose-dependent studies.

A dose-dependent photo-induced polymerization study was carried out with both DABP and DABSB to compare the feature sizes of the structures created using different excitation wavelengths. The wavelengths were chosen to coincide with the peak of the two-photon cross-section for each of the dyes, i.e. 730 nm for DABSB and 520 nm for DABP. The two excitation beams were delivered collinearly into the MPL set-up and the relevant wavelength was selected using appropriate bandpass filters. The MPL apparatus consisted of a 10X expansion telescope that was used to effectively overfill the objective (60× oil immersion Plan Apochromat, NA = 1.4, Nikon) that focused the laser beam into the resin. The coverslip upon which structures were fabricated was positioned to be facing the objective with the adhesion-promoted side in contact with the resin (i.e. light was focused on the near surface of the sample cell). Fabrication was performed by translating the sample using a computer-controlled 3D positioning stage (MP-285, Sutter Instruments). The incident laser power was controlled using a pair of calcite polarizers. Dosimetry studies were performed by laser writing of free-spanning lines that were written at various incident average laser powers and stage scan speeds. The range of laser powers was chosen to span the range from the threshold power for polymerization to the power at which damage to the sample occurred. For each excitation power, lines were fabricated at four different scan speeds: 60, 40, 20 and 10 μm/sec. The scan speed was limited on the high end by the repetition rate of laser used (1 kHz). Both the lateral and axial dimensions of the written lines were determined using scanning electron microscopy (1530, LEO).

The lines were written by scanning the focus of the laser beam between pre-fabricated support structures. Two different types of support structures were utilized. The first type of structure, as illustrated in Figure 4.2(a), consisted of parallel rectangular

walls (20 μm wide, 30 μm tall, 1 cm long) spaced by gaps that ranged from 2 to 5 μm. Due to the large dimensions of these structures, the 82 MHz repetition rate laser system was used in conjunction with a high-speed precision translation stage (XPS, Newport). These structures were written using the DABSB-triacrylate resin described above. The structures were developed and then backfilled with either the DABSB or DABP-triacrylate resin for line writing. The second type of support structure, shown in Figure 4.2(b), was a rectangular "stack of logs" structure (20 μm wide, 15 μm tall, 100 μm long, 5-10 μm spacing). These structures were fabricated in the same resin with the same laser source and excitation wavelength used for the dosimetry studies. Since using the lower repetition rate amplified system (Spitfire) required greater fabrication time, this porous structure was chosen over the more solid structure.

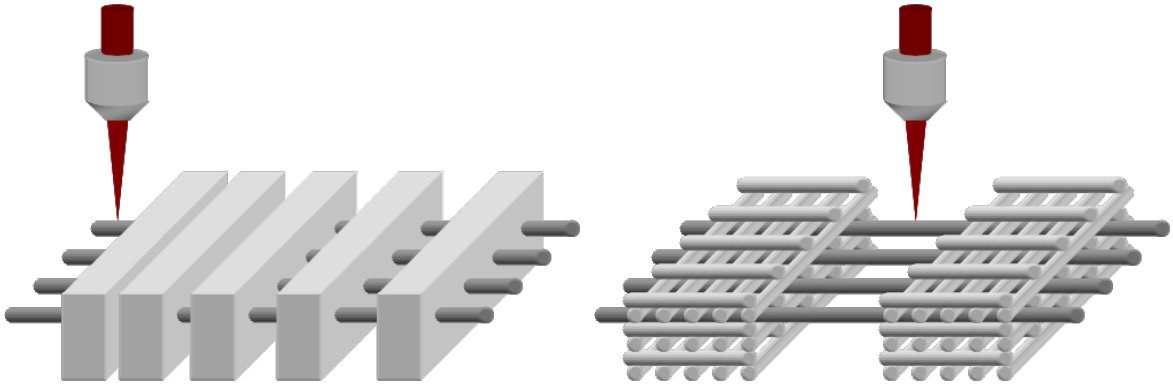

(a) (b)

Figure 4.2. Schematic illustrations of both types of support structures used for dosimetry studies: (a) rectangular solid walls and (b) rectangular "stack of logs" structure.

4.2.3 PC Fabrication And Stop-Band Characterization

Woodpile-type face-centered tetragonal photonic crystal structures [1] were fabricated using the DABP-triacrylate resin to demonstrate the applicability of short

wavelength MPL in the fabrication of free-standing microstructures. Woodpile structures were fabricated with lateral line-to-line spacings of 0.5 μm or 0.85 μm, vertical layer spacings of ~0.34 μm, and a height of 10 unit cell layers, with overall dimensions of 20 μm × 20 μm. The wavelength-dependent transmission spectra were characterized using a white-light continuum (spectral bandwidth 450 - 1200 nm) that was generated by focusing 2-3 μJ of 1.3 μm excitation from the optical parametric amplifier into a 2 mm calcium fluoride window. This light was focused into the PC sample and the transmission spectrum was collected using a liquid nitrogen cooled CCD array (LN/CCD-1100-PB, Princeton Instruments) coupled to a spectrograph (SP150, Acton). The PC samples were mounted on a rotation stage and transmission spectra were collected for various angles of incidence.

4.3 Results and Discussion

4.3.1 Feature Sizes And Thresholds

Arrays of lines were written between supports, as discussed above, at various powers and scan speeds in order to establish both the threshold for multiphoton writing of polymeric lines and the minimum feature sizes that could be obtained reliably with laser wavelengths of 730 and 520 nm for the resin systems examined. In order to provide statistically meaningful data to support this analysis, between three and six lines have been analyzed for a given power and scan speed. Furthermore, multiple measurements have been performed on any given line (made possible by their considerable lengths) thereby increasing the number of data points for analysis. The threshold power has been defined as the lowest average laser power at which the line survival probability (ratio of the number of lines that survived the developing or rinsing process to the total number of lines written) is more than 80%. This definition provides not only a statistical metric for the threshold power but also makes physical sense for the fabrication of reliable

structures. Survival probabilities are expected to decrease at lower powers due to the reduction of feature size as well as crosslinking density both of which result in reduced mechanical strength of the polymerized structure. For this reason, the choice of support structure employed can have an effect on the threshold power. This will be addressed below.

A representative set of fabricated lines for each resin system is shown in Figure 4.3. These sets of lines were written at their respective threshold powers at a scan speed of 60 μm/sec. Figure 4.3(a) depicts lines written in the DABSB-triacrylate resin at 730 nm with a threshold power of about 0.9 μW (the power quoted is that at the sample). The resulting lines exhibit diameters of 200 ± 15 nm. This sub-diffraction limited resolution (the diffraction limited spot-size should be about 320 nm) is typical for MPL and results from the superlinear dependence of multiphoton absorption (MPA) on intensity coupled with the thresholding nature of the polymerization process [10]. This same resin system has been investigated for MPL at 730 nm [6] using a similar optical layout but employing the same Ti:Sapphire oscillator system described above. The feature resolution determined at threshold using this laser oscillator system is consistent with the findings discussed in this work using the amplified laser system. Furthermore, when taking into account the dependence of the absorbed excitation dose on repetition rate and pulsewidth, the average laser powers at threshold found using each source are also consistent with one another. However, the aspect ratios of the polymerized structures determined in the two works are somewhat different. Individual voxels fabricated by MPL are known to take the shape of ellipsoids of revolution where the height in the axial direction is greater than the widths in the lateral directions. This aspect ratio was determined to be roughly 3:1 using the high repetition rate laser system [6] whereas a ratio of 5:1 was found in this work for the amplified kHz laser. Given the significantly larger peak powers used with the amplified system compared to the oscillator system (nearly 300 times greater), it is

possible that the unusually high aspect ratios found here are due to self-focusing and self-trapping effects that can lead to polymerization beyond the typical Rayleigh range [17].

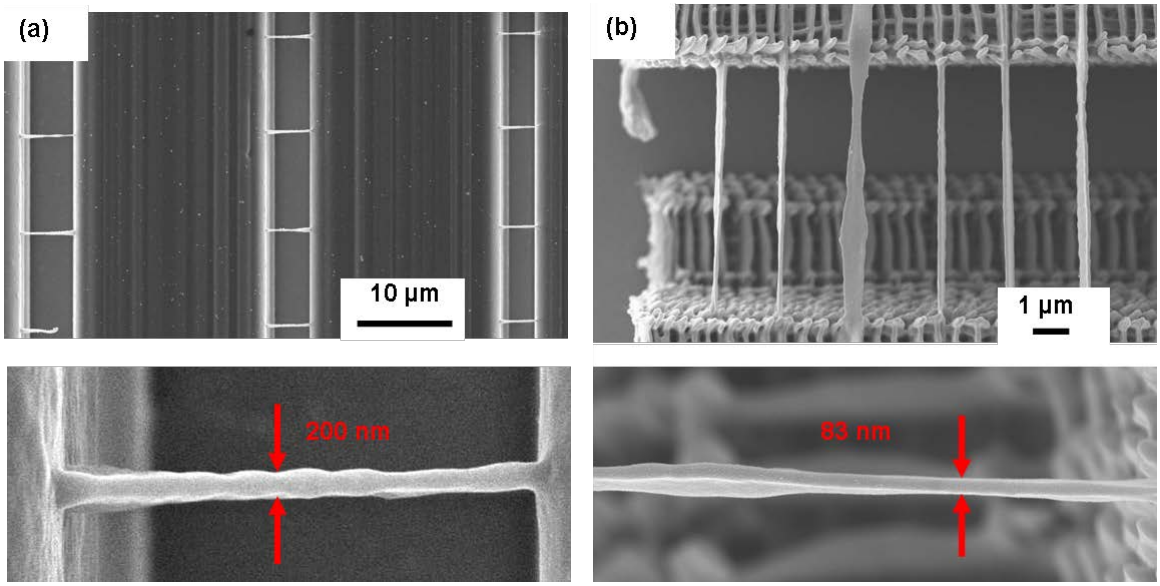

Figure 4.3. SEM overview images of lines fabricated at threshold powers with (a) 730 nm excitation using DABSB-triacrylate resin and with (b) 520 nm excitation using DABP-triacrylate resin. Aerial views of support structures described in Figure 4.2 are clearly visible in each image. Magnified images of a single line are shown below their respective overview images.

Figure 4.3(b) shows lines written at 520 nm using the DABP-containing resin system. At the determined threshold power of about 0.7 µW (at the sample), the diameters of the resulting written lines are 80 ± 5 nm. A number of observations can be made regarding MPL using the DABP-triacrylate resin. Firstly, as for the DABSB system, sub-diffraction-limited features are observed (the diffraction-limited spot-size is ~225 nm for 520 nm excitation). However, the roughly 2.4 times reduction in feature size compared to structures fabricated with 730 nm excitation illustrates that the resolution is fundamentally tied to the wavelength of the excitation. It should be noted that although dispersion of the refractive index of the resin system results in a slightly

larger refractive index at 514.5 nm (1.496) compared to 730 nm (1.485), the effect on the resulting numerical aperture (and consequently the focal spot size) is negligible. Secondly, not only are these feature sizes some of the smallest to be written by MPL, but the mechanical stability of these free-spanning lines are evident by their high survival probability despite the large length-to-width ratios of the lines (nearly 100 to 1). Thirdly, the DABP initiator system exhibited a comparable power threshold to that of the DABSB system which itself has been shown to outperform a number of commercially available photoinitiators when used for two-photon microfabrication [6]. Finally, the voxel aspect ratio (of height to width) was found to be 7:1. While self-focusing or self-trapping effects may again play a role here it is not clear why the ratio is higher than that of the DABSB system. However, this may be due to a linear dispersion effect resulting in a higher index change upon polymerization at 520 nm or a nonlinear dispersion effect that gives rise to a larger nonlinear refractive index at 520 nm. This large aspect ratio is evident in Figure 4.3(b) where the lines have experienced some torsional forces, most likely during development, leading to some twisting of the lines. This torsion should be ameliorated for support structures providing smaller gaps (smaller length-to-width line ratios), and threshold powers should also decrease for such support structures. This will be elaborated on below.

4.3.2 Dosimetry And Order Of Multiphoton Absorption Process

The results of the dose-dependent photo-induced polymerization study for the DABSB-triacrylate resin system are shown in Figure 4.4. Figure 4.4(a) plots line widths (or diameters) versus inverse scan speed (proportional to exposure or dwell time) for a number of different excitation powers. Clearly, line widths initially grow larger and then approach a constant value with increasing dwell time for a given power. The features also grow larger for increasing power at a particular inverse scan speed. The minimum feature size of 200 nm and the threshold power of 0.90 μW are clearly evident in the

graph. Assuming that a written voxel can be described as an ellipsoid of revolution with equivalent widths in both lateral directions (given by the data in Figure 4.4(a)) and a height dictated by the 5:1 aspect ratio described above, the voxel volume versus dwell time (or inverse scan speed) can be plotted. This is shown in Figure 4.4(b).

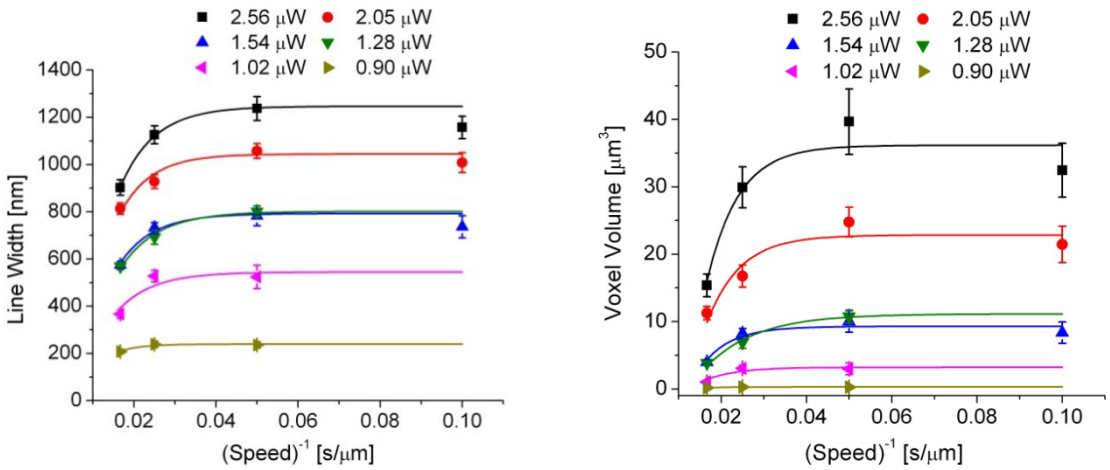

(a) (b)

Figure 4.4. Dosimetry studies on lines fabricated with 730 nm excitation using DABSB-triacrylate resin. Measured (a) line widths and (b) calculated voxel volumes (see text) as a function of inverse scan speed for different excitation powers. Error bars are given by standard deviations of experimentally measured line widths. The solid lines in (a) are guides for the eye whereas in (b) they represent fittings according to Eq. (1) as described in the text.

The data in Figure 4.4(b) can be fitted to the following equation [6],

$$V = A[1 - \exp(-B \cdot t)] \qquad (1)$$

where V is the volume of the polymerized voxel, t is the exposure time (proportional to the inverse scan speed) and A and B are fitting parameters. The polymer growth rate is then given by the product of these two parameters, i.e. $R_P = A*B$. The growth rates

determined from the fitting curves in Figure 4.4(b) are plotted versus the corresponding average laser power in Figure 4.5. It has been shown that the rate of polymer growth is proportional to $(I)^{N/2}$ [18] where I is the intensity of the laser source (linearly proportional to the average laser power) and N is the order of the MPA process involved in the polymerization process. Therefore, by fitting the data in Figure 4.5 to a power law function of the form

$$R_P = C \cdot \left| P - P_{th} \right|^{N/2}, \qquad (2)$$

where C is a constant, P is the average power, and P_{th} is the threshold power, the order of the MPA process can be determined. The fit to the data in Figure 4.5 reveals a power law dependence of $N \approx 3.1$ suggesting that an effective three-photon process correctly describes the MPA process involved in the photoinduced polymerization. Thus, while it is clear that the DABSB chromophore exhibits a strong two-photon resonance at 730 nm, absorption of at least one additional photon is involved in the photoinitiation process. As such, the process can be thought of as a 2PA event followed by one-photon absorption, or a 2+1 MPA event. It should be noted that the determination of the order of this process may be affected by non-local effects such as diffusion, which have not been taken into account in this analysis. The threshold power is identified as 0.66 μW by the fitting curve in Figure 4.5. The discrepancy between this value of P_{th} and the value of 0.90 μW found in the dosimetry studies discussed above stems from the influence of the developing process. A larger threshold power ensures greater crosslinking of the polymer resulting in the requisite survival probability.

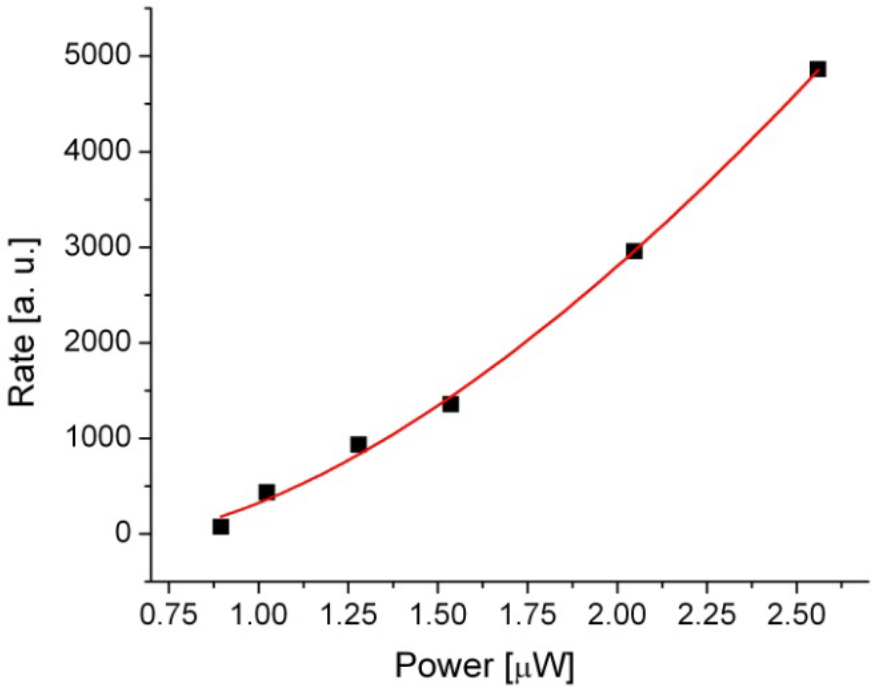

Figure 4.5. Polymer growth rates (as determined in text) derived from the dosimetry studies shown in Figure 4.4(b) as a function of excitation power. The experimentally determined values are given as filled black squares and the red solid line indicates a fitting according to Eq. 2. The fitting parameters are: C = 1770, P_{th} = 0.66, and N = 3.14.

Figure 4.6 shows the dosimetry results for the DABP-triacrylate resin system. Once again, the trends of the line widths as a function of dwell time and the power are consistent with the results found for the DABSB-triacrylate resin system described above. Furthermore, a threshold power of 0.70 μW along with the corresponding 80 nm minimum feature size is also evident in the graph. However, a reliable study of the polymerization kinetics, similar to the one performed above for the DABSB-triacrylate resin, was not possible due to the larger errors associated with these line width measurements. This was mainly attributed to the smallness of the feature sizes and their tight grouping (the difference between the smallest and largest feature size measured was

a mere 35 nm, as opposed to nearly 1000 nm for the DABSB data using 730 nm excitation). More detailed work on these polymerization kinetics studies will be conducted in the future using a more stable source of visible wavelength, high repetition rate, femtosecond pulse excitation to accurately determine the order of the MPA process involved.

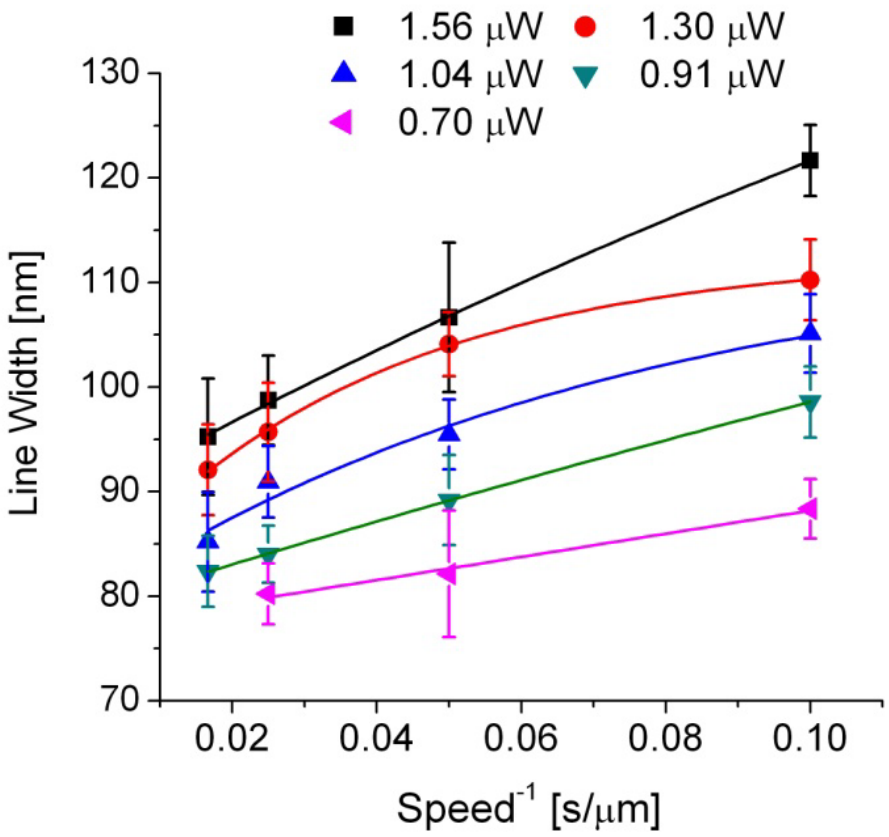

Figure 4.6. Dosimetry studies on lines fabricated with 520 nm excitation using the DABP-triacrylate resin. Error bars are given by standard deviations of experimentally measured line widths. The solid lines are guides for the eye.

4.3.3 PC Structures And Stop-Band Spectra

Using the DABP-triacrylate resin system, woodpile-type face-centered tetragonal PC structures were fabricated. Compared to the previous lines fabricated between

supporting walls separated by 5-10 µm, these PC structures provide smaller separation between anchoring points and therefore more structural support for the lines written by MPL. Consequently, since these structures enhance the survival probability of the line features, even smaller features than the 80 nm diameter lines reported above have been achieved in these structures. Figure 4.7 shows two typical PC structures written at 520 nm with the DABP-triacrylate resin. In all, three sets of PCs were fabricated with powers of 0.75, 0.60 and 0.45 µW at a scan speed of 60 µm/sec with lateral spacings of either 0.50 µm or 0.85 µm. Average widths of the measured lines were 81 ± 7 nm, 75 ± 5 nm, and 63 ± 5 nm, respectively. It is immediately apparent that this more mechanically supportive structure lowers the threshold power for polymerization and thereby allows for finer resolution structures to survive.

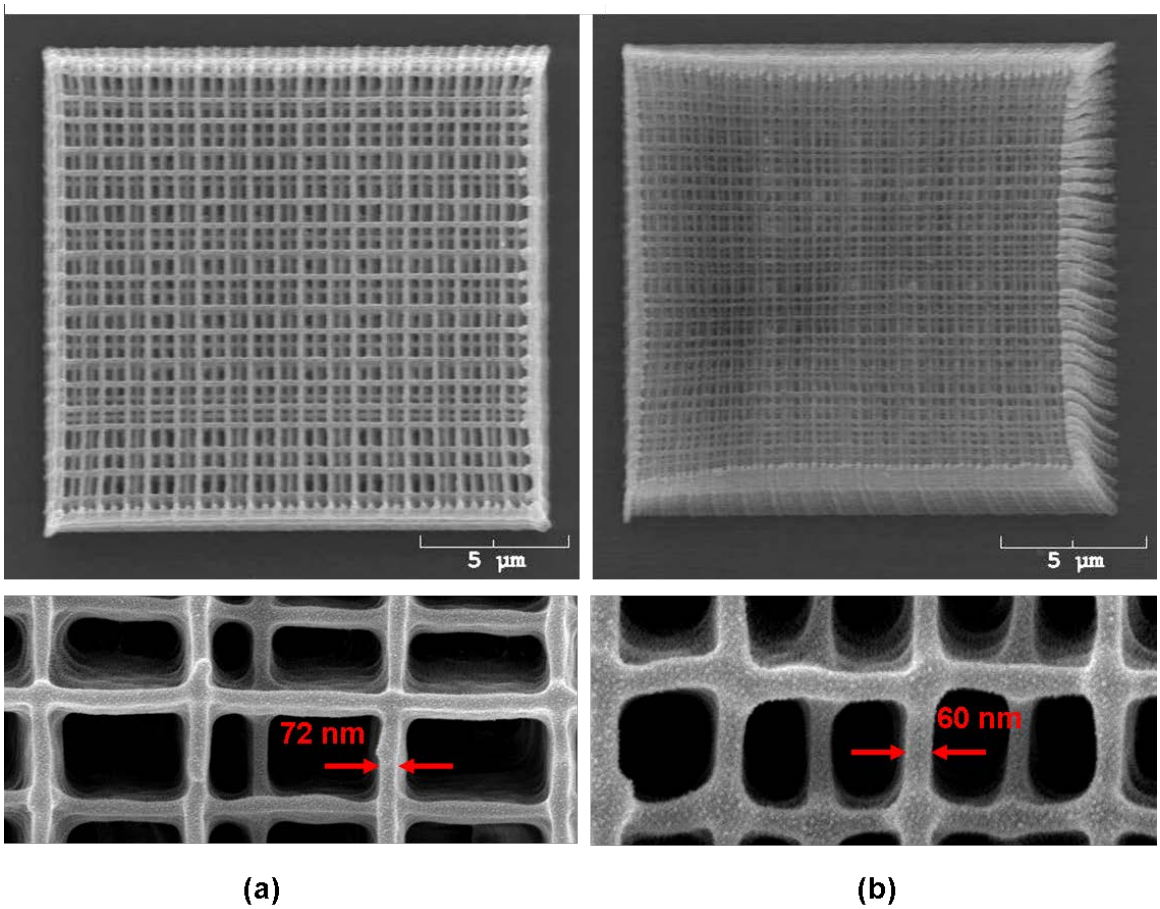

Figure 4.7. SEM overview images of woodpile-type PC structures fabricated with 520 nm excitation at (a) 0.60 μW and at (b) 0.45 μW using the DABP-triacrylate resin. Fabrication parameters of PCs were: lateral line-to-line spacings of (a) 0.85 μm and (b) 0.5 μm, axial layer-to-layer spacings of ~0.34 μm, and scan speeds of 60 μm/sec. Magnified images of the PC structures are shown below their respective overview images.

Transmission spectra for several of the PC structures described above were collected according to the procedures detailed in Section 4.2.3. The spectra for different angles of incidence for one of these structures are shown in Figure 4.8. Fringes are observed at longer wavelengths (> 900 nm) and the period corresponds to a film thickness of ~14 μm consistent with the height of the PC structure. Stop bands have been observed and are indicated by arrows and appear at 717 nm, 810 nm, 890 nm, and 986 nm for incident angles of 0, 10, 20, and 30 degrees, respectively. This trend of the red-shifting of PBG stop bands with increasing angle of incidence has been observed previously [19]. It is apparent that the ability to fabricate PBGs with high-resolution mechanically stable lines permits the design of structures possessing fundamental stop bands in the short-wavelength portion of the near-infrared spectral region. In fact, the spectral position of the stop band is primarily dictated by the axial layer-to-layer spacing of the PBG. The large aspect ratio of the lines written at 520 nm using the DABP-triacrylate resin gave rise to large line heights (~0.34 μm) and therefore placed a lower limit on the axial spacing that could be achieved with these PBGs. Stop bands in the visible portion of the spectrum could, therefore, be achieved by reducing this line height resulting in smaller axial layer-to-layer spacings. The contrast in the observed stop bands can be enhanced by improving the fidelity of the fabricated PBG structures and by utilizing higher index materials.

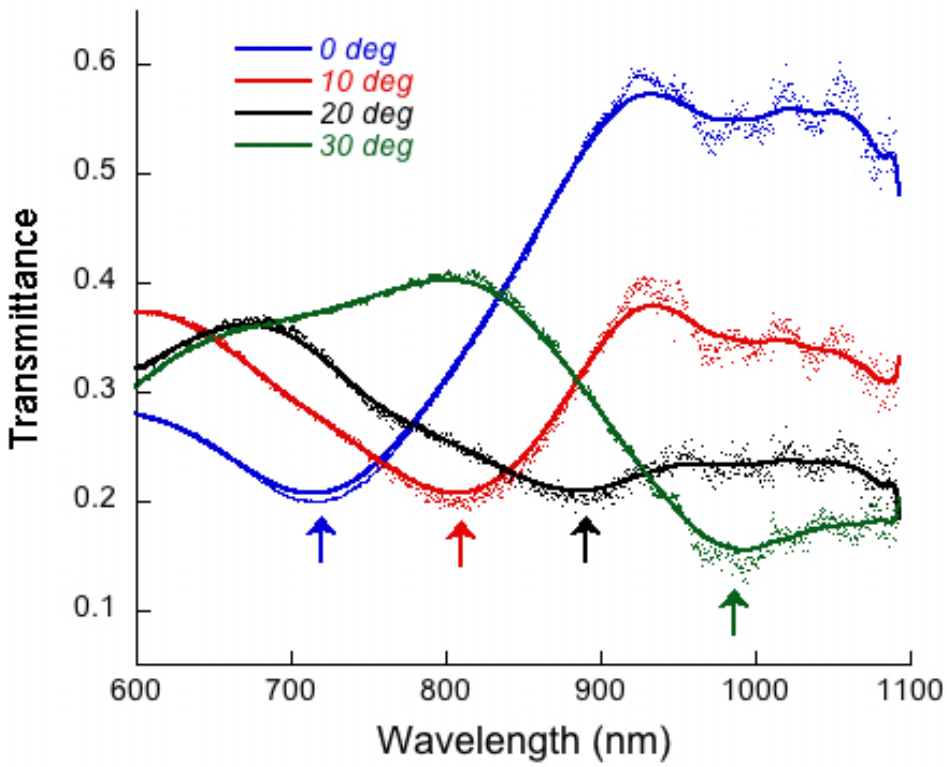

Figure 4.8. Transmission spectra of PBG structure fabricated with 520 nm excitation at 0.60 µW using the DABP-triacrylate resin. The dotted lines indicate experimentally observed spectra while the solid lines are merely guides for the eye. Observed stop bands have been indicated by appropriately colored arrows. Fabrication parameters of PBG were: average line width of 75 nm, lateral line-to-line spacing of 0.5 µm, axial layer-to-layer spacing of ~0.34 µm, scan speed of 60 µm/sec.

4.4 Conclusion

The use of laser-induced polymerization using a photoinitiator with a sizable two-photon absorption cross-section in the visible wavelength region (520 nm) has allowed for multiphoton 3D lithography with nanoscale lateral feature resolution: line widths of 80 nm for long, free-spanning lines and 65 nm line widths in woodpile photonic crystal structures. Comparative studies with two-photon absorbing initiators at 730 and 520 nm show that the minimum lateral feature sizes are below the diffraction limit for the resin

systems examined at both excitation wavelengths, while the height to width aspect ratio for the features written with high intensity pulses at a 1kHz repetition rate is two to three times greater than typically observed for writing with high repetition rate sources. The fabrication of nanoscale lines via visible wavelength MPL has been utilized to fabricate initial polymeric photonic crystal structures with lateral periods of 500 nm, which gave stop bands in the near infrared spectral region. The capability for reliable formation of nanoscale features using MPL should have a substantial impact on the fabrication of photonic, electronic and MEMS devices, among others.

ACKNOWLEDGMENTS

Support of this work by the Office of Naval Research APEX Consortium (N00014-05-0303) and the National Science Foundation, through the Science and Technology Center for Materials and Devices for Information Technology Research (DMR-0120967), is gratefully acknowledged. We wish to thank Dr. Mariacristina Rumi for providing preliminary two-photon absorption data on the DABP photoinitiator compound. We also thank Greg Walker for a sample of the DABSB compound.

REFERENCES

1. B. H. Cumpston, S. P. Ananthavel, S. Barlow, D. L. Dyer, J. E. Ehrlich, L. L. Erskine, A. A. Heikal, S. M. Kuebler, I. Y. S. Lee, D. McCord-Maughon, J. Qin, H. Rockel, M. Rumi, X.-L. Wu, S. R. Marder, and J. W. Perry, "Two-photon polymerization initiators for three-dimensional optical data storage and microfabrication," Nature **398**, 51-54 (1999).

2. W. Zhou, S. M. Kuebler, K. L. Braun, T. Yu, J. K. Cammack, C. K. Ober, J. W. Perry, and S. R. Marder, "An Efficient Two-Photon-Generated Photoacid Applied to Positive-Tone 3D Microfabrication," Science **296**, 1106-1109 (2002).

3. J. Serbin, A. Egbert, A. Ostendorf, B. N. Chichkov, R. Houbertz, G. Domann, J. Schulz, C. Cronauer, L. Fröhlich, and M. Popall, "Femtosecond laser-induced two-photon polymerization of inorganic organic hybrid materials for applications in photonics," Opt. Lett. **28**, 301-303 (2003).

4. F. Stellacci, C. A. Bauer, T. Meyer-Friedrichsen, W. Wenseleers, V. Alain, S. M. Kuebler, S. J. K. Pond, Y. Zhang, S. R. Marder, and J. W. Perry, "Laser and Electron-Beam Induced Growth of Nanoparticles for 2D and 3D Metal Patterning," Advanced Materials **14**, 194-198 (2002).

5. M. Rumi, J. E. Ehrlich, A. A. Heikal, J. W. Perry, S. Barlow, Z. Hu, D. McCord-Maughon, T. C. Parker, H. Röckel, S. Thayumanavan, S. R. Marder, D. Beljonne, and J.-L. Brédas, "Structure−Property Relationships for Two-Photon Absorbing Chromophores: Bis-Donor Diphenylpolyene and Bis(styryl)benzene Derivatives," Journal of the American Chemical Society **122**, 9500-9510 (2000).

6. S. M. Kuebler, M. Rumi, T. Watanabe, K. Braun, B. H. Cumpston, A. A. Heikal, L. L. Erskine, S. Thayumanavan, and J. W. Perry, "Optimizing Two-Photon Initiators and Exposure Conditions for Three-Dimensional Lithographic Microfabrication," Journal of Photopolym. Sci. Technol **14**, 657-668 (2001).

7. M. Deubel, G. von Freymann, M. Wegener, S. Pereira, K. Busch, and C. M. Soukoulis, "Direct laser writing of three-dimensional photonic-crystal templates for telecommunications," Nat Mater **3**, 444-447 (2004).

8. P. Galajda, and P. Ormos, "Complex micromachines produced and driven by light," Applied Physics Letters **78**, 249-251 (2001).

9. J. D. Pitts, P. J. Campagnola, G. A. Epling, and S. L. Goodman, "Submicron Multiphoton Free-Form Fabrication of Proteins and Polymers: Studies of Reaction Efficiencies and Applications in Sustained Release," Macromolecules **33**, 1514-1523 (2000).

10. S. Kawata, H.-B. Sun, T. Tanaka, and K. Takada, "Finer features for functional microdevices," Nature **412**, 697-698 (2001).

11. K. Takada, H.-B. Sun, and S. Kawata, "Improved spatial resolution and surface roughness in photopolymerization-based laser nanowriting," Applied Physics Letters **86**, 071122 (2005).

12. K. Takada, H.-B. Sun, and S. Kawata, "The study on spatial resolution in two-photon induced polymerization," (SPIE, 2006), p. 61100A.

13. J. Saulius, and et al., "Two-photon lithography of nanorods in SU-8 photoresist," Nanotechnology **16**, 846 (2005).

14. M. Straub, and M. Gu, "Near-infrared photonic crystals with higher-order bandgaps generated by two-photon photopolymerization," Opt. Lett. **27**, 1824-1826 (2002).

15. G. Lemercier, J.-C. Mulatier, C. Martineau, R. Anémian, C. Andraud, I. Wang, O. Stéphan, N. Amari, and P. Baldeck, "Two-photon absorption: from optical power limiting to 3D microfabrication," Comptes Rendus Chimie **8**, 1308-1316 (2005).

16. M. Rumi, School of Chemistry and Biochemistry and Center for Organic Photonics and Electronics, Georgia Institute of Technology, Atlanta, Georgia 30332-0400, unpublished results (2006).

17. A. S. Kewitsch, and A. Yariv, "Self-focusing and self-trapping of optical beams upon photopolymerization," Opt. Lett. **21**, 24-26 (1996).

18. S. M. Kuebler, B. H. Cumpston, S. Ananthavel, S. Barlow, J. E. Ehrlich, L. L. Erskine, A. A. Heikal, D. McCord-Maughon, J. Qin, H. Roeckel, M. C. Rumi, S. R. Marder, and J. W. Perry, "Three-dimensional microfabrication using two-photon-activated chemistry," in *Proc. SPIE 3937*(SPIE, 2000), pp. 97-105.

19. S. Y. Lin, J. G. Fleming, D. L. Hetherington, B. K. Smith, R. Biswas, K. M. Ho, M. M. Sigalas, W. Zubrzycki, S. R. Kurtz, and J. Bur, "A three-dimensional photonic crystal operating at infrared wavelengths," Nature **394**, 251-253 (1998).

CHAPTER 5

FABRICATION OF PHOTONIC CRYSTALS WITH SUB-100 NM FEATURES USING MULTIPHOTON LITHOGRAPHY WITH SWOLLEN-GEL PHOTORESISTS

5.1 Introduction

Improving the resolution of fabricated features is a relentless pursuit in research on photolithography. For multiphoton photolithography, which typically utilizes laser excitation in the range of 700-800 nm, the generation of line features as fine as 200 nm has been reported for free-standing structures, for example stack-of-logs woodpile photonic crystals [1]. While the multiphoton excitation process provides sub diffraction-limited resolution, the minimal feature size achievable is still limited by the optical excitation wavelength. Several methods to generate finer individual line features have been demonstrated that are based on multiphoton exposure at slightly above crosslinking threshold and extraction of unreacted monomers during solvent development. Careful control of acid diffusion during post exposure bake in SU-8 was used to form nanorods as small as 30 nm [2], high concentration of radical quenchers in acrylate resin was used to limit radical diffusion [3], or stretching of polymerized rods spanning supports that undergo shrinkage [4]. These attempts have achieved finer resolution down to 30 nm but the created features are highly dependent on the support structure geometries and cannot be used for building free-form 3D structures.

Some recent developments in multiphoton lithography have been inspired by stimulated-emission-depletion microscopy wherein one laser beam provides excitation and a second laser beam, typically with a ring-shaped intensity distribution, is used to selectively deplete excited-state population in the outer lateral region of the multiphoton excited

focal volume via stimulated emission [5]. This process has been demonstrated to produce feature sizes down to ~130 nm laterally and ~180 nm axially in photonic crystal structures [6]. This process however is limited to photoinitiators with an excited state that can efficiently undergo stimulated emission as opposed to excited-state absorption processes. Furthermore, the complex optical geometry and instrumental configuration are barriers to the widespread use of this technique.

Alternative approaches to reducing the size of fabricated lines based on post-fabrication etching, baking, or the use of condensation reactions to expel small molecules have been reported. Post-fabrication plasma etching of polymeric photonic crystals [7] has been used to reduce the size of fabricated lines, however this method produces inhomogeneous polymer removal from the top down within the structure. Thermal treatment of structures in an organic-inorganic material at 300ºC was used to decompose the organic moieties, and the volatilized organic species resulted in a reduction of feature sizes [8]. While feature sizes as small as 86 nm was reported, the lower surface to volume ratio at the interconnects of the photonic crystals compared to the free-spanning regions resulted in inhomogeneous size reduction. Another approach involves a two-step shrinkage process wherein a solvent is used to remove unpolymerized material in photocrosslinked sol-gel matrix during the development step, followed by condensation of the alkoxy groups in the sol-gel matrix during baking. This method produced a 35% reduction of line widths yielding a demonstrated linewidth of 160 nm [9]. However, this process creates significant structural shrinkage (18% for a 25 x 25 μm^2 structure) and requires a design for offsetting the structures from the substrate by support posts to allow for relief of the shrinkage induced stress. Significant warping and displacement of the processed structure from designated location resulted.

In this chapter, the use of a swollen-gel photoresist (gel-resist) in multiphoton lithography as a meas of reducing fabricated feature sizes is reported. In this method, a gel resist

comprising triacrylate monomers and a polymer binder is swollen by in-diffusion of an index matching oil. Using this method, we have achieved line widths as small as 85 nm with conventional MPL at 730 nm via a mode-locked Ti:sapphire laser. A systematic study of the swelling was performed by use of laser-scanning microscopy through the thickness of the gel resist and detection of fluorescence from an initiator dye in the resin. We obtain spatial profiles of the dye fluorescence through the gel resist, that allow us to monitor the degree of swelling as a function of time. The oil used was Cargille Type A immersion oil, which is a mixture of substances. We also examined the swelling behavior induced by the individual major components of the immersion oil. These studies have shown that the mechanism of the swelling of the gel resist matrix is due primarily to the diffusion of hydrogenated terphenyls (HT) and the concomitant volume expansion of the polystyrene-*co*-acrylonitrile host polymer physical network [10]. In the swollen-gel, multiphoton excitation under a constant exposure dose creates fewer crosslinks per excitation volume as compared to a non-swollen-gel, due to the dilution of reactive groups by in-diffusion of the oil. The subsequent solvent development process removes both unreacted monomer species and absorbed oil, so that upon drying the polymer network reorganizes to minimize surface energy resulting in smaller features. The features possess sufficient mechanical strength to allow the fabrication of functional microstructures with lines spanning across gaps of 1 μm. Using the swollen-gel resist method, uniform photonic crystals with an area of 100 x 100 μm^2 that exhibit photonic stopbands with peak reflectivity of 60 to 90% have been fabricated. The positions of the stopbands can be tuned essentially continuously from 1 to 2 microns (and possibly below). Structural and optical characterization indicates that distortions due to longitudinal stress have a minimal impact on the fabricated photonic crystals. This swollen-gel resist method provides a simple fabrication approach that produces finer features in a homogeneous manner from the top to the bottom of multilayer photonic crystal structures and could be applied to wide range of photonic structure designs.

5.2 Identification of Swelling Components

5.2.1 Identification of Swelling Solvents

Immersion oils are mixtures of organic liquids with different refractive indices, viscosities and thermoconductivities. Formulation of the immersion oil, by the relative ratio of its components, is based on the application and the desired properties at a specific wavelength. Cargille Type A immersion oil is a widely used index matching fluid (n = 1.51-1.52 in the visible wavelengths) for microscope objectives with high numerical apertures, e.g. 60×, 1.4 N.A. objectives. This swelling effect was first observed in gel resists that experienced prolonged exposure to the immersion oil. The immersion oil, which was initially a colorless, transparent liquid, took on a greenish color of the photoinitiator after exposure to the gel resists, suggesting possible oil in diffusion into the gel resist and swelling.

Cargille Type A immersion oil and a representative of its components were investigated to determine which specie/species contributed to the gel resist swelling. The components of the immersion oil were identified from its materials safety data sheet to include terphenyl, hydrogenated terphenyl (HT), natural hydrocarbons and polybutenes. Each of the identified components is a mixture in itself, variation in the isomerisation, degree of hydrogenation, length of the carbon chains, and molecular weights respectively. We identified several representative compounds to the best of our knowledge and commercial availability. Terphenyl was not investigated due to its minute presence (<5%) in typical formulations. HT is the product of partially hydrogenated terphenyls, which consists of three isomers (ortho, meta, and para linkage to central benzene), resulting in a wide range of possible species. The closest available option identified was 3-phenylbicyclohexyl (BCHP) (Aldrich, mixture of isomers) which is composed of 57-69% meta-isomer at 30-35% hydrogenation. The natural hydrocarbon was identified to be white mineral oils

Kaydol and/or Gloria (Sonneborn) from a 1975 Cargille immersion oil formulation patent [11]. Polybutene (Aldrich, M_n ~920) was chosen based on similarity in molecular weight with the M_n ~1400 found in the same patent [11].

5.2.2 Raman Characterization

We characterized the immersion oil and the identified components using a Fourier-transformed Raman spectrometer (Bruker, MultiRAM) with a 5 mm pathlength, silver-backed cuvette. Acquisition of the spectra involved the averaging of 50 scans. Aromatic C-H stretching bands (3060, 2940, and 2850 cm^{-1}) were shared by BCHP and immersion oil. Other C-H stretching modes from Kaydol and polybutene, although not distinct, were also present in the same 3000 – 2850 cm^{-1} region. In the fingerprint region, distinct aromatic C=C bending (1600 cm^{-1}) and C-H in plane bending (1000 cm^{-1}) were present in both the BCHP and immersion oil, C=C stretching (1650 cm^{-1}) was shared by polybutene and immersion oil, and C-H_2 bending (1450 cm^{-1}) was shared by all components and immersion oil itself.

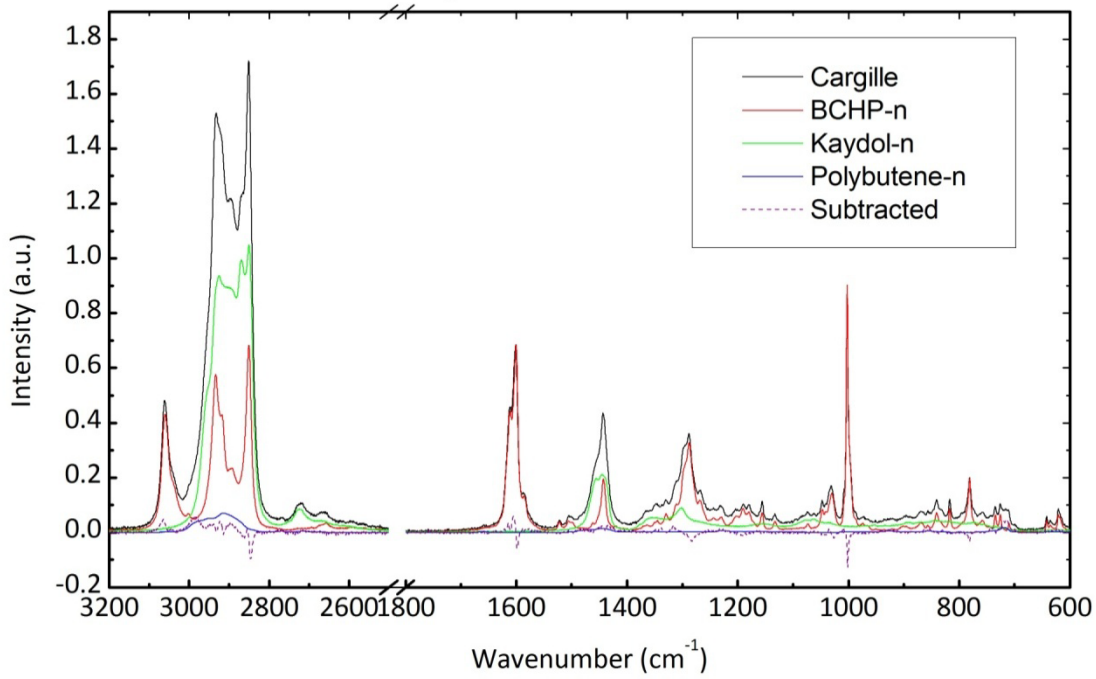

Figure 5.1. Raman spectra of Cargille immersion oil and the representative components scaled to Kaydol 59.1%, BCHP 32.8%, Polybutene 4.2% (96.1% total).

Figure 5.1 shows the absorption spectra for the immersion oil, scaled components, and the residual after subtraction of scaled components from the immersion oil. Although the components do not add up perfectly to the immersion oil spectra, the small residual indicates the components examined qualitatively represent the formulation of the immersion oil.

5.3 Experiment

5.3.1 Gel Resist Preparation

To prepare the gel resist, photosensitive resin was first prepared by dissolving polystyrene-*co*-acrylonitrile (Polyscience, Inc., 75:25 styrene:acrylonitrile), triacrylate monomers SR9008 (Sartomer)and SR368 (Sartomer) in 30:35:35% weight ratio in equivalent volume of 1,4-dioxane (Aldrich, spectrophotometric grade 99%) as the casting solvent. Next, the multiphoton radical initiator *E,E*-1,4-*bis*[4-(*N,N*-di-n-butylamino)styryl]-2,5-dimethoxybenzene (DABSB), shown in Figure 5.2, was employed at 0.1 wt% relative to the resin matrix. This chosen initiator has been shown to be an extremely effective with a maximum two-photon absorption cross-section of 900 GM at 730 nm [12]. All the chemicals were used as received.

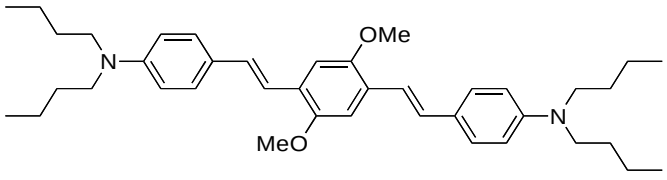

Figure 5.2. Molecular structures of photoinitiator DABSB.

Subsequently, the resin solution containing DABSB was blade-casted at a thickness of 100 µm onto a microscope slide substrate (drawing in Figure 5.3). Prior to the casting, the acetone cleaned glass microscope slide was treated with 10 %vol 3-(trimethoxysilyl)propyl methacrylate (Aldrich, 98%) in ethanol (Aldrich, 200 proof, anhydrous, 99.5%) and baked on a hot plate at 130°C for three cycles to promote the adhesion of acrylic structures to the substrate. This blade-casted pre-resin film was placed in a dark drying chamber overnight allowing the casting solvent to evaporate slowly to form a layer of semi-dried gel resist with uniform thickness. With a 5-hour vacuum drying proceeded as the final step, a 50 µm thick gel resist was obtained.

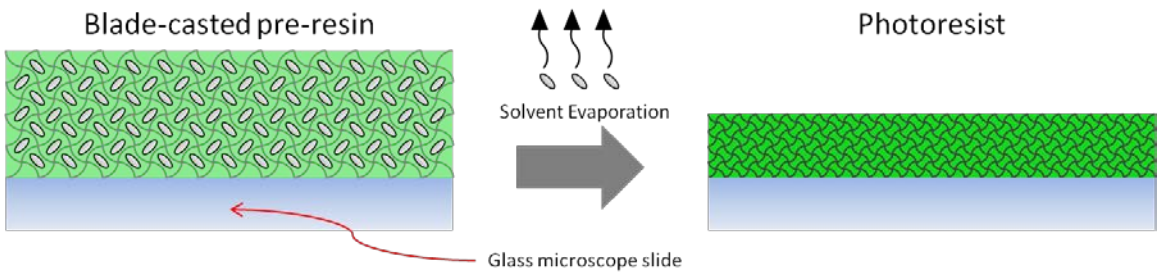

Figure 5.3. Gel resist preparation from blade-casting of pre-resin to dried gel resist.

5.3.2 Gel Resist Swelling

Fluorescence of DABSB in the gel resist was utilized to monitor the degree of swelling via multiphoton excitation. This excitation laser was focused by a high numerical aperture oil immersion objective to generate the highest axial resolution. Due to the limited working distance, the objective was brought within 200 µm to the sample, mediated by the immersion oil. In order to prevent turbulence and mixing from the

sample's movement during the course of the experiment, a liquid sample cell was constructed around the gel resist. The gel resist was trimmed to fit within the inner diameter of a 100 µm thick Teflon ring spacer (Aldrich) as depicted in the drawing (Figure 5.4) below:

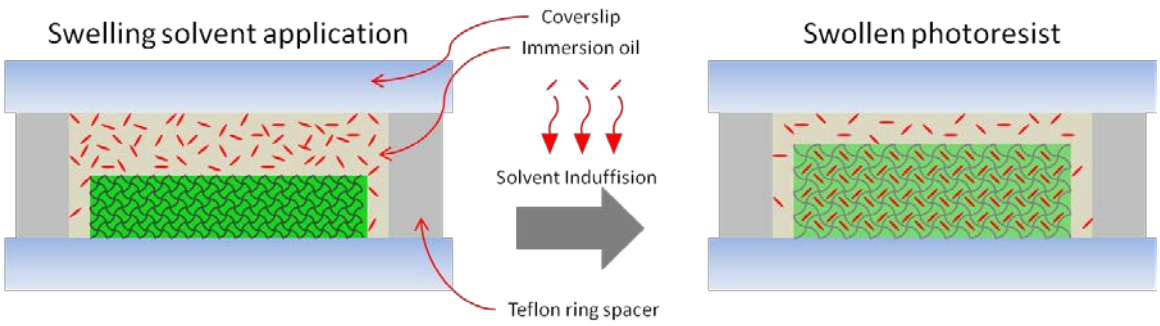

Figure 5.4. Cross section view of a constructed liquid sample cell, with a non-swollen and swollen-gel resist.

An excess amount of swelling solvent was applied to the gel resist prior to capping with a #0 coverslip to ensure a bubble-free, constant pathlength cell for fabrication. The coverslip was secured with tape to prevent slippage. Immersion oil was added on top of the cell for index matching prior to fluorescence scanning. The degree of swelling was controlled by varying interaction time with the swelling

5.3.3 Swelling Characterization

The swelling kinetics was monitored by multiphoton-excited fluorescence from DABSB in the gel resists, schematic shown in Figure 5.5. The sample cell was mounted on a 3-axis translational stage to allow for the positioning of a fixed focal point anywhere in the sample cell. The stage was computer controlled through a high-performance motion controller (Newport Corporation, XPS-C4). Excitation of DABSB was achieved by

focusing a 80 MHz, 730 nm beam from the mode-locked Ti:Sapphire laser (Spectra-Physics, Tsunami) into the sample cell with a 60x oil immersion objective (Nikon, VC). The fluorescence signal generated from DABSB in the sample cell was collimated with the same objective and diverted from the excitation path with a dichoric mirror (Chroma Technology, 710dcxr). The fluorescence was transmitted through a 550 nm short pass filter to eliminate excitation and room light, focused via a fiber collimator into a fiber coupled photodetector (New Focus, FemtoWatt).

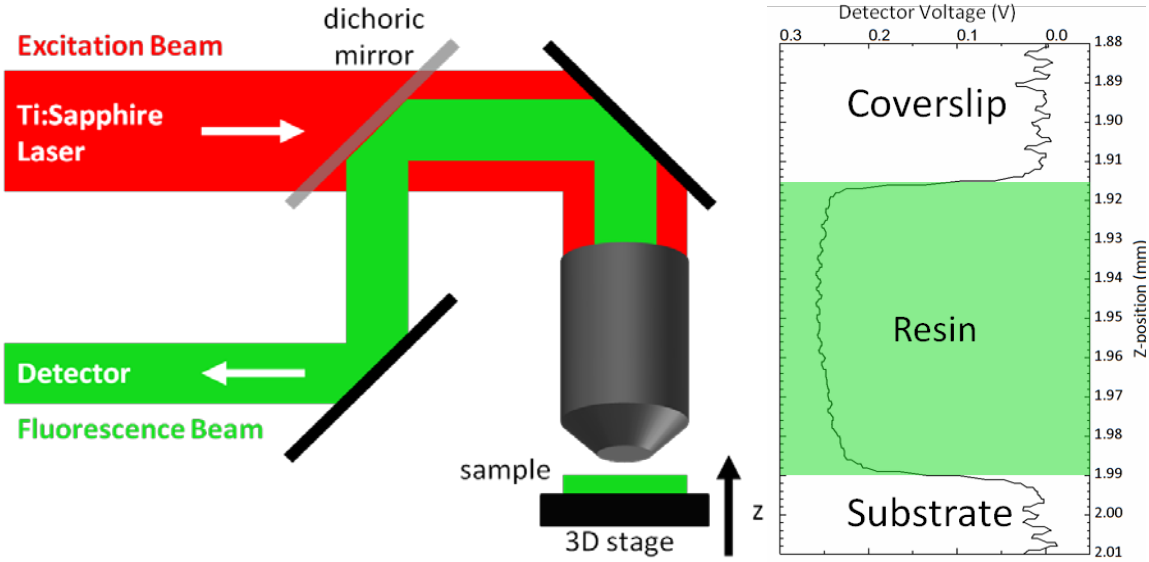

Figure 5.5. Laser excitation and fluorescence detection setup (left) and an example of fluorescence scan (right).

The experimental setup of this multiphoton-excited fluorescence measurement is shown in Figure 5.5 left and an example of fluorescence profile is shown in the right. Fluorescence profiles were obtained by simultaneous translation of the sample along the z-axis and collection of fluorescence signal. The scans were initialized by focusing the excitation beam within the bottom substrate, where no fluorescence was observed,

followed by translating the gel resist into the laser focus, where fluorescence was detected, and finished as the immersion oil within the cell and then the top coverslip moved into the focus. Fluorescence scans were collected at fixed time intervals to monitor the swelling induced changes to the gel resist.

5.3.4 Effects of Swelling in MPL

Crosslinking of the gel resist was achieved, using the same experimental setup described above, by increasing the laser excitation intensity above the initiation threshold (>3x power used in fluorescence scans). The exposed volumes were rendered insoluble by multiphoton initiated radical crosslinking reaction. Development in 4-methyl-2-pentanone (MIBK, Aldrich, 99%) dissolves unexposed monomers while exposed volume above the crosslinking threshold was not affected. The crosslinking density was controlled by the excitation intensity, exposure volume and duration. A set of macro-scaled block structures, as depicted in Figure 5.6, were fabricated to assess the effect of gel resist swelling on multiphoton photopolymerization.

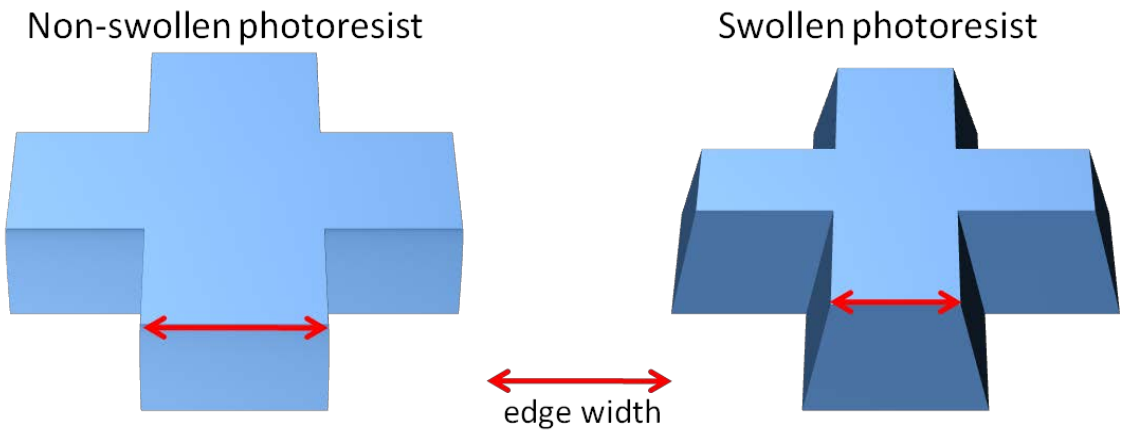

Figure 5.6. Macrostructures used for swelling analysis and edge widths employed for analysis.

Laser exposure was performed in alternating x and y direction for each layer, creating a cross-shaped structure with clear edges for analysis. The laser volume exposure pattern was fixed and structures were fabricated at various oil immersion time.

The effects on the individual writing elements were investigated by stack-of-logs type photonic crystals. Woodpile PCs with a body centered tetragonal lattice, alternating rod direction along the stacking direction, as depicted in Figure 5.7, were fabricated to characterize the shrinkage.

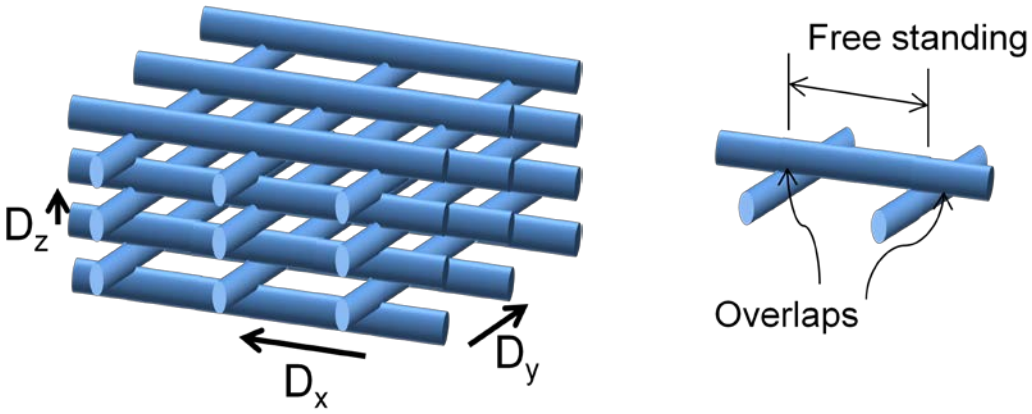

Figure 5.7. BCT lattice with line-to-line spacing (Dx=Dy) of 1 micron and layer spacing (Dz) of 650 nm.

Thes structures offer free-spanning cords of 1 micron length between overlapping volumes with adjacent layers, allowing for multiple points of line width measurements. Exposure dose ranging from 2 to 4 mW were used to fabricate 8-layered PCs. Special care was taken in the reference, non-swollen, sample where fabrication proceeded immediately upon oil application and the experiments were completed in less than 3 hours. These steps minimized swelling effects, where fluorescence profile indicated the

writing volume at and near the substrate was not altered. Fabrication in swollen gel resist began after 18 hours, well after equilibration period according to the fluorescence z-scans.

5.4 Results and Discussion

5.4.1 Swelling of Gel Resists

Fluorescence scans of the gel resist prior to any appreciable degree of swelling indicated DABSB chromophores were initially trapped within the gel resist, indicated by the high fluorescence intensity localized within 40-50 μm of the substrate (1.995 mm in Figure 5.8). As the immersion oil began to diffuse into the gel resist, a broadening to the fluorescence signal is observed. As the gel resist became saturated with the immersion oil, DABSB began to diffuse into the surrounding immersion oil, resulting in the observed increase in fluorescence signal detected outside of the gel resist volume (Figure 5.8).

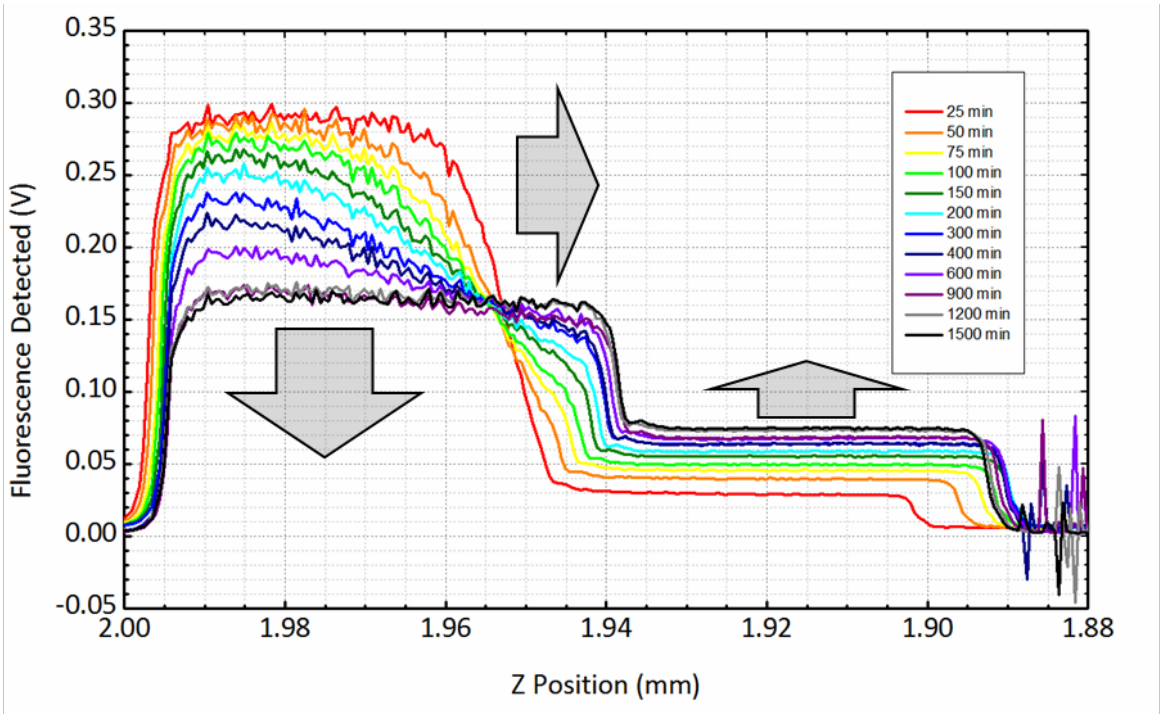

Figure 5.8. Cargille swelling representative fluorescence profile.

An equilibrium point where no further changes to the fluorescence profile were observed was reached at ~18 hours. The final degree of swelling was determined to be ~30% increase in thickness (Figure 5.9).

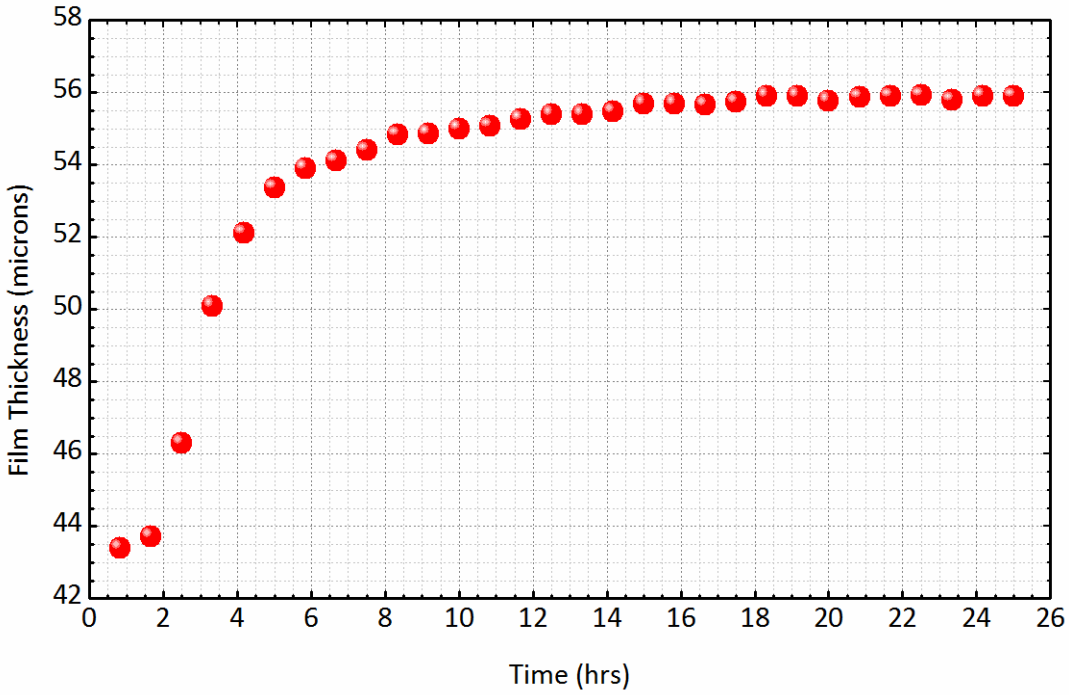

Figure 5.9. Gel resist thickness plotted as a function of immersion time.

A similar investigation was performed for each component of the immersion oil to determine if there was a particular component dominating the swelling. Immersion of the gel resist with the mineral oil Kaydol and polybutene resulted in negligible changes to the fluorescence profile over time. Swelling with BCHP (as shown in Figure 5.10) resulted in significant changes: 1) an increased degree of swelling was observed (estimated to be

~40%), 2) DABSB showed stronger affinity to BCHP than the gel resist itself, resulting in an inverted fluorescence profile.

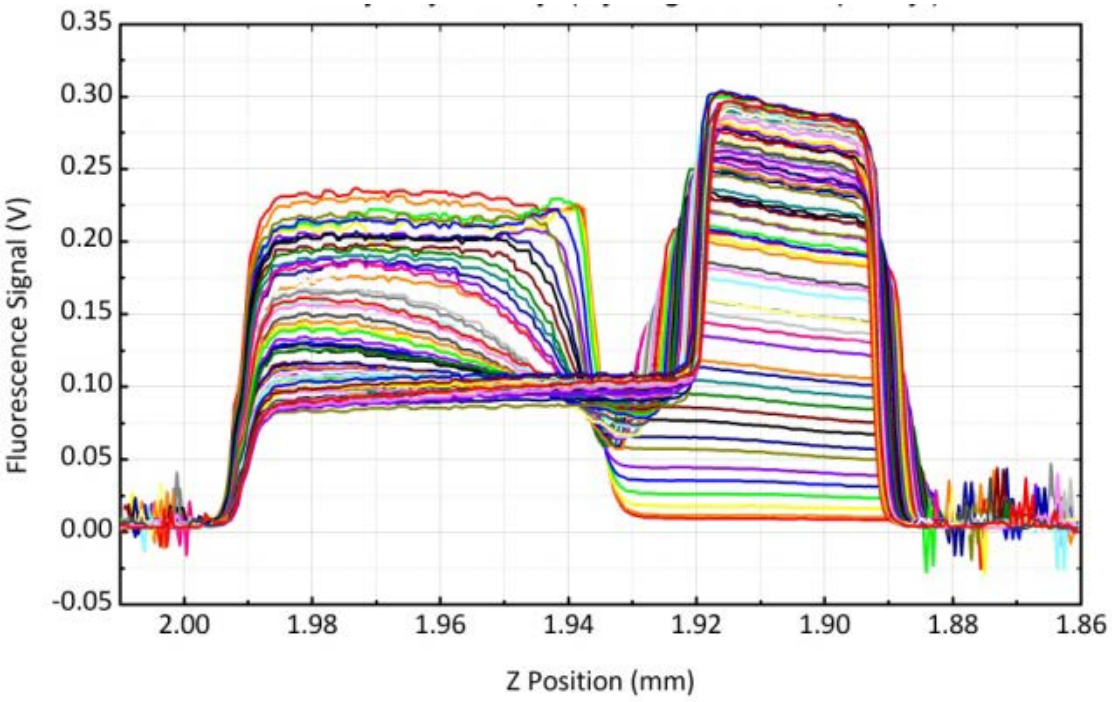

Figure 5.10. Gel resist swelling profile in BCHP.

This observation is likely the result of the phenyl groups from a more favorable solvation energy for the DABSB in BCHP as compared to the interaction between DABSB and the PSAN/triacrylate resin environment, perhaps due to stronger ππ-stacking or induced dipole-induced dipole interactions with BCHP. The low concentration of BCHP in the Cargille immersion oil and the low swelling effect of the other components results in an equilibrium swelling and fluorescence profile observed in the immersion oil.

Swelling studies were also performed with gel resists in immersion oil bath, without confinement to a liquid cell, to investigate if the gel-like swelling behavior is due to the formulation of the gel resist and not the experimental geometry. After immersion for

several days, there was no indication of film dissolution, confirming the gel resist acts as a physical gel in the immersion oil.

5.4.2 Effect of Swelling on Macro-scaled Structures

Scanning electron microscopy images (in Figure 5.11) of two block structures fabricated at early time (4 hours) and long time (20 hours) indicate tapering of the structures away from the substrate.

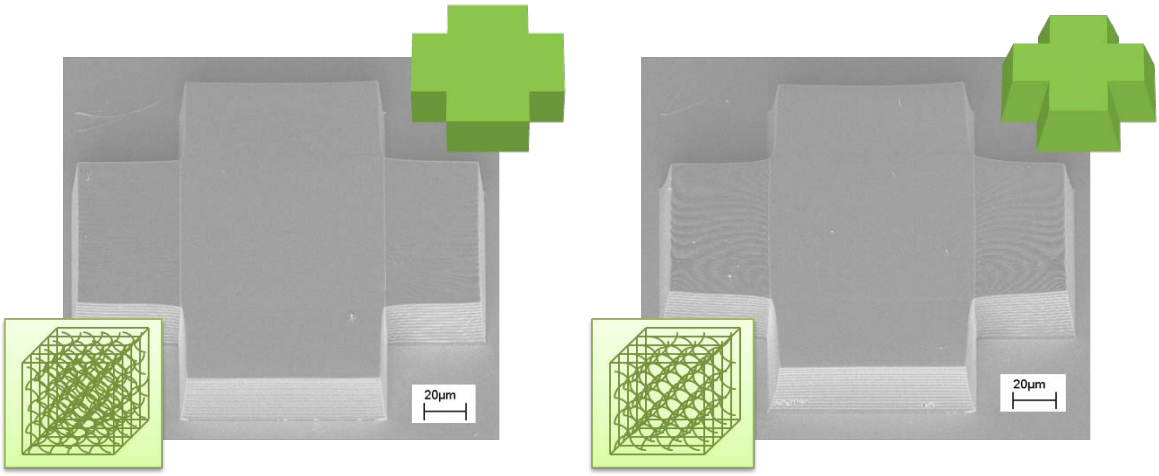

Figure 5.11. Cross structure fabricated at 4 hours (a) and at 20 hours (b) of immersion.

The footprints of the structures are fixed due to their attachment to the underlying glass substrate while the tops are free to relax by lateral shrinkage. A minor degree of tapering (1-5 % depending on exposure conditions) observed at early times is caused by volume shrinkage upon crosslink formation between acrylate monomer units. High degree of tapering was evident in structures fabricated at extended immersion times, the results of edge widths versus immersion time are shown in Figure 5.12 below.

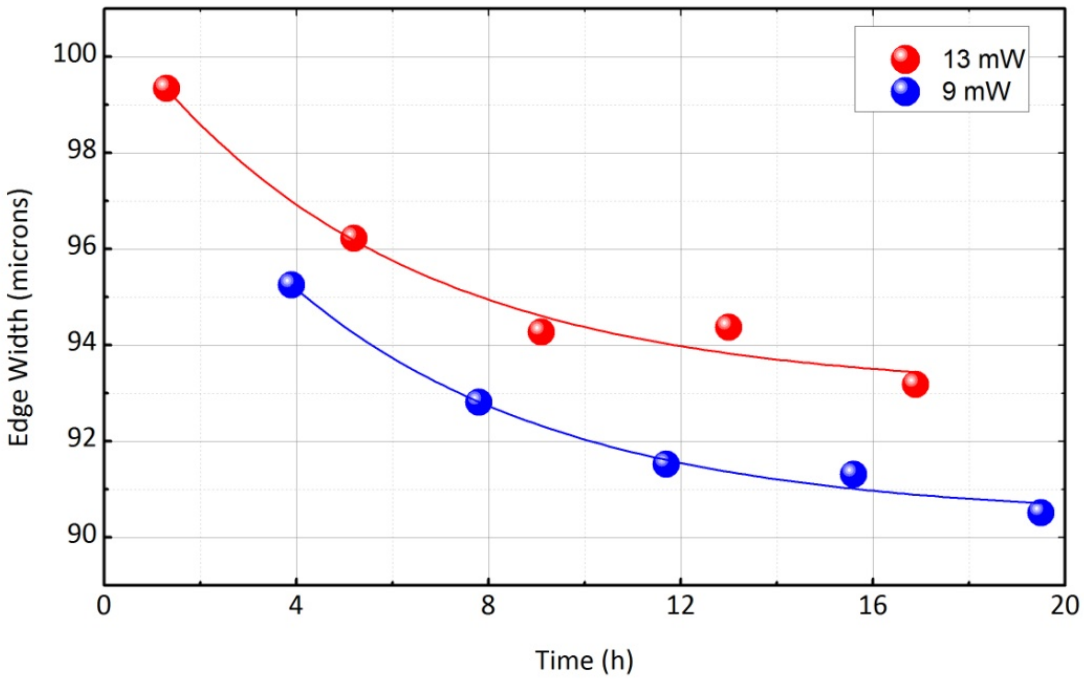

Figure 5.12. Edge width measurements of two sets of cross-shaped structures fabricated at different powers as a function of immersion time.

This decrease in edge width is attributed to reduced crosslinkable material as a function of swelling. Since the exposure parameters were fixed, the only variable was the time dependent immersion oil diffusion. As the oil penetrates into the gel resist, the gel matrix was swollen as depicted in the inset schematic above giving reduced number of photoinduced crosslinks per unit excitation volume. Upon development, the immersion oil was extracted by the same solvent as the developer for uncrosslinked material. The loosely networked polymer matrix reorients to minimize surface energy upon drying, resulting in additional shrinkage in the final structures.

5.4.3 Effect of Swelling on Microstructures

Representative comparison of PCs fabricated in the reference and swollen-gel resists are shown below (Figure 5.13).

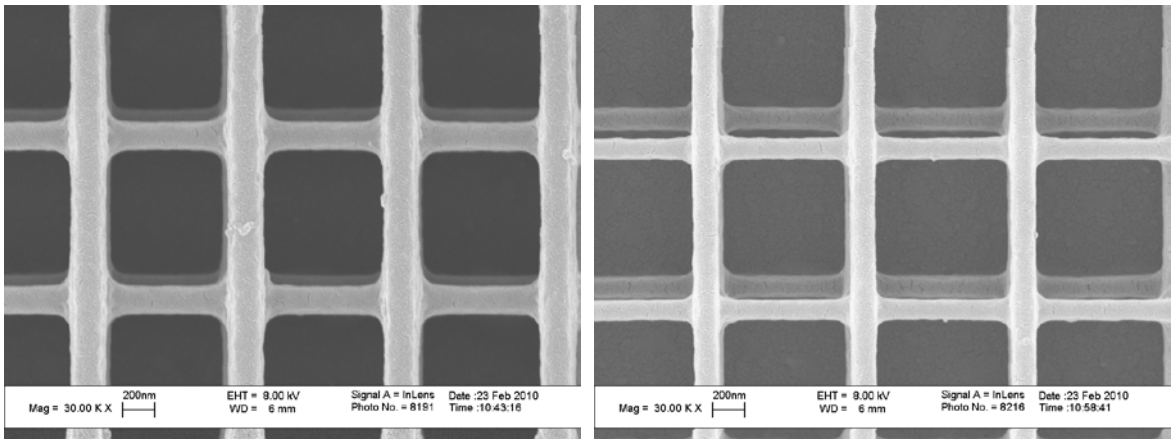

Figure 5.13. PC fabricated with 2 mW immediately upon oil application (left), and PC fabricated after 20 hours of immersion (right).

Results showed little to no distortion of the periodic 1 micron grid pattern is observed, indicating any stress from structural shrinkage is relieved uniformly in both the non-swollen and the swollen cases. The difference between the mechanical modulus of the polymer and glass substrate, however, caused a shift of the lattice at the substrate layer for both cases. Line width measurements of the reference sample, plotted in Figure 5.14, showed the characteristic trend as seen in the literature [13]. The swollen sample showed a reduction in widths compared to the similarly exposed non-swollen sample. These results are expected from the model from the macro structure case, where less crosslinks are formed per unit exposed volume in the swollen-gel resist, however the line widths versus exposure power showed more of a linear trend, suggesting additional mechanisms are involved.

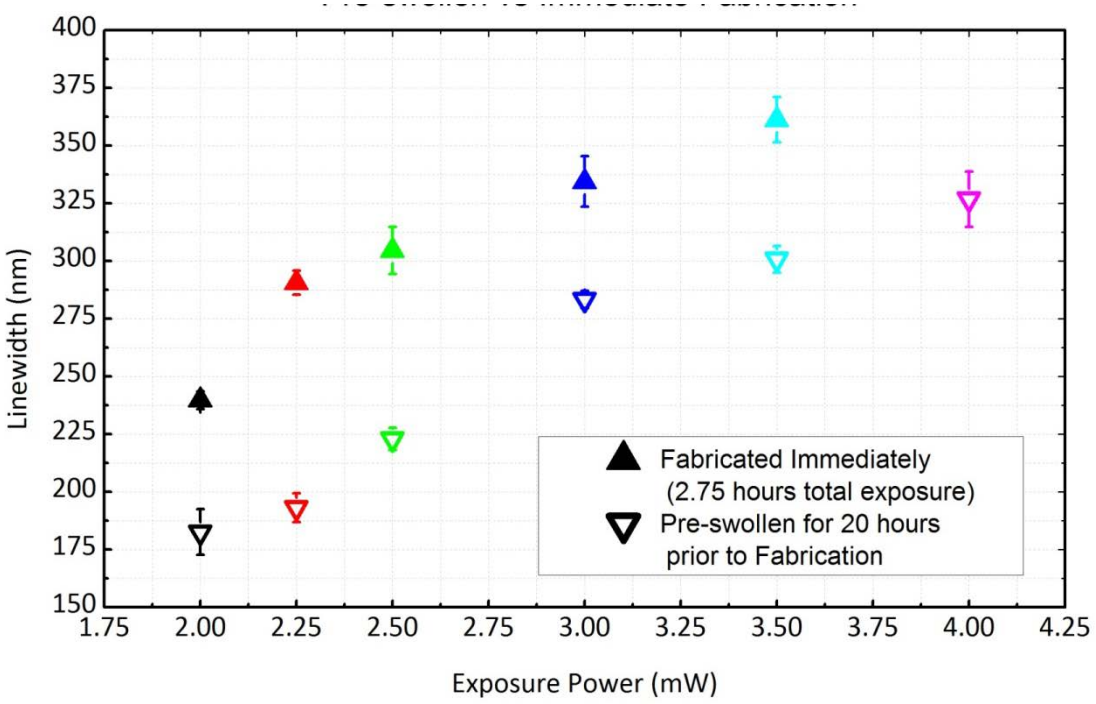

Figure 5.14. Dosing characteristics in reference (immediately after oil application) and swollen-gel resists.

5.4.4 Swelling Kinetics

To gain further insight into the dynamics of swelling, a series of PCs with same lattice and exposure parameters were fabricated at various degree of swelling. In additional to resolution measurements, the photonic stopband property was used to provide an additional monitor for the degree of swelling. These stopbands arise from the interaction of light with the periodic arrangement of polymer rods, creating constructive and destructive interference through multiple interactions within the PC. As the cord dimensions (both lateral and axial resolution) decreases, the resultant PCs were modified in two ways: 1) polymer fill-fraction decreases, lowering the effective refractive index,

and 2) layer spacing is reduced. Both of these effects contribute to blue-shifting photonic stopband positions by using Bragg's equation.

Support frame structures were fabricated immediately prior to each PC to provide anchoring points to prevent solvent turbulence related distortion and collapse during the development process. The support frames were fabricated with conditions similar to that of the blocks discussed in the previous section, under these higher dosing condition, the effect of shrinkage is minimal (<5%). The PC's layers were increased to 32 layers for depth-dependent size-reduction analysis and improved stopband intensities.

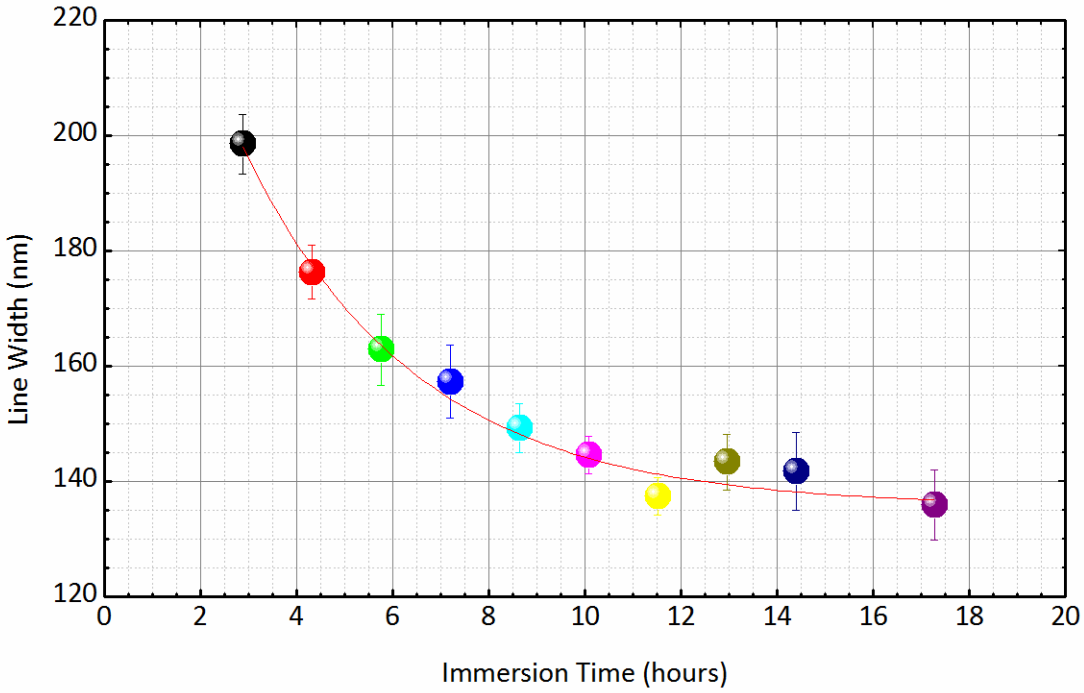

Figure 5.15. Line widths vs immersion time. The line widths measured at the saturation point were 136 ± 6 nm.

Cord width reduction as a function of swelling follows a single exponential decay, fitting reveals a lifetime of 3.6 ± 0.5 hours (Figure 5.15). Infrared reflection spectra were collected using a Fourier-transform infrared microscope spectrometer (FTS7000-UMA600, Agilent). PCs were measured with a 15× Cassegrain objective, 80 × 80 μm^2 aperture, and a gold mirror as the background. The PC spectra are plotted in the Figure 5.16.

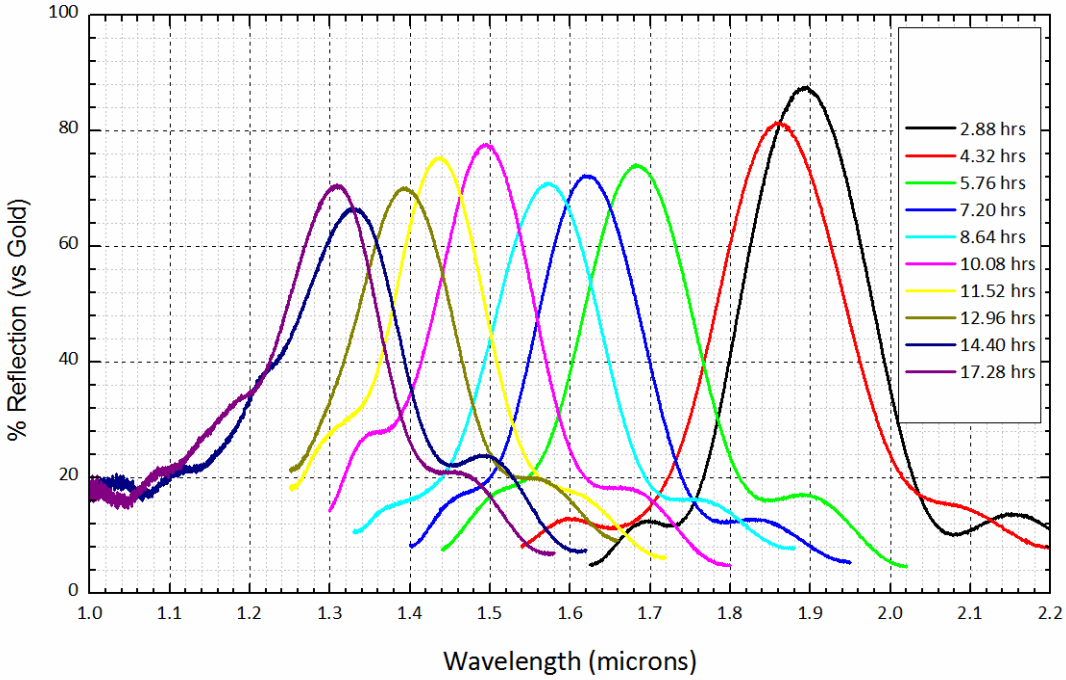

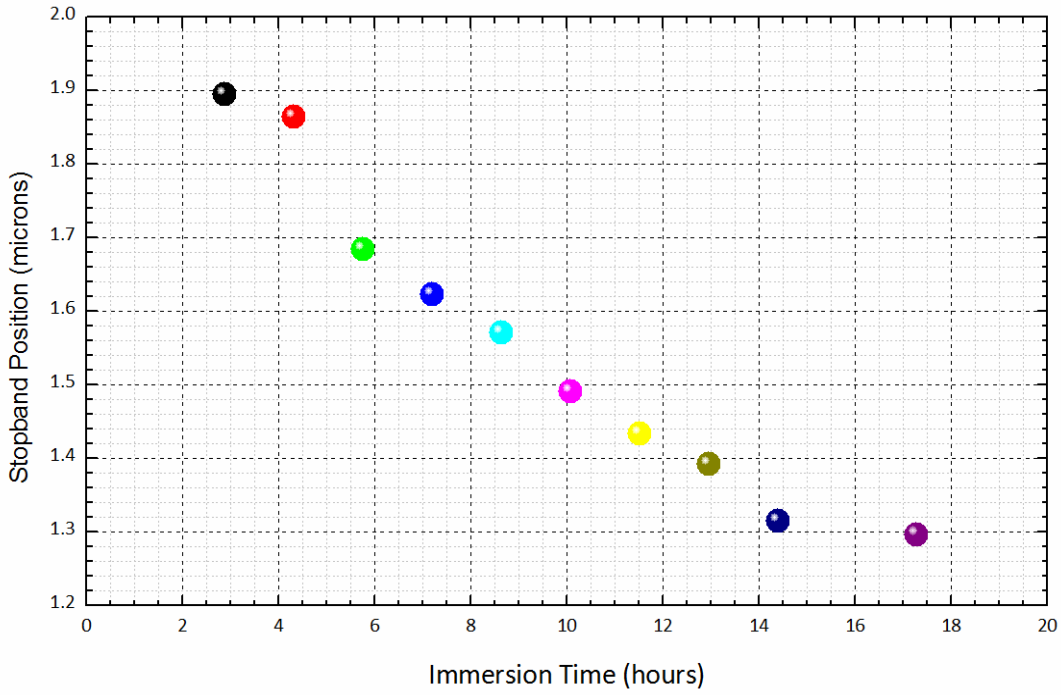

Figure 5.16. Infrared spectra (top) and stopband peak positions (bottom) for PCs fabricated with layer spacings of 800 nm, line spacings of 1000 nm, and exposure power of 2.25 mW as a function of immersion time.

All structures showed strong reflectance (> 60%) and a systematic blue shift is observed. Three distinct stages of stopband shifts were evident: 1) an initial induction period (<5 hours) where swelling throughout the fabricated volume was not uniform, 2) a linear regime where the stopband peak positions blue-shifts linearly between 5 and 14 hours, 3) an equilibrium regime where minute changes to the stopband position at swelling time of > 14 hours.

Band structure calculations were performed using a commercially available simulation software, BandSOLVE (RSoft), in order to verify the observed trend of the blue shifting stopband positions as a function of decreased feature sizes. The simulation result shown in Figure 5.17, was performed using the line widths to factor in the effect of swelling,

with the line heights and layer spacings scaled to the widths at an aspect ratio of 2.66 and 30% vertical overlap between layers.

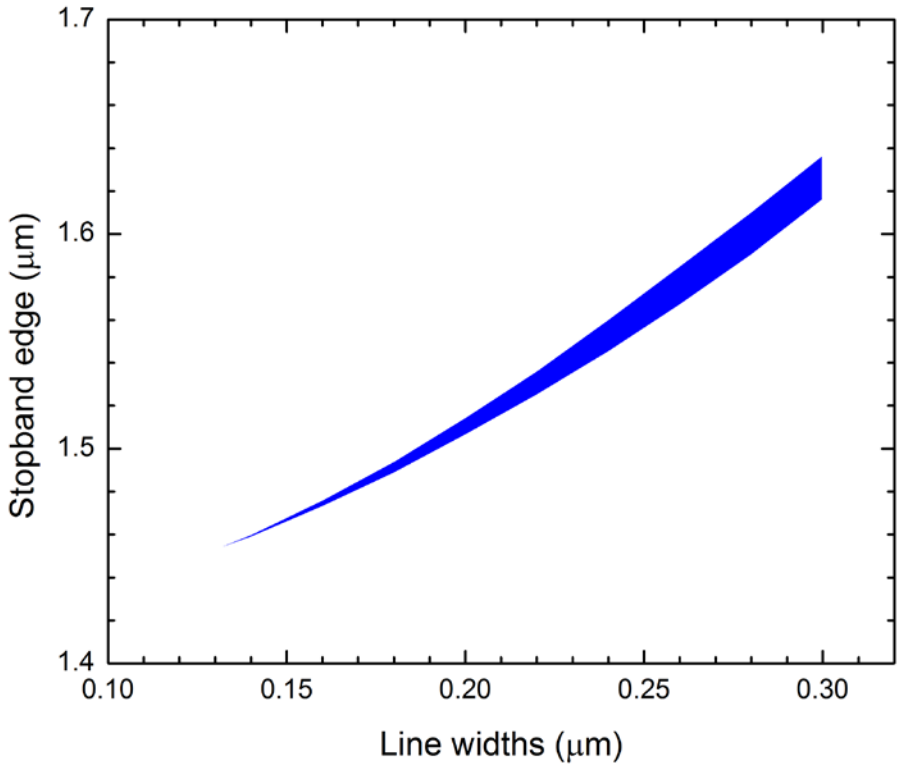

Figure 5.17. Stopband positions for normal incidence (along the PC stacking direction) as a function of reduced line widths due to swelling.

The simulation result demonstrates the stopband shift towards shorter wavelengths is consistent with the overall reduced PC lattice parameters. Whereas Figure 5.17 shows only the bandgap at normal incidence, the focusing geometry of the infrared microscope has a broad range of incidence angles, which is like the cause of discrepancies between the simulated and experimentally observed stopband positions.

5.4.5 Application of Swollen Gel Resist for PC Fabrication

To ascertain the feasibility of utilizing the swollen-gel resist for reliable fabrication of photonic crystal structures, the structure distortion was characterized by scanning electron microscopy. To investigate the effect on feature uniformity from the swelling process, the interior of the PC had to be investigated. Focused ion beam etching (FEI, Nova Nanolab 200) was attempted to interrogate the PC interior, however the milling process induced significant distortion to the structure. Fracturing of the substrate, while the least precise or repeatable, provided the least apparent distortion and one example of cleanly fractured structures is shown in Figure 5.18.

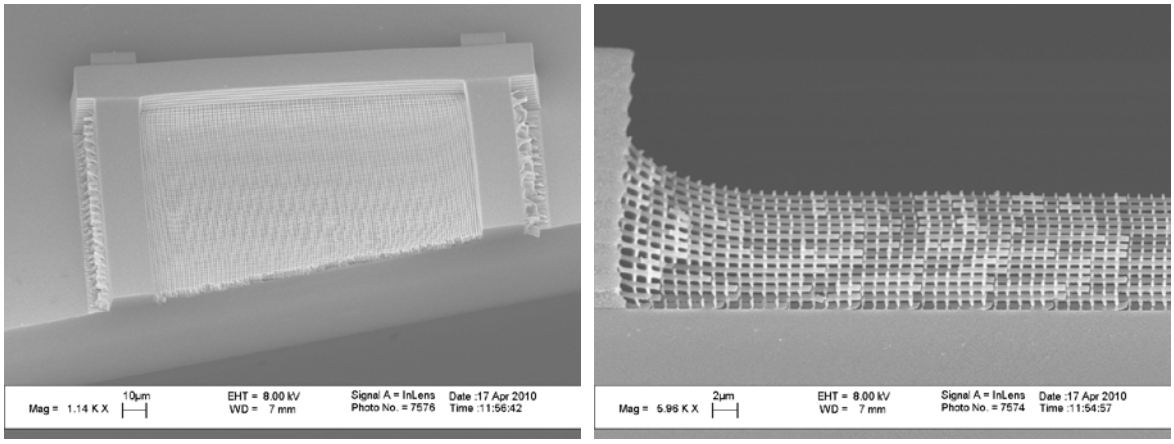

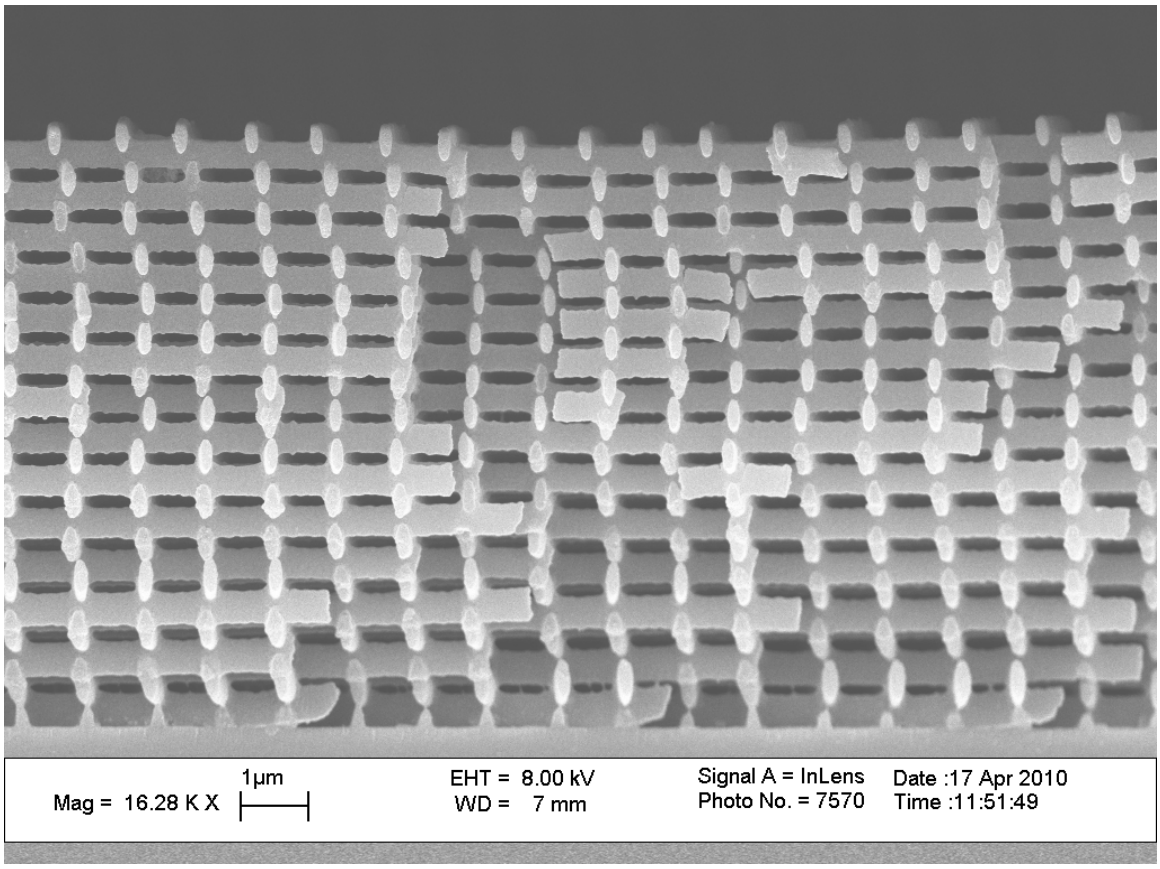

Figure 5.18. 160 mm × 160 mm × 32-layered PCs with BCT lattice were fabricated with a rod spacing of 1 µm and layer spacing of 550 nm at 2 mW. Overview of fractured structure (top left), crossectional view of the edge (top right) and center (bottom) region.

The difference in crosslink densities between the frame and the PC was the primary cause of distortion observed in the outer region of the PCs. The difference in the shrinkage ratio led to stretching of the features close to the edge, as depicted in above Figure 5.18 top right, this distortion was dissipated by 12 µm into the PC region, leaving the center uniform area of > 100 × 100 μm^2. Within this central region, the lateral spacing distortions was negligible (< 2%) due to the support from the adjacent cells. A higher degree of shrinkage was observed in vertical direction of the lattice (45%), since the lattice was able to freely compress. The cord features exhibit good uniformity throughout

the depths of structure, comparing the top layer to the substrate layer, with a 7% variation in line width (156 ± 7 nm at the top vs 168 ± 20 nm at the bottom) and 12% in line height (396 ± 14 nm at the top and 450 ± 28 nm at the bottom). Aspect ratios between the line width to height were 1:2.54 at the top 1:2.68 at the bottom, which are consistent with typical features obtained in non-swollen gel resists and liquid resins [1], suggesting the reduction in volume is isotropic. It should be noted similar experiments performed without supporting frames resulted in the same averaged lateral spacings, however the cord features with their elongated height tends to tilt sideways, resulting in registration errors between successive layers in the PC.

The PCs fabricated exhibit strong photonic stopband in the infrared region. Since the position and magnitude of the stopband are directly related to the periodicity of the structure, it was used to assess the reproducibility of the PCs generated from the swollen-gel resists.

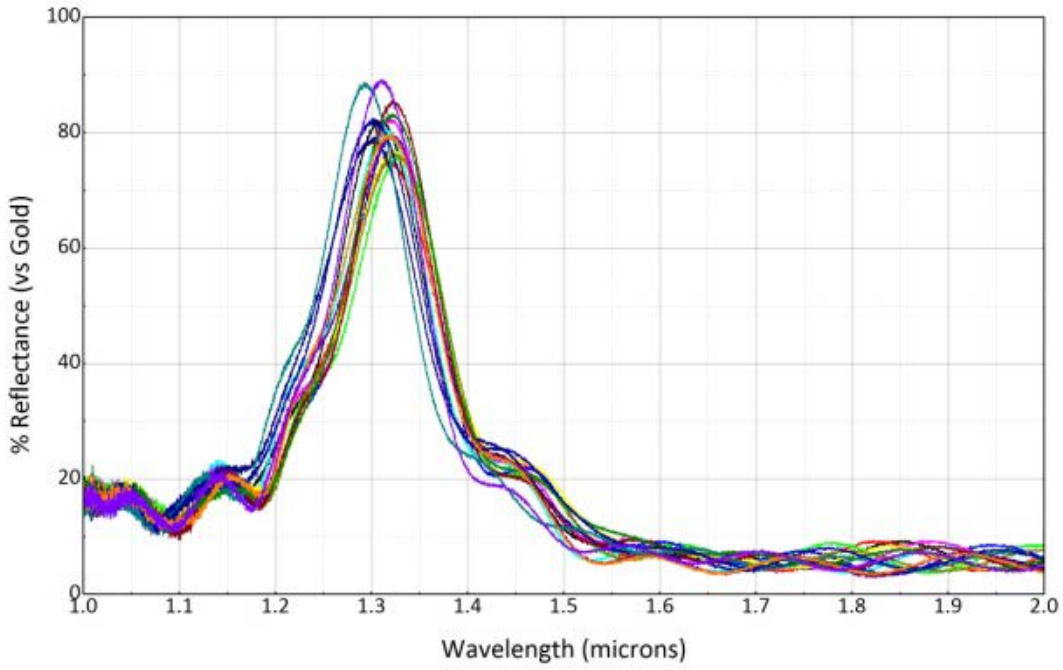

Figure 5.19. Infrared reflection spectra of 16 identical PCs.

FTIR reflection spectra of 16 PCs of the same fabrication parameters are shown in the Figure 5.19 above, with a gold mirror as reference. The stopbands showed good reproducibility both in terms of magnitude (81 ± 4% reflectance) and position (1.32 ± 0.01 µm).

Tuning of the PC stopband could be achieved statically using swollen-gel resist after saturation time was reached or dynamically by fabrication at different degree of swelling. Static tuning by varying the layer spacing from 800 to 550 nm resulted in the stopband shifting from 1.4 to 1.1 µm as demonstrated in the Figure 5.20 below.

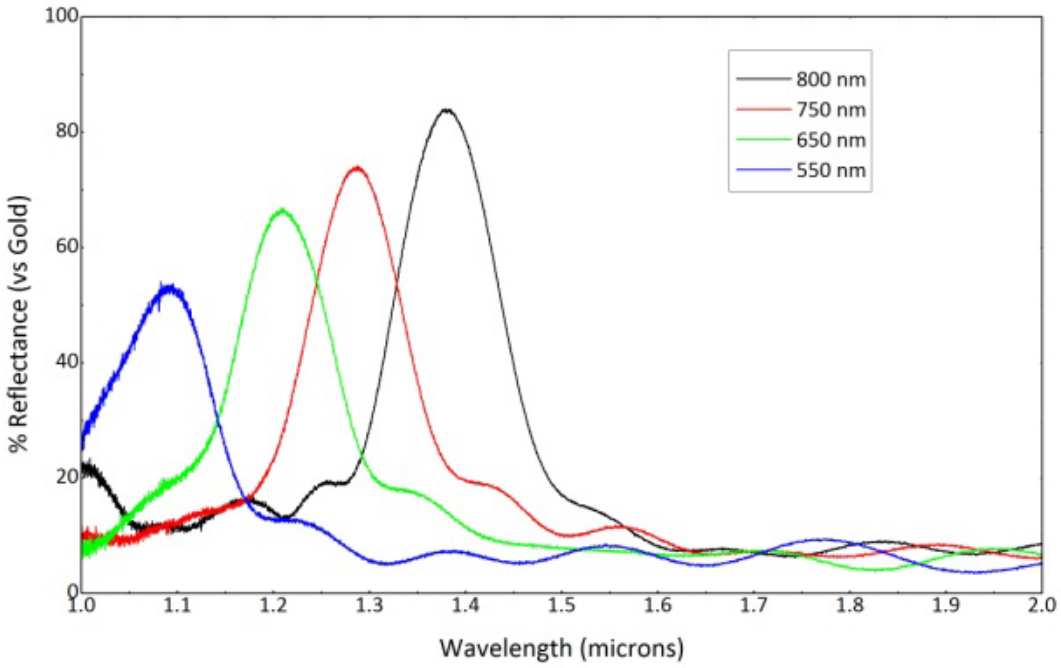

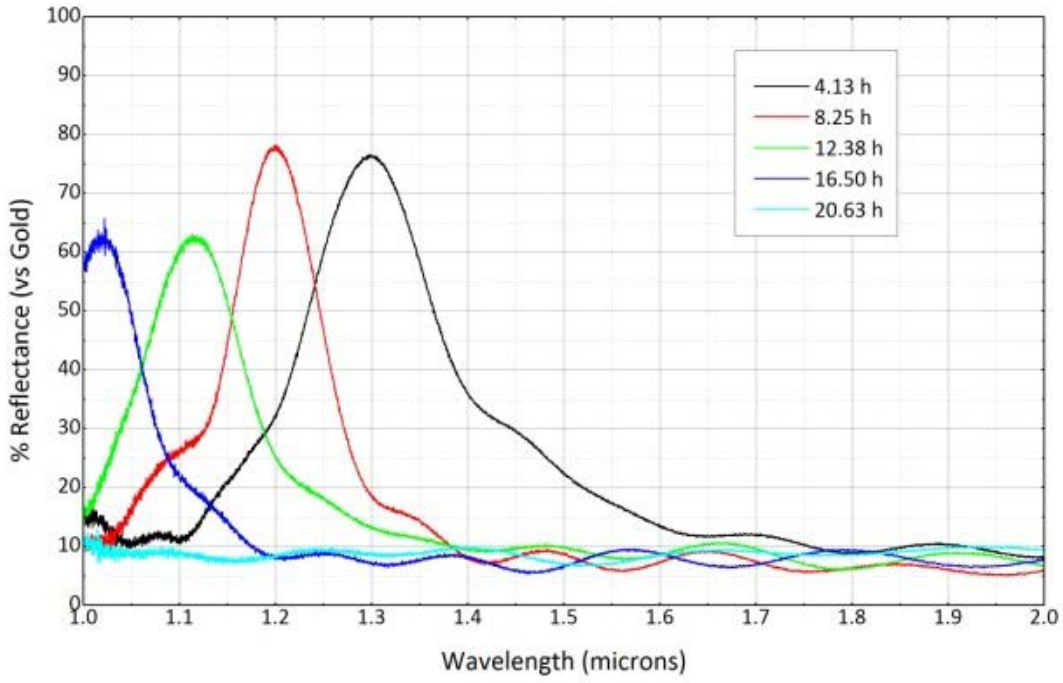

Figure 5.20. Static tuning by changing layer spacings (top) and dynamic tuning by swelling time (bottom).

An example of such dynamic tuning has been demonstrated in the previous section for 2.25 mW exposure, a similar experiment at 1.50 mW resulted in the same tuning trend (Figure 5.20 bottom), except the same degree of swelling resulted in more blue-shifted stopand positions from 1.3 to 1 μm, corresponding to the lower fill fraction from the lower exposure power.

5.4.6 Finest Resolution Achievable

In order to determine the highest resolution achievable with this system, additional dosage experiments were carried out with lower exposure powers and smaller layer spacings (650 nm) to improve the structure rigidity. The results of the study are shown in Figure 5.21.

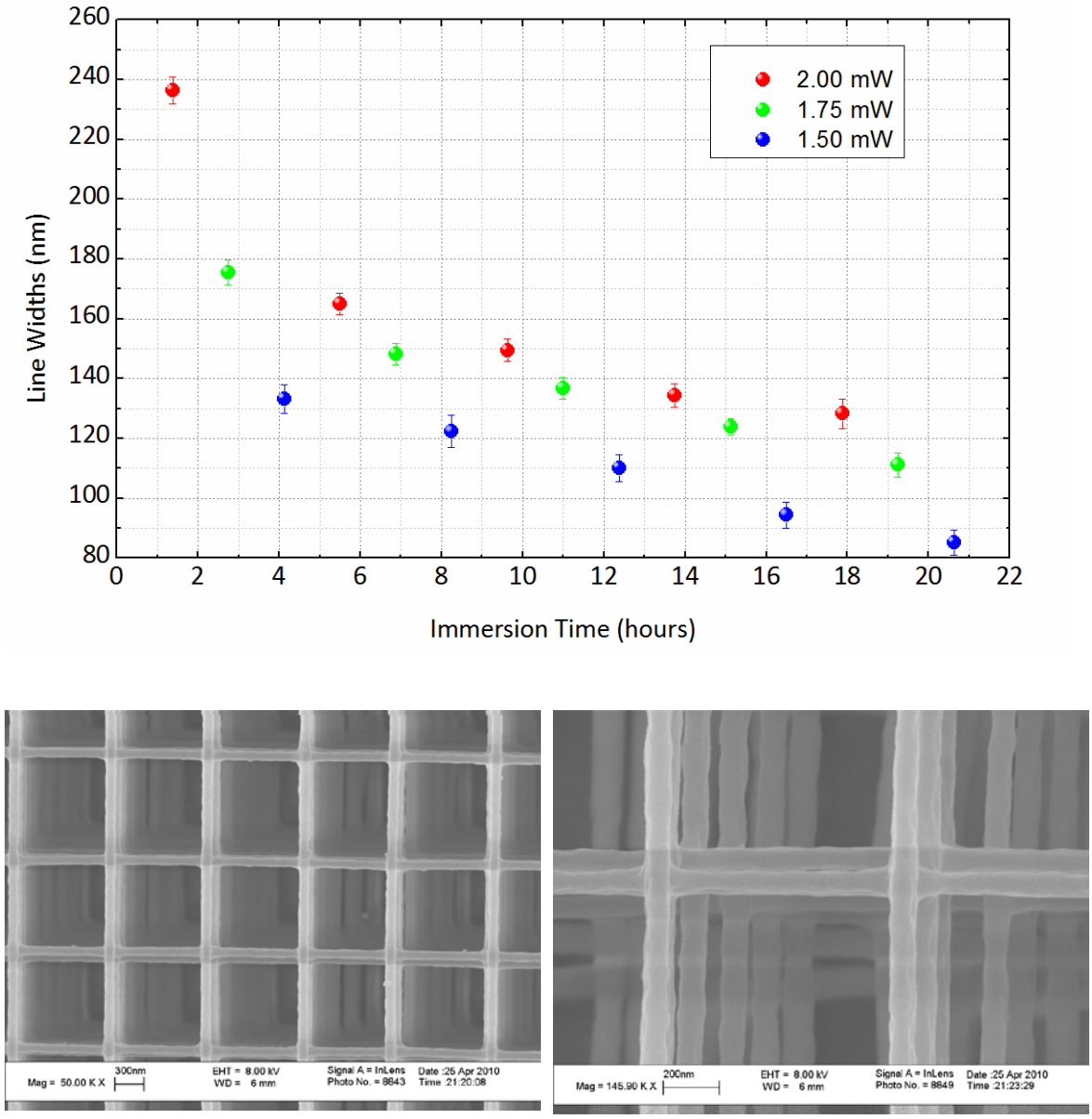

Figure 5.21. (Top) line widths versus immersion time for a set of three exposure powers. (Bottom left) PC at 1.5 mW, t=16.5 hrs. (Bottom right) PC fabricated at 1.5 mW at t=20.6 hrs (saturation).

Line width measurements of the fabricated structures show sub-100 nm features when an exposure power of 1.5 mW was used. Resolution of 94 ± 4 nm and 85± 4 nm were

observed from PC fabricated at 16.5 and 20.6 hours of swelling, respectively. Further reduction in power or extended swelling time resulted in delamination of the PC from its support frame or structural collapse in more severe cases, indicating the mechanical stability of the rods (with the lattice parameters chosen) was not sufficient to survive development process reliably.

5.5 Conclusion

In summary, swollen-gel resist offers a simple, facile means to achieve improved resolution with widely used near-infrared Ti:sapphire multiphoton microfabrication systems. The combination of exposure volume in the swollen gel resist matrix and the post development shrinkage provided up to 50% homogeneous reduction in feature sizes. This swelling approach was used to fabricate photonic crystals with strong reflection stopbands (> 60% relative to gold) in the near-IR range (1-2 μm). Further optimization of the lattice parameters by reducing the line and layer spacings will increase the degree of overlapping volumes between rods to minimize distortion caused by solvent development and could afford feature sizes smaller than the 85 nm reported here. Investigation into monomers with higher functional groups to molecular size ratio could further improve the structural stability. The low polymer fill-fraction in these photonic crystals widens their applicability as templates for surface chemistries and sensing applications. For applications in 3D volumetric structures, the difference between exposed volumes and the final structure could be compensated by the characterization of shrinkage parameters in conjunction with coordinates modification of the input data [14].

REFERENCES

1. S. M. Kuebler, M. Rumi, T. Watanabe, K. Braun, B. H. Cumpston, A. A. Heikal, L. L. Erskine, S. Thayumanavan, and J. W. Perry, "Optimizing Two-Photon Initiators and Exposure Conditions for Three-Dimensional Lithographic Microfabrication," Journal of Photopolym. Sci. Technol **14**, 657-668 (2001).

2. J. Saulius, and et al., "Two-photon lithography of nanorods in SU-8 photoresist," Nanotechnology **16**, 846 (2005).

3. K. Takada, H.-B. Sun, and S. Kawata, "Improved spatial resolution and surface roughness in photopolymerization-based laser nanowriting," Applied Physics Letters **86**, 071122 (2005).

4. L. Yan, and et al., "Nonuniform shrinkage and stretching of polymerized nanostructures fabricated by two-photon photopolymerization," Nanotechnology **19**, 055303 (2008).

5. L. Li, R. R. Gattass, E. Gershgoren, H. Hwang, and J. T. Fourkas, "Achieving λ/20 Resolution by One-Color Initiation and Deactivation of Polymerization," Science **324**, 910-913 (2009).

6. J. Fischer, and M. Wegener, "Three-dimensional direct laser writing inspired by stimulated-emission-depletion microscopy [Invited]," Opt. Mater. Express **1**, 614-624 (2011).

7. G. von Freymann, T. Y. M. Chan, S. John, V. Kitaev, G. A. Ozin, M. Deubel, and M. Wegener, "Sub-nanometer precision modification of the optical properties of three-dimensional polymer-based photonic crystals," Photonics and Nanostructures - Fundamentals and Applications **2**, 191-198 (2004).

8. J. Li, B. Jia, and M. Gu, "Engineering stop gaps of inorganic-organic polymeric 3D woodpile photonic crystals with post-thermal treatment," Opt. Express **16**, 20073-20080 (2008).

9. A. Ovsianikov, X. Shizhou, M. Farsari, M. Vamvakaki, C. Fotakis, and B. N. Chichkov, "Shrinkage of microstructures produced by two-photon polymerization of Zr-based hybrid photosensitive materials," Opt. Express **17**, 2143-2148 (2009).

10. G. M. Kavanagh, and S. B. Ross-Murphy, "Rheological characterisation of polymer gels," Progress in Polymer Science **23**, 533-562 (1998).

11. A. N. Bautis, "Immersion Oil Formulations For Use In Microscopy And Similar Fields," U. S. Patents, ed. (R. P. Cargille Laboratories, Inc., US, 1975).

12. M. Rumi, J. E. Ehrlich, A. A. Heikal, J. W. Perry, S. Barlow, Z. Hu, D. McCord-Maughon, T. C. Parker, H. Röckel, S. Thayumanavan, S. R. Marder, D. Beljonne, and J.-L. Brédas, "Structure−Property Relationships for Two-Photon Absorbing

Chromophores: Bis-Donor Diphenylpolyene and Bis(styryl)benzene Derivatives," Journal of the American Chemical Society **122**, 9500-9510 (2000).

13. S. M. Kuebler, B. H. Cumpston, S. Ananthavel, S. Barlow, J. E. Ehrlich, L. L. Erskine, A. A. Heikal, D. McCord-Maughon, J. Qin, H. Roeckel, M. C. Rumi, S. R. Marder, and J. W. Perry, "Three-dimensional microfabrication using two-photon-activated chemistry," in *Proc. SPIE 3937*(SPIE, 2000), pp. 97-105.

14. H.-B. Sun, T. Suwa, K. Takada, R. P. Zaccaria, M.-S. Kim, K.-S. Lee, and S. Kawata, "Shape precompensation in two-photon laser nanowriting of photonic lattices," Applied Physics Letters **85**, 3708-3710 (2004).

CHAPTER 6

SILVER COATED PHOTONIC CRYSTALS: TUNING PHOTONIC CRYSTAL PROPERTIES WITH SURFACE MODIFICATION

6.1 Introduction

Metallic photonic crystals (MPCs) have been of considerable interest because of their electromagnetic and high temperature properties for applications including enhancement of metal absorption [1] and suppression of thermal emission [2]. While MPCs with centimeter-scale lattices operating at gigahertz frequencies have been achieved by use of conventional machining methods [3, 4] in the late 1980s and early 1990s, subsequent interest in MPCs that could operate at terahertz frequencies (infrared wavelengths) required the use of different fabrication methods to achieve miniaturization of the lattice dimensions to the micron scale was necessary. Tungsten MPCs with a wide photonic bandgap in the IR region were fabricated using a layer-by-layer 2D lithography and etching along with metalloorganic chemical vapor deposition (MOCVD) technique[5] were reported in 2002. The desire to investigate various microstructure lattice designs and to incorporate well defined "defect" features into various periodic lattices led researchers to explore other fabrication approaches that are more suitable for free-form rapid prototyping.

Multiphoton lithography (MPL) is a powerful technique for fabricating 3D micro- and nano-structures with feature sizes down to 65 nm [6]. The ability to induce photochemistry in arbitrary 3D patterns makes MPL a versatile tool for the fabrication of tailored photonic crystal (PC) structures [7, 8]. The applications of polymeric PCs, however, have been limited by virtue of their low refractive indices, preventing the

formation of complete photonic bandgaps. The most direct approach to obtaining metalized photonic crystal structures was afforded by CVD of silver onto polymer gratings [9], however this deposition process requires high temperature, making it incompatible with polymer based structures, and requires extensive processing time.

Several groups have reported wet chemical approaches and polymer surface chemistries to achieve selective metal coatings. Farrer *et al*. have demonstrated deposition of gold and copper coatings on various microstructures (chains and coils) based on the preferential Michael reaction of amines with acrylates over methacrylates [10]. Formanek *et al*. have reported deposition of silver on microstructures containing styrenes [11]. Chen *et al*. have demonstrated electroless silver plating via amine modification of a polymer surface to obtain silver coated mirrors [12] and PCs [13]. The coating of PCs templates based on the epoxy polymer SU-8 with copper [14] and nickel [15], and the resultant modification to the optical characteristics have been explored. The resulting MPCs showed plasmonic band edges at ~ 3.5 μm indicated by the onset broadband infrared reflectance enhancements at wavelengths above this band edge. Despite the interest in MPCs for the manipulation of IR radiation, the control of the morphology and uniformity of the metal coatings within the 3D microporous networks of PCs is not well understood and the effect of these issues on the optical properties MPCs has not received sufficient attention.

In this chapter, the investigation several aspects of the wet-chemical methodologies used to apply silver coatings to polymeric PCs, the morphologies of the metal coatings, and the impact on the modifications of the PCs optical properties are reported. Experimental factors investigated include: 1) modification of the polymer template surface in-diffusion of tin ions that are catalytic for silver growth and the covalent chemical attachment of amines in attempts to control the density of nucleation sites to achieve varying degrees of silver surface coverage, 2) electroless plating

chemistries by reducing agents and capping agents to achieve varying deposition and morphologies, and 3) the use of directed microflow processes, by using a syringe pump, to introduce metal growth reactant infusion to improve reactant penetration into the microporous PCs and coating uniformity. Improved control of the morphology, uniformity throughout the microstructure, and the optical properties of the MPCs was obtained through the systematic studies performed. With improved process control, the MPC optical properties could be varied reproducibly from showing discrete stopbands with variable reflectivity in sparsely nanoparticle decorated PCs to strong broadband IR reflection with a plasmonic band edge at 1.75 μm for densely coated PCs.

6.2 Experiment

6.2.1 Fabrication of Microstructures

The instrumentation for MPL and the design and fabrication of microstructures have been described in detail in Chapter 3. The photoresist material used for this study was a liquid resin mixture of trifunctional acrylate monomers SR9008 and SR368 (Sartomer) at a 50:50 weight ratio. The concentration of a radical inhibitor, 4-methoxyphenol (Aldrich, 99%), in the resin was raised to 0.1% of the total resin weight to prevent thermal crosslinking during sample preparation and spreading of free radical polymerization outside the illuminated volume. Multiphoton radical initiator *E,E*-1,4-*bis*[4-(*N,N*-di-n-butylamino)styryl]-2,5-dimethoxybenzene (DABSB), whose structure is shown in Figure 6.1, was employed at 0.1 wt% [16].

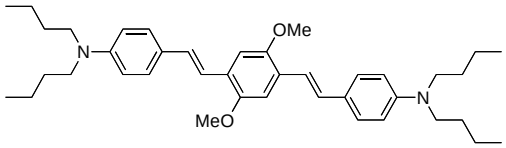

Figure 6.1. Molecular structure of photoinitiator DABSB.

The fluid resin was contained by an optical cell, comprising microscope slide which had been treated with an adhesion promoter and a microscope cover slip (Electron Microscopy Sciences, Gold Seal No. 0), separated by a 100 μm thick Teflon spacer spacer (Aldrich). The adhesion promotion of the slide surface was performed by spin coating of 10% by volume solution of 3-(trimethoxysilyl)propyl methacrylate (Aldrich, 98%) in ethanol (Aldrich, 200 proof, anhydrous, 99.5%) followed by baking at 130ºC. This process was repeated three times. Following laser scanning exposure of the desired pattern, post-exposure development was carried out using 4-methyl-2-pentanone (Aldrich, 99%) to dissolve and remove unexposed material.

6.2.2 Metallization Methods

Two metallization processes were investigated. For method 1, chemical sensitization of the surface of the polymer structure, physically swelling of the polymer surface and in-diffusion of Sn^{2+} ions into the polymer was performed using a solution of stannous chloride in a solvent followed by washing with alcohol to remove excess from the surface. Method 2 was involved a surface chemical modification of uncrosslinked acrylate groups on the polymer surface with a multifunctional amine via Michael addition [17]. The intial surface treatment was followed by treatment with a solution of silver ions which could bind with amine sites or undergo reduction by Sn^{2+} ions at the surface. In both cases, small silver nanoparticles were formed and then grown in a subsequent electroless deposition process.

6.2.2.1 Metallization via Tin Sensitization

This metallization procedure was developed in collaboration with Dr. Yadong Zhang. The silver nucleation chemistry was based on Formanek's work [11], where stannous chloride was used to catalyze the silver ion reduction. The selectivity in Formanek's work was based on addition of polystyrene into the crosslinkable resin and its affinity to Sn^{2+} ions. Our approach to selectivity was based on swelling of the polymer surface and trapping of Sn^{2+} ions on or just below the surface, thus preserving the established resin materials and fabrication conditions. A schematic of this metallization process is shown in Figure 6.2.

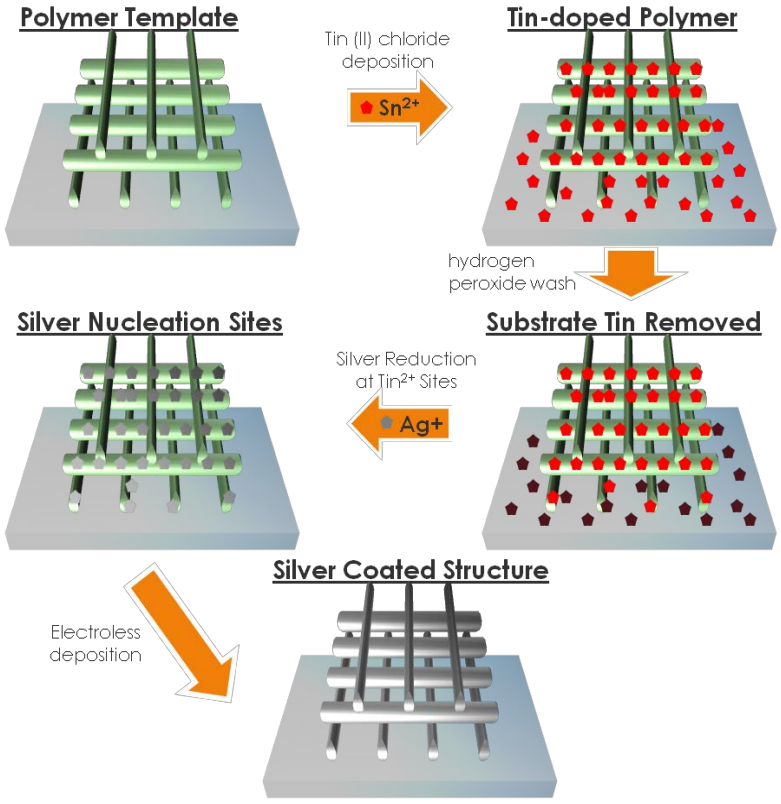

Figure 6.2. Schematic representation of Metallization via tin sensitization.

Samples were subjected to a stannous chloride (Aldrich, $SnCl_2 \cdot 2H_2O$, 98%) saturated solution of propylene glycol monomethyl ether acetate (Aldrich, PGMEA, 99%) for 2 hours. The PGMEA is able to weakly swell the fabricated polymer structure as well as dissolve the $SnCl_2$. The samples were then rinsed thoroughly with methanol

(Aldrich, spectrophotometric grade) and Sn^{2+} ions were trapped by the deswelling of polymer surface. Selectivity of the metallization process was achieved by rinsing for 35 seconds in an aqueous 3% H_2O_2 (VWR, 30% in H_2O). During this step, the hydrophobicity of the polymer should protect the absorbed Sn^{2+} ions, whereas unwanted ions on the hydrophilic glass substrate were oxidized to Sn^{4+}, which renders them inert towards silver reduction. The electroless deposition process was carried out using a Tollen's Reagent based commercial silver plating solution (Peacock Laboratories Inc., HE-300). Electroless plating of the fabricated and sensitized polymeric microstructures were carried out according to the manufacturer's directions wherein the silver ion containing solution was first combined with an activator solution and was allowed to mix for 5 minutes prior to the addition of the reducing solution. The substrates bearing polymer microstructures were submerged into the electroless plating solution at room temperature and the degree of plating was controlled by the duration of the submersion. The electroless deposition reaction was terminated by rinsing the samples with deionized water for three times.

6.2.2.2 Metallization via Surface Modification

Selective silver deposition in this approach was achieved through the surface modification of fabricated polymer microstructures by reaction of surface acrylate groups with difunctional or polyfunctional amines via Michael addition. Two reactants with different number of functional groups were investigated, one was a facile reaction with 20 vol% ethylenediamine (Sigma-Aldrich, 99%) in ethanol [10] at room temperature for 1 hour, and the other was a surface amplification process where alternating reactions with 5 wt% of *tris*(2-aminoethyl)amine (Aldrich, 96%) and 5 wt% of dipentaerythritol *penta*-/*hexa*-acrylate solutions in ethanol at 45ºC for 1 hour, a total of 3 cycles followed by a final amine treatment was used to amplify the number of amine surface functional groups [18]. In this case unwanted deposition of silver on the substrate was minimized by

treatment with bromotrimethylsilane (Fluka, 97%) for 1 hour to deplete hydroxyl concentration on the surface and render the substrate hydrophobic to avoid adsorption of silver ions. A schematic of this metallization process is shown in Figure 6.3.

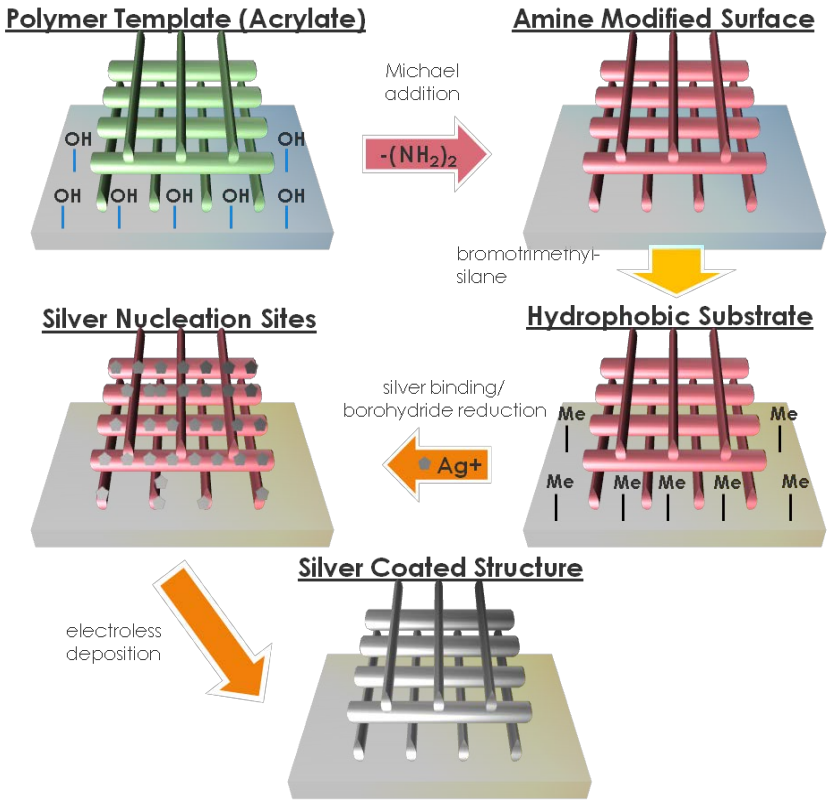

Figure 6.3. Schematic representation of Metallization via surface modification.

In order to achieve a silver surface coverage with the highest density and forming the thinnest conformal coating on the polymer microstructures for localized plasmon resonance effects, the silver seeding and the electroless plating steps were investigated and optimized separately. The seeding step was performed by binding silver ions to the amine sites on polymer surface by subjecting the sample into a silver nitrate (Sigma-Aldrich, 99%) solution for 30 minutes. After formation of silver seeds on the surface, three cycles of reductive growth of silver was performed by alternating treatments with sodium borohydride (Aldrich, 99%) and silver nitrate aqueous solutions[19] for 30 minutes each in a vial with constant stirring. A variation on this procedure used

acetonitrile as the solvent to ensure better wetting of the polymeric surfaces by the solutions and the high solubility of silver nitrate in acetonitrile. Electroless deposition was performed using aqueous solutions of silver nitrate, hydroquinone (Fluka, 99%) as selective reducing agent [20], and sodium citrate (Aldrich, trisodium citrate dihydrate) as the capping agent [21]. A stepwise growth of the plating thickness was achieved by using hydroquinone as the limiting reagent. Plating time was limited to 6 minutes per cycle due to a slow citrate induced nanoparticles seeding.

Samples prepared by both silver coating methods were analyzed with scanning electron microscopy (LEO/Zeiss Electron Microscopy, 1530 FE SEM) and Fourier transform infrared spectroscopy (Agilent, FTS7000-UMA600).

6.3 Results and Discussions

6.3.1 Metallization via Tin Sensitization

6.3.1.1 Metallization of Polymer Flats

Initial experiments were performed on flat, microfabricated polymer surfaces to investigate the increase in reflectivity as a function of deposited silver. In order to produce surfaces similar to those of the photonic crystal microstructures, the polymer flats were fabricated by MPL, similarly to the photonic crystals, by using very narrow spacings (50 nm) between scanned line features such that the surface becomes continuous and with a small surface roughness. Metallization of the flats using coating times of 2 – 3 minutes produced visibly highly reflective silver coatings selectively on the flats (Figure 6.4).

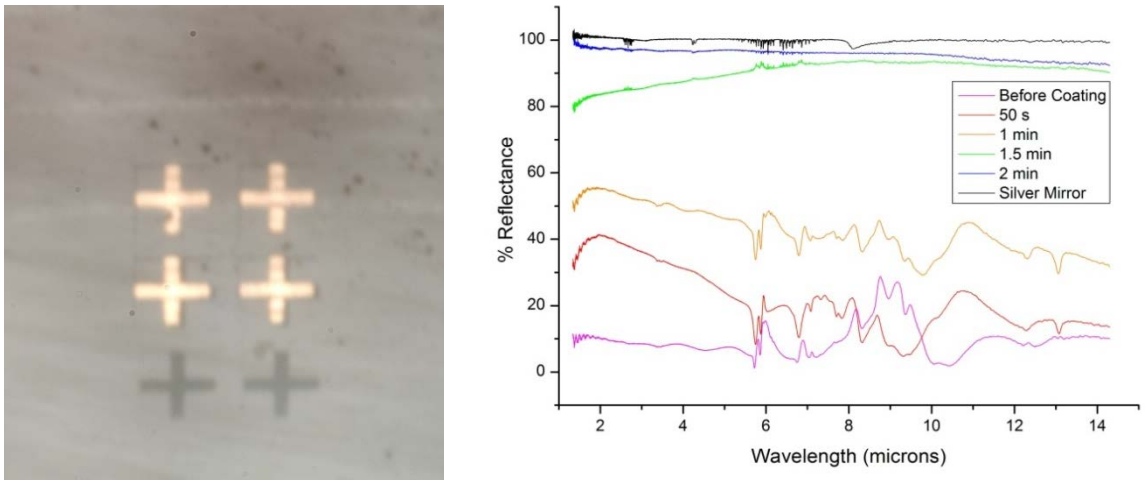

Figure 6.4. Optical image of metalized polymer flats subjected to 2 minutes of silver electroless plating (left). Infrared reflection spectra of polymer flats subjected to various times (50 sec. – 2 min.) for silver deposition (right).

Infrared reflectance spectroscopy of these structures showed an increasing reflectivity with increasing deposition time, as shown in Figure 6.4. An induction period for the development of high reflectance silver films similar to that reported by Tal *et al* for copper coatings [14] was observed, indicating that the initial deposition ($t < 1.5$ minutes) consisted of small metal islands, and the plating thickness approaches the skin depth of silver at ~2 minutes. Structures that were subjected to longer deposition times (from 2 minutes on) show reflection spectra similar to evaporatively deposited silver films. Results from this set of experiments demonstrated the methodology employed was successful in selectively deposit silver onto polymer surfaces.

6.3.1.2 Metallization of PCs

To study the metallization of PCs and the coating morphology, samples with 4 × 4 arrays of 16 PCs were fabricated with lattice parameters of 4 μm line and 1.5 μm layer spacings. The overall dimensions of the PCs were 100 μm × 100 μm × 24 μm.

Sensitization of the PCs was achieved using the same reaction condition as the optical flats. PCs with varying degrees of silver deposition were obtained by varying the immersion time of electroless plating from 1 to 5 minutes. Infrared reflectance spectra shown in Figure 6.5 below illustrate the progression of the PC stopband as a function of the thickness of the silver coating.

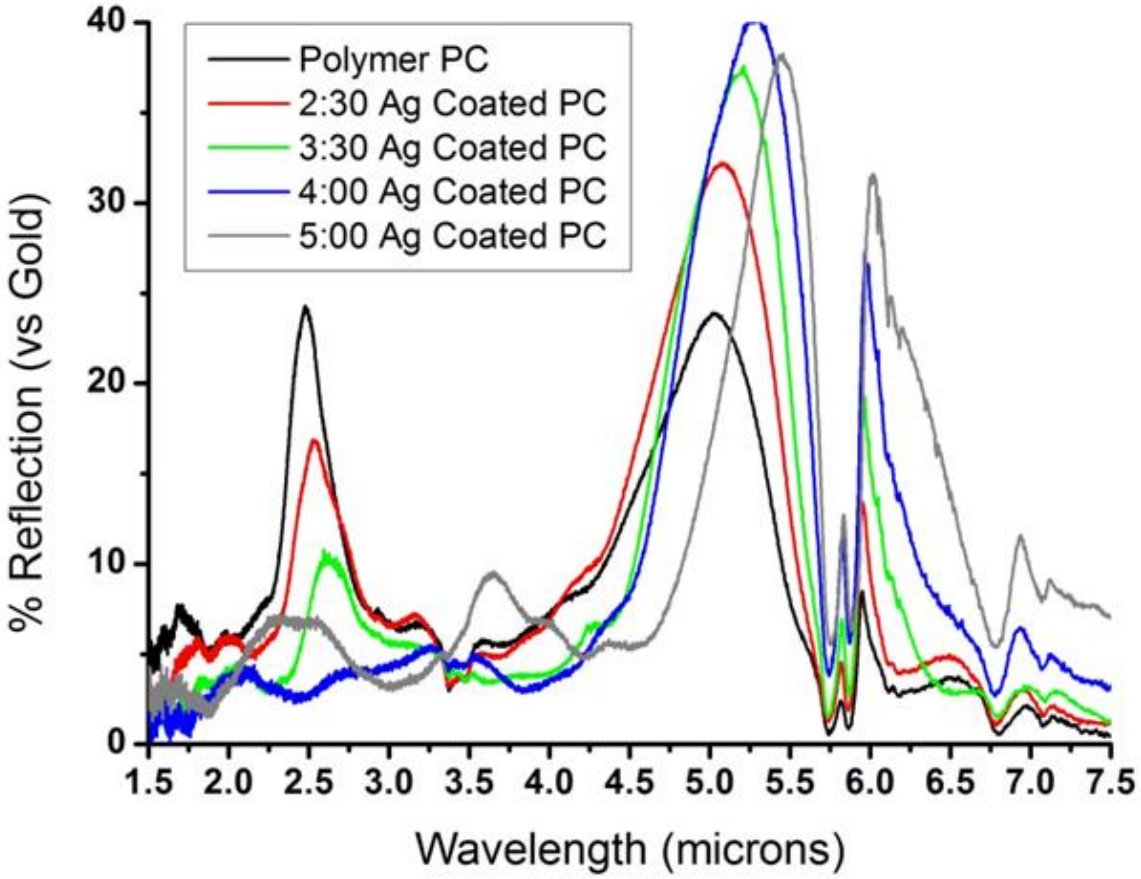

Figure 6.5. PC infrared reflection spectra from the unsilvered polymer PC (black) to a PC coated with silver with various times of growth..

Reflection spectra of these structures showed a small, long-wavelength shift of the stopbands from peak positions of 5 to 6 μm with longer deposition time. This red-shift corresponds to increased effective refractive index resulting from the metal attachment. This result is consistent with the observations and simulations by Buso *et al*. for increasing thickness of CdS electroless plating on PCs [22]. An increase in the stopband

reflectivity was also observed in conjunction with the long wavelength shift. The enhancement factor of the reflectance, relative to the initial stopband reflectance or the PC structure and the results for each of 16 structures for each silver film growth time are plotted in Figure 6.6.

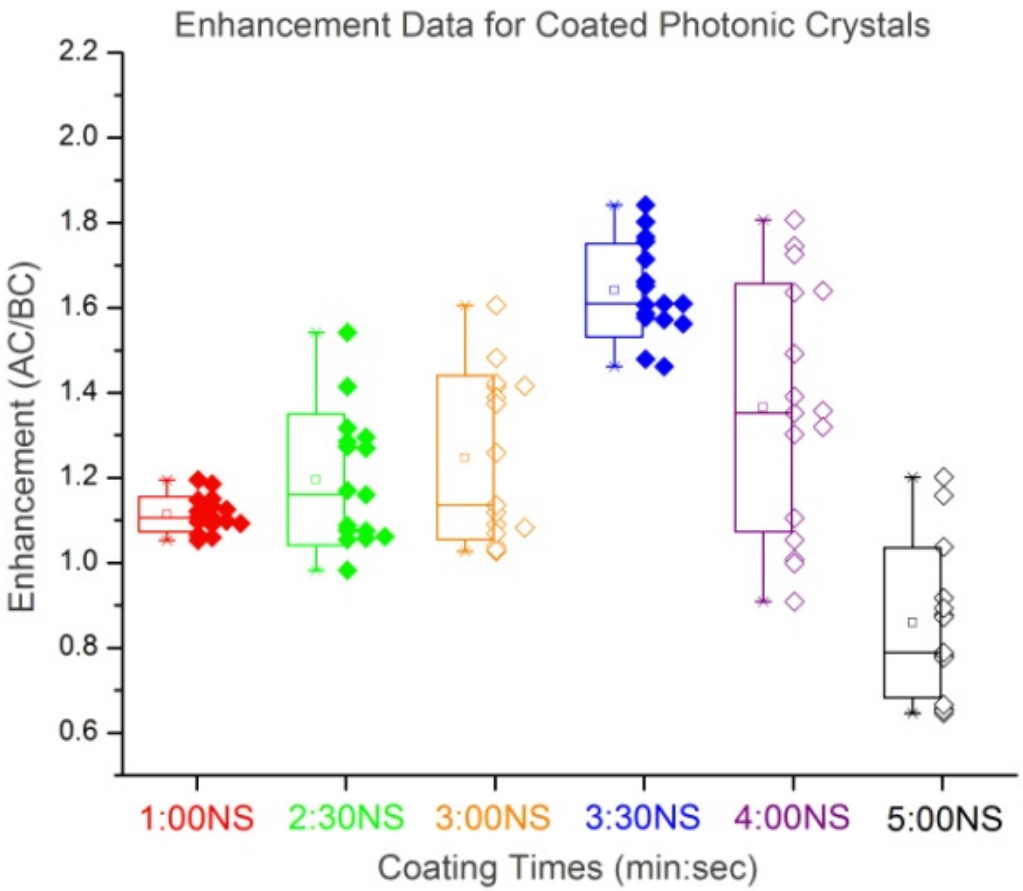

Figure 6.6. Stopband reflectance enhancement as a function of deposition time.

The maximum enhancement of the reflectance was a factor of 1.8× for the structures subjected to 3.5 to 4 minutes of coating, relative to the uncoated structures. These were conservative estimates since the stopband wavelength overlaps with the polymer's carbonyl absorption at 5.8 μm, obscuring the actual peak reflectance, and the metallization-induced shift causes an increasing overlap of the reflectance and the

carbonyl absorption band. This result is contrary to the case of copper [14] wherein a decrease in reflectivity as a function of deposition time was observed. The cause of this discrepancy is likely the due to difference between the PC's lattice parameters used in Ref. [14] and in this work. Buso *et al*. [22] observed a peak enhancement of the stopband intensity at the mid point tuning of their CdS coating thickness, suggesting the combination of effective refractive index and fill fraction at that thickness resulted in the optimum stopband performance.

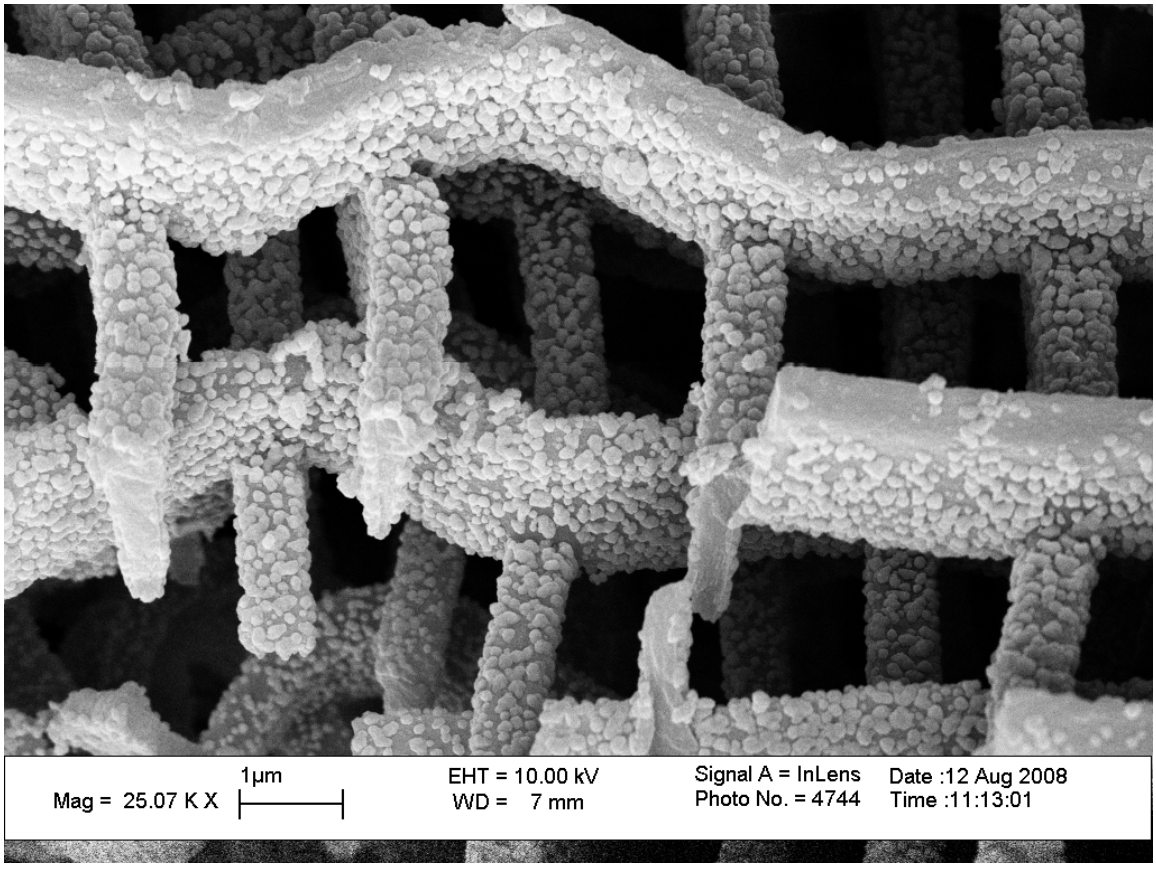

Figure 6.7. Cross sectional SEM of a silver coated PC that reveals the penetration of the silver deposition within the PC microstructure. The image was taken at an incidence angle of 45^{o} relative to the fracture surface.

In order to investigate the morphology of the silver coating and the penetration of into the PC structure, samples were fractured and used to obtain cross sectional SEM

images, an example of a 3.5 minute plated PC is shown in Figure 6.7. Silver islands appeared to decorate the surfaces with a relatively uniform coverage density within the entire structure; however the coverage in this case is relatively sparse. These results suggested initial Sn^{2+} ion coverage and the Ag seed density was insufficient to produce continuous coating. Another observation was that the average deposition at the top surface of the PCs was smaller than on the sides and interior. This is likely a result of the hydrogen peroxide treatment where the outer surface of the PCs and which most likely undergoes more oxidation of Sn^{2+} catalyst, reducing the density of silver seeds. The combination of the Sn^{2+} in-diffusion, peroxide treatment to oxidize Sn^{2+} on the substrate surface, and the use of a proprietary electroless silver coating solution made the optimization of the silver metallization chemistry difficult, using this combination of methods. As a result, we investigated the use of Method 2 described above which uses surface modification to both put coordinating amine groups on the polymer surface to enable silver seed formation and trimethylsilyl groups on the substrate to avoid silver seeding on the substrate, as well as a better defined chemically controlled silver reductive growth solution.

6.3.2 Metallization via Surface Modification

Silver seeding applied to PCs exhibited low conductivity, resulting in poor quality SEM images. While gold sputtering of the samples resulted in higher quality images, the contribution from the sputter coating is difficult to distinguish from the seeding itself. Therefore, electroless plating was applied to deposit additional silver onto the seeding sites to afford better quality images and distinction from the sputter coating. For these initial studies, the ethylenediamine modification was used for more rapid analyses. PC lattice parameter was reduced to 1.6 μm line spacings both to push initial stopband

positions to the telecommunications range (~1.4 μm) and to ensure the developed methodology is applicable to the micron-scaled pores.

6.3.2.1 Effect of Electroless Deposition Conditions on Spectral Modifications

While electroless plating solution with silver nitrate and hydroquinone resulted in highly selective deposition and no reaction was observed without the presence of seed particles, SEM images of the coating applied to the PCs indicated a large distribution of particle sizes (~10 – 180 nm) (Figure 6.8, left):

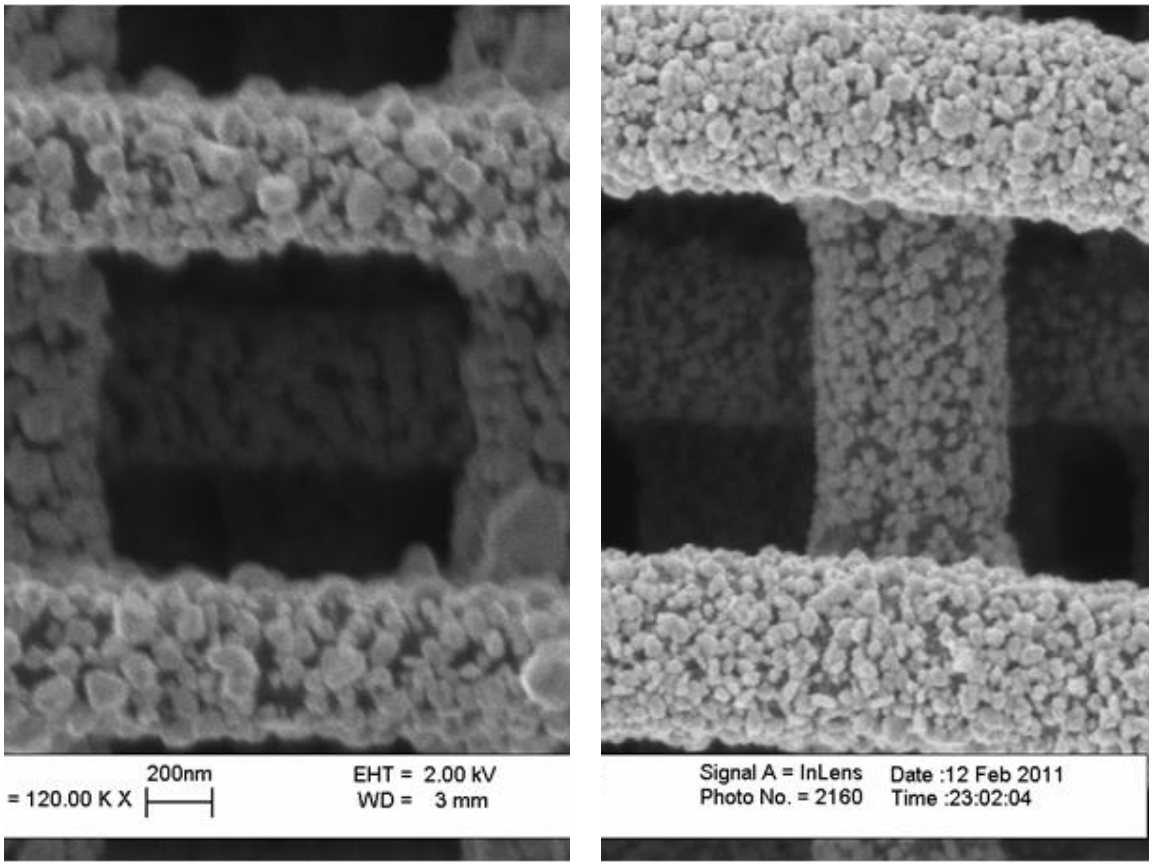

Figure 6.8. SEM images of PCs plated with silver nitrate and hydroquinone only (left), and plated with the addition of sodium citrate (right).

The deposition morphology with the addition of sodium citrate resulted in smaller and narrower size distribution of silver nanocoatings (~20 – 80 nm) as shown in Figure

6.8 (right), indicating the presence of citrate was effective in mediating the deposition kinetics. The incorporation of sodium citrate, however, resulted in *in situ* nanoparticles formation without the presence of seeds. This undesired side process was minimized by reducing the reactant concentrations to 1.33 mM $AgNO_3$, 3.33 mM sodium citrate and 0.33 mM hydroquinone, and by terminating the plating reaction prior to observable nanoparticles formation at ~ 6 minutes. The effect of silver deposition on the PCs' optical properties was monitored after each processing step and the resultant infrared spectra are shown below (Figure 6.9).

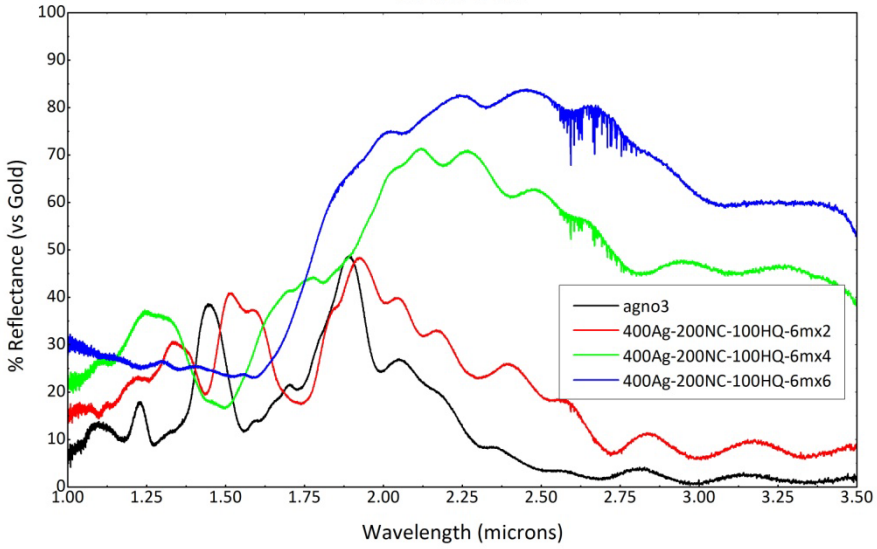

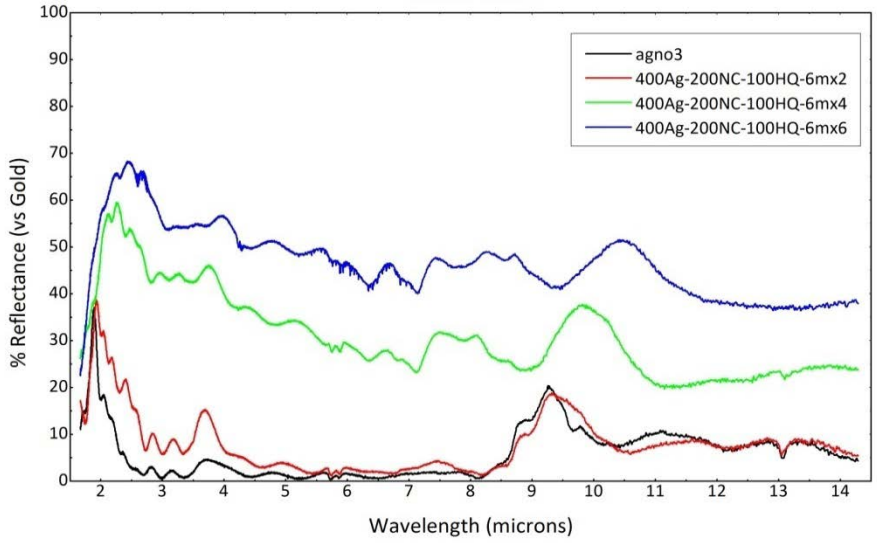

Figure 6.9. Infrared spectra of PCs and various degree of metallization in the near infrared (top) and mid infrared (bottom) from initial silver seeded PC to 2, 4, and 6 plating cycles.

Reflection spectra in the near infrared (Figure 6.9 top) indicated red-shifted stopband position upon the first 2 cycles of coating (from 1.45 to 1.60 μm), along with minimal changes to the mid infrared spectral range (Figure 6.9 bottom). The mid infrared reflectance showed rapid broadband enhancements between 2 and 4 cycles of coating, similar to the induction period observed in the coating of the optical flats (Figure 6.4). The difference between MPCs and optical flats is the formation of a step-like change to the reflectance, as demonstrated by the 6 cycles coated MPC at 1.75 μm. This step has been termed plasmonic band edge by Tal *et al* [14]. Whereas their reported plasmonic band edge was located at ~3.5 μm, the difference between their initial polymer stopband position (~4.3 μm) and ours (1.45 μm) led to our observation of this lattice-dependent plasmonic band edge at much shorter wavelength. Perfect MPCs behave like a plasmonic bandgap above this band edge, where broadband high reflectivities are expected as with bulk metals. The presence of organic impurities and the coating morphology (Figure 6.10) is likely the cause of lower reflectivities [14].

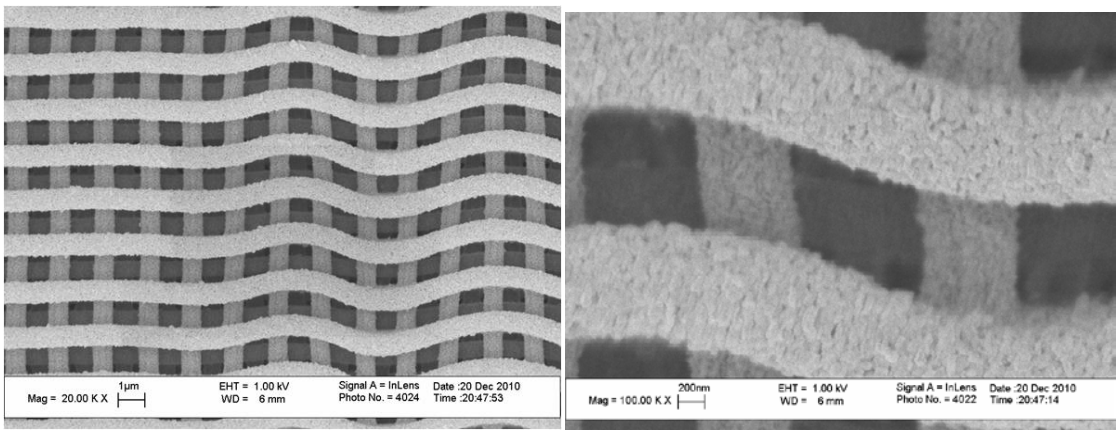

Figure 6.10. SEM images of the MPC, overview (left) and close up (right).

The deposited coating appeared to be granular in nature with a thickness ~ 140 nm, corresponding to approximately 23 nm per plating cycle. The extensive processing (each plating cycle involved 3× rinsing) led to deformations to the top most layers of the MPCs. This deformation to the MPC lattice could potentially alter the sharpness of the plasmonic band edge transition and the transmission below the band edge.

6.3.2.2 Effect of Surface Functionalization on Electroless Deposition

One approach to reduce the labor intensive processing necessary to achieve higher reflectivities is to improve the seeding coverage on the polymer surface such that less deposition is needed to fuse neighboring particles [23]. While the ethylenediamine modification can produce at most a 1:1 conversion of surface acrylates to amines, the amplification process (3.5 cycles) could potentially generate up to 2000 amines per acrylate.

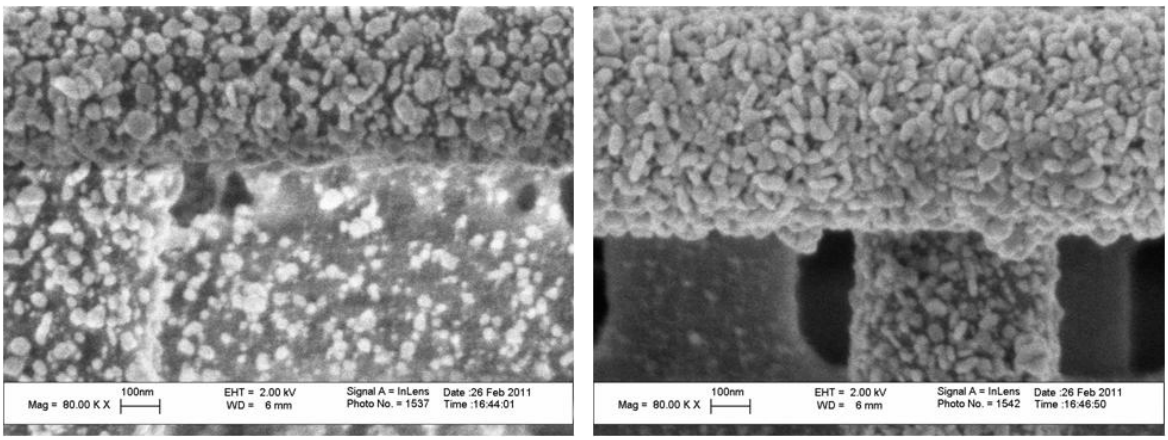

Figure 6.11. SEM images of PCs with surface modification using ethylenediamine (left) and 3.5× cycles of amplification (right). Samples were subjected to 3 cycles of electroless plating.

The difference in coating morphology resulting from the two different modification methods is demonstrated by SEM images in Figure 6.11. Ethylenediamine modified PC (Figure 6.11 left) resulted in lower degree of coverage than the amplified samples, the polymer surface on the top horizontal feature is still visible after 3 cycles of plating whereas the surface is completely covered in the amplified case. These results suggested the amplification process could potentially lead to a thinner continuous coating for localized plasmon resonance applications. Inhomogeneity in the coverage as a function of depths into the PCs was also evident from the SEM images, especially in the amplified sample where the surface coverage was significantly higher on the top layer (horizontal feature in the top half of the images) than the inner layers (vertical feature on the left). The results suggest several possible causes: 1) the mixing during electroless plating was insufficient, if reactants were unable to infiltrate into the pores of the PCs, the plating would be limited to the surface layers, or 2) the initial seeding was inefficient, reducing the number of nucleation sites for the electroless plating, or 3) the reaction rate was fast and the outermost surface of the PCs deplete a majority of the reactants as the solvent flow into the pores.

6.3.2.3 Improved Reactant Penetration with Infusion

Several mixing techniques were investigated in attempt to deliver the maximum amount of reactants into the interior of the PCs, from the initial stir bar mixing at 1200 rpm to vertical dipping (as in opal infiltration methods) to convection spinning [24], however all resulted in similar surface coverage and infrared spectra. Syringe pump infusion was found to be the most efficient when a flexible Teflon tubing was brought to close proximity (~100 μm) of the PCs at near normal angle. An additional benefit of this method was the hydrophobicity of the polymer PCs could be overcame by the directed flow, allowing the use of aqueous solutions for more favorable reduction chemistry.

In situ monitoring of seeding reaction under transmission optical microscope revealed an almost instantaneous color change of the sample from colorless to a brownish-yellow tint, indicating deposition of silver. This color change was completed within 15 seconds, after which no alteration was observed, indicating the amine sites have been saturated with silver. The infrared reflection spectra and the corresponding SEM images are shown in Figure 6.12.

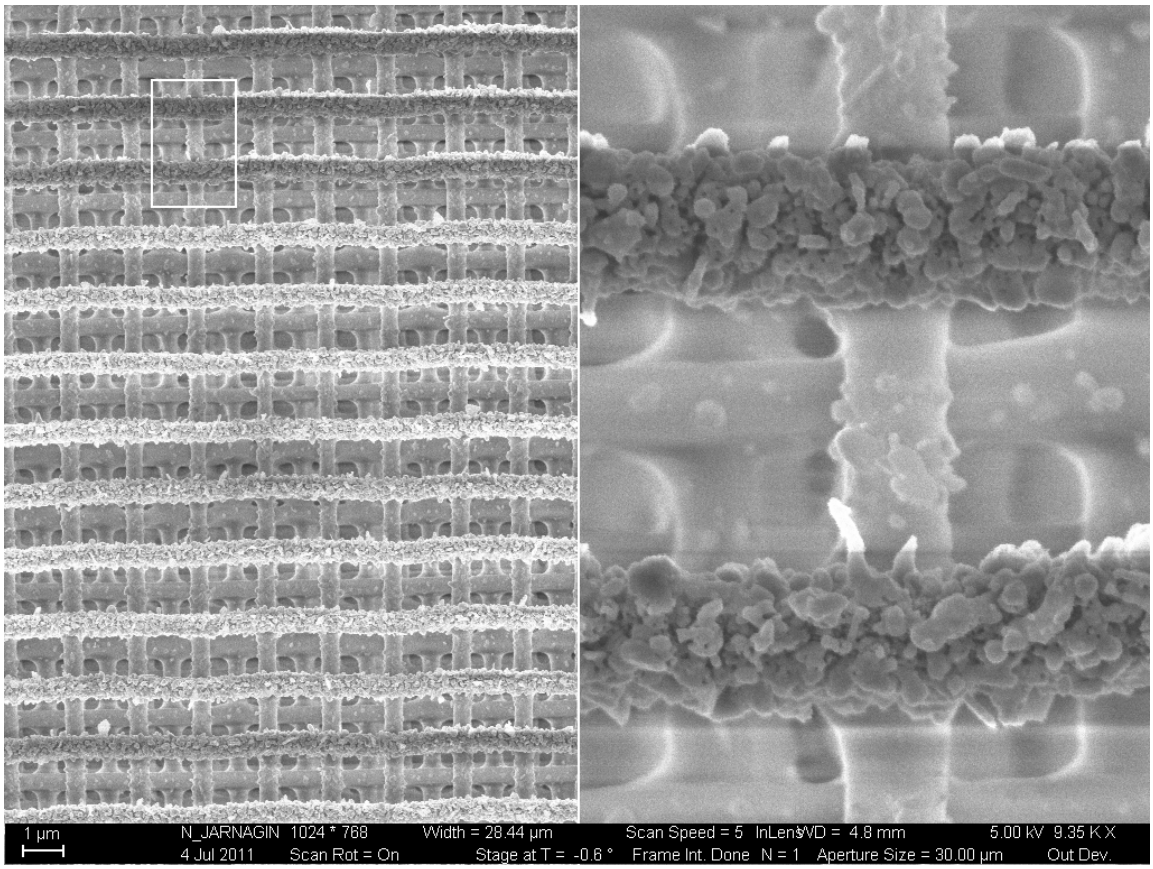

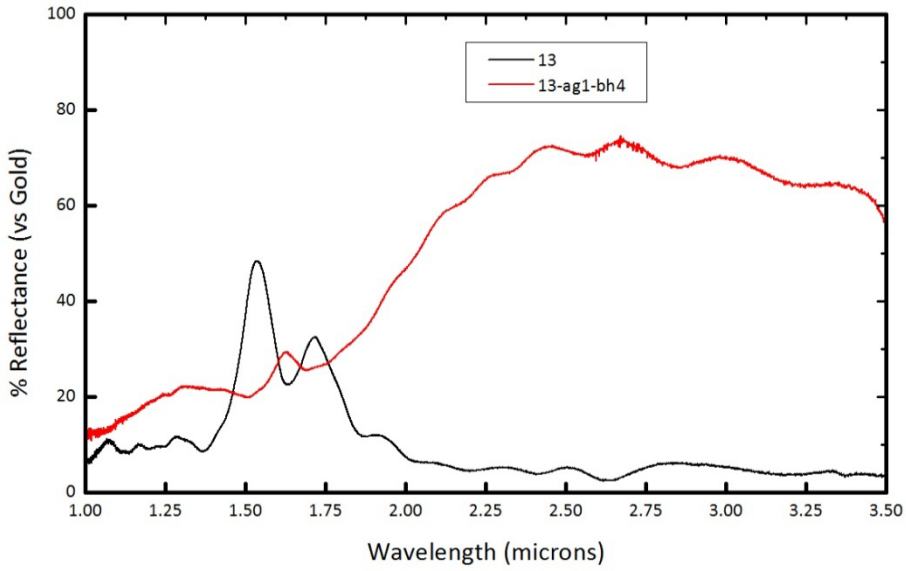

Figure 6.12. SEM image of a PC subjected to 2 cycles of silver nitrate and sodium borohydride with syringe pump infusion (2.5 minutes for each infusion) (top) and the infrared reflection spectra before and after the metal deposition (bottom).

Granular deposits at the top layer were evident from the SEM image, indicating the infusion time could be reduced. The reflection spectrum of this seeded PC exhibit similar intensities to samples prepared with 6 cycles of electroless plating using the previous conditions (Figure 6.9), indicating this method is significantly more effective in creating MPCs.

6.4 Conclusion

Photonic crystals with varying silver coating morphologies were achieved using two different deposition methodologies. Swelling-induced tin ion trapping in conjunction with commercial plating solution resulted in formation of sparse silver islands that exhibit wavelength-selective enhancement of up to 1.8× to photonic stopbands. Amine surface modification with silver nitrate seeding and subsequent electroless plating resulted in formation of highly silver coated photonic crystals that exhibit plasmonic band edge at 1.75 μm, even with the limited reactant penetration depth of ~3 layers. This result also suggests photonic crystals with fewer layers are needed to observe this plasmonic band edge. Investigation into the processing revealed traditional solution mixing methods were insufficient in delivering reactants into the hydrophobic micro-scaled pores of the polymer photonic crystals. Syringe pump infusion revealed rapid introduction of reactants and reaction under transmission imaging. This method produced MPCs that exhibited similar infrared reflectivity in less than 10 minutes of processing compared to hours with the previous methods. The reduced processing time also reduced deformations to the structures.

Further development into using syringe pump infusion with other processing steps, for example the amplification reactions and electroless plating could lead to improved morphologies of conformally coated metal photonic crystals with well-defined

plasmonic band edge to control infrared emission or transmission. Characterization of the samples under transmission electron microscope would provide additional information of the surface coverage when the metal coating at the seeding stage, eliminating the need for sputter coating or electroless plating needed for SEM. Substitution of the electroless plating with the binding of nanoparticles, with well-defined size and shape, could simplify the characterization process by removing the diffusion and kinetics issues to optimize stopband reflectivity for sensing applications.

REFERENCES

1. S. Y. Lin, J. G. Fleming, Z. Y. Li, I. El-Kady, R. Biswas, and K. M. Ho, "Origin of absorption enhancement in a tungsten, three-dimensional photonic crystal," J. Opt. Soc. Am. B **20**, 1538-1541 (2003).

2. S.-Y. Lin, J. G. Fleming, E. Chow, J. Bur, K. K. Choi, and A. Goldberg, "Enhancement and suppression of thermal emission by a three-dimensional photonic crystal," Physical Review B **62**, R2243 (2000).

3. D. F. Sievenpiper, M. E. Sickmiller, and E. Yablonovitch, "3D Wire Mesh Photonic Crystals," Physical Review Letters **76**, 2480 (1996).

4. E. Özbay, B. Temelkuran, M. Sigalas, G. Tuttle, C. M. Soukoulis, and K. M. Ho, "Defect structures in metallic photonic crystals," Applied Physics Letters **69**, 3797-3799 (1996).

5. J. G. Fleming, S. Y. Lin, I. El-Kady, R. Biswas, and K. M. Ho, "All-metallic three-dimensional photonic crystals with a large infrared bandgap," Nature **417**, 52-55 (2002).

6. W. Haske, V. W. Chen, J. M. Hales, W. Dong, S. Barlow, S. R. Marder, and J. W. Perry, "65 nm feature sizes using visible wavelength 3-D multiphoton lithography," Opt. Express **15**, 3426-3436 (2007).

7. B. H. Cumpston, S. P. Ananthavel, S. Barlow, D. L. Dyer, J. E. Ehrlich, L. L. Erskine, A. A. Heikal, S. M. Kuebler, I. Y. S. Lee, D. McCord-Maughon, J. Qin, H. Rockel, M. Rumi, X.-L. Wu, S. R. Marder, and J. W. Perry, "Two-photon polymerization initiators for three-dimensional optical data storage and microfabrication," Nature **398**, 51-54 (1999).

8. M. Deubel, G. von Freymann, M. Wegener, S. Pereira, K. Busch, and C. M. Soukoulis, "Direct laser writing of three-dimensional photonic-crystal templates for telecommunications," Nat Mater **3**, 444-447 (2004).

9. M. S. Rill, C. Plet, M. Thiel, I. Staude, G. von Freymann, S. Linden, and M. Wegener, "Photonic metamaterials by direct laser writing and silver chemical vapour deposition," Nat Mater **7**, 543-546 (2008).

10. R. A. Farrer, C. N. LaFratta, L. Li, J. Praino, M. J. Naughton, B. E. A. Saleh, M. C. Teich, and J. T. Fourkas, "Selective Functionalization of 3-D Polymer Microstructures," Journal of the American Chemical Society **128**, 1796-1797 (2006).

11. F. Formanek, N. Takeyasu, T. Tanaka, K. Chiyoda, A. Ishikawa, and S. Kawata, "Three-dimensional fabrication of metallic nanostructures over large areas by two-photon polymerization," Opt. Express **14**, 800-809 (2006).

12. Y. S. Chen, A. Tal, D. B. Torrance, and S. M. Kuebler, "Fabrication and Characterization of Three-Dimensional Silver-Coated Polymeric Microstructures," Advanced Functional Materials **16**, 1739-1744 (2006).

13. Y.-S. Chen, A. Tal, and S. M. Kuebler, "Route to Three-Dimensional Metallized Microstructures Using Cross-Linkable Epoxide SU-8," Chemistry of Materials **19**, 3858-3860 (2007).

14. A. Tal, Y.-S. Chen, H. E. Williams, R. C. Rumpf, and S. M. Kuebler, "Fabrication and characterization of three-dimensional copper metallodielectric photonic crystals," Opt. Express **15**, 18283-18293 (2007).

15. V. Mizeikis, S. Juodkazis, R. Tarozaite, J. Juodkazyte, K. Juodkazis, and H. Misawa, "Fabrication and properties of metalo-dielectric photonic crystal structures for infrared spectral region," Opt. Express **15**, 8454-8464 (2007).

16. S. M. Kuebler, M. Rumi, T. Watanabe, K. Braun, B. H. Cumpston, A. A. Heikal, L. L. Erskine, S. Thayumanavan, and J. W. Perry, "Optimizing Two-Photon Initiators and Exposure Conditions for Three-Dimensional Lithographic Microfabrication," Journal of Photopolym. Sci. Technol **14**, 657-668 (2001).

17. E. Müh, J. Marquardt, J. E. Klee, H. Frey, and R. Mülhaupt, "Bismethacrylate-Based Hybrid Monomers via Michael-Addition Reactions," Macromolecules **34**, 5778-5785 (2001).

18. M. R. Weatherspoon, M. B. Dickerson, G. Wang, Y. Cai, S. Shian, S. C. Jones, S. R. Marder, and K. H. Sandhage, "Thin, Conformal, and Continuous SnO2 Coatings on Three-Dimensional Biosilica Templates through Hydroxy-Group Amplification and Layer-By-Layer Alkoxide Deposition," Angewandte Chemie International Edition **46**, 5724-5727 (2007).

19. K. Miyoshi, S. Fujikawa, and T. Kunitake, "Fabrication of nanoline arrays of noble metals by electroless plating and selective etching process," Colloids and Surfaces A: Physicochemical and Engineering Aspects **321**, 238-243 (2008).

20. S. T. Gentry, S. J. Fredericks, and R. Krchnavek, "Controlled Particle Growth of Silver Sols through the Use of Hydroquinone as a Selective Reducing Agent," Langmuir **25**, 2613-2621 (2009).

21. A. Henglein, and M. Giersig, "Formation of Colloidal Silver Nanoparticles: Capping Action of Citrate," The Journal of Physical Chemistry B **103**, 9533-9539 (1999).

22. D. Buso, E. Nicoletti, J. Li, and M. Gu, "Engineering the refractive index of three-dimensional photonic crystals through multilayer deposition of CdS films," Opt. Express **18**, 1033-1040 (2010).

23. K. R. Brown, L. A. Lyon, A. P. Fox, B. D. Reiss, and M. J. Natan, "Hydroxylamine Seeding of Colloidal Au Nanoparticles. 3. Controlled Formation of Conductive Au Films," Chemistry of Materials **12**, 314-323 (1999).

24. K. H. Sandhage, and G. J. Yurek, "Direct and Indirect Dissolution of Sapphire in Calcia–Magnesia–Alumina–Silica Melts: Dissolution Kinetics," Journal of the American Ceramic Society **73**, 3633-3642 (1990).

CHAPTER 7

PHOTONIC STOPBAND ENGINEERING WITH CONFORMAL TITANIA COATING

Collaboration with Dr Yunnan Fang from Dr Ken Sandhage's Group

Department of Materials Science and Engineering

Georgia Institute of Technology, Atlanta, GA 30332

7.1 Introduction

Multiphoton photolithography (MPL) has proven to be versatile technique for rapid prototyping of microstructures [1]. Feature sizes ranging from tens of nanometers to microns could be produced using a focused femtosecond laser source to induce photocrosslinking or photodissociation in a small volume inside a photoresist or resin [2-5]. One inherent property of multiphoton excitation is that it provides the unique capability of a finite Z resolution whereby any random 3D pattern can be fabricated in one step as supposed to the layer-by-layer approach utilized in conventional UV photolithography.

MPL has been used to fabricate photonic crystals (PCs) that have various lattice parameters which gives rise to photonic stopbands ranging from the visible to infrared spectrum [6, 7]. One major task of the research of MPL is to achieve a complete photonic bandgap, calculations revealed a refractive index of ~ 2.5-2.7 is necessary for complete bandgap with woodpile type PCs [8, 9]. However, a majority of the published works have been based on acrylates or epoxys as the starting materials give the relatively low refractive index (~ 1.5 – 1.6), preventing the observation of complete bandgaps.

There have been several reports in literature using higher refractive index materials, such as organic-inorganic oxide complexes [10, 11] or Chalcogenide glasses such as As_2S_3 (n = 2.45) [9]. The changes in the materials chemistries, however, have led to reductions in structural qualities and aberrations. An alternative approach that preserves the fabrication methodology is infiltration of the low refractive index template with high index semiconductors or metal oxides. These processes have been widely explored in the fabrication of inverse opal PCs, for example titania (TiO_2, n = 2.2-2.7) infiltration by atomic layer deposition (ALD) [12], selenium (n = 2.5) by melt processing at 275ºC [13], cadmium selenide (n = 2.5) by electroplating [14], amorphous silicon (n = 3.5) by chemical vapor deposition (CVD) [15]. Most of these processes require high temperature processing conditions that are not compatible with the thermal stability of polymers and none are selective to the structure only. A few of these techniques have been adopted for polymer PCs fabricated, such as backfilling with liquid-phase titania [16], and surfacing coating with gas-phase titania ALD [17] or silicon CVD on silica inverted PC [18] techniques. Although these processes were able to generate higher index structures, the alteration to the structure design, non selective blanket coverage, the complex and extensive processing hinders their applicability.

Titania is an attractive material for increasing the refractive index of PCs due to its processibility as a sol-gel material. Titania possess different refractive indices depending on their phase, amorphous sol-gel derived coating exhibits n ~2.0 - 2.2 [19], anatase n = 2.5 [20], and rutile n = 2.45-2.71 at 1.5 μm [21]. The lower refractive index amorphous or anatase phases can be converted to rutile by high temperature treatment. Bisawa et al. [22] performed simulation on titania (n = 2.7) coated polyurethane (n = 1.5) woodpile PCs and determined enhancements to stopband intensities and complete photonic bandgap is achievable from the coated structures. Buso et al. [23] have recently demonstrated the effect of high index cadmium sulfide coating (n = 2.3) on low index PCs. Although the refractive index and the quality of the coating was insufficient to

produce a complete bandgap, a 17% enhancement of the original stopband intensity was observed, accompanied by red-shifted stopband positions.

This chapter focuses on the conformal coating using titania, with emphasis on its optical effect on PCs fabricated using MPL. A wet chemical, surface sol-gel approach was employed to apply a shape-preserving, conformal titania coating onto polymeric PCs fabricated from typical acrylate monomers. This titania coating was doped with tin oxide, which has been demonstrated to induce rutile titania formation at much lower sintering temperatures (450ºC vs 900ºC without dopant) [24], to improve processing compatibility with the PC templates. A variety of lattice parameters for the PCs were explored to position the photonic stopband at various wavelengths to investigate the effect of the increased refractive index due to the titania coating. Comparison of the infrared spectra collected prior to and after coating reveals the expected red-shifts due to increased refractive index. High temperature sintering of the titania coated PCs resulted in removal of the polymer template and the titania shell retained good structural quality with the presence of a stopband.

7.2 Experiment

Photosensitive resin was comprised of a 1:1 ratio of triacrylate monomers SR9008 and SR368 (Sartomer). The inhibitor (4-methoxyphenol, Aldrich, 99%) level in the resin was raised by 0.1 % of the total resin weight to prevent thermal crosslinking during sample preparation. The mixture was heated to 50ºC while stirring to obtain a clear liquid. *E,E*-1,4-*bis*[4-(*N,N*-di-*n*-butylamino)styryl]-2,5-dimethoxybenzene (DABSB) (Figure 7.1) had been shown to be extremely effective [25] as a multiphoton radical initiator and was employed at 0.1 wt% relative to the resin matrix.

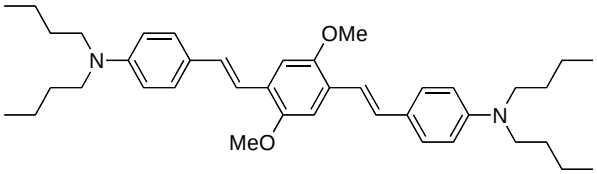

Figure 7.1. Molecular structure of photoinitiator DABSB.

The resin was injected into a fluid cell, formed by the microscope slide substrate and a #0 coverslip, separated by a 100 μm thick Teflon spacer (Aldrich). Glass microscope slides were cleaned with acetone (Aldrich, spectrophotometric grade), treated with 10 vol% 3-(trimethoxysilyl)propyl methacrylate (Aldrich, 98%) in ethanol (Aldrich, 200 proof, anhydrous, 99.5%) and then baked on a hot plate at 130°C for three cycles to promote the adhesion of acrylic structures to the substrate. Post fabrication development was carried out using methyl isobutyl ketone (Aldrich, spectrophotometric grade) to dissolve and remove unexposed material.

The instrumentation, design and fabrication of microstructures have been described in detail in an chapter 2. For this study, PC lattice parameters were varied with line (xy) spacing from 2 to 4 μm and layer (z) spacing from 0.8 to 1.1 μm to produce a range of stopband positions for investigation of the effect from the applied titania coating.

Two approaches were applied to achieve titania coating on the fabricated polymeric PCs. In the first approach, the sol-gel processing for titania coating was performed by Dr Yunnan Fang in Dr Ken Sandhage's laboratory. Samples were incubated alternatively with 5 wt% of *tris*(2-aminoethyl)amine (Fluka, 98%) and 5 wt% of dipentaerythritol *penta*-/*hexa*-acrylate (Sigma Aldrich) for four cycles to amplify the number of surface function groups via Michael addition [26]. Samples were then subjected to 60 cycles of TiO_2/SnO_2 deposition by surface sol-gel process using an isopropanolic solution of titanium (IV) isopropoxide (Alfa Aesar, 99%) containing 10

wt% of tin (IV) isopropoxide (Chemat Technology, 98%) as the precursor [24]. An illustration is shown below in Figure 7.2.

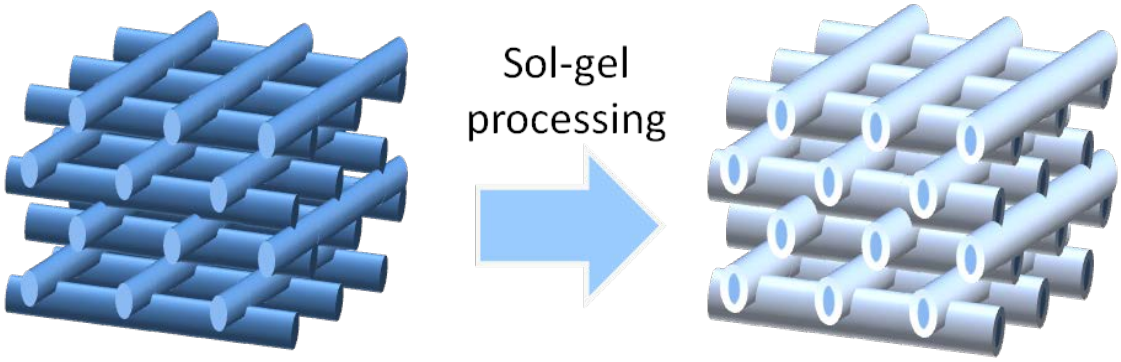

Figure 7.2. Illustration of titania deposition on the acrylate PC.

For the alternative, modified approach, the PC samples were treated with an amine-terminated polyacrylic acid (Mn=2,400) (Polymer Source) in ethanol to generate negative charges on the polymer surface. Protamine sulfate (Sigma-Aldrich) in a sodium phosphate buffer (pH 7.5) containing 5 vol% ethanol was then applied to electrostatically bind protamine onto the sample surface. Finally, a sodium phosphate buffer solution (5 vol% ethanol) of titanium(IV) *bis*(ammonium lactato) dihydroxide (Alfa Aesar) and a 20 mol% Na_2SnO_3 (Alfa Aesar) was applied to the protamine coated structures to form the titania shell.

Infrared reflection spectra of the stopband of PCs were collected using a Fourier-transformed infrared microscope spectrometer (Agilent, FTS7000-UMA600) before and after the titania deposition. PCs were measured with a 15× Cassegrain objective, 80 × 80 μm^2 aperture, and a gold mirror as the background. PC structures and titania coatings were analyzed with a field emission scanning electron microscope (LEO/Zeiss Electron Microscopy, 1530 FE SEM). Cross sectional views were acquired by focused ion beam etching (FEI, Nova Nanolab 200).

7.3 Results and Discussion

7.3.1 Coating Processing Optimization

MPL dosing studies were first performed to determine the polymer rod feature size required to generate high quality PCs across the range of lattice parameters (line (xy) spacing from 2 to 4 μm and layer (z) spacing from 0.8 to 1.1 μm). Rod a width of 600 nm was used to build PCs discussed in this section. The titania conformal coating process produced ~ 1 nm per coating cycle. The range of lattice parameters used for the PCs created a wide range of variability in the quality of the final coated structures. The SEM images indicated structures with largest layer spacing experienced the most distortion at the surface, due to lower degree of overlap between layers and hence less mechanical stability during solution processing. PCs with smaller line spacing were less resolved due to smaller openings for solvent to transport reactants in and out, for example the 2 μm line spacing PC in Figure 7.3. The best quality coated PCs has line spacing of 4 μm and 0.8 μm layer spacing as shown in Figure 7.3.

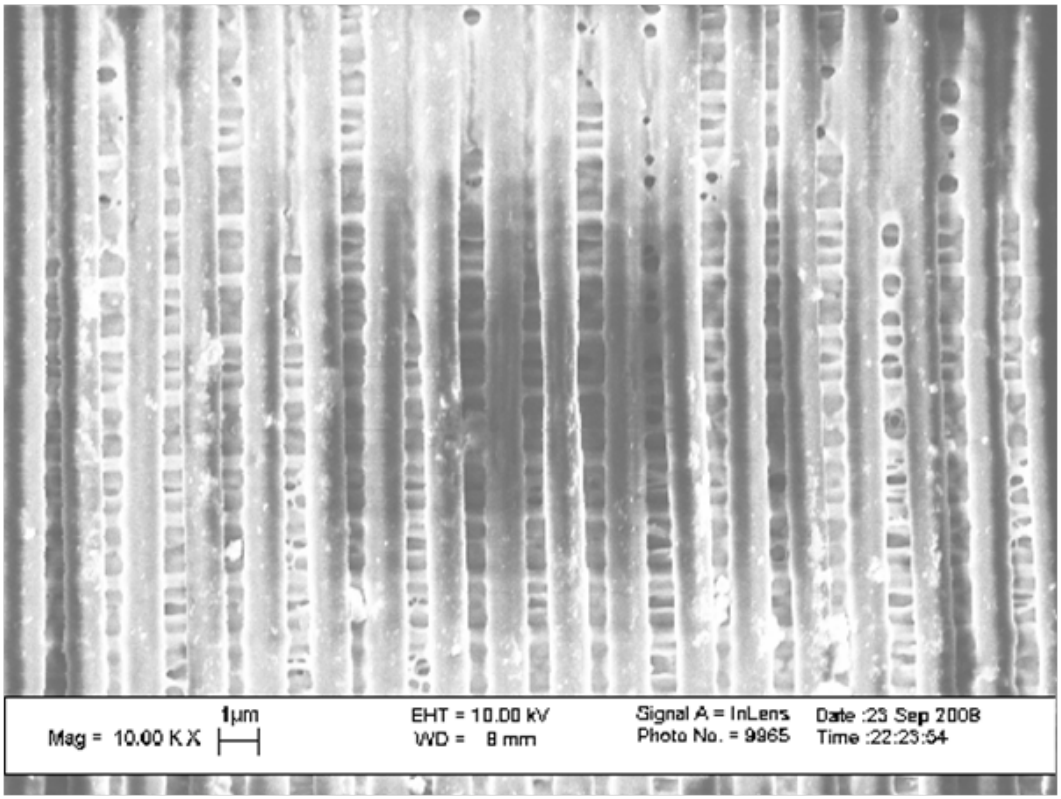

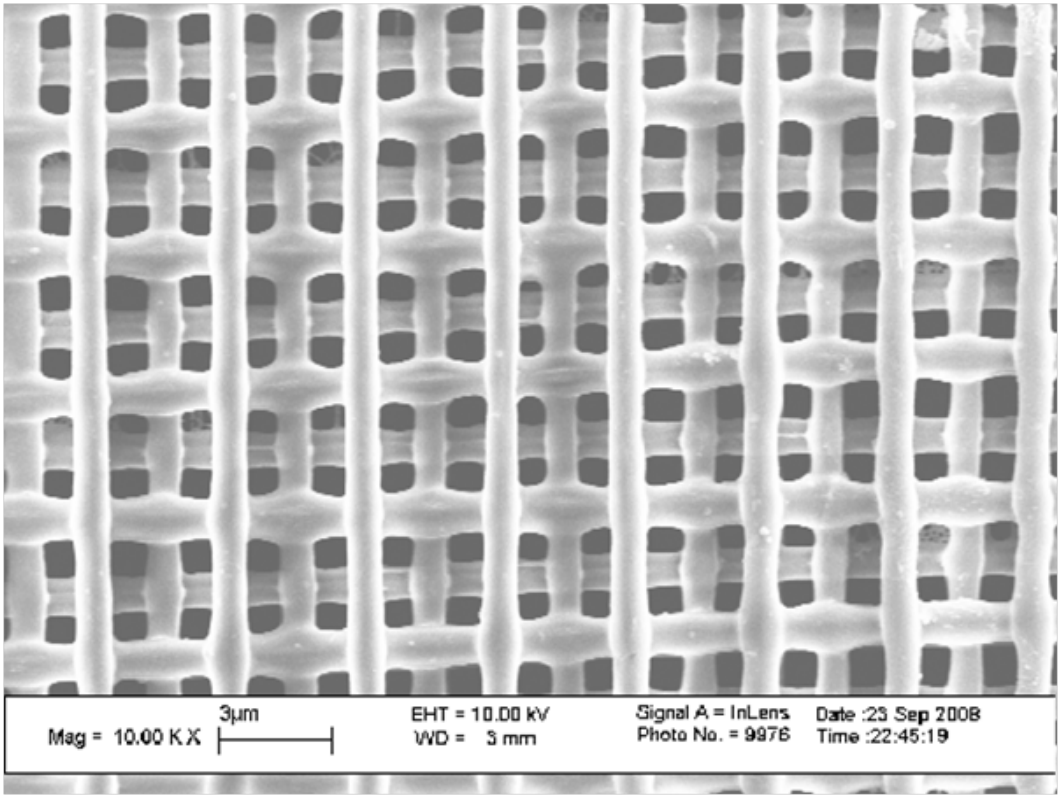

Figure 7.3. Titania coated PCs with lattice parameters of 2.0 µm (top) 4.0 µm (bottom) line and 0.8 µm layer spacing.

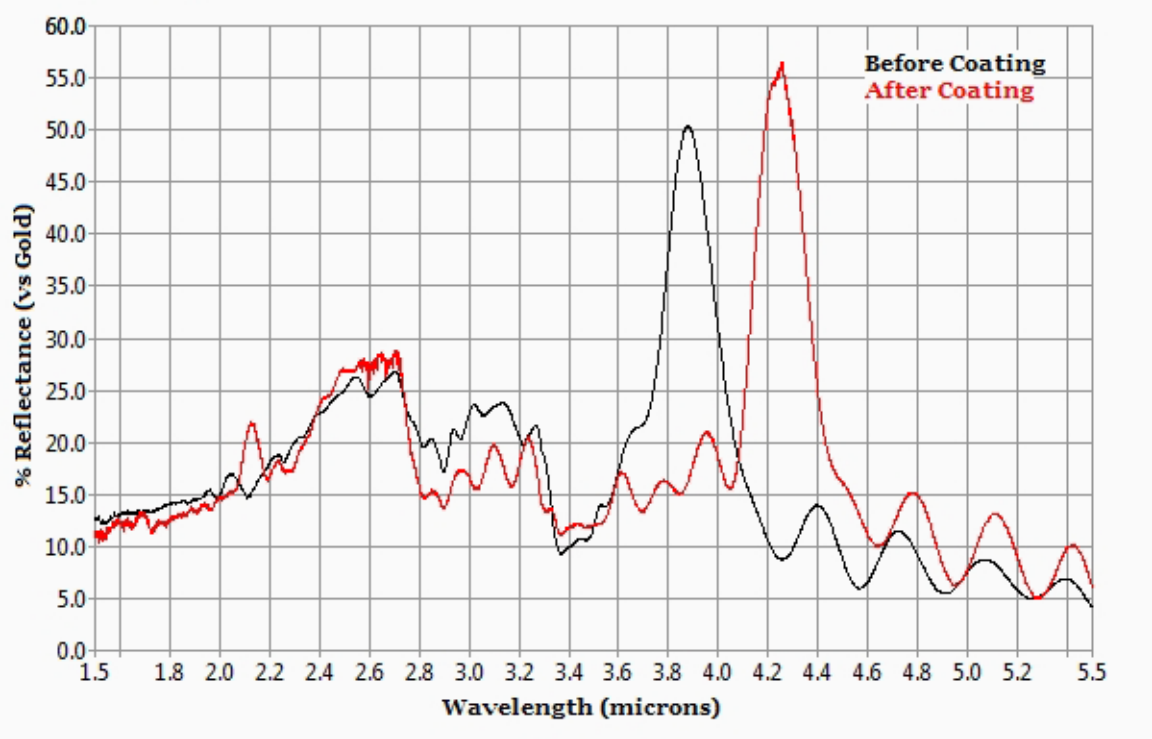

Figure 7.4. Infrared reflection spectra of a PC before and after titania coating (60 nm thickness).

Initial infrared reflection results indicated the expected red-shift of the photonic stopbands due to the increased refractive index from the deposited titania [23]. Varying degrees of red-shifts were observed (from 200 to 600 nm) for the various PC lattices, a set of representative spectra is shown in Figure 7.4. A trend of larger shifts corresponding to larger layer spacings within each set of line spacings. The presence of material absorption bands (OH, CH and C=O) created some ambiguities in determining the exact location of some stopbands. Distortions to the PCs during the coating process and the incomplete removal of reactive species due to this distortion may also alter the actual stopband positions and intensities. Tabulated results on the stopband positions and the reflectance with respect to the lattice parameters are shown in Table 7.1.

Table 7.1. Stopband positions measured for various lattice parameters before (BC) and after coating (AC), all units in μm.

Line Spacing	Layer Spacing	Position (BC)	Position (AC)	Shift (AC-BC)
2	0.8	3.198	3.661	0.463
2	0.9	3.879	4.256	0.377
2	1	4.11	4.616	0.506
2	1.1	4.605	5.004	0.399
2.5	0.8	3.308	3.67	0.362
2.5	0.9	3.972	4.348	0.376
2.5	1	4.09	4.69	0.6
2.5	1.1	4.585	4.96	0.375
3	0.9	3.86	4.078	0.218
3	1	4.256	4.53	0.274
3	1.1	4.506	4.751	0.245
4	0.8	3.154	3.309	0.155
4	0.9	3.719	4.017	0.298
4	1	4.062	4.684	0.622
4	1.1	4.382	4.983	0.601

In order to further increase the refractive index of the titania coating, a high temperature treatment at 450°C was applied to convert the titania from amorphous to rutile phase [24]. At these high temperatures however, both the volatilization of the polymer template and the reduction in the coating volume led to large distortion to the lattice as shown in the SEM image in Figure 7.5.

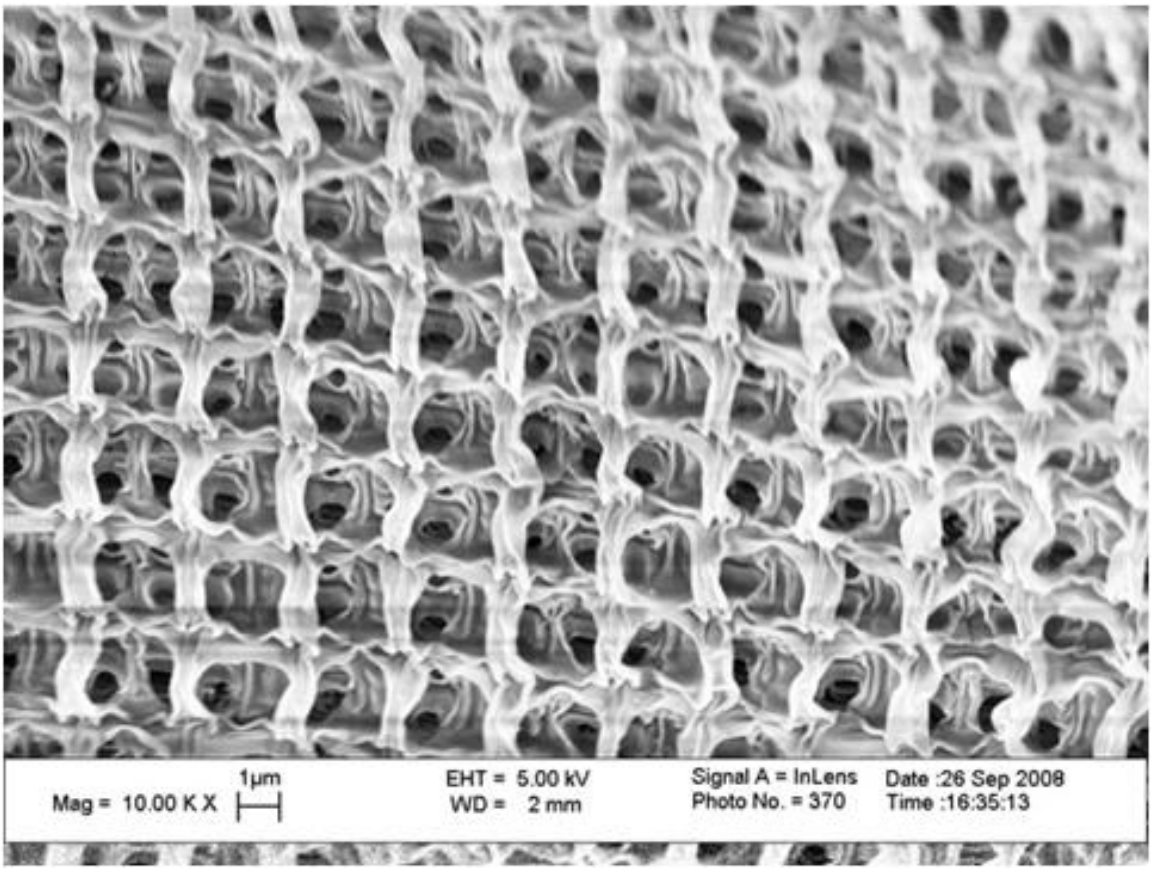

Figure 7.5. SEM of titania shell after polymer PC template removal.

Although the long range periodicity was lost and the structure delaminated from the substrate, SEM analysis revealed several microdomains that retained local periodicity in these post-sintered PC titania shell (Figure 7.5). This result indicated the coating process was successfully applied to the polymeric template, however the feature size and lattice parameters need to be scaled down to minimize the amount of volatile organics and improve mechanical rigidity of the titania shell.

7.3.2 PC Lattice Optimization

Modified PC with scale-downed lattice and feature sizes resulted in polymeric templates with better structural rigidity while retaining large openings for reactant

indiffusion. Top view and fractured cross section SEM of a PC with 2.8 µm line spacing and 1.0 µm layer spacing is shown in the Figure 7.6a.

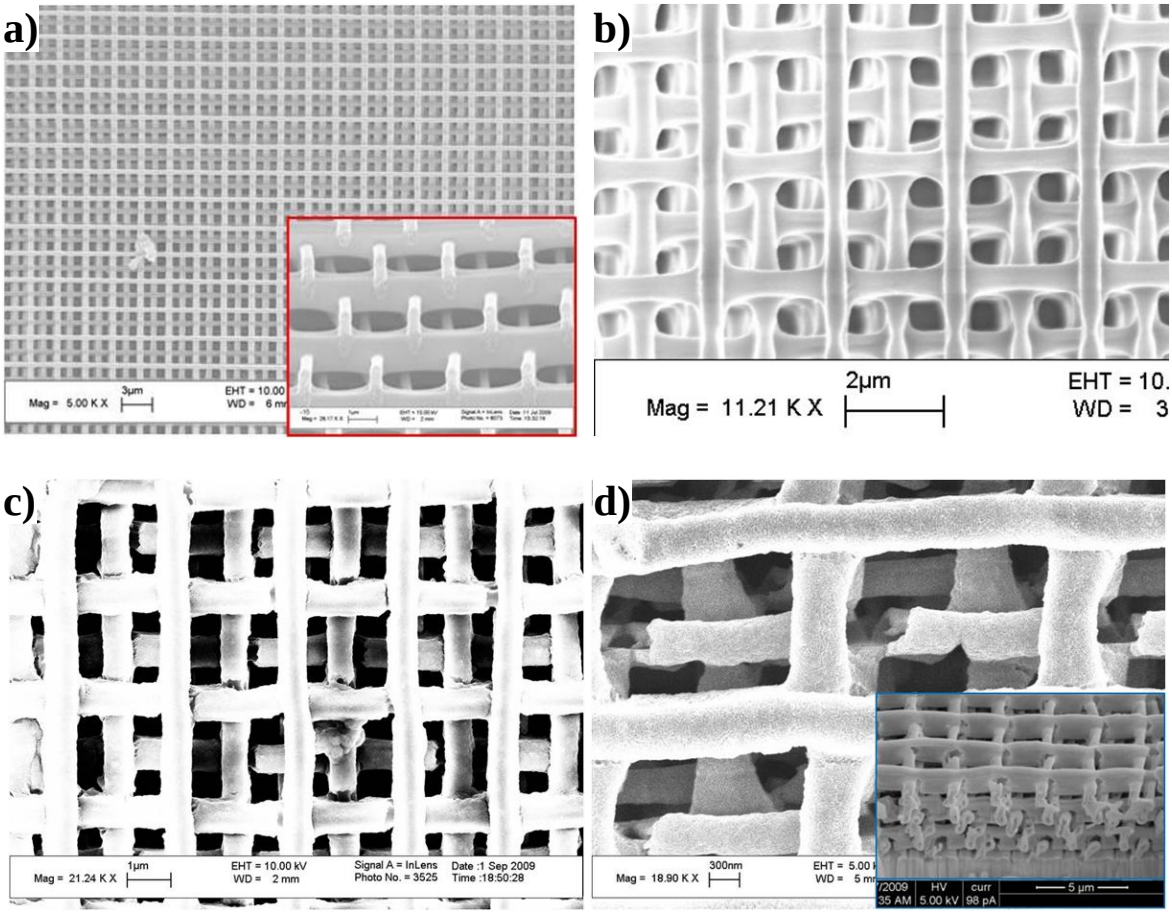

Figure 7.6. SEM of the coating process from the initial polymer template (a) and a fractured cross section view (inset), with 7 cycles of titania coating (b), with an additional 7 cycles (14 total) of coating (c), and the titania shell with the polymer template removed (d) and the FIB milled cross section (inset).

The modified, electrostatic, coating process was adopted to increase the titania deposition per sol-gel cycle (~10× the previous method). Rod width analysis of the SEM images indicated an average of 8 nm thick titania shell was applied for each cycle of coating. When the coating thickness is low, as in the 7 cycle-coated structure, the coating appeared smooth and continuous (Figure 7.6b). In the case of thicker coating (14 cycles),

cracks along the connection points within the PC became apparent (Figure 7.6c). The template removal process led to densification of the titania shell, resulting in a final shell thickness of 80 nm. While the gap distance in the cracks became more severe as the titania shell structure shrank (as shown in Figure 7.6d), the overall structure remained intact as observed in the FIB etched cross section (inset). This result is markedly improved from the previous experiments.

7.3.3 Optical Characterization of Improved Titania Coated PCs

Infrared spectra (Figure 7.7) were acquired at each step of the coating process to monitor the evolution of the optical properties. The polymer template exhibit stopband at shorter wavelengths than the last set of results due to the reduced polymer fill fraction. A systematic shift of the original stopband positions was observed, as demonstrated by the feature originating from 2.0 μm in the polymeric template (Figure 7.7a). This stopband shifted to 2.03 μm with 7 coating cycles (Figure 7.7b) and to 2.07 μm with 14 cycles (Figure 7.7c). This red-shift is consistent with the increased coating index associated with the additional titania deposition, as observed by Buso in apply cadmium sulfide coatings on polymer templates [23]. Although the high-temperature treated structure showed cracks and shrinkage, a high degree of periodicity was retained and the resultant stopband was observed at 1.97 μm (Figure 7.7d). This stopband shift in the reverse direction was resulted from a combination of the reduction of refractive index (due to the removal of polymeric core) and the shrinkage of the PC (due to the conversion from amorphous to crystalline titania).

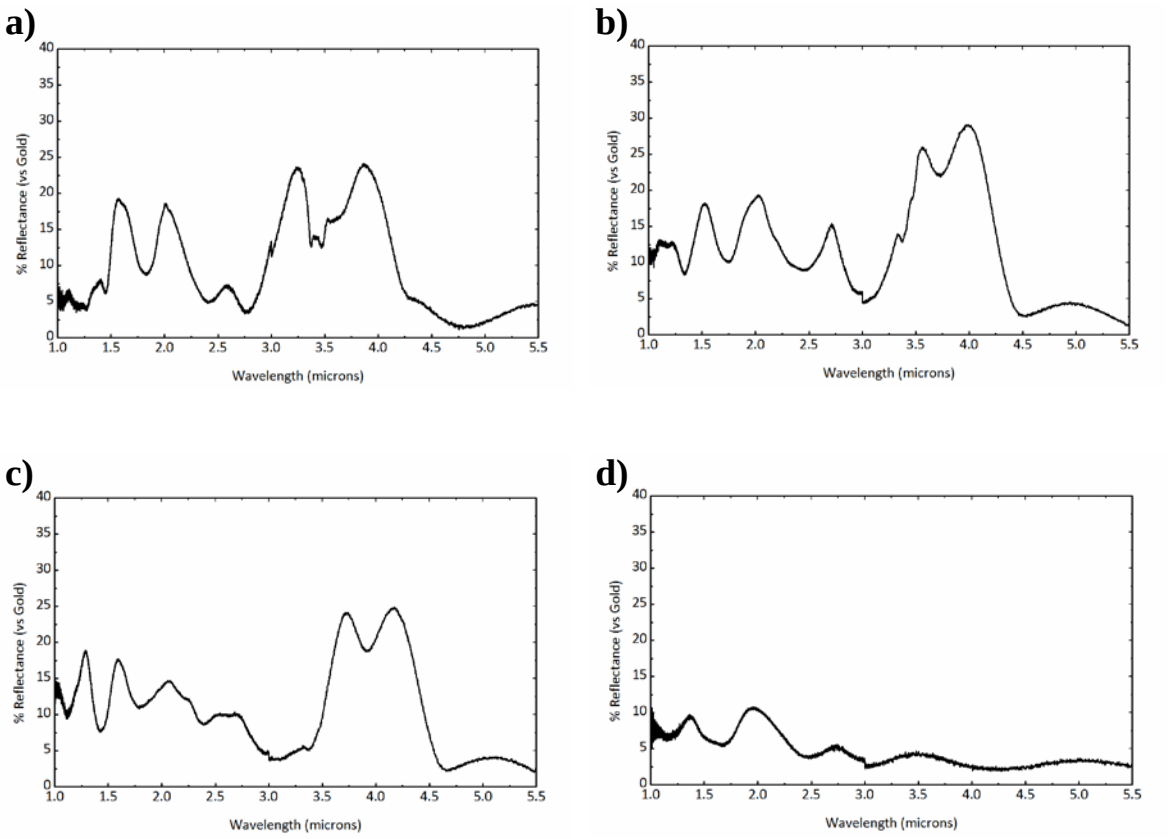

Figure 7.7. Infrared reflection spectra of the coating process from the initial polymer template (a), with 7 cycles of titania coating (b), with an additional 7 cycles (14 total) of coating (c), and the titania shell with the polymer template removed (d).

Band structure calculations were performed using the lattice parameters obtained through cross section images (Figure 7.6 (a, inset)) as the basis (RSoft, BandSOLVE). A series of increasing material index was used to simulate the stopband position and gap size while maintaining the overall size of the features. Whereas no complete bandgap was evident at the maximum achievable index of 2.5 for titania, the width of the stopband increases with increasing index, as shown in Figure 7.8, suggesting enhanced stopband performance could be expected even with moderate coating thicknesses.

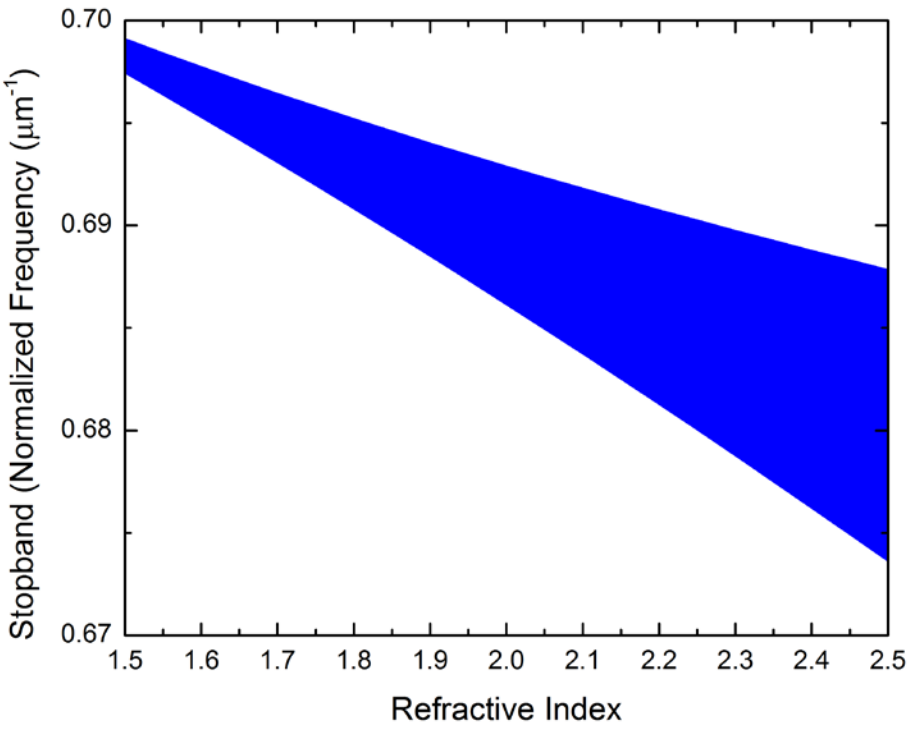

Figure 7.8. Simulation result showing decreasing stopband frequencies (red shifting wavelengths) with increased refractive index while lattice parameters and feature dimensions remained fixed.

The simulation also indicated the stopband observed at 2 μm is a higher order band and not fundamental stopband. The calculated stopband position was closer to the 4 μm feature in the infrared spectra, which also red-shifted with increasing coating thickness accompanied by a modest stopband enhancement (~5% vs Gold).

7.4 Conclusion

This surface sol-gel method had been demonstrated as a viable method to produce shape preserving replicas of the original polymeric template. The combination of PCs fabricated by MPL and this surface sol-gel method resulted in systematic increase in refractive index which led to red-shifting of the photonic stopband and higher order bands. Modification of the PC lattice parameters and the improved coating chemistry

resulted in marked improvement to the final titania shell structures. Additional simulation and tuning the fundamental stopband position into the near infrared region is needed to place the resultant stopband in the infrared region for telecommunication applications. Further reduction of the feature size, achievable via visible MPL [3] or STED-based MPL [6], and thicker titania coating will result in higher titania to polymer ratio, which will further improve the mechanical stability of the titania shell due to less organics removal during the sintering process.

REFERENCES

1. S. Kawata, H.-B. Sun, T. Tanaka, and K. Takada, "Finer features for functional microdevices," Nature **412**, 697-698 (2001).

2. B. H. Cumpston, S. P. Ananthavel, S. Barlow, D. L. Dyer, J. E. Ehrlich, L. L. Erskine, A. A. Heikal, S. M. Kuebler, I. Y. S. Lee, D. McCord-Maughon, J. Qin, H. Rockel, M. Rumi, X.-L. Wu, S. R. Marder, and J. W. Perry, "Two-photon polymerization initiators for three-dimensional optical data storage and microfabrication," Nature **398**, 51-54 (1999).

3. W. Haske, V. W. Chen, J. M. Hales, W. Dong, S. Barlow, S. R. Marder, and J. W. Perry, "65 nm feature sizes using visible wavelength 3-D multiphoton lithography," Opt. Express **15**, 3426-3436 (2007).

4. S. M. Kuebler, B. H. Cumpston, S. Ananthavel, S. Barlow, J. E. Ehrlich, L. L. Erskine, A. A. Heikal, D. McCord-Maughon, J. Qin, H. Roeckel, M. C. Rumi, S. R. Marder, and J. W. Perry, "Three-dimensional microfabrication using two-photon-activated chemistry," (SPIE, 2000), pp. 97-105.

5. L. Li, R. R. Gattass, E. Gershgoren, H. Hwang, and J. T. Fourkas, "Achieving λ/20 Resolution by One-Color Initiation and Deactivation of Polymerization," Science **324**, 910-913 (2009).

6. J. Fischer, and M. Wegener, "Three-dimensional direct laser writing inspired by stimulated-emission-depletion microscopy [Invited]," Opt. Mater. Express **1**, 614-624 (2011).

7. M. Deubel, G. von Freymann, M. Wegener, S. Pereira, K. Busch, and C. M. Soukoulis, "Direct laser writing of three-dimensional photonic-crystal templates for telecommunications," Nat Mater **3**, 444-447 (2004).

8. J. Serbin, A. Ovsianikov, and B. Chichkov, "Fabrication of woodpile structures by two-photon polymerization and investigation of their optical properties," Opt. Express **12**, 5221-5228 (2004).

9. S. Wong, M. Deubel, F. Pérez-Willard, S. John, G. A. Ozin, M. Wegener, and G. von Freymann, "Direct Laser Writing of Three- Dimensional Photonic Crystals with a Complete Photonic Bandgap in Chalcogenide Glasses," Advanced Materials **18**, 265-269 (2006).

10. R. Houbertz, P. Declerck, S. Passinger, A. Ovsianikov, J. Serbin, and B. N. Chichkov, "Investigations on the generation of photonic crystals using two-photon polymerization (2PP) of inorganic–organic hybrid polymers with ultra-short laser pulses," physica status solidi (a) **204**, 3662-3675 (2007).

11. I. Sakellari, A. Gaidukeviciute, A. Giakoumaki, D. Gray, C. Fotakis, M. Farsari, M. Vamvakaki, C. Reinhardt, A. Ovsianikov, and B. Chichkov, "Two-photon

polymerization of titanium-containing sol–gel composites for three-dimensional structure fabrication," Applied Physics A: Materials Science & Processing **100**, 359-364 (2010).

12. J. E. G. J. Wijnhoven, L. Bechger, and W. L. Vos, "Fabrication and Characterization of Large Macroporous Photonic Crystals in Titania," Chemistry of Materials **13**, 4486-4499 (2001).

13. P. V. Braun, R. W. Zehner, C. A. White, M. K. Weldon, C. Kloc, S. S. Patel, and P. Wiltzius, "Epitaxial Growth of High Dielectric Contrast Three-Dimensional Photonic Crystals," Advanced Materials **13**, 721-724 (2001).

14. P. V. Braun, and P. Wiltzius, "Electrochemical Fabrication of 3D Microperiodic Porous Materials," Advanced Materials **13**, 482-485 (2001).

15. Y. A. Vlasov, X.-Z. Bo, J. C. Sturm, and D. J. Norris, "On-chip natural assembly of silicon photonic bandgap crystals," Nature **414**, 289-293 (2001).

16. K. Awazu, X. Wang, M. Fujimaki, T. Kuriyama, A. Sai, Y. Ohki, and H. Imai, "Fabrication of two- and three-dimensional photonic crystals of titania with submicrometer resolution by deep x-ray lithography," Journal of Vacuum Science & Technology B **23**, 934-939 (2005).

17. J. S. King, E. Graugnard, O. M. Roche, D. N. Sharp, J. Scrimgeour, R. G. Denning, A. J. Turberfield, and C. J. Summers, "Infiltration and Inversion of Holographically Defined Polymer Photonic Crystal Templates by Atomic Layer Deposition," Advanced Materials **18**, 1561-1565 (2006).

18. N. Tétreault, G. von Freymann, M. Deubel, M. Hermatschweiler, F. Pérez-Willard, S. John, M. Wegener, and G. A. Ozin, "New Route to Three-Dimensional Photonic Bandgap Materials: Silicon Double Inversion of Polymer Templates," Advanced Materials **18**, 457-460 (2006).

19. B. Jia, "Near-infrared high refractive-index three-dimensional inverse woodpile photonic crystals generated by a sol-gel process," J. Appl. Phys. **102**, 096102 (2007).

20. J. E. G. J. Wijnhoven, and W. L. Vos, "Preparation of Photonic Crystals Made of Air Spheres in Titania," Science **281**, 802-804 (1998).

21. E. D. Palik, ed. *Handbook of Optical Constants of Solids* (Academic Press, Orlando, FL, 1985).

22. R. Biswas, J. Ahn, T. Lee, J.-H. Lee, Y.-S. Kim, C.-H. Kim, W. Leung, C.-H. Oh, K. Constant, and K.-M. Ho, "Photonic bandgaps of conformally coated structures," J. Opt. Soc. Am. B **22**, 2728-2733 (2005).

23. D. Buso, E. Nicoletti, J. Li, and M. Gu, "Engineering the refractive index of three-dimensional photonic crystals through multilayer deposition of CdS films," Opt. Express **18**, 1033-1040 (2010).

24. M. R. Weatherspoon, Y. Cai, M. Crne, M. Srinivasarao, and K. H. Sandhage, "3D Rutile Titania-Based Structures with Morpho Butterfly Wing Scale Morphologies," Angewandte Chemie International Edition **47**, 7921-7923 (2008).

25. S. M. Kuebler, B. H. Cumpston, S. Ananthavel, S. Barlow, J. E. Ehrlich, L. L. Erskine, A. A. Heikal, D. McCord-Maughon, J. Qin, H. Roeckel, M. C. Rumi, S. R. Marder, and J. W. Perry, "Three-dimensional microfabrication using two-photon-activated chemistry," in *Proc. SPIE 3937*(SPIE, 2000), pp. 97-105.

26. M. R. Weatherspoon, M. B. Dickerson, G. Wang, Y. Cai, S. Shian, S. C. Jones, S. R. Marder, and K. H. Sandhage, "Thin, Conformal, and Continuous SnO2 Coatings on Three-Dimensional Biosilica Templates through Hydroxy-Group Amplification and Layer-By-Layer Alkoxide Deposition," Angewandte Chemie International Edition **46**, 5724-5727 (2007).

CHAPTER 8

BIOLOGICALLY-ENABLED SYNTHESES OF FREESTANDING METALLIC STRUCTURES POSSESSING SUBWAVELENGTH PORE ARRAYS FOR SURFACE PLASMON-MEDIATED INFRARED TRANSMISSION

Yunnan Fang, Vincent W. Chen, John D. Berrigan, Ye Cai, Seth R. Marder, and Joseph W. Perry*, and Kenneth H. Sandhage*

[*] Prof. K. H. Sandhage, Dr. Y. Fang, J. D. Berrigan, Dr. Y. Cai
School of Materials Science and Engineering,
Georgia Institute of Technology, Atlanta, GA 30332

[*] Prof. J. W. Perry, V. W. Chen
School of Chemistry and Biochemistry
Georgia Institute of Technology, Atlantic Drive, Atlanta, GA 30332

Prof. S. R. Marder
School of Chemistry and Biochemistry
Georgia Institute of Technology, Atlanta, GA 30332

Copy of submitted manuscript

Material synthesis and chemical characterization were performed by Dr Sandhage's group

Optical characterization, calculations and FIB hole array designs were performed by Dr Perry's group.

8.1 Introduction

Nature provides impressive examples of organisms capable of forming organic and inorganic structures with intricate and controlled three-dimensional (3-D) hierarchical (nanoscale-to-macroscale) morphologies [1-6]. Among the most versatile of structure-forming organisms are diatoms, a type of aquatic single-celled algae [7-11]. Each diatom species forms a silica-bearing microshell (frustule) with a particular 3-D shape and with specific patterns of fine features (pores, ridges, channels, protuberances, etc.) [7-11]. Owing to the species-specific nature of diatom silica structure formation, a wide variety of 3-D silica morphologies can be found among the estimated 10^4-10^5 extant diatom species [7-11]. The sustained reproduction (repeated doubling) of a given species of diatom can yield enormous numbers of daughter diatoms with similarly-shaped frustules (e.g., 80 reproduction cycles corresponds to $2^{80} \sim 1.2 \times 10^{24} \sim$ twice Avogadro's number of frustule copies). Such massively-parallel, direct, and precise (genetically-controlled) self-assembly of structures with a wide selection of 3-D nano-to-microscale morphologies has no analogue among synthetic self-assembly processes [12]. Furthermore, the silica-based composition of diatom frustules can be altered via several shape-preserving approaches (e.g., by gas/silica displacement reactions [13-17], conformal coating [18-28], or combined coating and reaction methods [29-36]) to allow for a broader range of applications.

Certain centric diatom frustules possess organized distributions of 10^2-10^3 nm diameter pores, which has led to interest in the optical properties of these structures [37-41]. For example, the valves of *Coscinodiscus wailesii* diatoms have been found to exhibit wavelength selective optical transmission and optical diffraction, which have been attributed to a quasi-regular hexagonal pattern of pores on these valves [40]. This quasi-regular pore array has also enabled *C. wailesii* valves to act as micro-lenses; that is, red laser light of 100 μm diameter transmitted through these valves could be focused to a diameter of <10 μm [37, 38]. The girdle band of *C. granii* diatoms, which possesses a

square array of pores, has been reported to guide blue-green light [39]. The hexagonal pore pattern on *Melosira varians* frustules has been correlated to relatively strong apparent absorption of blue light by these frustules [41].

In this paper, we have utilized a scalable, conformal, wet chemical coating process to generate freestanding (silica-free) gold structures with intricate 3-D morphologies inherited from diatom frustules. We demonstrate, for the first time, that freestanding (silica-free) nanocrystalline gold structures with diatom-derived quasi-periodic subwavelength pore arrays can exhibit surface plasmon-mediated enhanced infrared transmission. Such enhanced IR transmission is a result of both the diatom-derived pore structure and the gold chemistry.

8.2 Experiment

8.2.1 Diatom Culturing

A *Coscinodiscus asteromphalus* (*CA*) diatom strain (CCMP1814) was obtained from the Provasoli-Guillard National Center for Culture of Marine Phytoplankton (Bigelow Laboratory for Ocean Sciences, West Boothbay Harbor, ME, USA). The *C. asteromphalus* culture was grown in NEPC medium [42] at 18^{o}C under continuous illumination (~5700$\pm$1100 lux) from cool white fluorescent bulbs for 3 weeks. The cultured diatom cells were harvested with the aid of a flow-through centrifuge operating at 18,180 g (Sorvall Evolution RC, Kendro Lab Products, Asheville, NC, USA). The resulting pellets containing a small amount of growth medium were then transferred to 50 ml Falcon tubes and further centrifuged for 5 min at 4,500 g (5804R centrifuge, Eppendorf North America, Hauppauge, NY, USA). The pellets were then refluxed with 8 M nitric acid at 100°C for 1 h to remove organic material. The frustules were then washed repeatedly with de-ionized water until the natant water became neutral in pH. The frustules were then dried at 60°C for >10 h.

8.2.2 Surface Amine Enrichment

Amine groups were introduced to the surfaces of *Aulacoseira sp.* and *C. asteromphalus* diatom frustules and glass slides (pre-cleaned micro slides, Catalogue No. 3010, Gold Seal Products, Portsmouth, NH, USA) via an aminosilanization treatment consisting of refluxing overnight in an aqueous solution containing 10 wt% 3-[2-(2-aminoethylamino) ethylamino]propyl-trimethoxysilane (Sigma-Aldrich, St. Louis, MO, USA) and 3.5 wt% concentrated NH_4OH (30% NH_3 in water, Fischer Scientific, Pittsburgh, PA, USA). The aminosilanized frustules and glass slides were then washed with de-ionized water, followed by washing with anhydrous ethanol. For some of the specimens, a dendritic polyacrylate/polyamine amplification treatment was used to amplify the amine groups on the template surfaces [44-45]. Aminosilanized specimens were first exposed to a solution of 50 wt% dipentaerythritol penta-/hexa-acrylate (DPEPHA, Sigma-Aldrich) in ethanol on a rotator (30 rpm, Tube Rotator, VWR International, Suwanee, GA, USA) for 1 h at room temperature. This exposure was then followed by washing the specimens with anhydrous ethanol to remove unbound DPEPHA. The specimens were then exposed to a solution of 50 wt% tris(2-aminoethyl)amine (TAEA, Sigma-Aldrich) in ethanol on the rotator (30 rpm) for 1 h at room temperature, followed by rinsing with anhydrous ethanol to remove unbound TAEA. The process of alternating exposure to a DPEPHA solution and TAEA solution was repeated four times (for a total of five cycles).

8.2.3 Electroless Gold Deposition and Selective Silica Dissolution

Amine-enriched diatom frustules and glass slides were incubated with a solution of 5 wt% chloroauric acid ($HAuCl_4$, Sigma-Aldrich) in 60 vol% ethanol overnight at room temperature on the rotator (30 rpm). After rinsing four times with a 60 vol% ethanol solution, the diatom frustules and glass slides were incubated with a solution of 0.16 M sodium borohydride ($NaBH_4$, Alfa Aesar, Ward Hill, MA, USA) in 60 vol%

ethanol at room temperature at 300 rpm (Thermomixer R, Eppendorf North America) for 10 min. After rinsing four times with de-ionized water, the templates were immersed in a commercial electroless gold solution (Bright Electroless Gold, Transene Company, Inc., Danvers, MA, USA) that had been diluted by 50% in an aqueous 60 vol% ethanol solution. A solution of 0.16 M $NaBH_4$ in 60 vol% ethanol was then introduced and the mixture was stirred for 3 min at 300 rpm (Thermomixer R) at room temperature. After rinsing four times with de-ionized water and once with anhydrous methanol, the gold-coated specimens were dried at 60ºC for >10 h. Selective dissolution of the underlying silica from the gold-coated frustules was conducted by immersing the coated frustules in a 5 wt% aqueous HF solution overnight with shaking (500 rpm) at room temperature. The resulting freestanding gold structures were washed with DI water and then with anhydrous methanol, followed by drying in a 60°C oven overnight.

8.2.4 Patterning of Pores in Flat Gold Films

A dual beam, focused ion beam (FIB) instrument (Nova Nanolab 200, FEI Company, Hillsboro, OR, USA) was used to obtain cross-sections of the freestanding diatom-derived gold structures and to generate pore patterns within planar gold films on glass slides. In the latter case, periodic and aperiodic pore patterns were imported into the FIB operating system to allow for the selective milling of such patterned pore arrays into the gold films. Such FIB patterning was conducted using a gallium ion energy of 30 KeV, a beam current of 0.1 nA, an incident angle of 0^o, a dwell time of 100 μs, and a beam overlap of 50%.

8.2.5 Structural and Chemical Characterization

Scanning electron microscopy was conducted with a field emission scanning electron microscope (Leo 1530 FEG SEM, Carl Zeiss SMT Ltd., Cambridge, UK) equipped with an energy dispersive x-ray spectrometer (INCA EDS, Oxford Instruments,

Bucks, UK). Cross-sections of the freestanding frustule-shaped metallic structures were obtained using the FIB instrument. X-ray diffraction analyses (X-Pert Pro Alpha 1 diffractometer, PANalytical, Almelo, The Netherlands) were conducted with Cu Kα radiation with an incident beam Johannsen monochromator and an Xcelerator linear detector. X-ray photoelectron spectroscopy (SSX-100, Surface Physics, Inc., Bend, OR, USA) was conducted at a base pressure of 3×10^{-7} Pa using an Al Kα source (1486.6 eV) and step sizes of 0.1 eV.

8.2.6 Optical Characterization

Suspensions of the freestanding diatom-derived gold structures in ethanol were injected onto a glass slide (catalogue number 177399, Lab-Tek, Thermo Scientific, Portsmouth, NH, USA) and allowed to evaporate. Near- and mid-infrared reflectance and transmittance spectra of the freestanding gold replica structures on the glass slide were obtained using a Fourier-transform infrared spectrometer coupled to a microscope (FTS7000-UMA600, Agilent and Thermo Nicolet IN10MX mid-infrared microscope) that utilized a Cassegrain objective lens with a numerical aperture of 0.5 (giving inner and outer angles of the annular ring of light of 14 and 30 degrees, respectively). A variable aperture in the microscope was set to provide a field of view of 60 μm x 60 μm within a central region of the gold diatom replica structures. The reflectance spectra were normalized relative to an evaporatively-deposited gold mirror coating on a glass slide. Transmittance spectra of samples on a glass substrate in air were normalized relative to an uncoated glass slide. Transmittance and reflectance spectra were also measured for samples that had been infiltrated with, and coated on top by, an oil with a refractive index (Type A oil, refractive index = 1.5142 at 0.589 μm Cargille) matching that of the glass slide (1.523 at 0.589 μm), followed by capping with a cover slip (Gold Seal No. 0, Electron Microscopy Sciences, Hatfield, PA). Transmission spectra of the index-

matched samples were normalized to an assembly comprising a glass slide, a 15 μm thick layer of index-matching oil (defined by a 15 μm thick spacer), and a cover slip.

8.3 Results and Discussions

8.3.1. Conformal Gold Coatings

In order to coat 3-D diatom frustules with thin, conformal, continuous, and nanocrystalline gold films via electroless deposition, the relatively inert and non-conductive silica surfaces of these structures needed to be modified. Two surface functionalization approaches were examined. For the first approach, pendant amino groups were introduced to the frustule surfaces via an aminosilanization treatment. Subsequent exposure of these surface amines to a chloroauric acid solution was used to bind Au(III) complexes to the frustules. The surface-bound gold complexes were then reduced into elemental gold via reaction with sodium borohydride. The resulting gold nanoparticles were then utilized as preferred heterogeneous nucleation sites upon exposure to a commercial electroless gold deposition solution. For the second approach, a dendritic layer-by-layer process, involving sequential exposure to dipentaerythritol penta-/hexa-acrylate and tris(2-aminoethyl)amine [44, 45], was introduced after the aminosilanization treatment, in order to significantly enrich the amine concentration on the diatom silica surfaces, while keeping all other steps the same as for the first approach. Secondary electron (SE) images of *Aulacoseira sp.* diatom frustules before and after such surface functionalization and electroless gold deposition are shown in Figure 8.1. (Note: *Aulacoseira sp.* frustules, available in large quantities as diatomaceous earth, were used to establish the desired functionalization and electroless deposition protocols before application of these methods to the cultured *C. asteromphalus* diatom frustules.)

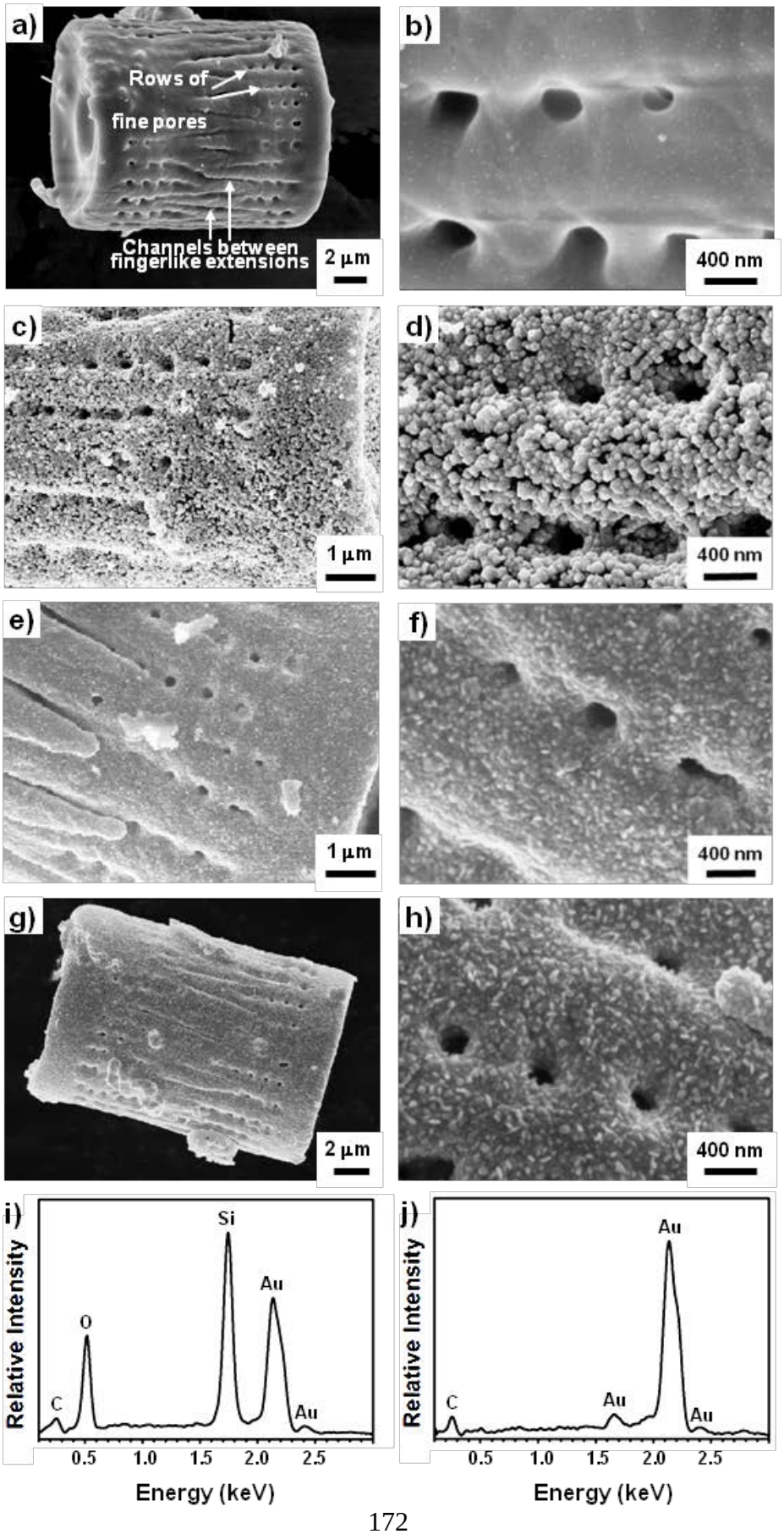
a)
Rows of
fine pores
Channels between
fingerlike extensions
2 µm
b)
400 nm
c)
1 µm
d)
400 nm
e)
1 µm
f)
400 nm
g)
2 µm
h)
400 nm
i)
Relative Intensity
C
O
Si
Au
Au
0.5
1.0
1.5
2.0
2.5
Energy (keV)
j)
Relative Intensity
C
Au
Au
0.5
1.0
1.5
2.0
2.5
Energy (keV)

Figure 8.1. Secondary electron (SE) images of: a), b) a starting *Aulacoseira sp.* diatom frustule, c), d) a gold-coated *Aulacoseira sp.* diatom frustule prepared with the use of a surface functionalization treatment (involving aminosilanization) followed by electroless gold deposition, e), f) a gold-coated *Aulacoseira sp.* diatom frustule prepared with the use of an amine-amplifying surface functionalization protocol (involving aminosilanization and poly-acrylate/polyamine dendritic amine amplification), followed by electroless gold deposition, g), h) a freestanding (silica-free) gold structure retaining the overall 3-D morphology of an *Aulacoseira sp.* diatom frustule prepared via selective dissolution of the silica from a gold-coated frustule of the type shown in e) and f). EDX analyses of: i) the gold-coated silica frustule shown in e) and f), and j) the freestanding gold structure shown in g) and h).

These frustules possessed a cylindrical shape and contained rows of fine pores and narrow channels between intercalating fingerlike extensions (Figures 8.1a and b). Gold-coated surfaces of frustules that had been treated according to the first surface functionalization protocol are shown in Figures 8.1c and d, whereas gold-coated frustules surfaces that had been exposed to the second functionalization approach (involving dendritic amine amplification) are shown in Figures 8.1e and f. The gold coating prepared without use of the dendritic amine amplification treatment consisted of relatively coarse agglomerates of particles that did not conform particularly well to frustule surfaces (Figures 8.1c and d). Noticeable gaps were also observed in the gold coating. The aminosilanization process alone appeared to yield a modest density of surface-bound amine groups onto which a correspondingly modest concentration of surface-bound gold(III) complexes could bind. Reduction of these complexes then yielded relatively few dispersed gold particles that grew, upon subsequent electroless deposition, into relatively coarse particle agglomerates that impinged with reduced interconnectivity on frustule surfaces (Figures 8.1c, d). However, the gold coating

formed on frustules that had been treated with the dendritic amine amplification process possessed significantly improved conformality and continuity (Figures 8.1e, f). The surfaces of these latter coated frustules also exhibited a finer granular appearance than for the coated frustules that had not been exposed to the amine amplification process. The enhanced population of gold(III) complexes that could bind to the amine-enriched frustule surfaces enabled the formation of a relatively high density of gold nanoparticles that could then grow and quickly impinge during subsequent electroless deposition, so as to yield a conformal and continuous coating (Figures 8.1e, f). To produce freestanding gold structures, the underlying silica within these coated frustules was selectively removed by dissolution in a HF solution. SE images of the resulting all-gold structures are shown in Figures 8.1g and h. Energy dispersive X-ray (EDX) analyses before and after exposure to the HF solution (Figures 8.1i and j, respectively) confirmed the selective dissolution of the underlying silica. (Note: while obvious cracks or gaps were not detected in SE images of gold-coated frustules of the type shown in Figures 8.1e and f, complete removal of the underlying silica by acid dissolution indicated that the gold coating was not hermetic.) Owing to the conformality and continuity of the gold coating, the freestanding (SiO_2-free) gold structures retained the 3-D frustule shape and nanoscale features (pores, channels).

The amine-enriched surface functionalization protocol and electroless deposition process were then applied to *Coscinodiscus asteromphalus* diatom frustules and planar glass substrates. SE images of the starting *CA* frustules are shown in Figures 8.2a-c.

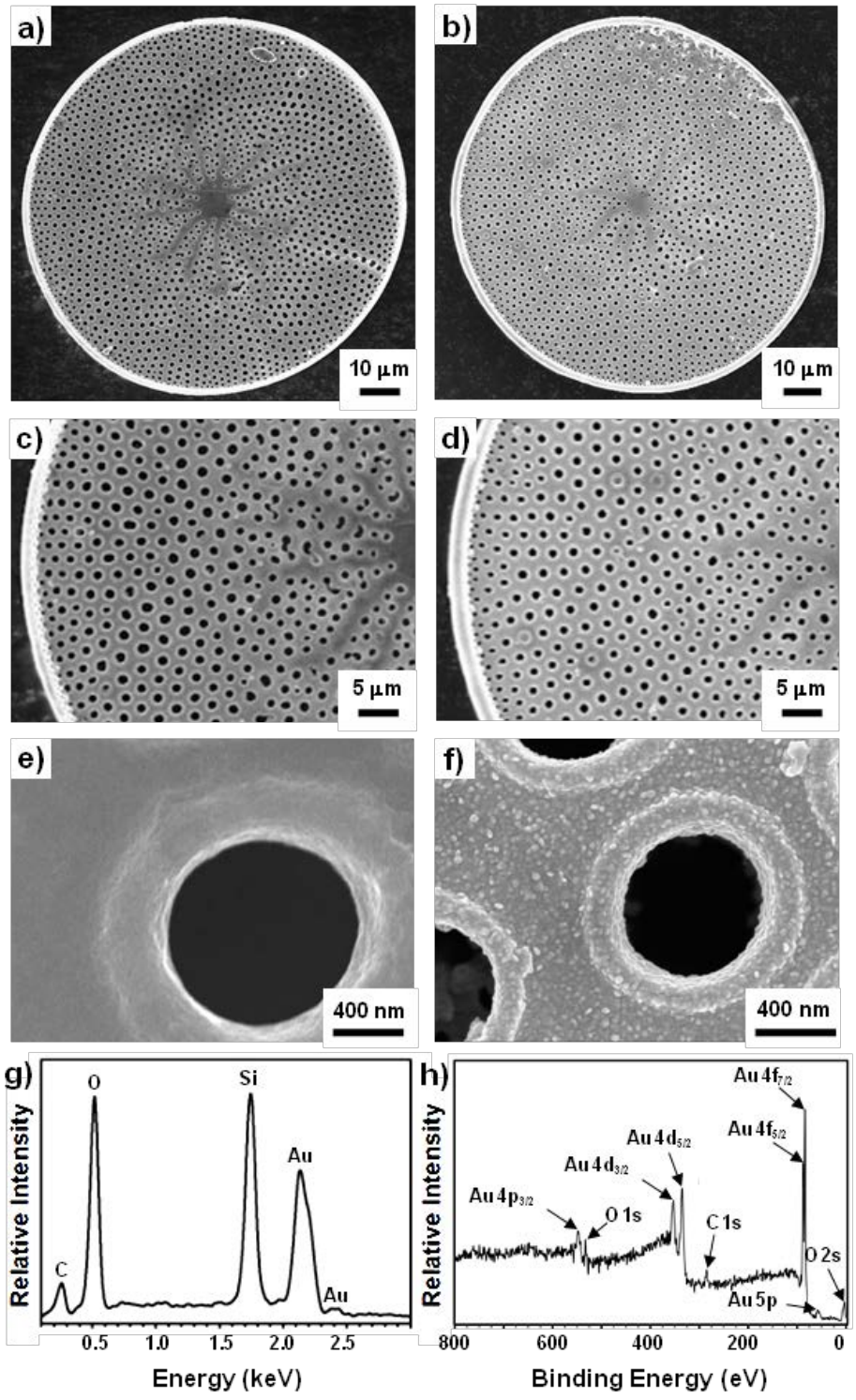

Figure 8.2. SE images of: a)-c) a starting *C. asteromphalus* diatom frustule valve, and d)-f) a gold-coated *C. asteromphalus* frustule valve. g) EDX and h) XPS analyses of such

gold-coated frustules.

The *CA* frustule valves were nearly circular in shape with a diameter of ~100 μm. The *CA* frustule valves also possessed characteristic radial rows of holes with an average diameter of 1.2 ± 0.2 μm distributed in an approximately hexagonal local (quasi-periodic) arrangement, with an average center-to-center nearest neighbor hole distance of 2.3 ± 0.3 μm (where the ranges refer to ± one standard deviation about the average values). Each of the holes was surrounded by an uplifted rim on one side of the frustule (Figure 8.2c). SE images of gold-coated CA frustules are shown in Figures 8.2d-f. Comparison of the higher magnification SE images in Figures 8.2c and 2f confirmed the conformality of the coating; that is, although the coated surfaces exhibited a more granular, nanocrystalline appearance than for the starting frustules, gaps or cracks in the coating were not detected and the surface features of the *CA* valves (e.g., the uplifted rims surrounding the circular holes) were well preserved. EDX analysis (Figure 8.2g), X-ray photoelectron spectroscopic (XPS) analysis (Figure 8.2h), and X-ray diffraction (XRD) analysis (Figure 8.3a) confirmed the presence of appreciable elemental gold on the coated frustules.

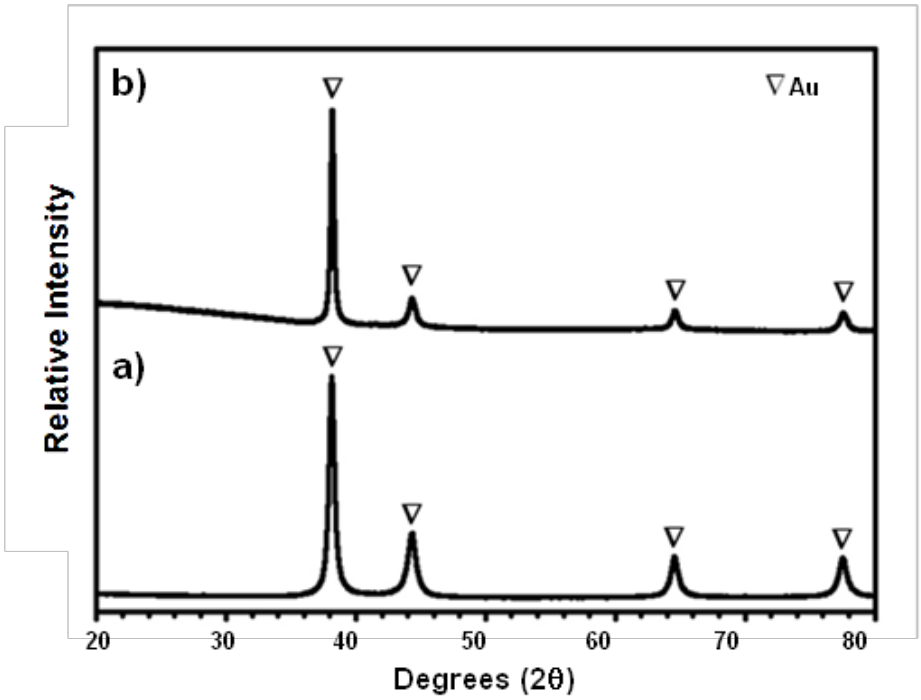

Figure 8.3. X-ray diffraction (XRD) analyses of: a) gold-coated *C. asteromphalus* diatom frustules and b) a gold-coated planar glass substrate.

The XPS analysis revealed the presence of peaks for gold but not for silicon (e.g., the Si 2p peak at 103 eV was absent), which indicated that the SiO_2 frustule surfaces were completely coated. Scherrer analysis of the gold diffraction peaks in Figure 8.3a yielded an average crystal size of 10.5 ± 0.2 nm. Analyses of SE images yielded a mean apparent gold nanoparticle size of ~22 ± 7 nm, which indicated that the gold nanoparticles were, on the average, comprised of two or more nanocrystals. A gold coating was also generated on a planar glass substrate, using the same process as for the *CA* diatoms (Figure 8.4).

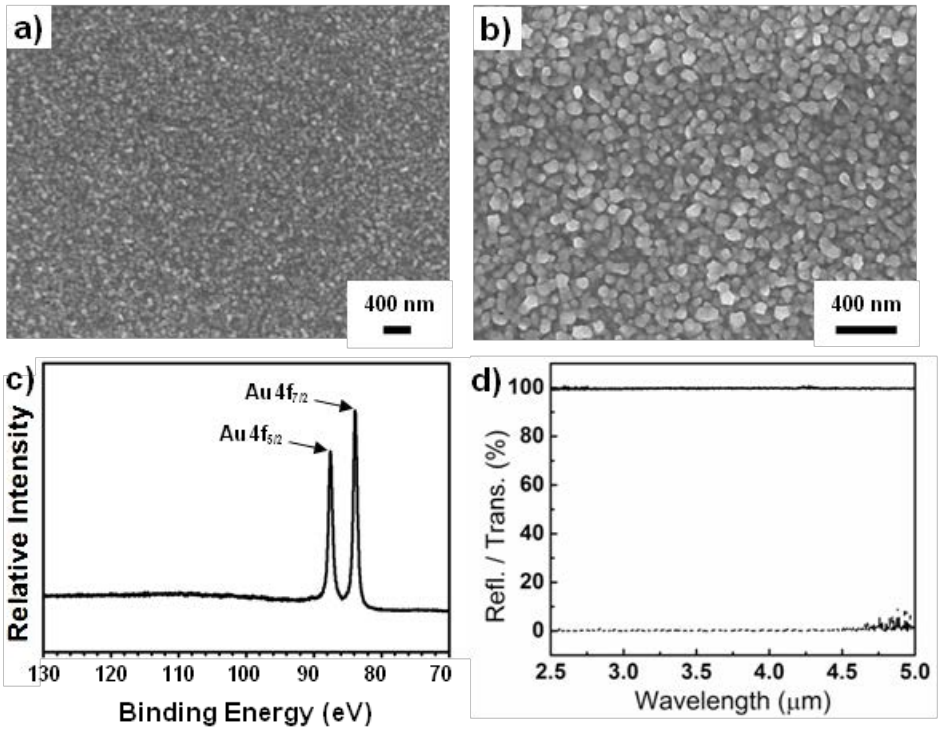

Figure 8.4. a), b) SE images and c) XPS analysis of a gold-coated planar glass substrate prepared in a similar manner as for the amine-amplified, gold-coated *C. asteromphalus* frustules. d) Reflectance (solid line) and transmittance (dashed) spectra of the planar gold-coated glass substrate, relative to an evaporatively deposited gold film.

The average thickness of the gold coating on this planar substrate was 84 ± 12 nm. The presence and absence of peaks for gold and silicon, respectively, in the XPS analysis (Figure 8.4d) confirmed the complete nature of the coating on the planar glass substrate. Scherrer analysis of the XRD pattern obtained from this film (Figure 8.3b) and analyses of SE images of this coating yielded average gold crystallite and particle sizes of 14.6 ± 0.2 nm and 53 ± 20 nm, respectively. These values, like those for the *CA* diatom-derived gold structures, were substantially smaller than the values of the mid- and near-IR wavelengths used in subsequent optical analyses (i.e., such fine gold particles and crystals should result in minimal scattering of IR light).

Selective dissolution of the underlying silica from the gold-coated *CA* frustules

yielded freestanding (hollow) gold structures that retained the overall 3-D morphology and fine features of the starting frustules. Top-down and cross-sectional SE images (the latter obtained via focused ion beam, FIB, milling) and EDX analysis of such gold structures are shown in Figure 8.5.

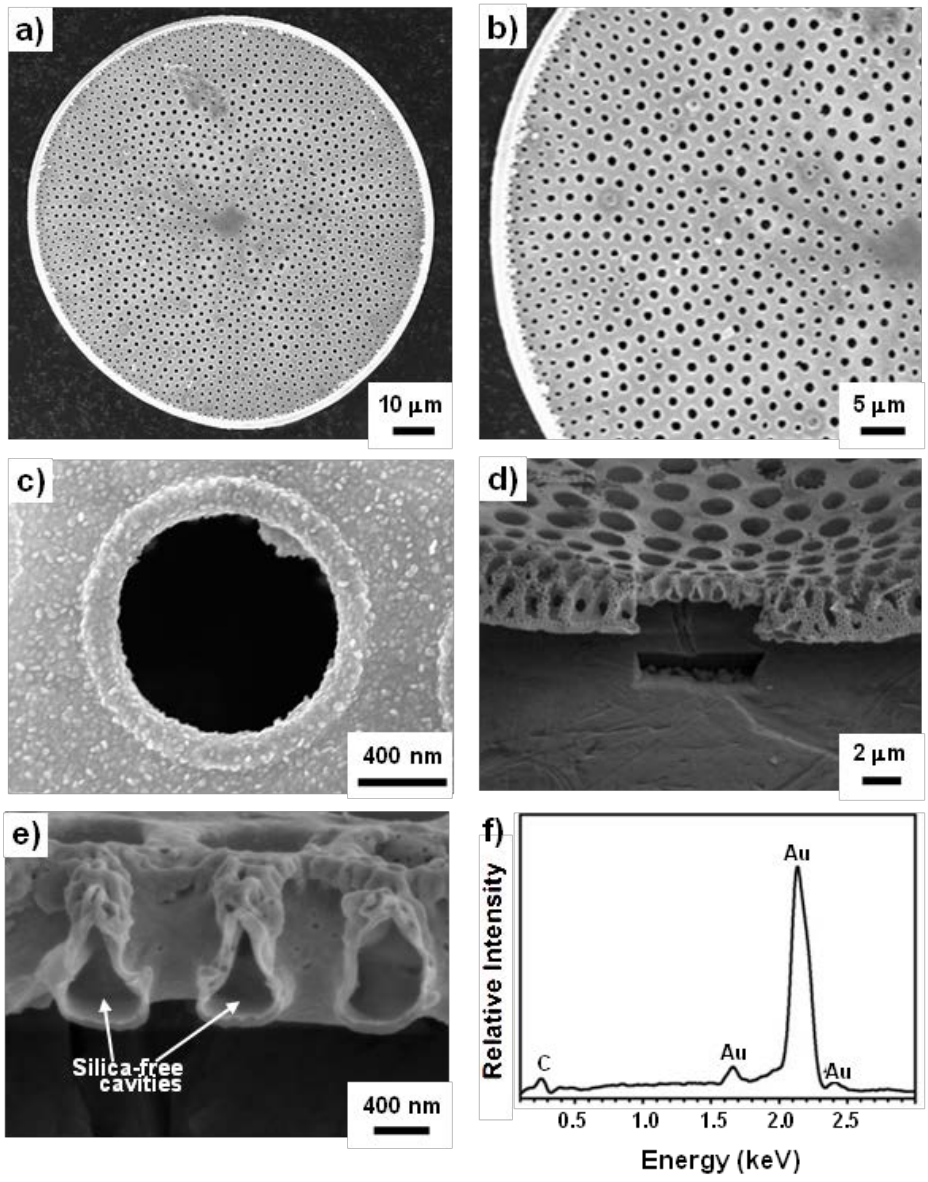

Figure 8.5. SE images of: a)-c) a freestanding (silica-free) gold structure retaining the morphology of a *C. asteromphalus* diatom frustule valve, and d), e) ion-milled sections of such a freestanding gold structure. f) EDX analysis of such a freestanding gold structure.

The absence of detectable Si and O peaks in the EDX pattern (Figure 8.5f) confirmed the removal of the underlying silica template. The conformality and continuity of the gold coating enabled the freestanding gold structures to retain the overall 3-D frustule shape and finer features (such as the rims around the micron-sized holes, Figure 8.5c). FIB cross-sections of a freestanding gold structure (Figures 8.5d and e) revealed the hollow nature of these structures that resulted from complete removal of the silica template. The FIB cross-sections also revealed that the continuous gold coating possessed an average thickness of 95 ± 12 nm.

8.3.2 IR Transmission/Reflection Properties

Optical (transmission, reflection) images of a freestanding *CA*-derived gold structure, and the normalized infrared reflectance and transmission spectra obtained from this structure (after infiltration/coating with an index-matching oil), are shown in Figure 8.6. A reflection minimum (28%) and a transmission maximum (13%) were observed at wavelengths centered at ~4.1 μm and ~4.3 μm, respectively. Such IR reflection minima/transmission maxima were observed in multiple *CA*-derived freestanding gold structures but were not observed for the starting (uncoated) *CA* frustules or for planar gold-coated glass substrates (Figure 8.4d), which indicated that these spectral features were a result of both the frustule-derived structure and the gold chemistry.

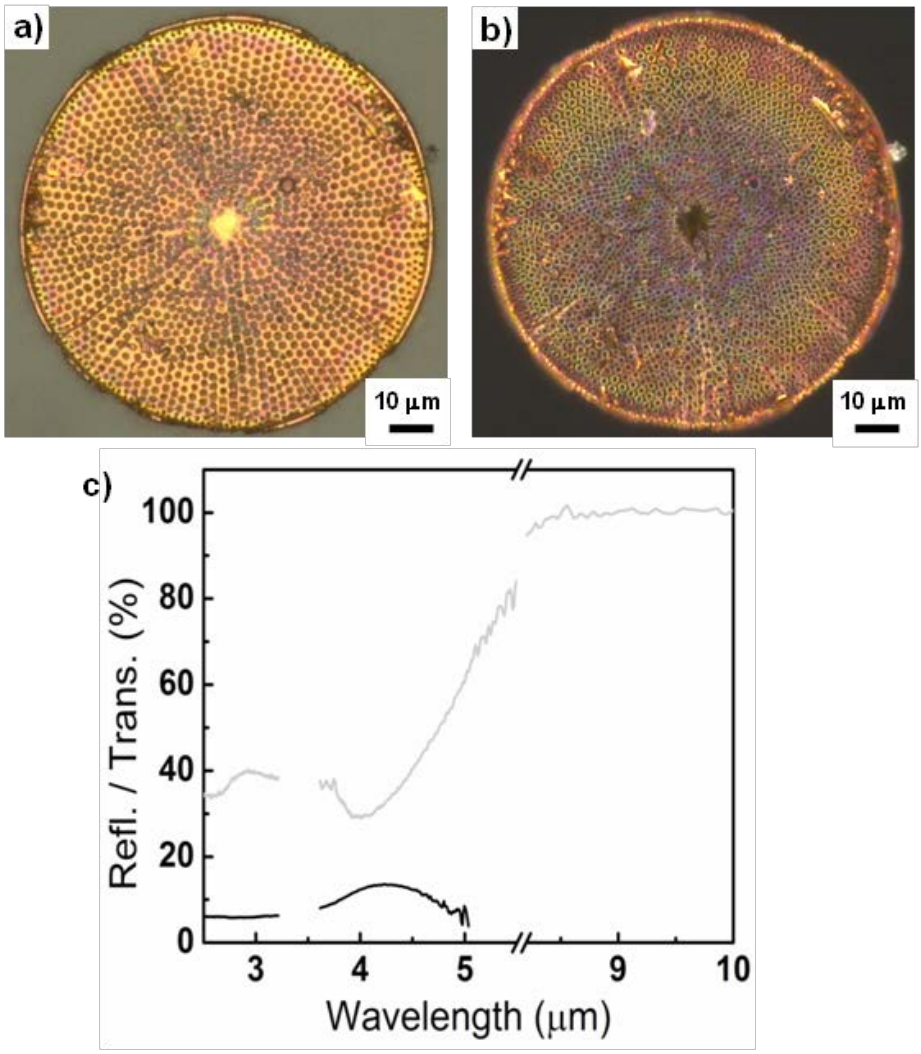

Figure 8.6. a) Reflection and b) transmission optical images of a *C. asteromphalus* frustule-derived freestanding (silica free) gold structure. c) Reflection (gray) and transmission (black) spectra of this freestanding gold structure (with the reflection and transmission data normalized relative to a planar gold film of the type shown in Figure 8.4 and an uncoated planar glass substrate, respectively). The freestanding CA-derived gold structure was placed on a glass slide, immersed in an index-matching oil, and capped with a cover slip. The planar gold reference film (on a glass slide) was covered with the index-matching oil and capped with a cover slip. The gap regions in the spectra in c) coincide with C-H stretching absorption bands of the oil at 3.3-3.6 µm. Because the

glass substrate became strongly absorbing at ~5 μm, the transmission spectrum was truncated at ≥ 5 μm.

The presence of such transmission maxima/reflection minima for the *CA*-derived gold structures suggested that the patterned array of holes present on these structures were sufficiently ordered as to support the transmission of light at wavelengths greater than the hole diameter (i.e., transmitted light of ~4.3 μm wavelength, holes of 1.2 μm average diameter). The transmission of light through metallic structures with patterned arrays of holes of subwavelength diameter, referred to as extraordinary optical transmission, has been reported for various metals and hole array patterns, including periodic, quasiperiodic, and aperiodic patterns [46-49].

To allow for comparison with the transmission results from the gold diatom replicas, planar gold films were prepared with hole patterns of the following types: i) a *CA* hole pattern (i.e., the pore pattern observed in the replica in Figure 8.6), ii) a randomly perturbed *CA* hole pattern, iii) a periodic hexagonal hole pattern, and iv) a randomly perturbed hexagonal hole pattern. The average center-to-center hole distance of 2.32 μm between nearest neighbours was used as the period of the hexagonal hole array. The *CA* and hexagonal hole arrays were randomly perturbed by shifting each hole position in a random direction and by a random distance, the size of which was constrained to be less than the average hole-to-hole distance minus the hole diameter. Each of these hole patterns was generated by FIB milling of continuous, conformal, and nanocrystalline planar gold films of the type shown in Figures 8.4a and b (prepared by the amine-enriched surface functionalization and electroless deposition process). SE images of the ion-milled gold films containing these patterned hole arrays are shown in Figures 8.7a-d.

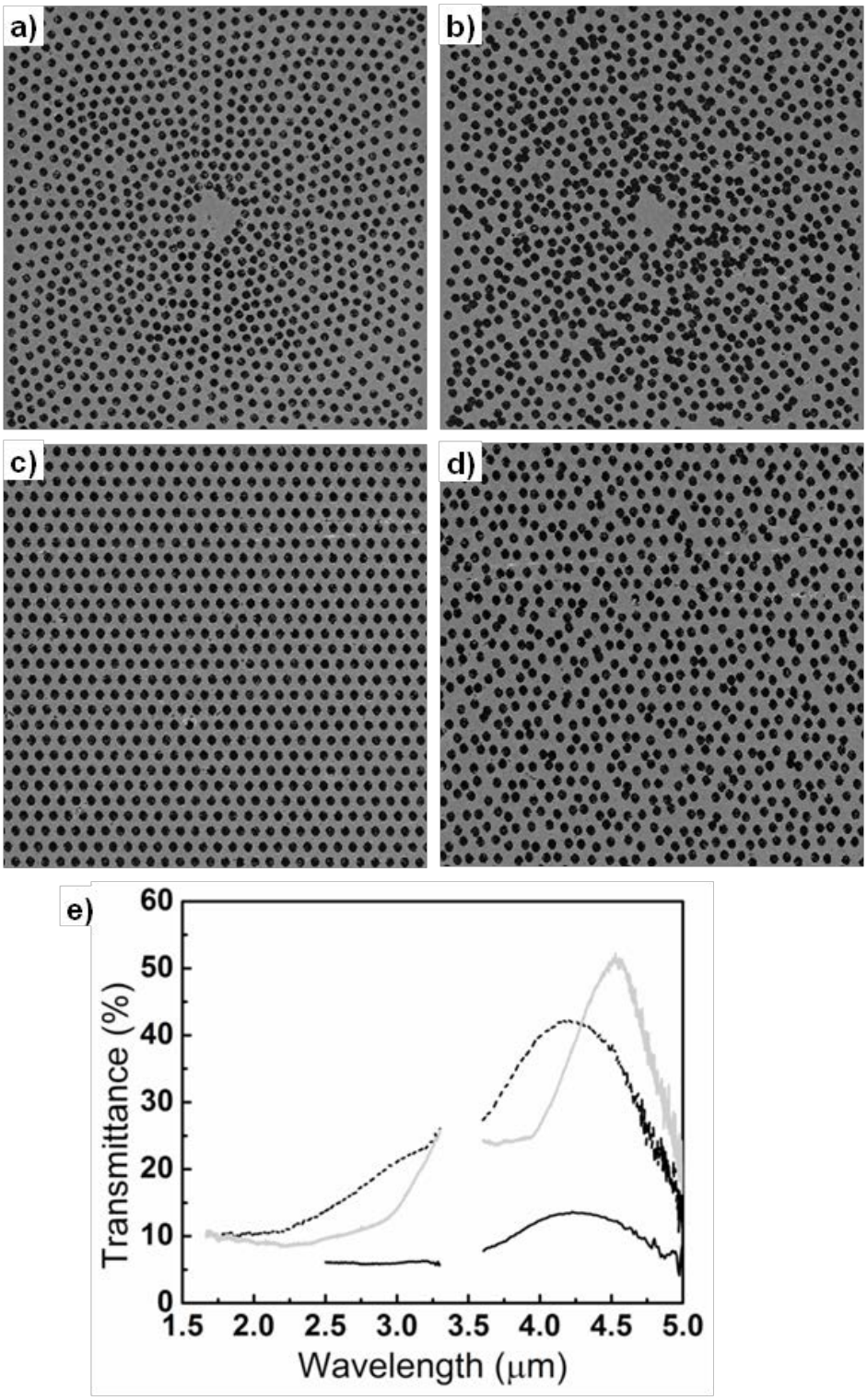

Figure 8.7. SEM images of planar gold films with various hole arrays fabricated by focused ion beam (FIB) milling: a) a hole pattern matching that of an actual quasi-

periodic *CA* hole array (see Figure 8.6), b) a *CA* array pattern with random perturbations to hole positions, limited to the average spacing of the native hole array pattern, c) a periodic hexagonal hole array pattern with a hole spacing of 2320 nm, and d) a hexagonal hole array with random perturbations to hole positions. e) Transmission spectra obtained from a gold replica of a native *CA* diatom frustule (solid black), a planar gold film (as shown in a)) with a quasi-periodic hole array pattern obtained from a native *CA* diatom frustule (dashed black), and a planar gold film (as shown in c)) with a periodic hexagonal hole array pattern (gray).

The gold *CA* replica (Figures 8.6a and b), and the planar gold films with FIB-generated hexagonal and *CA* hole arrays (Figures 8.7a and c, respectively), exhibited the normalized transmission spectra shown in Figure 8.7e. All three types of gold structures exhibited a relatively strong long-wavelength transmission resonance, with the positions of these primary transmission peaks centered between 4.2 and 4.5 μm, although the planar gold films with the periodic hexagonal and quasi-periodic *CA* hole arrays exhibited stronger transmission resonances (51% at ~4.5 μm and 42% at ~4.2 μm, respectively) than did the gold replicas derived from *CA* diatoms (13% at ~4.3 μm). Interestingly, the Au *CA* replica, and the planar Au film containing the *CA* hole pattern, exhibited transmission maxima centered at nearly the same wavelength (~4.3 vs ~4.2 μm, respectively).

8.3.3 Modeling of Hole Array Optical Properties

In order to gain insight into the optical transmission properties of the gold *CA* replicas and the hole-patterned planar gold films, transmission spectra were calculated using a surface plasmon interference model reported by Pacifici, et al. [47]. This model treats the optical transmission through films with hole arrays as being due to the following fundamental processes: 1) optical excitation of surface plasmon polaritons

(SPP) by scattering from individual holes, 2) propagation of SPPs to other holes in the array, which causes a phase shift ($k_{spp}a$, where k_{spp} is the SPP wavevector and a is the distance between holes) relative to the incident light at the neighboring holes (leading to interference between the SPP launched from neighboring holes and the incident field at a given hole), 3) transmission of the total field at each hole from the top through the hole, 4) launching and interference of SPPs from holes at the bottom surface, and 5) light emission by scattering of SPPs from holes on the bottom surface. This calculation yields the normalized (per hole) transmission for a given hole array pattern.

8.3.3.1 Calculation Of Normalized Transmission Spectra For Hole Array Structures

We calculated the normalized transmission spectra of various hole array structures examined in this paper using a surface plasmon polariton (SPP) interference model [47]. Two dimensional coordinates for the hole locations of the *CA* Au replica structures, *CA* patterned hole arrays and hexagonal hole arrays fabricated in planar Au films were used as inputs for the model calculations, along with the dielectric functions for the index matching oil, glass, and Au film. It was necessary to modify the SPP interference model reported previously in two ways. Firstly, we needed to be able to perform calculations on cases where the medium above and below the structure was air and glass, respectively, and thus of different dielectric functions, whereas the model of ref. 47 treated only the symmetrical case where the top and bottom media were the same. Secondly, it was necessary to treat the non-normal incidence of the optical geometry of our measurement, i.e. a focused annular cone of light with an angular spread of 14^o to 30^o, as well as the unpolarized character of the optical excitation. Eqs. 15 and 16 of ref. 10d for the H-field amplitude at the top and bottom surfaces of the given metal hole array, respectively, were modified to account for the asymmetrical arrangement of media on the top and bottom, by using different surface plasmon wavevectors calculated from the dielectric functions of air and Au for the top surface and glass and Au for the bottom surface. For the cases

where the medium above and below the Au hole array structure were the same, the only modification to treatment of ref. 47, was to account for the inclination of the incident upolarized light. The non-normal incidence, unpolarized excitation light was accounted for by using the following equation of for the total H-field at the top surface:

$$H_{m,top} = 1 + \sum_{j \neq m} \frac{\beta_0 \beta_0^{'} \left(\sin^2(\theta_{jm}) + \cos^2(\theta_i)\cos^2(\theta_{jm}) \right)}{\sqrt{a_{jm}}} \exp\left[i\left(k_{SPP}^{top} a_{jm} + \varphi + \Delta\phi \right) \right] \qquad (1)$$

Where $\beta_0 \beta_0^{'}$ = 0.12 is the product of surface plasmon launch efficiencies for the top and bottom surfaces, k_{SPP}^{top} is the surface plasmon polariton wavevector for the air-Au interface, $\varphi = \pi/2$ is the surface plasmon launch phase shift, and $\Delta\phi$ is the hole-to-hole phase shift for inclined incident light defined by $\Delta\phi = \frac{2\pi}{\lambda} n(\lambda) a_{jm} \sin\theta_i$, where θ_i is the angle of incidence, and the amplitude factor, $\sin^2(\theta_{jm}) + \cos^2(\theta_i)\cos^2(\theta_{jm})$, represents the projection of the plane of polarization unto the air-Au interface to account for the unpolarized nature of the incident light. The H-field at the bottom (Au-glass interface) is similar to that of the ref. 47 but uses an unit amplitude to represent unpolarized character of the plasmons launched from the top surface:

$$H_{m,bot} = H_{m,top} + \sum_{j \neq m} \frac{\beta_0 \beta_0^{'}}{\sqrt{a_{jm}}} H_{m,top} \exp\left[i\left(k_{SPP}^{top} a_{jm} + \varphi \right) \right] \qquad (2)$$

The normalized per hole transmission was calculated as described in ref. 10d, i.e.:

$$\eta_N = \frac{\left| \sum_{m=1}^{N} H_{m,bot} \right|^2}{N^2} \qquad (3)$$

where N is the number of holes in the array.

8.3.3.2 Modified Calculations to Account for Measurement Geometry

This model has been modified to match the experimental optical geometry of the

present work, which involved a ring of unpolarized light focused on the sample with angles of incidence varying from 14 to 30 degrees. The effect of this non-normal incidence was accommodated by introducing a phase shift of the form to account for the difference in optical path length for light reaching pairs of holes:

$$\Delta\phi = \frac{2\pi}{\lambda} n(\lambda) a_{jm} \sin\theta_i \qquad (4)$$

where θ_i is the angle of incidence, λ is the free space optical wavelength, and $n(\lambda)$ is the wavelength-dependent refractive index of the index-matching oil. An amplitude factor was also included to account for the projection of the plane of polarization onto the surface of each hole array. The calculated transmission spectra were averaged over the range of incidence angles (14 to 30 degrees).

8.3.3.3 Comparison of Simulation and Experimental Data

In order to evaluate the impact of the periodicity of the hole arrays on infrared transmission through the gold structures, the calculated and experimental transmission spectra were further normalized by taking the ratio of the transmission of a given hole array to that of a randomly perturbed version of the same array. Such calculated normalized transmission spectra (per hole) are shown in Figure 8.8a (note: in this figure, normalized transmission values above or below unity refer to enhanced or suppressed transmission, respectively, relative to a film with a randomly perturbed version of the same type of hole array). For a planar gold film with 992 holes arranged in the same quasi-periodic pattern as for a *CA* gold replica (the replica shown in Figure 8.6), the calculated normalized spectrum exhibited enhanced transmission peaks centered at ~4.3, ~3.2 and ~2.1 μm, and suppressed transmission valleys (minima) centered at ~3.4 and ~2.8 μm. This *CA*-based hole array possessed local hexagonal order (i.e., to within about 3-4 nearest hole neighbors) without extensive long-range periodicity. In light of such

short-range order, a similar calculation was conducted for a planar gold film containing a perfectly-ordered hexagonal array with only 16 holes. The calculated transmission spectrum for this 16-hole periodic hexagonal array (also shown in Figure 8.8a) was found to be in reasonably good agreement with that calculated for the 992-hole quasi-periodic *CA* array. Such agreement indicated that the short-range order of holes in a *CA*-based array played a dominant role in enabling IR transmission through gold structures with such a quasi-periodic hole pattern.

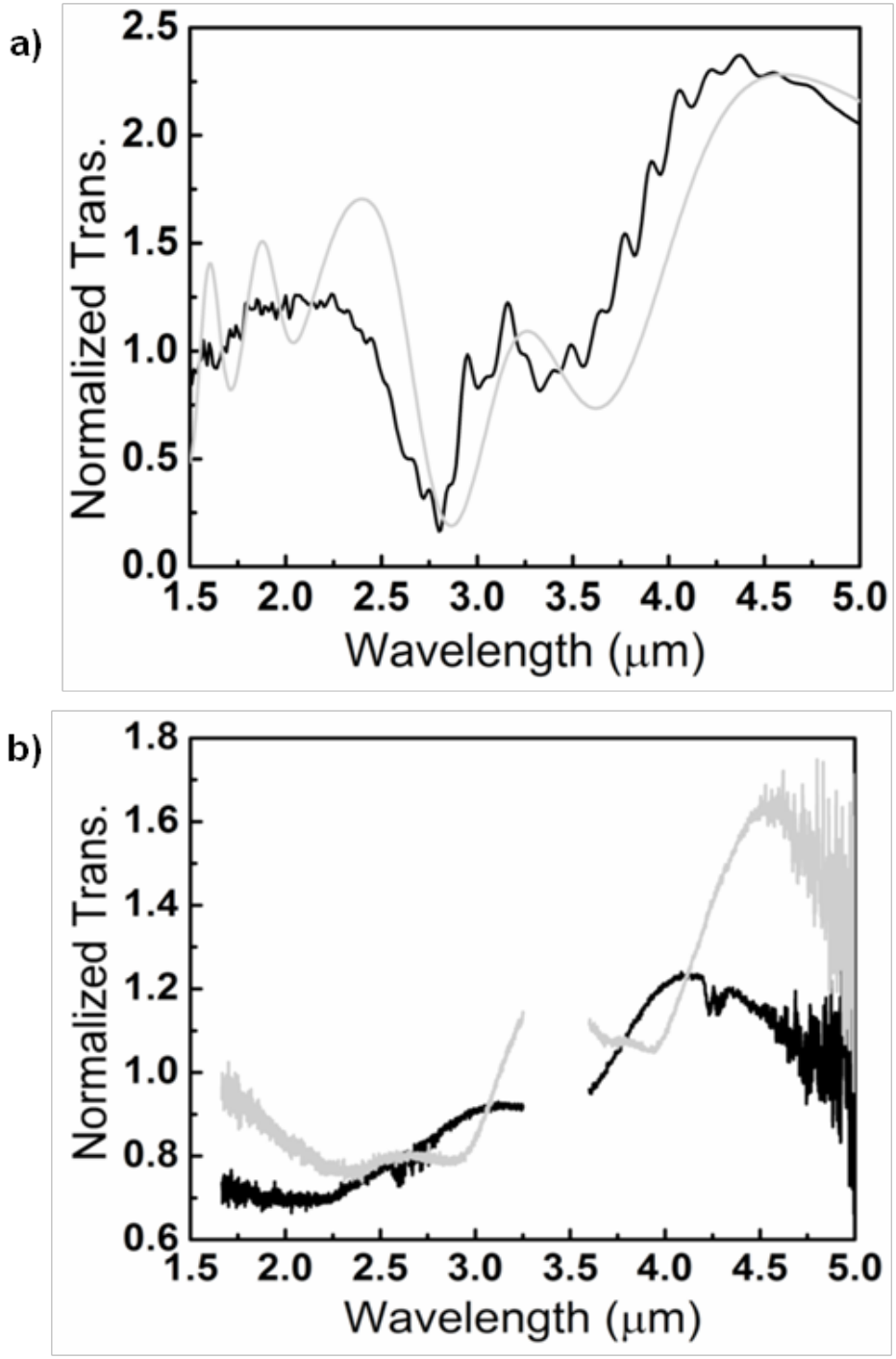

Figure 8.8. Normalized transmission spectra of hole-array structures fabricated in planar Au films using FIB milling. a) Calculated transmission efficiency spectra of gold films with a quasi-periodic *CA*-derived hole array pattern (black) and a periodic hexagonal array with 16 holes and a = 2320 nm (gray). Model parameters (plasmon coupling

parameter, phase shift upon launch of SPP) were taken to be the same as in reference 47. The dielectric function of our nanocrystalline Au film was found to be nearly identical to that reported by Palik [50]. The dielectric function of the substrate was very similar to that of the index matching oil, so the oil dielectric function was used for the bounding medium on the top and bottom of the Au film. b) Experimental spectra obtained from planar gold films with a quasi-periodic *CA*-derived hole pattern normalized to a randomly perturbed *C*A-derived hole array pattern (black) and a periodic hexagonal hole array pattern normalized to a perturbed hexagonal hole array pattern (gray).

The normalized transmission spectra calculated from the SPP interference-based model (Figure 8.8a) were then compared to the experimentally-measured normalized spectra shown in Figure 8.8b. Reasonably good agreement was observed between the calculated and experimentally-measured spectra at relatively long wavelengths; that is, for films possessing the periodic hexagonal and quasi-periodic *CA*-derived hole arrays, two transmission peaks (with the stronger primary peak detected at a longer wavelength) were observed at wavelengths greater than ~2.7 μm for both the calculated and measured spectra. For the film with the *CA*-derived quasi-periodic hole array, the strongest transmission peaks obtained from the calculated and experimentally-measured spectra were centered at ~4.3 μm (Figure 8.8a) and ~4.2 μm (Figure 8.8b), respectively. For the planar film with the periodic hexagonal hole array, the calculated and measured strongest transmission peaks were both centered at ~4.5 μm. Secondary transmission peaks in the calculated spectra were observed at ~3.2 μm and ~3.3 μm for the quasi-periodic CA-derived and periodic hexagonal hole arrays, respectively. For the measured spectra, such secondary transmission peaks also appeared to be located between 3.1-3.5 μm, although identification of the location of these measured secondary peaks was complicated by the presence of C-H absorption bands from the index-matching oil at 3.3-3.6 μm. A

suppressed transmission valley observed in the calculated spectra for the quasi-periodic CA-derived hole array at ~3.4 μm also appeared to be present in the measured spectra for this array between 3.3 and 3.6 μm. A suppressed transmission valley observed in the calculated spectra for the periodic hexagonal hole array at ~3.6 μm was present in the measured spectra for this array at ~3.9 μm.

At wavelengths below ~2.7 μm, the agreement between calculated and measured spectra in Figure 8.8 was relatively poor. This could be due to diffraction and/or guided-mode contributions to the measured transmission spectra that were not included in the SPP interference-based model of the present work. The SPP interference-based calculations also predicted more intense transmission at 4.2-4.5 μm than was measured for the gold *CA* frustule replicas. Structural features of the *CA* frustule replicas that may have influenced the extent of the measured transmission at these long wavelengths, and that were not considered in the model, include the curvature of the top and bottom surfaces of the gold replicas (seen in Figure 8.5d), the lateral variation in hole size (seen in Figure 8.5b), and the variation in hole size through the thickness of the *CA* frustule replica (seen in Figure 8.5e).

The location and intensity of the primary transmission resonance peaks for these patterned-hole gold structures were significantly influenced by the presence of the index-matching oil. When the oil was replaced with air, the transmission maximum shifted from a wavelength of ~4.3 μm to ~2.8 μm for the Au *CA* frustule replica. This change also resulted in a reduction in the peak transmission from 13% to 8.4%. Such shifts in peak transmission wavelength and changes in intensity were also observed for the planar gold films with periodic hexagonal hole arrays and quasi-periodic *CA*-derived hole arrays. These observations are consistent with the expected influence of the refractive indices of the media above and below the hole-patterned gold structures on the location of the transmission peaks associated with constructive interference of SPPs. For the oil-

bearing specimens, the effective SPP index at the interface between the oil and the upper surface of the gold structure is increased, leading to a larger effective SPP pathlength between holes and a shift of the transmission resonance to longer wavelength, as well as to better phase matching between the SPPs on the top and bottom giving an increase in transmission.

This work demonstrates that self-replicating biogenic templates with well-controlled 3-D shapes and patterned features can be converted, via a highly-conformal wet-chemical coating process, into metallic structures that retain the biogenic morphologies with a high degree of fidelity. By combining the attractive self-assembly characteristics of diatoms and other structure-forming organisms (i.e., massively-parallel, genetically-precise, direct 3-D assembly of structures with a wide selection of nano-to-microscale morphologies under ambient conditions) with such a readily-scalable chemical conversion process, metallic assemblies with a variety of selectable 3-D morphologies may be mass produced in a sustainable manner. Proper selection of a 3-D shaped/patterned template from the extensive range of available biogenic morphologies, followed by shape-preserving conversion into an appropriate nanocrystalline element or alloy, can yield complex 3-D metallic structures with new (non-biological) properties for a host of applications.

8.4 Conclusion

Freestanding 3-D microscale nanocrystalline gold structures, with complex morphologies and fine patterned features inherited from silica diatom frustules, were synthesized via combined use of an amine-amplifying surface functionalization process and electroless gold deposition. By using a cyclic polyacrylate/polyamine protocol to significantly amplify the pendant amino groups attached to aminosilanized diatom frustule surfaces, a high density of gold (III) complexes could be bound to such surfaces and then reduced to generate a high population of heterogeneous gold nucleation sites for

subsequent electroless gold deposition. Owing to the conformal and continuous nature of the resulting thin (<100 nm) nanocrystalline gold coatings, selective dissolution of the underlying silica template yielded freestanding gold structures that retained the 3-D shapes and fine patterned features of the starting frustules.

Freestanding diatom-derived gold structures with quasi-periodic hexagonal arrays of pores, inherited from *Coscinodiscus asteromphalus* diatom valves, exhibited transmission maxima and reflection minima at infrared wavelengths well above the average pore diameter. Such extraordinary optical transmission was not observed for the starting silica diatom valves or for flat nonporous gold films, which indicated that such optical behavior resulted from the combined effects of the *CA* diatom-derived quasi-periodic hole structure and the gold chemistry. Enhanced transmission at similar infrared wavelengths was also observed for a planar gold film containing 992 holes arranged in a quasi-periodic pattern matching that of a *CA* diatom valve, as well as from a planar gold film with only 16 holes arranged in a perfectly periodic hexagonal array. The latter observation indicated that the quasi-periodic order of holes on the *CA*-derived gold replicas (i.e., with local hexagonal order that extended out to only about 3-4 nearest hole neighbors) played a dominant role in such extraordinary IR transmission. Calculations based on a surface-plasmon interference-mediated transmission model yielded wavelengths for such enhanced IR transmission that were in reasonable agreement with those obtained from experimental measurements of these patterned-hole gold structures.

The scalable wet-chemical process described in this work for generating thin, continuous, and highly-conformal metallic coatings (dendritic amplification of surface amines coupled with electroless deposition) on non-conductive 3-D templates may be extended to a variety of other self-replicating biogenic, or self-assembling synthetic, templates to provide micro/nanopatterned metallic structures for a range of optical, electrical, chemical, or structural applications.

ACKNOWLEDGEMENTS

This work was supported by the U.S. Air Force Office of Scientific Research (Awards No. FA9550-09-1-0162, FA9550-09-1-0669, and FA9550-10-1-0555) and the U.S. Department of Energy, Office of Basic Energy Sciences (Award No. DE-SC0002245). The authors acknowledge the Georgia Tech FIB2 Center established under NSF funding. The authors thank Prof. D. Pacifici of Brown Univ. for helpful discussions on the transmission modeling, Dr. Jianing Sun of Woollam, Inc. for measurement of the mid-IR dielectric function of our nanocrystalline gold films, and Mr. Craig Cameron for optical microscopy images of Au coated *CA* diatoms.

REFERENCES

1. M. Srinivasarao, "Nano-Optics in the Biological World: Beetles, Butterflies, Birds, and Moths," Chemical Reviews **99**, 1935-1962 (1999).

2. J. Aizenberg, A. Tkachenko, S. Weiner, L. Addadi, and G. Hendler, "Calcitic microlenses as part of the photoreceptor system in brittlestars," Nature **412**, 819-822 (2001).

3. M. Cusack, and A. Freer, "Biomineralization: Elemental and Organic Influence in Carbonate Systems," Chemical Reviews **108**, 4433-4454 (2008).

4. P. Vukusic, and J. R. Sambles, "Photonic structures in biology," Nature **424**, 852-855 (2003).

5. J. C. Weaver, J. Aizenberg, G. E. Fantner, D. Kisailus, A. Woesz, P. Allen, K. Fields, M. J. Porter, F. W. Zok, P. K. Hansma, P. Fratzl, and D. E. Morse, "Hierarchical assembly of the siliceous skeletal lattice of the hexactinellid sponge Euplectella aspergillum," Journal of Structural Biology **158**, 93-106 (2007).

6. J. R. Young, S. A. Davis, P. R. Bown, and S. Mann, "Coccolith Ultrastructure and Biomineralisation," Journal of Structural Biology **126**, 195-215 (1999).

7. R. Gordon, F. A. S. Sterrenburg, and K. H. Sandhage, "A Special Issue on Diatom Nanotechnology," Journal of Nanoscience and Nanotechnology **5**, 1-4 (2005).

8. M. Hildebrand, "Diatoms, Biomineralization Processes, and Genomics," Chemical Reviews **108**, 4855-4874 (2008).

9. N. Kröger, and N. Poulsen, "Diatoms—From Cell Wall Biogenesis to Nanotechnology," Annual Review of Genetics **42**, 83-107 (2008).

10. D. Mann, and S. Droop, "3. Biodiversity, biogeography and conservation of diatoms," Hydrobiologia **336**, 19-32 (1996).

11. F. E. Round, R. M. Crawford, and D. G. Mann, *The Diatoms: biology & morphology of the genera* (Cambridge University Press, New York, NY, 1990).

12. K. H. Sandhage, S. M. Allan, M. B. Dickerson, C. S. Gaddis, S. Shian, M. R. Weatherspoon, Y. Cai, G. Ahmad, M. S. Haluska, R. L. Snyder, R. R. Unocic, F. M. Zalar, Y. Zhang, R. A. Rapp, M. Hildebrand, and B. P. Palenik, "Merging Biological Self-Assembly with Synthetic Chemical Tailoring: The Potential for 3-D Genetically Engineered Micro/Nano-Devices (3-D GEMS)," International Journal of Applied Ceramic Technology **2**, 317-326 (2005).

13. Z. Bao, M. R. Weatherspoon, S. Shian, Y. Cai, P. D. Graham, S. M. Allan, G. Ahmad, M. B. Dickerson, B. C. Church, Z. Kang, H. W. Abernathy Iii, C. J. Summers, M. Liu, and K. H. Sandhage, "Chemical reduction of three-dimensional

silica micro-assemblies into microporous silicon replicas," Nature **446**, 172-175 (2007).

14. Y. Cai, S. M. Allan, K. H. Sandhage, and F. M. Zalar, "Three-Dimensional Magnesia-Based Nanocrystal Assemblies Via Low-Temperature Magnesiothermic Reaction of Diatom Microshells," Journal of the American Ceramic Society **88**, 2005-2010 (2005).

15. K. H. Sandhage, M. B. Dickerson, P. M. Huseman, M. A. Caranna, J. D. Clifton, T. A. Bull, T. J. Heibel, W. R. Overton, and M. E. A. Schoenwaelder, "Novel, Bioclastic Route to Self-Assembled, 3D, Chemically Tailored Meso/Nanostructures: Shape-Preserving Reactive Conversion of Biosilica (Diatom) Microshells," Advanced Materials **14**, 429-433 (2002).

16. S. Shian, Y. Cai, M. R. Weatherspoon, S. M. Allan, and K. H. Sandhage, "Three-Dimensional Assemblies of Zirconia Nanocrystals Via Shape-Preserving Reactive Conversion of Diatom Microshells," Journal of the American Ceramic Society **89**, 694-698 (2006).

17. R. R. Unocic, F. M. Zalar, P. M. Sarosi, Y. Cai, and K. H. Sandhage, "Anatase assemblies from algae: coupling biological self-assembly of 3-D nanoparticle structures with synthetic reaction chemistry," Chemical Communications, 796-797 (2004).

18. X. Cai, G. Zhu, W. Zhang, H. Zhao, C. Wang, S. Qiu, and Y. Wei, "Diatom-Templated Synthesis of Ordered Meso/Macroporous Hierarchical Materials," European Journal of Inorganic Chemistry **2006**, 3641-3645 (2006).

19. Y. Fang, Q. Wu, M. B. Dickerson, Y. Cai, S. Shian, J. D. Berrigan, N. Poulsen, N. Kröger, and K. H. Sandhage, "Protein-Mediated Layer-by-Layer Syntheses of Freestanding Microscale Titania Structures with Biologically Assembled 3-D Morphologies," Chemistry of Materials **21**, 5704-5710 (2009).

20. C. S. Gaddis, and K. H. Sandhage, "Freestanding microscale 3D polymeric structures with biologically-derived shapes and nanoscale features," Journal of Materials Research **19**, 2541-2545 (2004).

21. S. M. Holmes, B. E. Graniel-Garcia, P. Foran, P. Hill, E. P. L. Roberts, B. H. Sakakini, and J. M. Newton, "A novel porous carbon based on diatomaceous earth," Chemical Communications, 2662-2663 (2006).

22. U. Kusari, Z. Bao, Y. Cai, G. Ahmad, K. H. Sandhage, and L. G. Sneddon, "Formation of nanostructured, nanocrystalline boron nitride microparticles with diatom-derived 3-D shapes," Chem Commun (Camb), 1177-1179 (2007).

23. D. Losic, J. G. Mitchell, and N. H. Voelcker, "Complex gold nanostructures derived by templating from diatom frustules," Chemical Communications, 4905-4907 (2005).

24. E. K. Payne, N. L. Rosi, C. Xue, and C. A. Mirkin, "Sacrificial biological templates for the formation of nanostructured metallic microshells," Angew Chem Int Ed Engl **44**, 5064-5067 (2005).

25. N. L. Rosi, C. S. Thaxton, and C. A. Mirkin, "Control of nanoparticle assembly by using DNA-modified diatom templates," Angew Chem Int Ed Engl **43**, 5500-5503 (2004).

26. Y. Yu, J. Addai-Mensah, and D. Losic, "Synthesis of self-supporting gold microstructures with three-dimensional morphologies by direct replication of diatom templates," Langmuir **26**, 14068-14072 (2010).

27. J. Zhao, C. S. Gaddis, Y. Cai, and K. H. Sandhage, "Free-standing microscale structures of nanocrystalline zirconia with biologically replicable three-dimensional shapes," Journal of Materials Research **20**, 282-287 (2005).

28. H. Zhou, T. Fan, X. Li, J. Ding, D. Zhang, X. Li, and Y. Gao, "Bio-Inspired Bottom-Up Assembly of Diatom-Templated Ordered Porous Metal Chalcogenide Meso/Nanostructures," European Journal of Inorganic Chemistry **2009**, 211-215 (2009).

29. M. W. Anderson, S. M. Holmes, N. Hanif, and C. S. Cundy, "Hierarchical Pore Structures through Diatom Zeolitization," Angew Chem Int Ed Engl **39**, 2707-2710 (2000).

30. Z. Bao, E. M. Ernst, S. Yoo, and K. H. Sandhage, "Syntheses of Porous Self-Supporting Metal-Nanoparticle Assemblies with 3D Morphologies Inherited from Biosilica Templates (Diatom Frustules)," Advanced Materials **21**, 474-478 (2009).

31. Y. Cai, M. B. Dickerson, M. S. Haluska, Z. Kang, C. J. Summers, and K. H. Sandhage, "Manganese-Doped Zinc Orthosilicate-Bearing Phosphor Microparticles with Controlled Three-Dimensional Shapes Derived from Diatom Frustules," Journal of the American Ceramic Society **90**, 1304-1308 (2007).

32. Y. Cai, and K. H. Sandhage, "Zn2SiO4-coated microparticles with biologically-controlled 3D shapes," physica status solidi (a) **202**, R105-R107 (2005).

33. E. M. Ernst, B. C. Church, C. S. Gaddis, R. L. Snyder, and K. H. Sandhage, "Enhanced hydrothermal conversion of surfactant-modified diatom microshells into barium titanate replicas," Journal of Materials Chemistry **22**, 1121-1127 (2007).

34. Y. Wang, Y. Shang, J. Zhu, J. Wu, S. Ji, and C. Meng, "Synthesis of magadiite using a natural diatomite material," Journal of Chemical Technology & Biotechnology **84**, 1894-1898 (2009).

35. M. R. Weatherspoon, S. M. Allan, E. Hunt, Y. Cai, and K. H. Sandhage, "Sol-gel synthesis on self-replicating single-cell scaffolds: applying complex chemistries to nature's 3-D nanostructured templates," Chemical Communications, 651-653 (2005).

36. M. R. Weatherspoon, M. S. Haluska, Y. Cai, J. S. King, C. J. Summers, R. L. Snyder, and K. H. Sandhage, "Phosphor Microparticles of Controlled Three-Dimensional Shape from Phytoplankton," Journal of The Electrochemical Society **153**, H34-H37 (2006).

37. L. De Stefano, I. Rea, I. Rendina, M. De Stefano, and L. Moretti, "Lensless light focusing with the centric marinediatom Coscinodiscus walesii," Opt. Express **15**, 18082-18088 (2007).

38. E. De Tommasi, I. Rea, V. Mocella, L. Moretti, M. De Stefano, I. Rendina, and L. De Stefano, "Multi-wavelength study of lighttransmitted through a single marinecentric diatom," Opt. Express **18**, 12203-12212 (2010).

39. T. Fuhrmann, S. Landwehr, M. El Rharbi-Kucki, and M. Sumper, "Diatoms as living photonic crystals," Applied Physics B: Lasers and Optics **78**, 257-260 (2004).

40. J. Noyes, M. Sumper, and P. Vukusic, "Light manipulation in a marine diatom," Journal of Materials Research **23**, 3229-3235 (2008).

41. S. Yamanaka, "Optical properties of diatom silica frustule with special reference to blue light," J. Appl. Phys. **103**, 074701 (2008).

42. P. J. Harrison, R. E. Waters, and F. J. R. Taylor, "A BROAD SPECTRUM ARTIFICIAL SEA WATER MEDIUM FOR COASTAL AND OPEN OCEAN PHYTOPLANKTON1," Journal of Phycology **16**, 28-35 (1980).

43. G. J. Wang, Y. N. Fang, P. Kim, A. Hayek, M. R. Weatherspoon, J. W. Perry, K. H. Sandhage, S. R. Marder, and S. C. Jones, "Layer-By-Layer Dendritic Growth of Hyperbranched Thin Films for Surface Sol-Gel Syntheses of Conformal, Functional, Nanocrystalline Oxide Coatings on Complex 3D (Bio)silica Templates," Advanced Functional Materials **19**, 2768-2776 (2009).

44. G. Wang, Y. Fang, P. Kim, A. Hayek, M. R. Weatherspoon, J. W. Perry, K. H. Sandhage, S. R. Marder, and S. C. Jones, "Layer-By-Layer Dendritic Growth of Hyperbranched Thin Films for Surface Sol–Gel Syntheses of Conformal, Functional, Nanocrystalline Oxide Coatings on Complex 3D (Bio)silica Templates," Advanced Functional Materials **19**, 2768-2776 (2009).

45. M. R. Weatherspoon, Y. Cai, M. Crne, M. Srinivasarao, and K. H. Sandhage, "3D Rutile Titania-Based Structures with Morpho Butterfly Wing Scale Morphologies," Angewandte Chemie International Edition **47**, 7921-7923 (2008).

46. H. F. Ghaemi, T. Thio, D. E. Grupp, T. W. Ebbesen, and H. J. Lezec, "Surface plasmons enhance optical transmission through subwavelength holes," Physical Review B **58**, 6779-6782 (1998).

47. D. Pacifici, H. J. Lezec, L. A. Sweatlock, R. J. Walters, and H. A. Atwater, "Universal optical transmission features in periodic and quasiperiodic hole arrays," Opt. Express **16**, 9222-9238 (2008).

48. Q. Wang, "Enhanced optical transmission through metal films with rotation-symmetrical hole arrays," Appl. Phys. Lett. **87**, 091105 (2005).

49. J. Xue, B.-Q. Dong, X. Wang, R. Yang, Z.-C. Xu, Y. Chen, E. Huq, W. Zeng, X.-P. Qu, and R. Liu, "Surface plasmon enhanced transmission through gold planar crystals with various aperture arrangements," Microelectronic Engineering **87**, 1340-1343 (2010).

50. E. D. Palik, ed. *Handbook of Optical Constants of Solids* (Academic Press, Orlando, FL, 1985).

CHAPTER 9

CONCLUSION

9.1 Thesis Conclusions

This dissertation work consisted of the investigation of resolution improvement in the fabrication of photonic crystals (PCs) by multiphoton photolithography (MPL) as well as surface modifications of PCs to improve their photonic properties and to broaden their applicability to other areas of scientific research.

The resolution of features fabricated by MPL for PCs have been limited to ~ 200 nm under typical conditions, which had imposed a lower limit on the stopband position of between 1.0 – 1.3 μm. Whereas several reports on post fabrication processing have resulted in improved resolution, the resultant structural distortions and anisotropic volume reductions have been less than ideal. We have developed two methods to achieve improved resolution via MPL without compromising the PC structural integrity:

3. We have demonstrated the use of the wavelength-dependent nature of the diffraction-limited focal volume to improve the fabrication resolution of MPL in Chapter 4. MPL using 520 nm excitation produced feature sizes down to 65 nm, compared to 200 nm sized features when typical excitation conditions were employed, i.e. 700-800 nm.

4. We have utilized the chemically-induced swelling of photoresists to reduce the number of crosslinkable groups within the excitation focal volume which resulted in controlled reduction of feature sizes. This method also produced improved isotropic volume reduction compared to other post fabrication processing techniques, resulting in essentially continuously tunable photonic

stopbands with greater than 60% stopband reflectivity between 1 and 2 microns as reported in Chapter 5.

These two approaches take advantage of existing instrumentations and resist materials to produce feature sizes with resolution approaching that achieved by more complex instrumentation that utilizes advanced activation-depletion techniques. Furthermore, the fidelity of the currently produced structures exceeds that found using the aforementioned post fabrication methods. The simplicity of the current methods implies that they can be more widely adopted, since the photoinitiation and materials processing remain largely unchanged. Consequently, fundamental resolution limits can be explored since they are largely determined by structural design and mechanical stability of the fabricated features.

We have developed a fabrication system, described in Chapter 3, where PC templates can be fabricated efficiently in large quantities to facilitate 1) the production of PCs with reproducible photonic bandgap spectra, 2) the optimization of PC lattice parameters to ensure mechanical stability under various solution processing conditions, and 3) the investigation of the optical behavior of PCs with various coating morphologies. Silver and titania possess promising optical properties that can significantly impact PCs when used as coating materials; for example, metallic PCs can be used for terahertz filtering and thermal emission suppression while titania possesses a refractive index sufficiently high enough to produce complete bandgaps. Towards these applications, we used Michael addition to convert the unreacted acrylate at the polymer surface with amines which provided binding sites for material depositions:

4. We have concluded, in Chapter 6, from detailed analyses of silver electroless deposition studies that the coating morphology is strongly dependent on the transport of reactive species into the microporous domains of PCs. Whereas

plating reactions on flat 2D surfaces produce uniform coatings mirror-like surfaces, the coating dynamics for microporous, large surface area PCs were more complex and required more rigorous interrogation.

5. We have demonstrated conformal coatings of PCs with titanium dioxide using a surface sol-gel method which resulted in stopband positions that were dependent on the coating thickness due to increased effective refractive indices and volume fill-fractions. The uniformity of the coating allowed for a free-standing titania shell to remain after polymer template removal and this hollow PC still possessed a photonic stopband (Chapter 7).

6. We have developed two surface modification methods to achieve varying silver coating morphologies in Chapter 6. In the low surface coverage regime, sparsely coated PCs led to increased effective refractive index contrast between the polymer rods and air, resulting in enhanced stopband performance. Conversely, in the high coverage regime even with limited reactant penetration, densely-coated PCs exhibited plasmonic bandgap properties with large broadband reflectivity and a band edge at 1.75 μm.

These studies demonstrate that a wide range of materials can be used to both enhance the optical properties of polymeric PCs and impart novel functionalities for a broader class of applications. With low material coverage or optically-thin coatings, the functionalization of polymeric PCs provides a flexible way to fine-tune the stopband positions and intensities. With large coating thicknesses, the PCs assume the bulk properties of the applied material, mating the free-form fabrication benefits of MPL with the optical properties of a broad range of materials thereby allowing for production of devices that may otherwise be difficult to fabricate by traditional techniques.

We have also demonstrated that metallization of naturally occurring diatoms resulted in wavelength selective enhancement of transmission due to the periodic nature of their pore arrangements. Interestingly, the metallization of these free-floating structures with straight channels proved to be more facile than for the surface-bound MPL fabricated PCs.

9.2 Future Work

Numerous promising pathways have been presented throughout the course of this work. Two of the most obvious directions are the combination of high resolution features generation with titania coating methodologies to achieve complete bandgaps or to pursue thin conformal silver coatings to exploit localized surface plasmon resonance effects. Several more fundamental investigations are described below.

9.2.1 Resolution Limit

During the continuing pursuit of resolution improvement for MPL, there has been little focus on the mechanical stability of fabricated features and their role in achieving self-supporting structures. Although the swollen gel resist approach can be further optimized by increasing the concentration of hydrogenated terphenyls in the formulation, the increase in refractive index of the resulting mixture will likely induce beam aberrations in the focal volume during MPL. Shorter wavelength excitation than the 520 nm discussed herein could be achieved; however the combination of photoresist absorption with the limited number of photoinitiators that exhibit substantial TPA in this spectral region may limit the improvement possible using this method.

Utilizing the swollen gel resist in conjunction with short wavelength MPL could provide an immediate resolution improvement; extrapolating the size reduction observed from the longer wavelength excitation, feature sizes below 50 nm should be readily achievable. Such feature sizes would not only allow for the fabrication of PCs wth stopbands in the visible portion of the spectrum but also permit the investigation of the mechanical properties of these minute features through systematic variations of the PC lattice parameters and through investigation by nanoindentation or atomic force microscopy.

Another interesting aspect of these crosslinking features formed using near threshold power levels is the reorganization of the polymerized network upon development and deswelling. While we have demonstrated that the aspect ratio of the voxel generated in a swollen gel resist remains similar to traditional methods (1:2.6), as the crosslink density is further reduced, an open question remains: Will the reorganization of the uncrosslinked branches result in a decrease in the voxel aspect ratio?

9.2.2 Photonic Stopband Optimization

Electroless plating provides a facile means to rapidly deposit metals onto PCs, however the limited transport of reactants into the microporous domains and the rapid deposition rate of typical electroless plating solutions led to inhomogeneous deposition throughout the PC. A more controllable and homogenous coating could be achieved though the binding of metal nanoparticles to the same amine modified PCs. Well characterized nanoparticles with narrow size distributions could be synthesized or purchased in the range of 10 – 100 nm and their coverage density on PCs could be varied

by the degree of amine functionalization, this type of control could provide a high degree of precision in the tuning of the effective refractive index.

The plasmonic bandgap effect observed from samples with metallized PCs where only the top 2-3 layers were coated with a thick layer of silver suggests that the interaction pathlength of the incident probing light is limited. This reduction in pathlength translates to fewer layers needed to generate plasmonic bandgap effects. Metallization of PCs with fewer layers is advantageous in several respects, 1) reduced fabrication time, 2) improved mechanical stability, and 3) reduced coating contrast for the inner layers near the surface.

Another route to achieve metalized PCs with high conductivity is by electrodeposition. To retain the same structural design, an inverse of the structure could be fabricated using MPL on conducting indium-tin-oxide coated glass substrate, followed by electroplating and finally through the use of chemical or oxygen plasma etching of the polymer template. The main advantages using this technique are the versatile nature of the template formation using MPL and a bottom-up filling of the template to eliminate microporous effects.

APPENDIX 1

PHOTOPHYSICS OF A BISSTYRYLBENZENE TWO-PHOTON RADICAL INITIATOR

A.1 Introduction

Multiphoton photolithography has been of much interest in the past two decades as this nonlinear absorption process provides the unique capability to induce localized crosslinking inside a tightly confined excitation volume [1-3]. The translation of this excitation volume, a voxel, provides a means to generate any arbitrary 3D structure that would be both time-consuming and expensive through traditional 2D layer by layer technique. The mechanism for photoinitiation via this nonlinear excitation process had been broadly attributed to the formation of initiator radicals that promotes polymerization through photocleavage, as in the case of commercially available Irgacure 369 [4], or via hydrogen abstraction, for example in benzophenone-based chromophores [5]. In these mechanisms, as illustrated in Figure A.1, the radicals are generated by two photon excitation to a two-photon-allowed excited state, followed by rapid internal conversion relaxation to the lowest excited state and subsequent intersystem crossing to the triplet state where the initiator undergoes photocleavage or hydrogen abstraction. For such radical-based initiation, it is generally believed that initiators possessing high fluorescence quantum yields are less desirable since the radiative decay rate exceeds that of the intersystem crossing rate thereby reducing the excited state population that can effectively produce radicals [6].

E,*E*-1,4-*bis*[4-(di-*n*-butylamino)styryl]-2,5-dimethoxybenzene (DABSB), molecular structure shown in Figure A.2, was found to efficiently initiate polymerization in the presence of acrylate monomers when irradiated with excitation in the two-photon absorption (TPA) band [1, 7]. Contrary to the typical properties of the aforementioned

two-photon radical-based initiators, DABSB exhibits 1) a large fluorescence quantum yield [8] suggestive of preferential deactivation of the excited state via radiative decay and hence a low triplet yield, 2) a cubic irradiance dependence for induced polymerization [9] while other initiators used in the literature exhibit quadratic dependencies [7], and 3) low UV polymerization efficiencies where > 2 hours of illumination was necessary for 2D patterning compared to < 5 minutes for a similarly prepared resin including a well-known UV photoinitiator, i.e. Irgacure 369. These properties suggest the initiation mechanism of DABSB is different from other radical initiation systems in the literature and further investigation is necessary to elucidate the mechanisms of initiation.

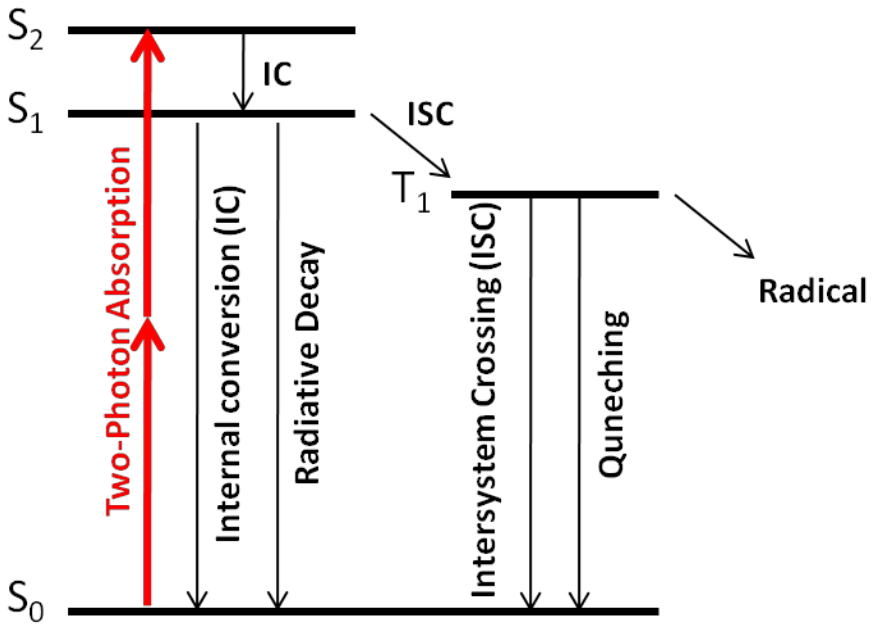

Figure A.1. Typical excitation, initiation and deactivation pathways of radical-based two-photon initiators [4].

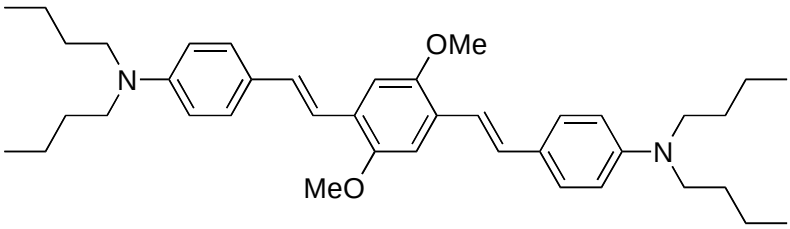

Figure A.2. Molecular structures of photoinitiator DABSB.

There are a number of potential initiation pathways for DABSB including 1) reaction from the triplet state, 2) electron transfer from a singlet excited state, 3) multiphoton ionization, or 4) thermal initiation. Based on the observations listed above, the triplet state would be formed with a very low efficiency and consequently reaction from this state is unlikely. Furthermore, the higher-order irradiance dependence for multiphoton excitation coupled with inefficient one-photon induced polymerization suggests that higher lying singlet states are likely involved in the initiation mechanism. In this chapter, femtosecond transient absorption (TA) studies are performed to aid in the understanding of the photophysical processes of DABSB involved in initiating polymerization.

TA measurements under one-photon excitation conditions were performed as a control experiment to investigate the photophysical dynamics of DABSB from the S_1 state, whereas two-photon excitation was used to approximate conditions used for multiphoton lithography. As mentioned above, under multiphoton excitation conditions one route for initiation is via electron transfer from a higher-lying excited state (Figure A.3a). This was a distinct possibility as the S_1 excited state exhibited a strong absorption band (see below) that coincided with the TPA maxima (i.e. λ_{exc} = 730 nm). Another potential pathway for initiation is multiphoton ionization (Figure A.3b). For multiphoton ionization, evidence of the generated cation should be present even in the absence of an

acceptor, whereas photoinduced electron transfer requires the presence of an acceptor to facilitate its process. Accordingly, two-photon pumped TA experiments were performed on solutions of DABSB at concentrations typically used for multiphoton lithography both in the presence and in the absence of the triacrylate monomer. To increase the likelihood of observing the photoinduced cationic spectrum, an alternative acceptor with a much stronger electron-accepting affinity than the monomer (i.e. duroquinone [10]) was also investigated in solutions of DABSB.

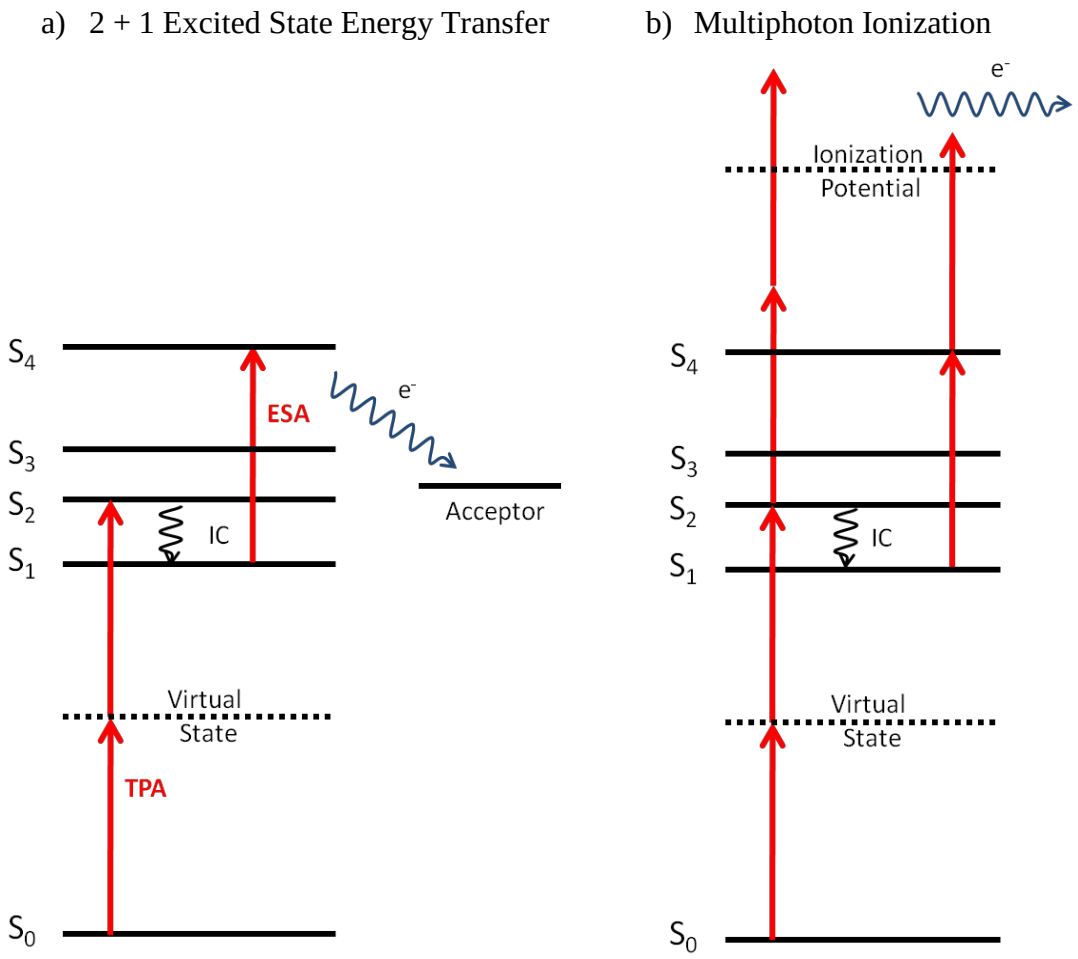

Figure A.3. Depictions of potential routes for initiation in DABSB: (a) electron transfer from an upper excited state and (b) multiphoton ionization. Energy levels are scaled to the transitions observed in both linear absorption and TA spectra with the ionization

potential set at 6 eV.

A.2 Experiment

To investigate the photophysics of DABSB and the formation of DABSB radical cations, DABSB solutions in various conditions were prepared. First, DABSB solution of 1.826 mM in dioxane without the addition of acceptor was prepared as a reference sample to understand the photophysics of DABSB molecule and to determine whether the initiation species is formed instantaneously via multiphoton ionization. Second, to aid in the formation of DABSB radicals, the DABSB solution in dioxane with 0.3 M duroquinone (Aldrich, 97%) was prepared; this concentration was chosen to ensure close the acceptors shared close proximity with the DABSB's solvation shell. Third, a DABSB solution of 1.826 mM in acrylate monomer (Sartomer, SR9020) was prepared for an *in situ* TA study of the actual multiphoton photolithography process. For the TA experiments, all three sample solutions were filled in 2 mm path length cells and were stirred continuously throughout the acquisition process.

Excitation wavelengths of 475 and 730 nm were chosen to study the one- and two-photon pumped photophysics of DABSB and its radicals. The 475 nm excitation corresponds to the transition between the ground and lowest energy excited state (2.90 eV), which should provide information about decay pathways from this lowest singlet state. Two-photon pumping was performed at the peak of the TPA spectrum (730 nm) to generate a population of molecules in this excited state (3.4 eV), see Figure A.4. Irradiance-dependent measurements were performed for all sample solutions and at all excitation wavelengths. The TA spectra were probed in both the visible (400 – 850 nm) and infrared (800 – 1600 nm) spectral regions.

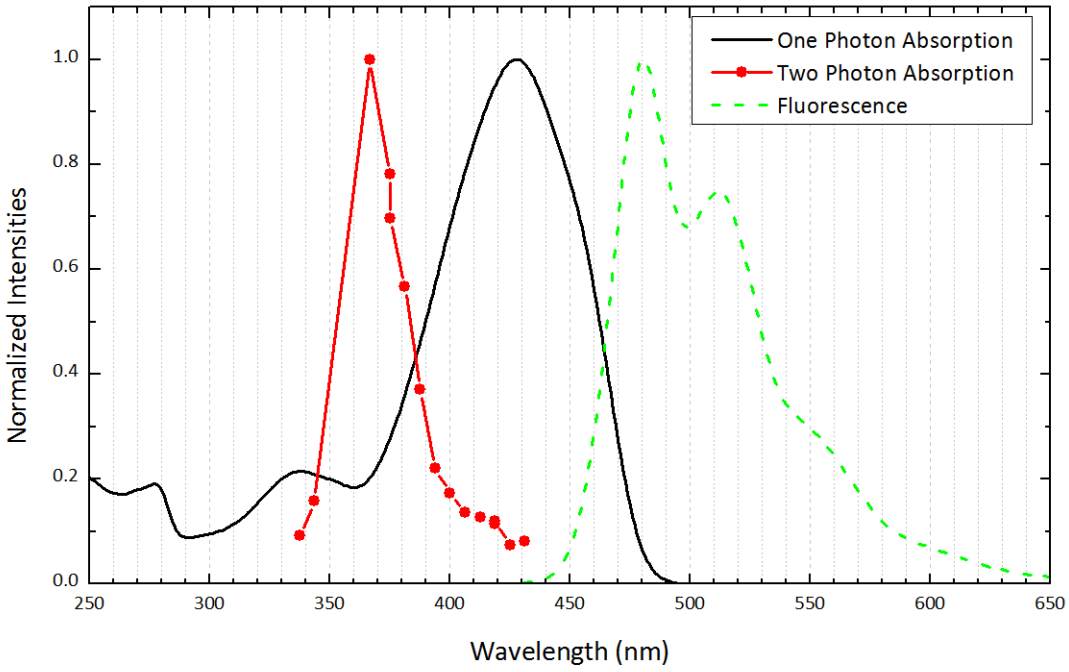

Figure A.4. Linear absorption spectrum of DABSB in dioxane, TPA [8] and fluorescence spectra of DABSB in toluene.

Femtosecond TA studies were carried out using a commercial pump-probe spectroscopy system (Ultrafast Systems, Helios), see Figure A.5, where the excitation wavelengths (470, and 730 nm) were generated by an automated ultrafast OPA (Spectra-Physics, TOPAS), and the probing beam was a white-light continuum (WLC) generated by splitting a portion (~5%) of 800 nm amplified femtosecond pulses (Spectra-Physics, Spitfire) and focusing into an appropriate crystal. The pump and the probe beams were spatially overlapped in the sample. The probed signal was detected by a fiber optic cable coupled to a multichannel spectrometer with a Silicon (400-900 nm) or InGaAs sensor (800-1600 nm). The resolvable temporal delay window extended up to 3 ns. The pump beam was chopped at 500 Hz to obtain, sequentially, the WLC spectrum without pump and alternately with the pump, which was used to calculate the transient spectra

represented as a change in optical density (ΔOD). Each transient spectrum at a given time delay was averaged for 1.5 seconds. A chirp correction function for the WLC probe was determined using measurements of the instantaneous response of the solvent and was applied to all transient spectra.

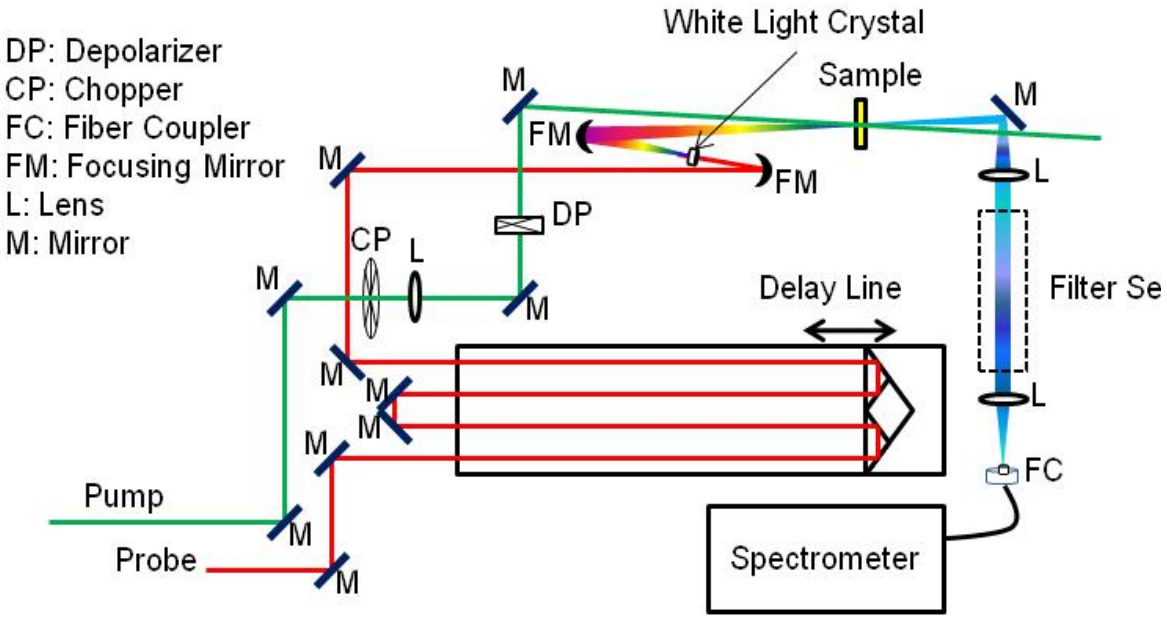

Figure A.5. The optical layout of femtosecond transient absorption spectrometer [11].

The resultant kinetics were fitted using a sum of exponential decay functions to account for the depopulation dynamics from the excited state,

$$\Delta OD = y_0 + A_1 e^{-(t-t_0)/\tau_1} + A_2 e^{-(t-t_0)/\tau_2} + A_3 e^{-(t-t_0)/\tau_3} \qquad (1)$$

where A is the amplitude of a transient absorbing species with lifetime of τ, and y_0 is the offset. The amplitude relates to the relative populations of the present species and whether these species are in the process of being populated or depleted. The offset term corresponds to long-lived species that exhibit lifetimes greater than the measurement window, for example triplet excited states.

A.3 Results and Discussion

A.3.1 One-photon excitation at 475 nm

One-photon excitation of DABSB in dioxane revealed the spectral evolution of TA as shown in Figure A.6. The most pronounced spectral feature was an excited state absorption band centered on 730 nm, along with a weaker band at 660 nm and stimulated emission at 520 nm. The decay kinetics were globally fit with equation (1) and the ratio of the pre-exponential amplitudes indicated a single dominant decay component with a lifetime of 1.30 ns, accompanied by a fast component that exhibited a lifetime of 3 ps. The fast decaying component is likely related to conformational reorientation or vibrational relaxation after excitation. The decay of the slow component is in good agreement with reported lifetime of 1.38 ns in acetonitrile [8] and 1.29 ns in tetrahydrofuran [12] by picosecond time-correlated single photon counting, corresponding to the depopulation of the lowest singlet excited state.

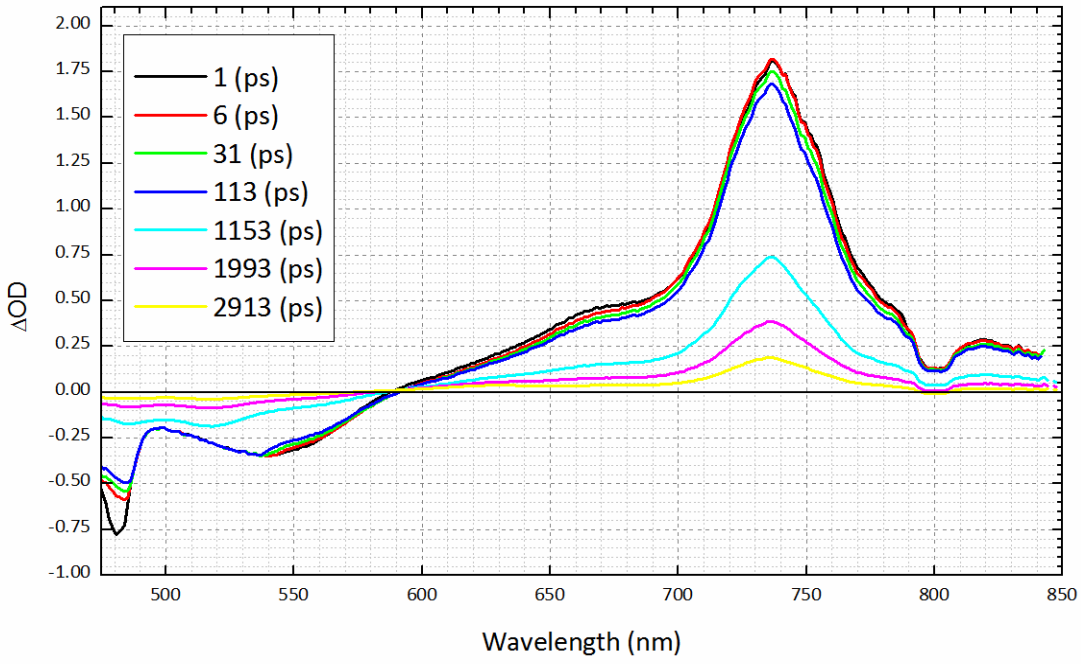

Figure A.6. Transient spectra of DABSB in dioxane at pumping power of 2.7 mW

(excitation = 475 nm).

In the presence of duroquinone, the slow component of the decay (1.30 ns) observed in the dioxane solution was reduced to 66 ps, suggesting that a new pathway with a large electron transfer rate may now exist for the formation of charged species. The comparison of the two decays at 720 nm is shown in Figure A.7.

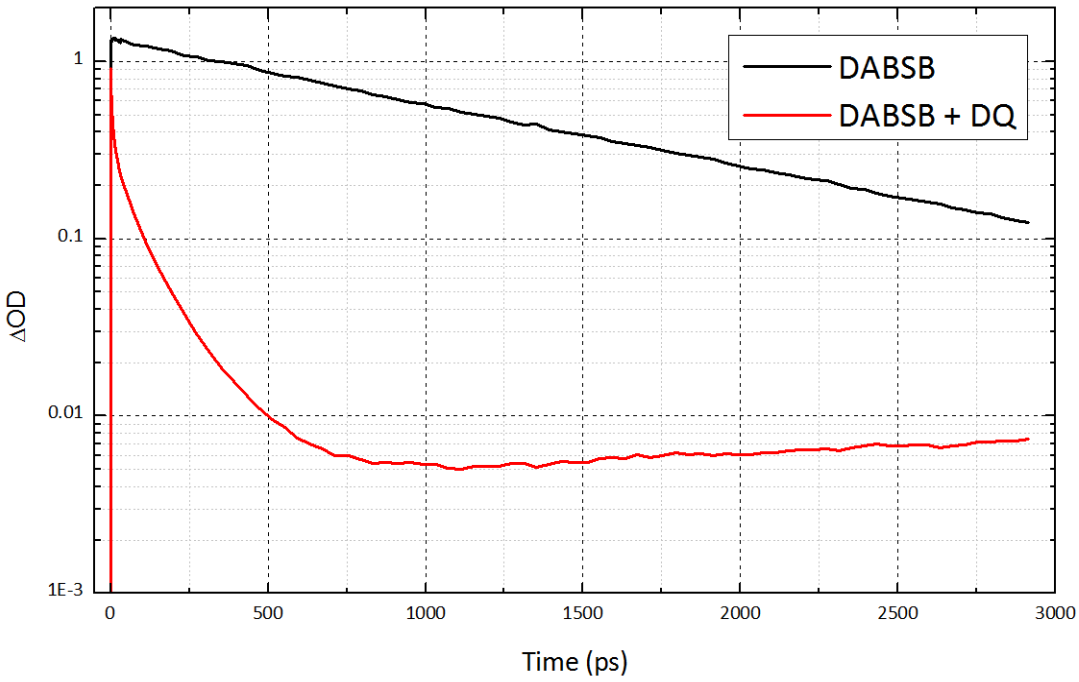

Figure A.7. Decay kinetics at 720 nm of DABSB with and without the presence of DQ acceptor at pumping power of 2.7 mW (excitation at 475 nm).

The TA spectrum observed immediately after excitation (i.e. 1 ps, see Figure A.8) is identical to the excited-state absorption spectrum found for DABSB previously. The formation of a long-lived species was observed at approximately 700 ps after the

excitation pulse (Figure A.7). This newly formed species showed broad absorption peaks at 660 and 740 nm (Figure A.8), similar to that of the chemically generated cation of DABSB in dichloromethane (691 and 782 nm, respectively, Figure A.9). The observed hypsochromic shift between the two spectra may be attributed to differences in solvent polarity. If one assumes that the peak absorption cross-sections of the excited-state and the cation are similar, the relative number of excited-state carriers versus generated charged species can be gauged by comparing the transient spectra in Figure A.8. Accordingly, it seems that the charged species have been reduced by nearly a factor of 100 compared to the initially prepared excited state. This discrepancy could be explained by noting that rapid recombination of the cations and electrons is likely due to the close proximity of the donor and acceptor. The residual cationic signal present at long delays may therefore simply originate from charge species that have diffused from the initial site of generation prior to recombination. This may also explain the delay in the observation of the cation-like spectrum following the initial decay of the excited state.

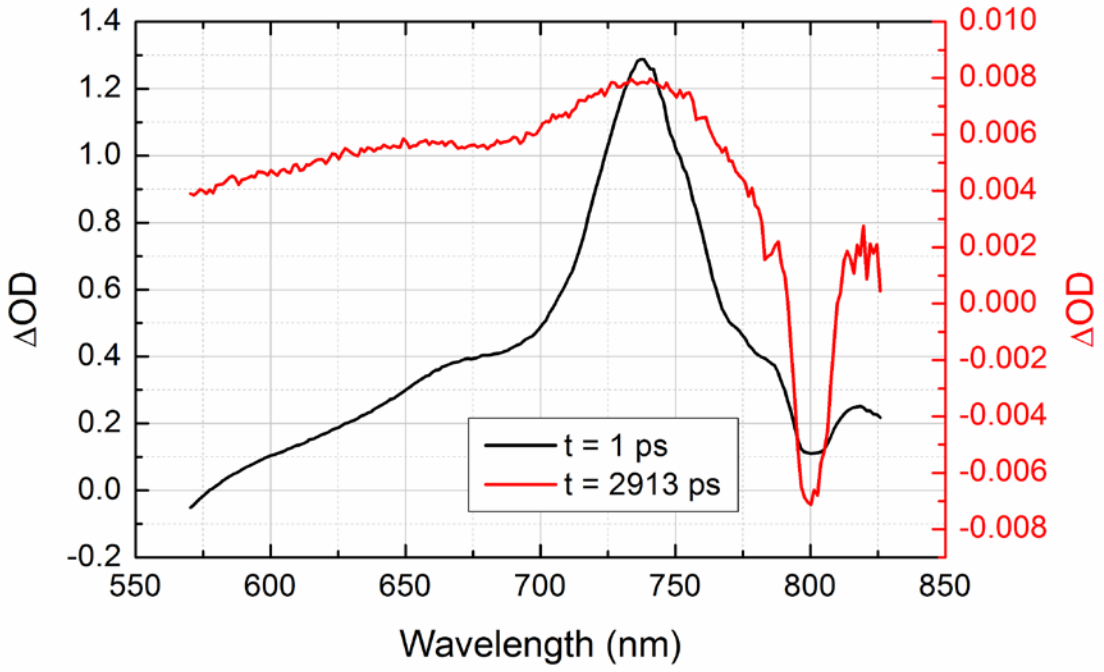

Figure A.8. Transient spectra of DABSB with DQ at pumping power of 2.7 mW

(excitation at 475 nm).

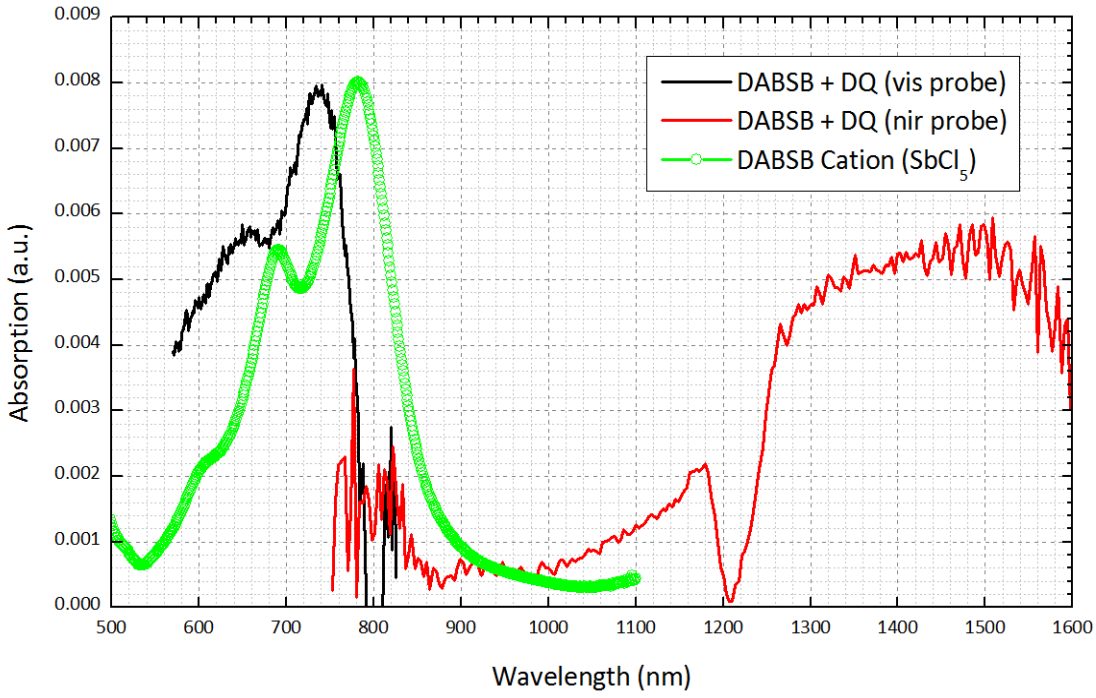

Figure A.9. Overlay of TA spectra of DABSB with acceptor (DQ) at 3 ns delay following excitation collected from visible and near infrared probes along with the DABSB cation spectrum generated by antimony pentachloride in dichloromethane (Cation data courtesy of Dr Mohanalingam Kathaperumal and Dr Thayumanvan Sankaran)

Near infrared probing of the DABSB dioxane solution revealed weak TA bands at 850 nm and 1400 nm (Figure A.10) that have lifetimes of 3 ps and 1.30 ns, suggesting the same decay from the lowest excited state as in the visible probing case. The lifetime of this species in the presence of duroquinone was also significantly shortened to 91 ps and a broad absorption band with a maximum at 1500 nm (Figure A.10) was observed at the same delay time as the cation species observed with the visible probe. The location

of this near-infrared absorption band is in close proximity to the cation spectrum of a closely-related *bis*-styryl benzene chromophore [13].

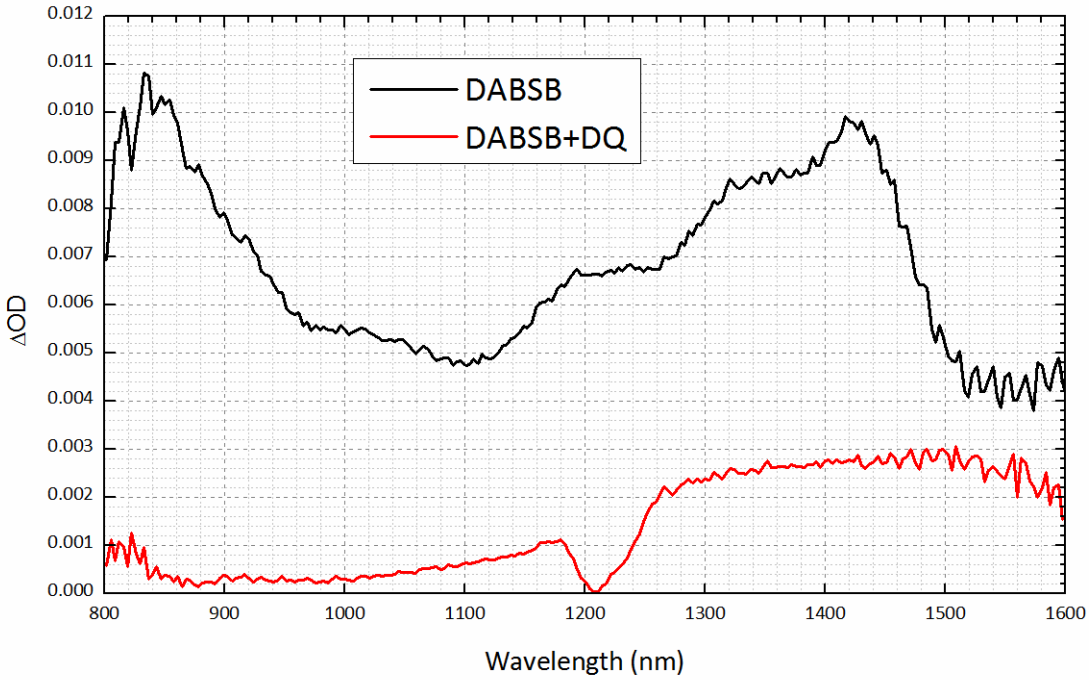

Figure A.10. Transient absorption spectra collected at 3 ns after excitation with and without the presence of acceptor (DQ) at pumping power of 2.7 mW (excitation at 475 nm). (Note the sharp dip at 1210 nm is an artifact and is not a feature of the cation absorption).

Linear excitation of DABSB in the acrylate monomer solution revealed similar spectral evolutions and decay kinetics as for the dioxane solution under the same excitation conditions. The decay kinetics showed two dominant decay components: the slow component exhibited the same lifetime of 1.30 ns, while the fast component showed a slower kinetic of 90 ps in acrylate versus 3 ps in dioxane, the latter difference likely resulting from conformational reorientation for solvents with different viscosities. Although no cation-like species was evident in the transient spectra, crosslinking of the

monomer in an unstirred solution was observed, suggesting that the number of cations needed to initiate the chain polymerization may simply be much lower than the number necessary for observation of TA. Given the weak efficiency for one-photon induced polymerization via UV excitation for this initiator/resin system, the observation of polymerization via one-photon excitation here was initially puzzling. However, given that the excitation pulses at 475 nm employed for TA deliver significant irradiances to the sample, the proposed routes for polymerization, either step-wise absorption induced electron transfer or multiphoton ionization, are still quite possible.

A.3.2 Two-photon excitation at 730 nm

Two-photon pumping at 730 nm of DABSB in dioxane showed excited state spectral features (Figure A.11) that were very similar to the one-photon pumped case. The early time kinetics however indicated a growth of this excited state absorption (lifetime of ~10 ps), suggesting rapid relaxation from a higher-lying two-photon excited state to the lowest one-photon excited state through internal conversion. This lowest one-photon excited state gave a lifetime of 1.0 ns in dioxane; this lifetime is shorter than the 475 nm excitation due to the additional rate of the population from the two-photon excited state. The two-photon pumping of the DABSB solution was meant to test the proposed mechanism of multiphoton ionization for initiation. There was no evidence of the cation-like species even at long temporal delays. Unfortunately, as mentioned above, this may simply be the result of an insufficient number of charged carriers being generated for the observation of the TA spectra.

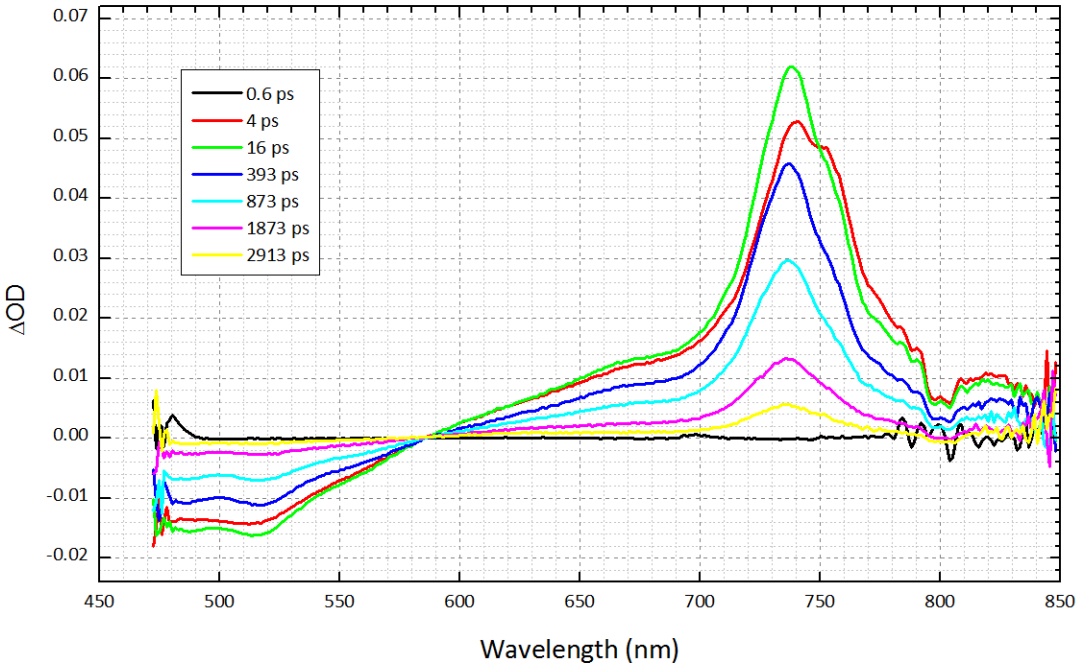

Figure A.11. Transient spectra at various delay times without acceptor at 3.2 mW excitation power (excitation at 730 nm).

Two-photon pumping of the duroquinone containing solution revealed a shortened lifetime from 1.00 ns to 55 ps, similar to the one-photon pumping case (Figure A.12). However, negligible cation absorption (691 and 782 nm) was observed in this case, likely due to the difference in excitation conditions. Whereas in one-photon excitation the number of molecules promoted to the excited state is proportional to the irradiance, two-photon pumping results in a quadratic irradiance dependence giving rise to a significantly yield of excited states. Comparison of the ΔODs for each excitation condition (Figures A.8 and A. 12) resulted in a 60 times reduction in the excited state population due to two-photon pumping (after accounting for the effective pathlengths). Given the small fraction of cations produced via one-photon pumping, it is clear that any

cation absorbance signal here would be reduced to well below the noise levels of the system.

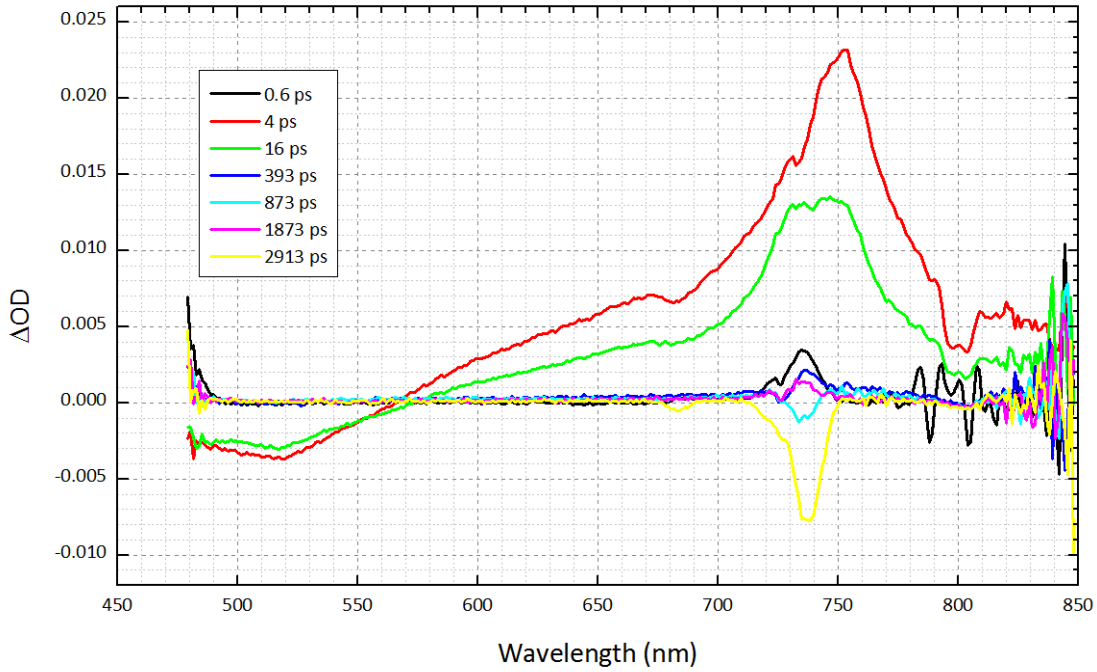

Figure A.12. Transient spectra at various delay times with acceptor at 3.0 mW pumping power (excitation at 730 nm).

Transient experiments in the monomer solution revealed early time kinetics similar to the 730 nm pumped dioxane solution. A 10 ps rise time was observed as the lowest excited state was populated after TPA. The decay from this excited state followed similar trends as the two-photon pumped dioxane sample and the one-photon pumped dioxane and monomer solutions with a lifetime of 1.00 ns. As with the one-photon pumped monomer solution, crosslinking was observed in the non-stirred sample with no observation of any cation-like signatures.

A.4 Conclusion

Femtosecond transient experiments of DABSB in solution revealed an S_1 excited-state that was populated under both one- and two-photon excitation conditions. This excited state exhibited strong absorption at 730 nm, which coincided with the maximum in the TPA spectrum. This suggested that the proposed initiation mechanism of step-wise excitation to a higher lying excited state followed by charge-transfer was plausible. This was further supported by TA spectra of DABSB in the presence of a duroquinone acceptor at delays >1 ns after excitation which were found to be similar to the chemically generated DABSB cation spectrum. Unfortunately, cation-like spectra were not observed in the monomer-containing solutions despite evidence of photoinduced crosslinking under both excitation conditions; however, this was likely due to the generation of a small population of charge carriers. Cation-like spectra in the DABSB-only solution under two-photon excitation were also not observed. This does not provide support for the proposed initiation mechanism of multiphoton ionization, however generation of a small population of carriers may once again prevent this. Consequently, transient absorption studies did not provide definitive support for either of the two proposed mechanisms for initiation. Additional investigations may provide a means for discriminating between these mechanisms. For example, crosslinking experiments with varying the redox levels of the accepting monomers could be used to determine the energy level at which initiation occurs for DABSB. Alternatively, a wavelength dependent one-photon crosslinking experiment of the triacrylate monomer containing solution could reveal the energy of the excited state that leads to initiation. As to the possible thermal initiation pathway, a calculation of the heat deposition under typical

microfabrication conditions or a temperature dependent crosslinking threshold study could reveal a difference in polymerization thresholds.

REFERENCES

1. B. H. Cumpston, S. P. Ananthavel, S. Barlow, D. L. Dyer, J. E. Ehrlich, L. L. Erskine, A. A. Heikal, S. M. Kuebler, I. Y. S. Lee, D. McCord-Maughon, J. Qin, H. Rockel, M. Rumi, X.-L. Wu, S. R. Marder, and J. W. Perry, "Two-photon polymerization initiators for three-dimensional optical data storage and microfabrication," Nature **398**, 51-54 (1999).

2. S. Kawata, H.-B. Sun, T. Tanaka, and K. Takada, "Finer features for functional microdevices," Nature **412**, 697-698 (2001).

3. L. Li, R. R. Gattass, E. Gershgoren, H. Hwang, and J. T. Fourkas, "Achieving λ/20 Resolution by One-Color Initiation and Deactivation of Polymerization," Science **324**, 910-913 (2009).

4. L. H. Nguyen, M. Straub, and M. Gu, "Acrylate-Based Photopolymer for Two-Photon Microfabrication and Photonic Applications," Advanced Functional Materials **15**, 209-216 (2005).

5. A. Rosspeintner, M. Griesser, N. Pucher, K. Iskra, R. Liska, and G. Gescheidt, "Toward the Photoinduced Reactivity of 1,5-Diphenylpenta-1,4-diyn-3-one (DPD): Real-Time Investigations by Magnetic Resonance," Macromolecules **42**, 8034-8038 (2009).

6. J.-F. Xing, W.-Q. Chen, X.-Z. Dong, T. Tanaka, X.-Y. Fang, X.-M. Duan, and S. Kawata, "Synthesis, optical and initiating properties of new two-photon polymerization initiators: 2,7-Bis(styryl)anthraquinone derivatives," Journal of Photochemistry and Photobiology A: Chemistry **189**, 398-404 (2007).

7. S. M. Kuebler, M. Rumi, T. Watanabe, K. Braun, B. H. Cumpston, A. A. Heikal, L. L. Erskine, S. Thayumanavan, and J. W. Perry, "Optimizing Two-Photon Initiators and Exposure Conditions for Three-Dimensional Lithographic Microfabrication," Journal of Photopolym. Sci. Technol **14**, 657-668 (2001).

8. M. Rumi, J. E. Ehrlich, A. A. Heikal, J. W. Perry, S. Barlow, Z. Hu, D. McCord-Maughon, T. C. Parker, H. Röckel, S. Thayumanavan, S. R. Marder, D. Beljonne, and J.-L. Brédas, "Structure−Property Relationships for Two-Photon Absorbing Chromophores: Bis-Donor Diphenylpolyene and Bis(styryl)benzene Derivatives," Journal of the American Chemical Society **122**, 9500-9510 (2000).

9. W. Haske, V. W. Chen, J. M. Hales, W. Dong, S. Barlow, S. R. Marder, and J. W. Perry, "65 nm feature sizes using visible wavelength 3-D multiphoton lithography," Opt. Express **15**, 3426-3436 (2007).

10. R. C. Dorfman, Y. Lin, and M. D. Fayer, "Experimental investigation of donor-acceptor electron transfer and back transfer in solid solutions," The Journal of Physical Chemistry **93**, 6388-6396 (1989).

11. S.-H. Chi, "Third-Order Nonlinear Optical Properties of Conjugated Polymers and Blends " (Georgia Institute of Technology, Atlanta, GA, 2009).

12. H. Xia, J. Yang, H.-H. Fang, Q.-D. Chen, H.-Y. Wang, X.-Q. Yu, Y.-G. Ma, M.-H. Jiang, and H.-B. Sun, "Efficient Two-Photon Excited Amplified Spontaneous Emission from Organic Single Crystals," ChemPhysChem **11**, 1871-1875 (2010).

13. S. Barlow, C. Risko, S.-J. Chung, N. M. Tucker, V. Coropceanu, S. C. Jones, Z. Levi, J.-L. Brédas, and S. R. Marder, "Intervalence Transitions in the Mixed-Valence Monocations of Bis(triarylamines) Linked with Vinylene and Phenylene−Vinylene Bridges," Journal of the American Chemical Society **127**, 16900-16911 (2005).

VITA

VINCENT WINGSANG CHEN

Vincent Chen was born in Hong Kong, China. He attended The King's School (Gloucester, United Kingdom) from 1994-1996, followed by John Dickinson High School (Wilmington, DE) from 1997-1999, received a B.A. in Chemistry from Boston College, Chestnut Hill, Massachusetts in 2003 before coming to Georgia Tech to pursue a doctorate in Chemistry and Biochemistry.